ROTOR-STATOR INTERACTION IN RADIAL FLOW PUMPS AND FANS AT SHUT-OFF CONDITIONS.

By

Timothy Mark Newton. BEng. (Hons) (Newcastle)

A Thesis submitted for the degree of

Doctor of Philosophy

University of Newcastle upon Tyne

1998.

ACKNOWLEDGEMENTS

The author wishes to extend his gratitude to his supervisor Dr. I. Potts for his invaluable guidance, enthusiasm, constructive criticism and enlightening and interesting discussions throughout this project.

The author also wishes to thank the following:

- ◊ EPSRC and Ingersoll-Dresser Pumps (Gateshead, UK) for funding this project.
- ◊ Professor Braiden, for allowing the use of the facilities available within the Department of Mechanical, Materials and Manufacturing Engineering at the University of Newcastle-upon-Tyne.
- ◊ The following technicians for their excellent work in constructing the experimental rig and help and advice throughout the project Mr D.Ross, Mr S.McGowan, Mr D.Simms, Mr M.Devine
- ◊ Mr D. Glennie for his invaluable help in the design, construction and integration of the electronic elements of the experimental rig.
- ◊ Mr. R. Palgrave for sharing his invaluable knowledge of the commercial design of pumps.
- ◊ Colleagues who have contributed directly or indirectly in completing the research.
- ◊ Olivia, for constant support and putting up with my long working hours.
- ◊ My family, for their constant support and encouragement throughout the project. In particular my parents for proof reading this thesis (Thanks).

ABSTRACT

The prediction of shut-off head within a centrifugal pump or fan has historically relied on the use of a combination of empirical formulae, together with experience. This reliance has been forced on designers due to both a lack of information regarding the flow at shut-off and the available tools with which to gain more accurate insights.

To improve understanding the following investigation examines the capability of the commercial CFD package, FLUENT, to model the flow in a centrifugal pump at shut-off conditions.

The computational model was validated using experimental measurements from a purpose built two-dimensional centrifugal pump rig. The rig used air as the working fluid and was similar in design to that used by Miner. Measurements were made of both the fluctuating velocities, using LDA, and the fluctuating pressures, using microphones, within the volute of the pump.

The CFD model uses a sliding mesh which enables the full time-dependent rotor/stator interaction of the pump to be modelled.

The results show the volute flow contains two patterns, a recirculating eddy in the outlet duct and a volute flow circulating around the rotor. This volute flow separates partway around the volute, with re-attachment on the discharge side of the tongue.

The major effect of the volute at shut-off is to act as a diffuser with a strong circumferential pressure gradient over approximately the first 120^0 after the tongue.

A comparison of the experimental and computational results showed that good qualitative agreement was obtained at most positions at shut-off and considerable insight was gained into the flow mechanisms.

However, the results showed that the CFD model over predicted the measured shut-off head by 25%. This was attributed to an over prediction of the effective viscosity due to the use of the k-ε turbulence model.

CONTENTS

Nomenclature

General

a	Casing coefficient, Eq. 1.17
a	Coefficient containing convection and diffusion contributions, Eq. 3.58
a	Radius of particle, Eq. 4.3
a	Speed of sound, Eq. 4.4
A	Coefficient containing convection and diffusion contributions
A	Area, Eq. 1.9
A	Ratio of impeller inlet radius/outlet radius, Eq. 1.16
A	Area normal to cell centre, Eq. 3.43
AR	Ratio of rotor outlet area/volute throat area, Eq. 1.23
b	Depth or height of blade
b	Pressure source term, Eq. 3.51
B	Ratio of outlet radius / cutwater radius, Eq. 1.16
C	Absolute velocity component.
C_μ	Constant, k-ε turbulence model, Eq. 3.27
	Constant, RNG k-ε turbulence model, Eq. 3.31
$C_{1\varepsilon}$	Constant, k-ε turbulence model, Eq. 3.29
$C_{2\varepsilon}$	Constant, k-ε turbulence model, Eq. 3.29
C_m	Dimensionless torque, Eq 1.24
d_f	Fringe spacing
d_m	Diameter of measurement volume
D	Diameter
D_{ij}	Curvature related term, Eq. 3.33
D_T	Diameter of Impeller, Eq. 4.1
E	Empirical constant, Eq. 3.36
E_{ij}	Mean deformation of fluid element.
f	Function, Eq. 3.55
f_U	Frequency of fluctuations, Eq. 4.3
g	Gravitational acceleration.

h_O	Impeller slip factor, Eq. 1.23
H	Head
H_d	Design Head, Eq. 1.20.
H_e	Euler Head, Eq. 1.9
H_i	Input Head, Eq. 1.13.
J	Flux, Eq. 3.44
k	Turbulent Kinetic energy
k_P	Turbulent kinetic energy at point P, Eq. 3.37 and 3.38
K	Impeller eye flow constant, Eq. 1.21
K_{HO}	Casing Constant, Eq. 1.15
l	Length
l	Length of tapping, Eq. 4.4
m	Mass, Eq. 1.1
nsq	Specific speed, Eq. 1.19
N	Impeller rotational speed, Eq. 120
N_f	Number of fringes
N_m	Minimum number of complete cycles required by signal processor
N_S	Dimensionless specific speed
p	Pressure
P_2	Impeller blade pitch at outlet, Eq. 1.24
Pe	Peclet Number, Eq. 3.47
q	Leakage flow rate
Q	Volume flow rate.
Q_d	Design flow, Eq. 1.20
r	Radius, Eq. 1.3.
r_m	Mean radius of volute, Eq. 1.27
r_4	Maximum radius of volute, Eq. 1.27
Re	Reynolds Number
Re_{ROT}	Rotational Reynolds Number, Eq. 4.1
R_{VOL}	Radius of volute, Eq. 4.2
S	General source term

S	Source term, Eq. 3.40
S	Area, Eq. 4.4
S_{ij}	Curvature related term, Eq. 3.33
S_{MX}	Source term, Eq. 3.3
u	Tangential velocity.
u_P	Local mean velocity, Eq. 3.37
u'	Fluctuating velocity component, Eq. 3.17
u^+	Dimensionless velocity, Eq. 3.34
v	Volume of cavity, Eq. 4.4
v	Voltage, Eq. 4.5
v_j	Velocity due to the movement of the grid, Eq. 3.56
w	Relative velocity.
w	Work done on the fluid per unit mass, Eq. 1.4.
y_P	Displacement from wall, Eq. 3.38
y^+	Dimensionless distance from wall, Eq. 3.34
z	Number of blades

Coordinates

i, j, k	Computational coordinate system
r, θ, z	Cylindrical coordinates
x, y, z	Rectilinear coordinates

Greek

α_S	Swirl constant, Eq. 3.32
β	Impeller blade angle
β_2	Angle between relative and tangential velocity
Γ	Diffusion coefficient, Eq. 3.45
δ	Area, Eq. 3.59
δ_A	Deviation Angle, Eq 1.24
ε	Dissipation of turbulent kinetic energy
η_H	Hydraulic efficiency

κ	Von Karman's constant, Eq. 3.36
θ	Angle, Eq. 4.2
θ_2	Blade angle at exit, Eq.1.23
θ	Tangential (subscript)
μ	Absolute viscosity
μ_{eff}	Effective viscosity
μ_{mol}	Molecular viscosity, Eq. 3.31
μ_t	Turbulent viscosity
ρ	Density
ρ_P	Destiny of the particle, Eq. 4.3
σ	Slip Factor
σ_ε	Constant, k-ε turbulence model, Eq. 3.28
σ_k	Constant, k-ε turbulence model, Eq. 3.29
σ_S	Stodola's slip Factor, Eq. 1.11
τ	Torque
τ_{ij}	Surface stress tensor
$\tau_{ij,t}$	Reynolds stress tensor, Eq.3.57
τ_O	Wall shear stress, Eq. 3.37
ϕ	General conserved quantity
ϕ_r	Recirculatory flow coefficient, Eq 1.23 and Eq1.25
υ	Kinematic viscosity.
ψ	Flow factor
ω	Angular velocity
Ω	Angular velocity of impeller, Eq. 1.27.

Subscript & Superscript

'	Corrected value, Eq. 3.51
'	Ideal conditions.
*	Guessed value, Eq. 3.49
1	Impeller inlet

2	Impeller exit
4	Cutwater, Eq. 1.18
e	East
e	Euler
imp	Impeller
n	North
N	Nominal flow rate
o	Zero Flow
r	Radial
s	South
s	Suction pipe
so	Shut - off
t	Time
TOTAL	Total
vol	Volute
w	West
z	Axial

List of Figures

List of Tables

CHAPTER 1:
INTRODUCTION & BACKGROUND

1.1 Overview

Today's centrifugal pumps are expected to operate efficiently and stably over a wide range of flow rates. To produce this level of performance detailed knowledge of the flow structure within the volute and impeller is essential. The acquisition of this data can be accomplished either experimentally by the taking of measurements or by the generation of a computational model to predict data.

Computational prediction methods have many advantages over experimental methods. Lower operational costs are incurred with no need to manufacture or operate expensive test rigs. Alterations can be made to the pump's geometry within the computational model with relative ease. The pressure and velocity data can be obtained at any point within the computational domain, instead of at fixed measuring points in an experimental rig.

However, while these advantages are significant, it is necessary to show caution over the validity of the numerical results produced from computer modelling. For this reason, before any computational method can be seriously considered as an alternative to experimental measurements, testing is required to verify its accuracy.

Researchers within the pump industry have already started the process of verifying computational models with experimental data. However, most have concentrated on obtaining flow data at design conditions, and only brief consideration has been given to other flow rates.

This study is a continuation of research into the validation of computational models using experimental data. The primary focus has been the rarely

researched aspect of flow distribution at shut-off, rather than the more frequently researched design flow.

Flow patterns at shut-off have received little attention by industry. Consequently they are less well understood and are believed by many to be the most complicated flow patterns to be found in centrifugal pumps. This lack of understanding is underlined by the continued use of empirical formulae to predict shut-off head in new pump designs, which may have had the effect of impeding the advancement in the development of pumps.

Computationally, a major difference between this study and previous work on centrifugal pumps, is the application of the sliding mesh method to the model. The use of the sliding mesh enabled the full interaction between the impeller and volute to be modelled thus allowing the unsteady velocity and pressure data to be obtained.

This thesis presents a comparison between computational and experimental results for a two-dimensional centrifugal pump operated at shut-off. The objective of the study was to determine the validity of a computational model, and then to use this data to gain an insight into the flow structure within a centrifugal pump at shut-off condition.

Experimentally, the unsteady pressure field was measured using a condenser microphone in conjunction with static tappings within the volute. The pressure measurements were supplemented with velocity field data collected within the volute using Laser Doppler Anemometry (LDA).

The computational results were generated using the commercial Computational Fluid Dynamics (CFD) package, Fluent version 4.4. This package is a finite volume, full Navier-Stokes solver. In this study, Fluent has been used to model simultaneously both the impeller and volute thus enabling the interaction between the two components to develop naturally.

Comparisons are made between the experimental data and the solution obtained from Fluent thus enabling an evaluation to be made of the effectiveness of using CFD to model pump flow at shut-off.

Before proceeding it is important to define exactly what the terms shut-off or closed valve head actually mean. A common misconception is that shut-off is zero flow on the head-flow characteristic. This is only true if measures are taken to eliminate leakage flow. For most pumps there will always be a small, but finite amount of leakage from the high-pressure exit of the impeller back to the low-pressure inlet via the shroud and casing (Figure 1.1). However leakage in the majority of pumps is small, approximately one to five percent of the design flow, depending on the sealing and clearances. This means that the difference between shut-off head with no leakage and shut-off with leakage is usually small enough to be neglected.

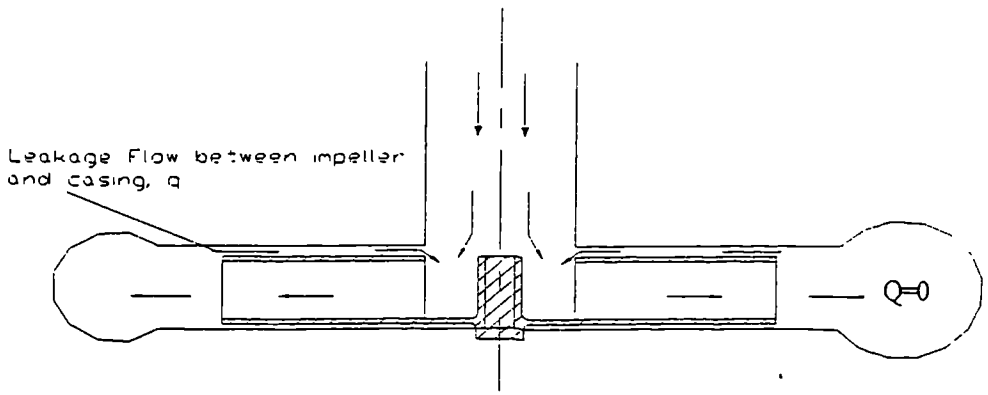

Figure 1.1. Leakage within in a Centrifugal Pump.

1.2 Background - An Introduction To Predicting Performance

For any new pump, the designer needs to know how that pump will behave at different flow rates. A starting point is the application of the Euler pump equation, which considers the transfer of energy from the impeller to the fluid by applying Newton's second law of motion to a stream of fluid particles passing through the rotating impeller.

The method is based on the relationship:

> Torque about an axis = Rate of increase of angular momentum about that axis

Applying the above statement to a system of mass, m, the sum of the external torques acting on the system, about an axis, is equal to the time rate of change of angular momentum. This can be written as,

$$\tau = m\frac{d}{dt}(rc_\theta) \qquad (1.1)$$

where r is the normal distance to the centre of the mass from the axis of rotation and c_θ is the velocity component perpendicular to both the axis and the radius vector **r**.

The law of moment of momentum can be applied to a control volume enclosing an impeller. Figure 1.2 displays a typical centrifugal pump impeller in which swirling fluid enters the control volume at r_1 with tangential velocity, $c_{\theta 1}$ and leaves at radius r_2 with tangential velocity, $c_{\theta 2}$. For one dimensional steady flow through the impeller,

$$\tau = \dot{m}(r_2 c_{\theta 2} - r_1 c_{\theta 1}) \qquad (1.2)$$

The rate at which the rotor does work on the fluid is given as

$$\tau\omega = \dot{m}(u_2 c_{\theta 2} - u_1 c_{\theta 1}) \qquad (1.3)$$

where the blade speed is $u = \omega r$.

The Euler pump equation gives the work done on the fluid per unit mass, *w* as:

$$w = \frac{\tau\omega}{\dot{m}} = u_2 c_{\theta 2} - u_1 c_{\theta 1} \qquad (1.4)$$

The Euler pump equation can be combined with the steady flow energy equation to give the ideal or theoretical head developed in an impeller. This is named the Euler head equation and is given as,

$$H_e = (u_2 c_{\theta 2} - u_1 c_{\theta 1})/g \qquad (1.5)$$

The equation does not take into account losses within the pump, or the effect the volute may have on the flow. It can only supply a theoretical maximum possible head rise for a particular pump impeller.

It is usual to assume zero pre-rotation at the impeller inlet. In this case the absolute velocity at inlet $c_{\theta 1}$ is taken as zero so $c_1 = c_{r1}$. The Euler head equation is now reduced to

$$H_e = (u_2 c_{\theta 2})/g \qquad (1.6)$$

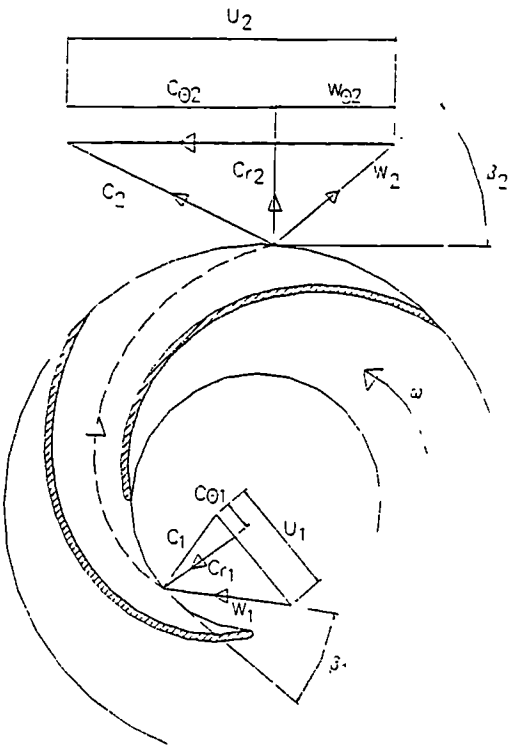

Figure 1.2 Velocity Triangles Applied to the Inlet and Outlet of a Centrifugal Pump Impeller.

Assuming that the fluid leaves the impeller with relative velocity fixed by the vane angle β'_2, as in Figure1.2, it is possible to rewrite the absolute tangential velocity at exit $c_{\theta 2}$ as follows:

$$c_{\theta 2} = u_2 - w_{\theta 2} = u_2 - c_{r2}\cot\beta'_2 \qquad (1.8)$$

The Euler head equation can now be written as

$$H_e = u_2\left(u_2 - \left(Q/A\right)\cot\beta'_2\right)/g \qquad (1.9)$$

where A is the flow area at the impeller outlet.

Equation(1.9) predicts a linearly falling head rise characteristic, with the maximum head being

$$He_o = u_2^2/g \qquad (1.10)$$

at zero flow. This prediction of shut-off head can only regarded as a limiting value, however, since the Euler pump equation is derived assuming a steady mass flow through the impeller, which is clearly not the case here. Nevertheless, this result provides a useful reference value for shut-off head correlations.

The derivation of the Euler head equation assumed the fluid leaving the impeller left the blade passage with the same angle as the blade exit angle (β'_2). This would be true if the impeller had an infinite number of blades to perfectly guide the flow. Most centrifugal pumps, however, have only a few blades and a phenomenon called fluid slip occurs. Slip causes the fluid at the impeller exit to leave at an angle different from the blade exit angle. This, in turn results in a reduction in the absolute tangential velocity at exit (reduced $c_{\theta 2}$).

A simple explanation of the effect of slip can be given in terms of a relative eddy, and this is described by Dixon(1975). For a frictionless fluid entering the impeller without rotation, then at the outlet of the impeller the fluid must also be irrotational. If the impeller rotates with an angular velocity, ω,

then the flow relative to the impeller must have an angular velocity -ω, to maintain this condition of irrotationality at outlet.

The relative flow at the outlet of an impeller may be regarded as a through flow on which a relative eddy is superimposed. The consequence of these two motions is that, at exit, the flow leaves the impeller with an angle β_2 instead of β'_2, and the value of the absolute whirl velocity, $c_{\theta 2}$ is reduced (see Figure 1.3). The difference between the ideal $c'_{\theta 2}$ and the reduced $c_{\theta 2}$ is referred to as slip, and a slip factor maybe defined as:

$$\text{SLIP FACTOR} = c_{\theta 2} / c'_{\theta 2} = \sigma \qquad (1.11)$$

There have been many publications that present slip prediction methods within pumps and compressors. A comprehensive review paper was presented by Wiesner(1967) which examined a large selection of these slip prediction methods.

One of the earliest methods for approximating slip using a relative eddy within the blade passage was presented by Stodola(1927). A derivation of Stodola's slip factor can be found in Sayers(1990) or Dixon(1975). Stodola's slip factor is given as

$$\sigma_s = 1 - (\pi \sin\beta_2) / \{Z[1 - (C_{r2} / U_2)\cot\beta'_2]\} \qquad (1.12)$$

where *Z* is the number of impeller blades.

A mathematically exact solution for the relative eddy was obtained by Busemann(1928). He applied his theory to the special case of a two-dimensional impeller with logarithmic blades, and this is discussed in length in Wislicenus(1947). The Busemann slip factor can be written as

$$\sigma_B = (A - B\phi_2 \tan\beta'_2) / (1 - \phi_2 \tan\beta'_2) \qquad (1.13)$$

where *A* and *B* are functions of r_2/r_1, β'_2 and the number of blades.

The purpose of the slip factor is to modify the Euler head equation to take account of the relative eddy. The new head equation with slip accounted for, is called the 'input head' and is given as,

$$H_i = \sigma H_e \qquad (1.14)$$

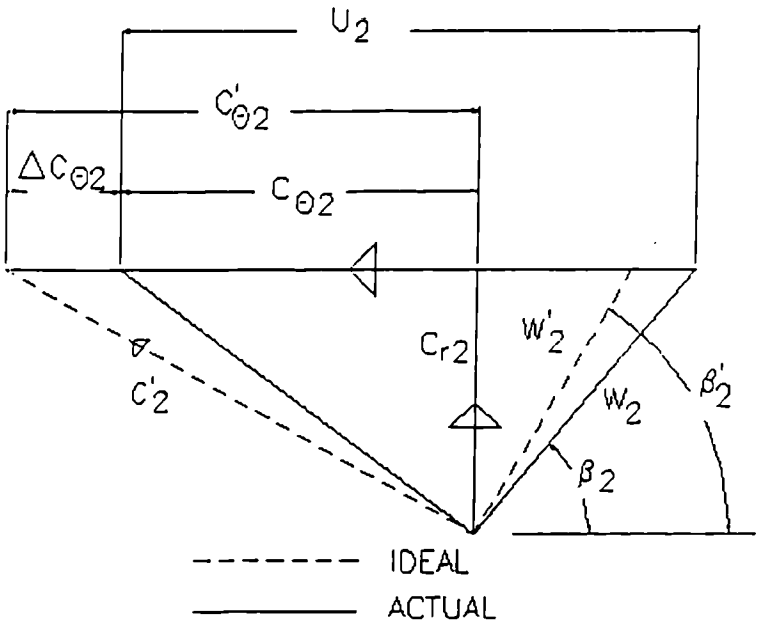

Figure 1.3. Velocity Distribution at Impeller Exit with Slip accounted for.

A comparison between experimental measurements obtained by Miner(1988) with the Euler head equation, with and without slip, is presented in Figure 1.4. The results show that the use of the slip factor reduces the theoretical Euler head and produces improved agreement with the experimental data. This is particularly true near the design flow of $0.0063 m^3/s$, where the Euler head equation without slip, over predicts the measured value by 95% while the Euler head equation using the Stodola slip factor over predicts by 25%. At shut-off, the Euler head was found to over predict by 80%, whereas the Euler head using Stodola over predicted by 60%.

The Euler pump equation with slip correction is particularly suited to design conditions. However it is less useful as a prediction tool when determining shut-off head. This inability to predict shut-off head demonstrates a difficulty that has faced pump designers for a long time.

From Figure 1.4 it can be seen that the shut-off head provides a useful starting point on the actual head-flow characteristic curve of a pump. Pump designers also know from experience that the value of the shut-off head and the shape of the characteristic curve near it also give an indication of the stability of the pump at low flows.

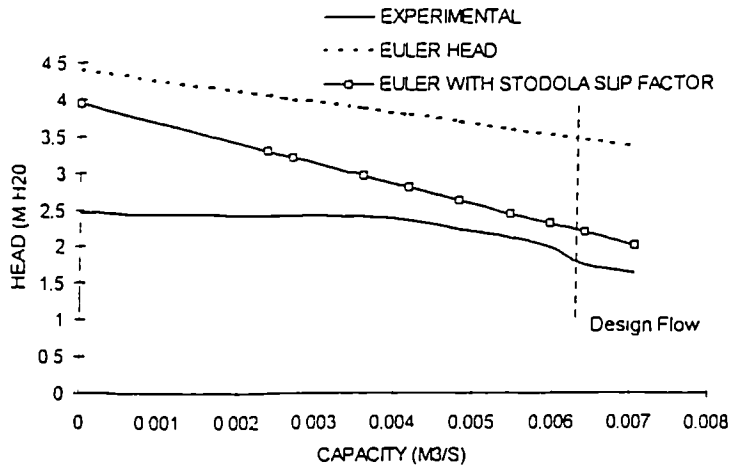

Figure 1.4. Characteristic Curve For Miner's(1988) Pump Comparison between Prediction and Measurement.

It is common practice within the pump industry to produce pumps with steadily rising head-flow characteristics. That is, the head is expected to increase steadily with a reduction in the flow rate. However, this is not always possible and in practice the head in some pumps, at low flow rates, will start to decrease as the flow rate decreases. This causes what is generally known as a drooping characteristic.

There is strong popular opinion amongst pump users that a drooping characteristic curve will cause instabilities during operation and this is

commonly reflected in pump specification codes. However, Yedidiah(1993), demonstrated that in practice these instabilities are infrequent. He proposed the general rule: whenever the shut-off H_o of the pump is higher than the head against which the fluid is to be delivered, the droop in the characteristic curve cannot cause any instabilities in the performance of the pump.

The ability to accurately predict the shut-off head can assist pump designers in two ways. Firstly, it can allow a pump with a steadily rising characteristic to be designed in order to satisfy common user requirements. Secondly, it can allow a pump with a drooping characteristic to be designed in such a way that the pump will still operate stably at low flows, based on Yedidiah's criteria.

An extensive literature search found there had been few attempts to formulate a method for predicting shut-off. One reason for the lack of procedures is that at shut-off the flow in the pump is very complicated. In fact, Worster(1963) noted this when he remarked that 'pump behaviour near zero delivery is the greatest problem facing the pump designer today'. Most of the available methods for predicting shut-off are empirically based, derived from experimental measurements over a range of pumps, or from fine tuning previous results and methods.

1.3 Background - Shut-Off Head Prediction Methods

The following section of work examines shut-off head prediction methods accessible from the literature. However, these are not the only prediction methods in existence, as pump manufacturers will, of course, have their own confidential formulas and procedures.

One of the first shut-off head prediction methods to appear in print was produced by Stepanoff(1957). He proposed a simple formula for calculating shut-off head as

$$H_{SO} = \Psi_{SO} \frac{u_2^2}{g} \qquad (1.15)$$

The method is based on the basic Euler head equation(1.10) with a shut-off head factor. The value of the factor was given as ψso=0.585 and is constant and independent of the pump geometry for which the formula is being applied. Stepanoff does not specify in his work how the value of the shut-off head factor was obtained and one can only assume it had been derived from experimental data.

A method for designing pumps was presented by Peck(1968). He was interested in determining the shut-off head to ensure the stability of a pump when operating at low flows. The formula proposed was given as,

$$H_{SO} = \frac{K_{HO}}{2}\left(\frac{u_2^2}{g}\right) \qquad (1.16)$$

The value of constant K_{HO} depends on the type of pump under consideration. For a volute casing pump K_{HO} =1.0 to 1.1, and for a pump using diffuser vanes K_{HO} = 1.15 to 1.25. No explanation was given for how the values of K_{HO} were obtained. This prediction method is again based on the Euler head equation.

In an investigation into the effect of geometry on the shut-off head, Thorne(1988) used a complex formula derived by Pfleiderer(1961) for calculating the shut-off head. The expression given by Thorne is as follows:

$$H_{SO} = \frac{u_2^2}{g}\left[\frac{1}{SLIP} - \left(\frac{C_{1r}}{2U_1}\right)\left(A^2 + \frac{B^2}{SLIP^2}\right)\right] \qquad (1.17)$$

where *A* is the ratio of impeller inlet radius/outlet radius and B is the outlet radius /cutwater radius.

Thorne defines 'Slip' as,

$$SLIP = 1 + \left(\frac{a}{Z}\right)\left(\frac{1+\beta_2}{60}\right)\left(\frac{2}{1-\left(\frac{D_1}{D_2}\right)^2}\right) \qquad (1.18)$$

The value of the casing coefficient '*a*' is assumed to be constant and equal to 0.77. However, the equation quoted by Thorne differs from the original formula given by Pfleiderer, whose expression for shut-off head is:

$$H_o = \frac{u_2^2}{g}\left\{\frac{1}{1+p} - \frac{\psi}{2}\left[\left(\frac{D_1}{D_2}\right)^2 + \left(\frac{D_2}{D_4}\right)^2\left(\frac{1}{1+p}\right)^2\right]\right\} \qquad (1.19)$$

where slip is represented by $1/(1+p)$ and is the same as the $1/(SLIP)$ term presented by Thorne. D_1/D_2 is equivalent to A and D_2/D_4 equivalent to B.

The discrepancy between Pfleiderer and Thorne is the value given to ψ(equation 1.19). Thorne defined ψ as a flow coefficient taken at design conditions. Pfleiderer, on the other hand, defined a value for ψ which contained the hydraulic efficiency as well as a flow coefficient at design. As Frost(1991) pointed out, this is a clear inconsistency, although the values obtained by Thorne did give good agreement for a range of geometries and blade numbers.

A method for predicting the complete characteristic for a centrifugal pump, from shut-off to design flow, was developed by Patel(1981). An expression was obtained for the shut-off head by testing a range of pumps within the 12 - 50 specific speed range. A graph was then plotted showing the relationship between a shut-off head factor and the pump's specific speed. Patel identified a trend in his results and obtained the following expression for the shut-off head factor from the experimental data:

$$\Psi_{SO} = 0.65 - 0.004nsq \qquad (1.20)$$

where nsq is the metric specific speed and is given as:

$$nsq = NQ_d/(H_d)^{3/4} \qquad (1.21)$$

where N is the pump speed Q_d is the volume rate of flow at design and H_d is the output head at design.

The shut-off head is given by

$$H_{SO} = \Psi_{SO} He_o = \Psi_{SO} u_2^2 / g \qquad (1.22)$$

He_{SO} is the theoretical Euler pump head at shut-off. The method combines the Euler head equation, to obtain the maximum head rise within the pump, with a shut-off head factor, obtained from experimental data.

An empirical method for predicting the performance within a pump from known impeller and volute data was presented by Chiappe(1982). The method involved constructing a dimensionless velocity diagram on a specially designed grid. The empirical formula used to calculate the shut-off head, is given as

$$H_{SO} = k\Psi_{SO} u_2^2 \frac{\eta_H}{g} \qquad (1.23)$$

The hydraulic efficiency, η_H is assumed constant at 90%. The value of constant *k* can vary between 0.8 and 0.72 depending on the flow conditions at the impeller eye. The value of the shut-off head factor, ψ_{so}, is obtained by following a series of procedures on a graph presented by Chiappe(1982).

Stirling's(1982) method for predicting the performance of a centrifugal pump used NEL methods. The shut-off head comprised two contributions, one from the impeller and the other from the volute. The contribution from the impeller, was derived by Levin and Poliokovsky(1965) who investigated recirculatory flow in a free impeller at shut-off. Stirling assumed that the expression obtained by Levin would remain valid when a volute enclosed the impeller. The expression for the impeller head rise is,

$$H_{SO}^{IMP} = \frac{1}{2g}\left[u_2^2 - \frac{u_1^2}{2}\right] \qquad (1.24)$$

The contribution from the volute is, however, much more complicated to calculate. Stirling assumed that in addition to the head rise across the impeller there was also recirculatory flow through the volute. This flow impacts against the stationary flow in the volute throat and causes a head rise in the volute outlet. The volute contribution is given as:

$$H_{SO}^{VOL} = \frac{u_2^2}{2g}\left[h_O - \frac{\phi_R}{\tan(\theta_2 - \delta_A)}\right]\phi_R AR \qquad (1.25)$$

where AR is the ratio of rotor outlet area to volute throat area. The impeller slip factor, h_O is Wiesner's(1967) approximation of Busemann's slip factor. θ_2 is the blade angle at impeller exit, and δ_A the 'deviation' angle is given by Myles(1965) as:

$$\delta_A = 1.75 \times 10^{-3}\left(\frac{P_2}{C_m}\theta_2\right) \qquad (1.26)$$

where P_2 is the impeller blade pitch at r_2 and C_m is a coefficient which takes into a account the thickness of a rotating disc when calculating it's disc friction.

A recirculatory flow factor, ϕ_R, was evaluated empirically by analysing a number of machines, and given as:

$$\phi_R = -0.2331\left(\frac{r_1}{r_2}\right) + 0.1952 \qquad (1.27)$$

The most significant work to date on the prediction of shut-off head has been by Frost and Nilsen(1991). Like Stirling, they proposed a model that estimated the separate contributions developed by the impeller and the volute at shut-off with the sum of these two contributions providing the final shut-off head. The most important difference between the two procedures is the way in which a solution is obtained. The method proposed by Stirling is entirely empirically based whereas Frost's method was analytically based.

The contribution of the impeller to the overall head rise in Frost's method was determined on the assumption that the flow obeyed solid body rotation. This is given as:

$$H_{SO}^{IMP} = \frac{u_2^2}{2g}\left[1 - \left(\frac{r_1}{r_2}\right)^2\right] \qquad (1.28)$$

Frost and Nilsen were uncertain of the value of r_1 and identified three possibilities:

◊ The impeller blade inlet radius.

◊ The radius of the suction pipe.

◊ Zero, due to the fact that forced vortex rotation will spread to the centre-line.

The head contribution of the volute was obtained by assuming that the velocity distribution within the diffuser satisfied the following three flow conditions:

◊ The velocity at the exit of the impeller is equal to the blade velocity.

◊ There is no net flow in the discharge duct.

◊ There is continuity of the recirculating flow in the volute(see Figure 1.5)

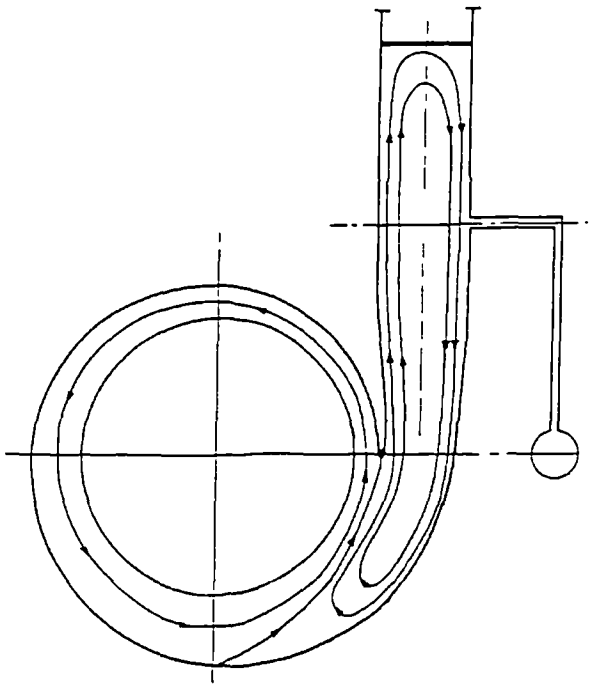

Figure 1.5 Frost's (1991) Proposed Flow Pattern at Shut-off.

Taking the above assumptions into account, Frost proposed the contribution of the volute to be:

$$H_{SO}^{VOL} = \left(\frac{\Omega r_2}{r_m - r_2}\right)^2 \left[r_m^2 \ln\frac{r_4}{r_2} - 2r_m(r_4 - r_2) + \frac{r_4^2 - r_2^2}{2} \right] \frac{1}{g} \qquad (1.29)$$

where r_4 is the maximum radius of the volute at the outlet branch and r_m =(radius at tongue + r_4)/2, defined in Appendix A. The final shut-off head is given by the sum of the impeller(equation 1.28) and volute(equation 1.29) contributions as:

$$H_{SO}^{TOTAL} = H_{SO}^{IMP} + H_{SO}^{VOL} \qquad (1.30)$$

The prediction methods examined in this chapter can be split into two groups.

Group 1 methods are based on obtaining a fraction of the maximum possible head rise for an impeller. This head rise, in each case, has been found using the Euler head equation. The difference between each of the methods in group one is the procedure used to determine the value of the shut-off head factor. It is interesting to note that, although each method calculates the shut-off head factor based on different parameters, the final values obtained are surprisingly similar.

Table 1.1 compares values of shut-off head factor for a selection of calculation methods. The similarity in value was demonstrated experimentally by Nilsen(1989) who found the value of the shut-off head factor for a range of fourteen industrial pumps was $\psi_{SO} = 0.55 \pm 0.09$.

Author	Value of Shut-off Head Factor
Patel	0.526 ± 0.076
Peck	0.5 to 0.55
Stepanoff	0.585

Table 1.1 Comparison of Shut-Off Head Coefficients.

Engeda and Rautenberg(1989) commented in their study on the treatment of shut-off, "Even though the conditions at shut-off differ considerably from the ideal assumption of no flow, it is surprising that the head developed is actually nearly $u_2^2 / 2g$."

Group 2 are similar to group one methods in that they use the Euler head equation, however in group two methods the individual head contributions from the impeller and volute are calculated separately. As stated before, Stirling's method is completely empirically based and its application depends on the ability to determine the value of various coefficients for a particular pump design. This reliance on previously obtained experimental results limits the range of pumps for which Stirling's formula can be accurately applied. The method proposed by Frost and Nilsen only requires a pump's geometrical parameters to determine the shut-off head and so can be applied to a complete range of pumps. However, one must recognise that Frost's method depended on the validity of the flow distribution described in his paper being valid.

The previous section clearly demonstrates the problems facing designers when predicting shut-off head. Only the method suggested by Frost and Nilsen attempted to understand the flow structure in order to present an analytical prediction method.

Table 1.2 summaries all the prediction methods discussed, whilst a comparison of the methods when applied to Miner's pump geometry can be found in Appendix A.

Author	Formula For Calculating Shut-Off Head	Group
Chiappe	$H_{SO} = k\Psi_{SO}\eta_H \frac{u_2^2}{g}$	1
Patel	$H_{SO} = \Psi_{SO} \frac{u_2^2}{g}$	1
Peck	$H_{So} = \frac{K_{HO}}{2}\left(\frac{u_2^2}{g}\right)$	1
Pfleiderer	$H_{SO} = \frac{u_2^2}{g}\left[\frac{1}{SLIP} - \left(\frac{C_{1M}}{2U_1}\right)\left(A^2 + \frac{B^2}{SLIP^2}\right)\right]$	1
Stepanoff	$H_{SO} = \Psi_{SO} \frac{u_2^2}{g}$	1
Frost	$H_{SO} = \frac{u_2^2}{2g}\left[1 - \left(\frac{r_S}{r_2}\right)^2\right]$ $+\left(\frac{\Omega r_2}{r_m - r_2}\right)^2\left[r_m^2 \ln\frac{r_4}{r_2} - 2r_m(r_4 - r_2) + \frac{r_4^2 - r_2^2}{2}\right]\frac{1}{g}$	2
Stirling	$H_{SO} = \frac{1}{2g}\left[u_2^2 - \frac{u_1^2}{2}\right]$ $+\frac{u_2^2}{2g}\left[h_O - \frac{\phi_R}{\tan(\theta_2 - \delta_A)}\right]\phi_R AR$	2

Table 1.2 Formulas for Calculating Shut-off Head

1.4 Background - Shut-Off Head Experimental Results

Experimental data taken at shut-off, describing both the pressure and velocity field, would give the designer a greater understanding and lead to improved prediction methods.

A literature search reveals that to date, very little experimental work has been performed at shut-off conditions. The lack of experimental data explains why pump designers have had to rely on empirical prediction methods. However, it is important to understand that researchers may have been discouraged by the problems which occur when operating a pump at shut-off for any length of time. These problems include vibration, noise, excess wear and heating of the working fluid.

The following review examines current experimental work found in the literature in the public domain.

One of the first experimental studies which examined the flow at shut-off was performed by Acosta and Bowerman(1957). They used flow visualisation and blade surface pressure taps to examine an impeller operating in a circular tank, hence with no volute interaction. Their study found the flow in the impeller was split into two sections. At the inner section of the impeller, up to $r/r_2 \approx 0.8$, the flow demonstrated solid body rotation, whilst at the outer section a relative eddy was detected. Acosta and co-worker described this eddy as an "irregular pulsating rotation opposite to the direction of impeller rotation".

In his ground breaking paper, Worster(1963) considered the problem of pump behaviour near shut-off. He found the pressure across the volute throat was practically constant and equal to the delivery pressure, while the surface pressure on the rest of the volute was lower. He was aware of "considerable flow in and out of the impeller". Worster proposed this as the reason why the actual shut-off head never reaches the theoretical value

Worster's results also demonstrated that at shut-off, the volute was responsible for approximately twenty percent of the overall head rise. This suggests a serious flaw in methods based on calculating the head rise in the impeller only.

A flow visualisation study by Simpson and Cinnamond(1963) used a photographic technique to give qualitative measurements of the relative flow in a pump impeller. The measurements were made at low flow and shut-off conditions with the impeller discharging into a concentric casing. Like Acosta and Bowerman they found, at shut-off, a large eddy at the exit of the impeller that circulated in the opposite direction to that of the impeller. However, they also found an eddy at the impeller inlet that circulated with the impeller (Figure 1.6).

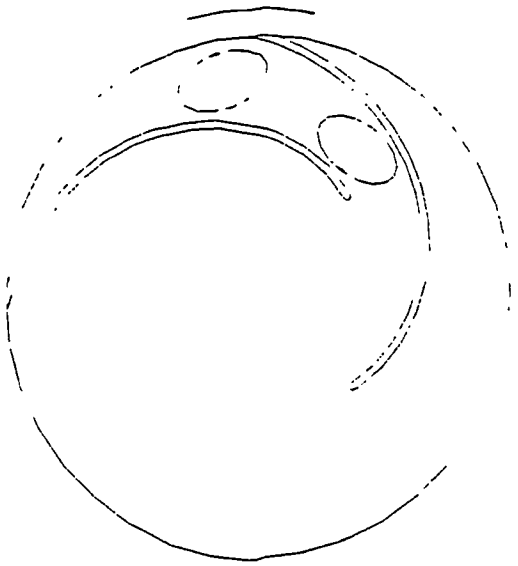

Figure 1.6. Flow Pattern at Shut-Off from Simpson and Cinnamond(1963).

A flow pattern similar to the one discovered by Simpson and Cinnamond, has been reported more recently by Senoo and Yamaguchi(1987). They examined a Francis-type pump, which had eight backswept vanes. The flow at discharge was collected by twenty guide vanes that were positioned at the outlet of the rotor.

A flow visualisation study using a hydrogen bubble technique was performed by Lennemann and Howard (1970). The study examined the unsteady relative flow in fourteen bladed, shrouded and unshrouded, radial impellers operating at shut-off. A vaneless diffuser with parallel walls was used to collect the flow.

Their study found similar flow patterns occurred in both impellers at shut-off. This pattern could be characterised by the flow in the blade passage coming almost to a standstill, except at the impeller discharge. Here a relative eddy rotated in the opposite direction to that of the impeller's rotation. The only difference between the two impellers was the strength of the eddying motion. This was found to be much stronger in the unshrouded impeller The investigators believed this relative eddy provided momentum exchange between the impeller and diffuser flows.

The flow pattern described by Lennemann and Howard agreed with the findings by Acosta and Bowerman in that there is solid body rotation at the impeller's inlet, and a relative eddy positioned towards the outlet. However, the flow patterns differ from those visualised by Simpson and Cinnamond and Senoo and Yamaguchi.

It is impossible, using the information given to attribute the differences between the experimental flow patterns to a single cause or factor. However, the results do demonstrate the importance of, the following:

- The influence of the geometry of pump including the impeller, volute and diffuser has on the final shut-off flow pattern.
- The experimental technique and equipment. The second vortex found at the inlet of the impeller by Simpson and Cinnamond and Senoo and Yamaguchi may have simply been 'missed' in the other investigations.

The importance of the geometry on the flow pattern found at shut-off suggests that for a new prediction method to be successful then it must

model both the impeller and volute simultaneously to enable their interaction to be accounted for.

Yedidiah (1985) made a study of shut-off head and its effect on the pump's characteristic curve. In his investigation a stroboscopic light was used to visualise the flow patterns in a centrifugal volute pump operated at closed valve conditions. From his results, Yedidiah presented two possible flow patterns at shut-off. For the casing with a potentially unstable characteristic, he observed that the flow at shut-off entered into the diffuser section, and from there returned back into the volute casing and into the impeller (Figure 1.7). For the pump with the stable characteristic, the flow entered the diffuser section and returned back to the volute, but this time did not return into the impeller (Figure 1.8).

The flow pattern described by Yedidiah gives credence to the flow model suggested by Frost and Nilsen in their prediction method.

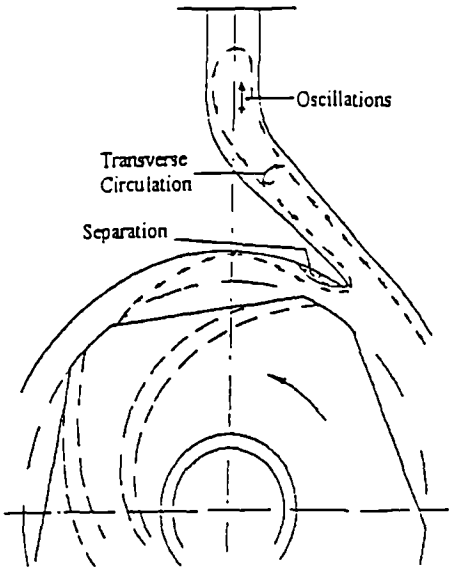

Figure 1.7. Fluid Motion at Shut-off, in a Casing Producing an Unstable Characteristic. Yedidiah(1985).

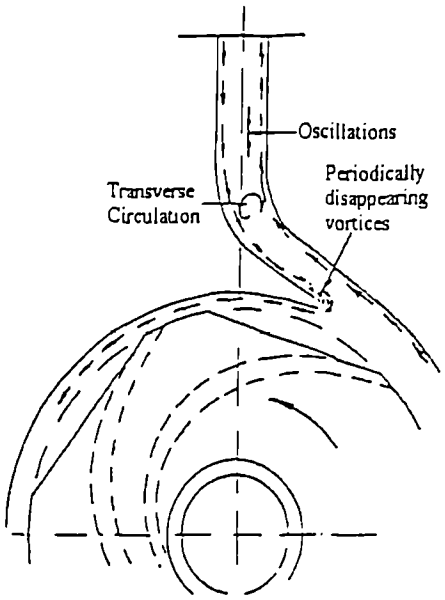

Figure 1.8. Fluid Motion at Shut-off, in a Casing Producing a Stable Characteristic. Yedidiah(1985).

The effect of flow rate on the radial force acting on a pump impeller was studied by Agostinelli et al.(1960), Uchida et al. (1971), Iversen et al. (1960) and Lipski (1979). They each conducted experiments to determine the cause and effect of the radial force acting on a centrifugal pump impeller. All the results showed that the radial force was a maximum at shut-off condition. This demonstrates the significance of the circumferential pressure distribution that exists around the volute at shut-off.

Iversen et al.(1960) took pressure measurements at twelve positions around the volute. The results showed that, at shut-off, that the circumferential pressure distribution increased from the tongue to the volute discharge with an abrupt pressure drop at the tongue (Figure 1.9).

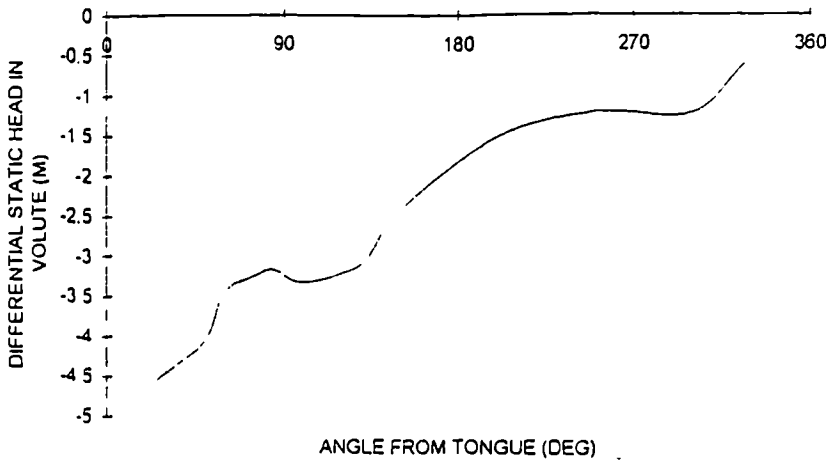

Figure 1.9. Circumferential Static Head Distribution in Volute. Iversen(1960).

Lipski(1979) measured the force acting on the tongue at different flow rates. At flow rates between shut-off and design he found the tongue was attracted towards the impeller. This demonstrated the pressure differential that must exist across the tongue, and revealed the presence of high pressure on the discharge side of the tongue and low pressure on the impeller side.

Abramian and Howard (1994a, 1994b) described in their paper the design of a rotating LDA system. This system allowed for measurements to be taken of the relative flow in an impeller fitted with a volute. The circumferential variation in the radial velocity, at the pressure and suction surfaces of a blade passage at shut-off condition was presented in their paper.

At the suction side it was found the passage flow was not affected by the presence of the volute and remained fairly constant (Figure 1.10). This is in contrast to the pressure side where flow reversal occurred as the impeller passage approached the tongue (Figure 1.11). The flow immediately accelerated past the tongue, with a mild reversal and recovery occurring midway around the volute, before the flow reversed again prior to reaching the tongue.

The result demonstrates a recirculatory type flow pattern over the majority of the volute. It also exhibits the properties consistent with the impeller momentum exchange mechanism proposed earlier by Lennemann and Howard(1970).

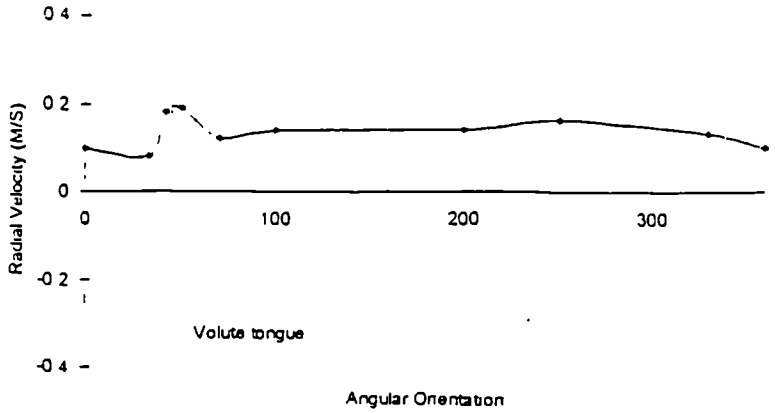

Figure 1.10. Circumferential Variation of the Ensemble-Averaged Radial Velocity at the Suction Side, Shut-Off conditions. Abramian and Howard(1994).

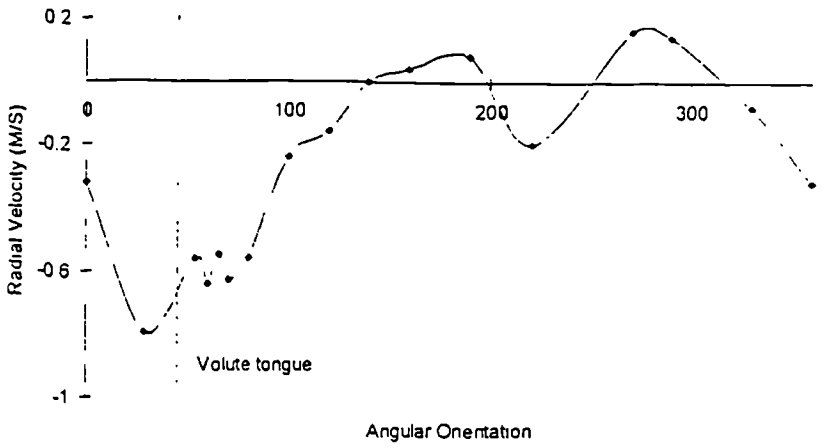

Figure 1.11 Circumferential Variation of the Ensemble-Averaged Radial Velocity at the Pressure Side, Shut-off conditions. Abramian and Howard(1994)

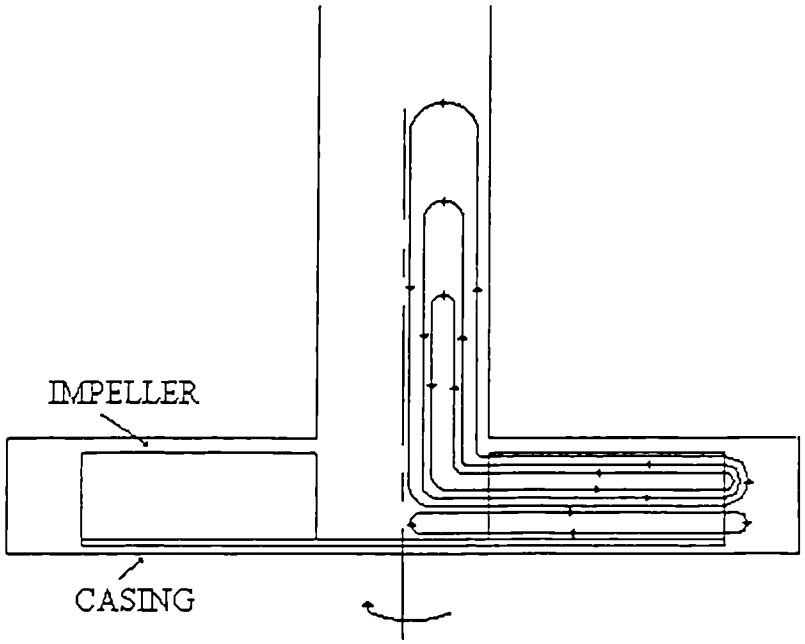

Figure 1.12. Velocity Distribution at the Inlet of a Radial Impeller at Shut-off. Levin and Poliokovsky(1965).

The flow pattern formed at shut-off at the inlet of a pump was considered by Levin and Poliokovsky(1965). Their experimental data showed at shut-off an axial circulation of the fluid within the impeller and inlet pipe (Figure 1.12) with reverse flow close to the inlet casing wall.

This was later substantiated by Peacock and Goulas(1985) who used LDA to determine the velocity profile at the inlet to an end suction volute pump. At shut-off, Peacock and Goulas(1985) also found reverse flow close to the inlet pipe wall, corresponding to the recirculation pattern predicted by Levin and Poliokovsky.

1.5 Objectives

The primary objective of the current research was to predict and understand the velocity and pressure distributions within a centrifugal pump operating at shut-off. This objective was achieved by the completion the following steps:

i) Measurement of the unsteady velocity and pressure field within the volute of a centrifugal pump using LDA and condenser microphones respectively.

ii) Analysis of the experimental data to determine the flow patterns within the volute at shut-off conditions.

iii) Development of a computational model to predict the flow within the volute and impeller using the commercial CFD package Fluent.

iv) Comparison and evaluation of the ability of CFD to model and predict pump flow at shut-off condition.

v) Identification of the major flow mechanisms at shut-off.

1.6 Outline of Chapters

The following section gives a brief description of the contents of each chapter within this thesis. Chapter 2 is a literature review examining the experimental and computational methods applied to pumps. Chapter 3 discusses the application of the computational model. It considers all aspects of the model including its generation, the physical models used, boundary conditions, and the solution method used. It also considers the sliding mesh technique that enabled the impeller and volute flow to be modelled simultaneously. Chapter 4 reviews the experimental procedures and techniques used to obtain the velocity and pressure measurements. Details of the design of the test rig are presented together with an error analysis. Chapter 5 presents a comparison of the measured and the computed velocity profiles within the volute. A comparison between the dynamic pressure measurements and the model is presented in Chapter 6. Finally, Chapter 7 presents the conclusions to the work and evaluates the computational model as a prediction tool. It also gives a detailed description of the flow patterns found within the impeller and volute at shut-off and suggests areas for further work.

CHAPTER 2:
LITERATURE REVIEW

2.1 Introduction

The literature review is split into two sections and examines significant research within the pump industry. The first section considers researchers who have used numerical and computational models to predict flow within centrifugal pumps. The second section examines relevant experimental work within the pump industry.

2.2 Numerical & Computational Models

With any new computational model, there must be validation between experimental and calculated data. This enables the researcher to gain an understanding of both the strengths, and more importantly, the weaknesses of the model. This knowledge can lead the researcher to develop more accurate and successful models in the future.

Until recently, practically all the prediction methods used in centrifugal pumps have been based on solving the potential flow. This extensive use of potential flow is due to two factors:
(1) It predicts the flow structures at design, where losses and disturbances within the impeller are at a minimum with surprisingly good accuracy.
(2) The ease with which potential flow methods can be applied makes them ideally suited to computers with limited resources and power.

A comparison of data obtained using a potential flow model with experimental measurements was conducted by Acosta (1954), Acosta and Bowerman (1957), and Bowerman and Acosta (1957). They conducted a series of experimental measurements on a number of different pump impellers, including two-dimensional centrifugal and Francis impellers.

The majority of their measurements were taken using impellers discharging into a test basin, hence with no volute interaction.

The results of their potential flow analysis were compared with the experimental data to ascertain how useful they were in predicting the flow. The best agreement was achieved at design flow conditions, where the analysis predicted to within fifteen percent of the experimental data at design.

A further study was made, this time adding a volute at off-design conditions. The researchers recognised from their experimental findings that the "non uniform velocity pattern at the impeller exit, results in a flow through the volute that does not resemble a potential flow." This clearly demonstrates a problem that has confronted pump designers when using potential flow methods to model flow at off-design conditions.

Over the last thirty years, designers have become increasingly aware of the limitations of potential flow analysis, particularly at low flow conditions. Kannemans(1980) compared experimental data, collected by using LDA in a typical centrifugal impeller, with a potential flow method. For flow rates near design conditions, good agreement was achieved between the predicted and experimental results. However, at low flow rates, the potential flow method exhibited trends that were opposed to the experimental data

An analysis of a two dimensional centrifugal pump was presented by Miner et al.(1988, 1989 and 1992). A finite element technique based on a potential flow method was used to model the pump. The researchers attempted to refine the prediction method by modelling the impeller and volute simultaneously. The impeller rotation within the volute was simulated by generating nine separate grids, each with a different, but fixed, impeller orientation.

The validation of the predicted flow was achieved by comparing the results with experimental data obtained using LDA, Miner et al.(1989). The results showed that at design flow the computational results were within seventeen percent of the measured velocity profiles. However, at flow rates below the design value Miner et al. came to the conclusion that the "potential flow solution is not suited to flows below design".

The three dimensional, incompressible, Navier-Stokes equations using a K-ε turbulence model, were used to obtain a solution for the flow patterns through an axial compressor rotor by Warfield and Lakshminarayana(1987). The predicted results were compared with the experimental data collected using LDA and hot wire anemometry, at two flow rates within a compressor passage. The numerical results agreed well with the measured results, with inaccuracies being attributed to low grid resolution. Warfield and co-workers came to the conclusion that with advances in Navier-Stokes methods, "accurate prediction of efficiency and losses could be obtained."

At the start of the nineties the interest in prediction methods based on potential flow was starting to wane, and Navier-Stokes solvers were gaining increased prominence. At this time computing power, both in terms of storage and processing had increased considerably. Despite these advancements, computers were still unable to solve the computationally intensive Navier-Stokes equations and achieve the necessary grid resolution to allow both the impeller and volute to be modelled simultaneously.

The problem for researchers was to simplify the computational model, reducing both its size and run times and hence provide greater accessibility to the industry. A computational model was developed based on a single blade passage with assumed rotational symmetry of the flow. The blade passage model could then effectively be solved using a rotating reference frame assuming steady state flow.

To enable the implementation of realistic boundary conditions the computational model was extended both up and down stream to incorporate a section of inlet pipe and diffuser. This allowed a constant pressure boundary to be applied at both the inlet and the outlet. All the computational models considered hereafter are based on this technique.

Researchers were now focused on demonstrating the advantages of Navier-Stokes solvers, and in particularly their ability to predict at off design flow rates, when viscous effects are prevalent.

Combes et al.(1992) solved the Navier-Stokes equations, together with a *k*-ε turbulence model, using finite elements, for a single blade passage of a centrifugal pump. Experimental measurements obtained using LDA were used to validate the model. These measurements were taken in the impeller and diffuser of a centrifugal pump, which operated at flow rates between $Q\backslash Q_N$ = 1.0 and 0.5. A comparison demonstrated good agreement in the velocity profiles between the experimental and predicted results.

A comparison of three commercial Navier-Stokes solvers with LDA measurements taken at the inlet and exit of an industrial pump was made by Schachenmann et al.(1993). The CFD codes considered were DAWES, STAR-CD and TASCFLOW.

The comparison showed that at fifty percent of the design flow, all the codes were unable to predict accurately the velocity profiles, when experimentally, the onset of recirculation occurred. However at twenty-five percent of design flow, where the recirculation patterns were strong, the CFD codes were all successful at predicting the velocity profiles. This demonstrates the ability of a range of commercial CFD packages to model accurately the flow structure at low flow conditions. It would be reasonable to assume that the recirculatory flow patterns at shut-off would also be

strong. The use of commercial CFD packages could, therefore, be assumed to be a useful prediction tool at shut-off conditions.

Graf(1993) compared results from three computational methods applied to a blade passage from a centrifugal pump impeller. The codes used in the investigation were TASCFLOW, Q-3D and a simplified approximation. Q-3D (Quasi three-dimensional) code was developed at NASA and solves a three-dimensional flow problem by replacing it with two two-dimensional problems; one in the meridional plane, and one in the blade-to-blade plane. The results from the three computational models were compared with flow visualisation data gathered experimentally. The object of the study was to compare the solutions obtained using the simplified methods with the full Navier-Stokes solver.

At design flow it was found that the simplified theory and Q-3D gave similar results to the Navier-Stokes solver. However, for flows below design, Q-3D and the simplified theory broke down as a predictive tool and did not produce the same accuracy as the Navier-Stokes solver.

More recent examples of the application of CFD to solving pump flow problems have been presented by Yates et al.(1995), Tourlidakis et al.(1995), and Hamill et al. (1995). However it is difficult to comment on their accuracy as they have all presented their computational predictions without experimental validation.

2.2.1 Summary of Numerical & Computational Models

Potential flow methods remain extensively used within the pump industry, due to their ability to predict the flow patterns at design conditions. Whilst the compressor and turbine industries have continued to invest in the development of computational methods based on the Navier-Stokes

equations, the pump industry, however, has continued to rely on the more traditional potential flow models.

Although aware of the limitations of potential flow, the pump industry has been sceptical of the ability of new CFD methods to predict the complicated flow structures found in pumps.

By developing new CFD models based on previous successes and backed by experimental validation, confidence in new techniques will grow.

2.3 Experimental Measurements

The following review will consider research work used when determining the important factors in both the design of the experimental rig and the development of the computational model.

When researchers take measurements within a centrifugal pump they are usually interested in obtaining data regarding the pressure and velocity field. Time-averaged static pressure measurements are the most common within the industry because they are easy to take. However, time-averaged pressures are unable to provide information concerning the periodic, fluctuating pressure field generated within the pump by the movement of the blades. These unsteady pressure measurements can only be obtained using a fast responding transducer, such as a condenser microphone. The measurement of fluctuating pressure has become more frequent in recent years as pump designers have tried to gain an understanding of the mechanisms of noise and vibration generated within a pump.

Gostelow(1977) presented one of the first papers to describe the phase-locked averaging (PLA) technique. Gostelow collected data on-line from either a microphone or hot-wire anemometer together with a position signal generated from the passing of an impeller blade. The position signal

enabled the raw experimental data to be synchronised, therefore allowing the data to be summed together. The process of summing together the raw experimental data with respect to a periodic passing of the blades was called phase-locked averaging(PLA).

Gostelow applied the PLA technique successfully to obtain the periodic pressure at different radii within a centrifugal pump impeller, however the actual flow rate the impeller was operated at was not given.

Many people have documented the importance of impeller volute interaction, particularly at low flow. One of the first studies into the pressure and velocity distributions within a centrifugal pump at low flow($Q/Q_N = 0.19$) was completed by Binder and Knapp(1958). Their research demonstrated that at low flow rates a non-uniform circumferential pressure distribution existed in the volute. This pressure distribution was found to decrease sharply after the tongue and then slowly increase around the volute. A similar pressure distribution was found by Iversen(1960) when he measured the circumferential pressure variation within a volute at shut-off.

The researchers noticed that at the tongue, where the low pressure region exists, a high amount of inflow occurs between the tongue and impeller. This inflow has been substantiated by a flow visualisation study using streak photography presented by Brownell et al.(1985). The object of their study was to determine the variation in the flow patterns with impeller blade position and flow rate.

At the lowest flow rate considered, $Q/Q_N = 0.3$, the tongue stagnation point moved to the discharge side of the tongue indicating a high amount of flow into the volute, past the tongue. Brownell et al. also discovered the tongue

separation zone oscillated with the blade orientation, thus demonstrating the interaction between the impeller and volute.

An investigation to determine the existence of a circumferential pressure distribution was presented by Kikuyama et al.(1987). They measured pressure at both the leading edge of an impeller blade and on the hub side of the volute wall, using phase-locked averaging. This allowed the researchers to obtain periodic data. They found that at design flow the pressure on the blade and volute remained unchanged, irrespective of the blade position. However, at off design conditions, the pressure on the volute wall and blade surface changed with blade position, which indicates a circumferential variation in pressure, generated by the volute interaction.

Binder and Knapp, Brownell et al., Iversen et al. and Kikuyama et al all indicate that at low flow rates, a circumferential pressure distribution exists due to the action of the volute. Therefore, for any new computational model to succeed at shut-off, the volute and impeller will have to be modelled simultaneously.

The following literature review shows velocity measurements are most commonly obtained using Laser Doppler anemometry (LDA or LDV, Laser Doppler Velocimetry). LDA has many advantages over the previous methods of hot-wire or hot-film anemometry.

LDA provides a non-intrusive measuring technique that is ideally suited to determining the recirculatory flows found within turbomachinery and, in particular, pumps. Single-component LDA systems are only capable of measuring one component of velocity at a time and are currently being superseded by two and three component systems. These new systems allow, not only the determination of mean velocity, but also the measurement of detailed turbulence quantities, such as the Reynolds stresses.

One of the first attempts at measuring the velocities in a radial impeller using LDA was presented by Adler and Levy(1979). They successfully measured the flow inside a shrouded impeller which had ten, straight backswept blades operating in an oversized volute. The results showed that at design conditions the flow at inlet was distorted. However by the exit to the impeller, the flow had become uniform.

Goulas and Truscott (1988) used LDA to measure the flow at the exit of an impeller operating in an end-suction volute pump. At low flow (Q/Q_N=0.27), they found the velocity vectors near the tongue were directed towards the tongue's clearance, indicating the presence of a low static pressure region. This substantiates the findings of Binder and Knapp, Brownell et al., Iversen et al. and Kikuyama et al.

Goulas and Truscott also discovered a reverse flow region past the tongue on the impeller side (see Figure 2.1). This reverse flow region is similar to that previously suggested by Yedidiah(1985).

The only real disadvantages in using LDA for the collection of experimental data are the need for specially designed test rigs to allow optical access for the laser and, the problems associated with seeding the flow with suitable light-scattering particles. For forward-scatter systems this requires optical access from both the front and the back of the rig. This allows the laser to enter through one side, to form the measurement volume in the pump, and the scattered light to be detected on the other side, allowing a velocity measurement to be taken.

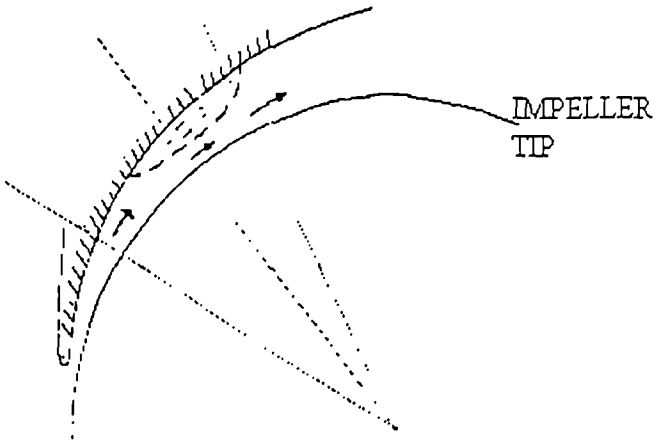

Figure 2.1 Reverse Flow Region Found at Low Flow.
Goulas and Truscott(1988).

A significant advancement has been the development of back-scatter LDA systems that require optical access from one side only. The disadvantage in using back-scatter LDA systems, is that a higher laser power is required to obtain a clean signal from the scattered light. Rose(1987) was one of the first researchers to use this type of system and he successfully presented a study of a three-dimensional impeller operating in water.

LDA data was collected, together with rotor position information from a shaft encoder, by Roco et al. (1990). They measured the velocity field within a slurry pump at two flow rates. In an attempt to gain an insight into dynamic effects in the flow structure, the data was plotted as a function of angular position and then videotaped to "animate" the data.

The use of the shaft encoder when obtaining LDA data allows velocities to be determined at a particular angular position of the blade thus enabling the interaction effects of the blades to be studied.

LDA with phase locked averaging was used successfully to obtain the tangential and radial velocity in a radial impeller by Hureau et al. (1993) and Stoffel and Weiss (1994). Their study considered the internal recirculation in pumps. From their measurements they were able to successfully define the onset of recirculation within the impeller. At the lowest flow rate considered (Q/Qn=0.11), they found that the absolute tangential velocity of the flow at inlet was higher than the tip speed of the rotating shroud. This indicated reverse flow was able to 'escape' out of the impeller and into the inlet section of the pump.

Dong et al. (1992a and 1992b) were the first to apply Particle Displacement Velocimetry (PDV) to obtain the pressure fluctuations in a centrifugal pump. The investigators were interested in the variations in flow structure associated with changes in flow rate and orientation of the impeller blades. Their results indicated that at off design conditions the flow was dominated by large flow structures. The size and strength of these flow structures depended on the blade orientation.

Recently, it has become popular to use air instead of water as the working fluid in experimental rigs. Air has many advantages over water because of the lower pressures and, therefore, stresses, developed during operation.

There has been debate as to whether test rigs using air can truly simulate tests using water. Researchers have now demonstrated, however, that with a high enough Reynolds number, Re, typically $Re > 5x10^5$, flow similarity can be obtained. The Reynolds number is defined as follows:

$$Re = \frac{\rho \Omega D_t^2}{2\mu} \qquad (2.1)$$

where ρ is the density of the fluid, Ω the angular velocity of the impeller, D_t is the diameter of the impeller and μ the viscosity of the fluid.

Ideally the Reynolds numbers should be matched to provide true dynamic similarity.

An experimental study measuring the unsteady pressure at the outlet of an impeller, using air as the working fluid, was completed by Yuasa and Hinata (1979). Their impeller had a rotational Reynolds number of $5x10^5$ (and the results, compared on a dimensionless basis, were identical to those using water. Their study also demonstrated the ability of condenser microphones to successfully obtain the unsteady pressure field.

Barrand et al. (1984) and Caignaert et al. (1985) both completed experimental investigations to determine a better understanding of the mechanisms of recirculation within an impeller. They compared the results from two similar pump models, one operated with water, the other with air. The Reynolds numbers for the models are given in Table 2.1.

A comparison of the results from the two test rigs found the critical flow rate, at which recirculation occurred, was marginally higher in the air test rig than in the water rig. This was, however, attributed to measurement inaccuracies between the two models together with increased leakage flow in the air model.

FLUID	SPEED (RPM)	ROTATIONAL REYNOLDS NO.	CRITICAL FLOW RATE (M^3/S)
Water[+]	1100	3.61×10^6	0.66
Air[•]	2500	1.17×10^6	0.65
	2000	9.33×10^5	0.64
	1700	7.93×10^5	0.65

[•]Air tests completed using a vaneless diffuser.

[+]Water tests completed using a narrow diffuser.

Table 2.1. Comparison of the Operating Data of the Impellers used by Barrand et al.(1984)

Tourret et al. (1985 and 1991) successfully measured the unsteady pressure field with condenser microphones in an industrial pump using air as the working fluid. Three flow rates were considered in the study, Q/Q_N = 1.5,1.0 and 0.5. The investigators noticed the pressure increased in the passageway of the impeller as it approached the tip of the tongue and then suddenly decreased. Tourret and co-workers noticed the tongue had a significant influence in the flow patterns within the rotating impeller.

This demonstrates the importance of modelling the impeller and the volute casing simultaneously, therefore allowing interaction effects to occur.

Condenser microphones have been successfully used in a number of studies to obtain the unsteady pressure field within the volute and impeller of a centrifugal pump. These researchers include Caignaert et al. (1988,1995), Lawless and Fleeter (1993) and Ubaldi et al. (1993,1996).

2.4 Summary

To summarise the literary review a number of conclusions can be reached. These are as follows:

i) Potential flow has been used successfully for many years to predict the flow patterns in an impeller. Many researchers have compared their potential flow solutions with experimental data, for a range of flow rates, and have reached similar conclusions. At design conditions potential flow can predict velocity profiles with good accuracy. However, at off-design conditions, and in particular at low-flow, potential solutions are unable to predict the flow structures. Therefore, if a computational model were to be used for the prediction of shut-off head, a different approach from the traditional potential flow method would be required.

ii) In recent years, with the emergence of more powerful computers with large storage facilities, numerical methods based on the Navier-Stokes equations have become more widely available. The literature review has

shown that commercial Navier-Stokes solvers have shown promising results for modelling a number of different impeller geometries and flow rates. It is believed this type of numerical solver is the way forward for the prediction of pump flows, especially at off-design conditions.

iii) The literature review suggests that all the pump models using Navier-Stokes solvers published to date are similar in their geometric assumptions. They all model the impeller as a single blade passage with extensions for inlet and diffuser. These extensions, up and down stream of the impeller, are required to allow pressure boundaries to be prescribed. Such boundary conditions are representative of a free impeller flow or an impeller operating at design flow. They do not, however, allow interaction between the impeller and volute to occur. Experimental researchers have noted the impeller volute interaction is very important, particularly at off-design conditions. To model flow in a pump accurately, and particularly at shut-off, requires the impeller and volute to be modelled simultaneously to reflect the influence one has on the other.

iv) Many experimental investigations have successfully used air, instead of water as the working fluid for measurements in centrifugal pumps. There is no definitive rule as to the required rotational Reynolds number to give dimensionless similarity between and air and water solutions. However, most experiments in air have an approximate Reynolds number $\approx 5x10^5$ or above.

v) The literature review demonstrates that condenser microphones have been used successfully in experimental investigations to measure the fluctuating pressure in turbomachinery flows. These fast measuring devices are able to measure the pressure field generated by a blade passing.

vi) The literature review demonstrates that LDA has been applied successfully in many turbomachinery experimental investigations to measure both the tangential and radial velocity components.

CHAPTER 3:
COMPUTATIONAL MODEL

3.1 Introduction

This chapter examines the methods and techniques used by Fluent v4.4 in the generation and calculation of a computational model. The first section introduces the basic conservation law form of the continuity and Navier-Stokes equations.

The second section examines the turbulence models used in this study and considers their relative strengths and weaknesses. An investigation then follows, comparing the results of three turbulence models when applied to the computational model of the pump.

The third section considers the main principals of a general finite volume solver. It examines the discretisation scheme used by Fluent and also the pressure-velocity coupling algorithm, SIMPLE.

The fourth section looks at the time dependence model used by Fluent and presents a study into the effect of the time step length on a flow solution.

The fifth section investigates the operation of the sliding mesh model and the transport of fluxes across the slipping plane from the rotational grid to the stationary grid.

The sixth and final section considers the procedures used to generate the computational model. It also presents a comparison of the solutions from three grids, each with a differing grid resolution.

Much of the work in this chapter relates to principals which can be found in any good textbook on CFD, however, for more detailed explanations see Versteeg and Malalasekera(1995).

3.2 Basic Equations

The laws governing the motion of a fluid are constructed from the conservation laws of physics. The three laws of particular importance are:

- ◊ Conservation of mass (Continuity equation).
- ◊ Conservation of Momentum – Newton's Second Law of Motion (Momentum equation).
- ◊ Conservation of Energy - First Law of Thermodynamics (Energy equation).

In this investigation, the working fluid is considered to be incompressible, so there will be no variation in the density. With no variation in density, there is no link between the First Law of Thermodynamics and the other two conservation equations, thus the flow field can be solved by use of the mass and momentum equations only.

3.2.1 Conservation of Mass

The principal of conservation of mass describes the transfer of mass flow into and out of a control volume. It relates the rate of increase of mass in a control volume to the net rate of flow of mass into the control volume. In this study, for brevity, only the final result will be quoted, however a full derivation is presented by Versteeg and Malalasekera(1995).

The three-dimensional mass conservation equation for an incompressible fluid is:

$$\frac{\partial u}{\partial x}+\frac{\partial v}{\partial y}+\frac{\partial w}{\partial z}=0 \qquad (3.1)$$

This can be written in a more compact form as:

$$\text{div}\ \mathbf{u} = 0 \qquad (3.2)$$

3.2.2 Momentum & Navier Stokes Equations

For a fluid particle, Newton's Second Law of motion states that the rate of change of momentum is equal to the sum of the forces acting on that particle. The forces acting on a fluid element fall into two groups. The first group relates to surface forces, such as pressure and viscous forces. The second group covers body forces, including the forces caused by rotation, such as the centrifugal and Coriolis forces.

The contributions made by surface forces are expressed as individual terms in the momentum equations whereas the effects of the body forces are grouped together to form a single source term.

There are many textbook derivations of the momentum equations, so for brevity only the final result will be quoted, equation(3.3). A full derivation can be found in Versteeg and Malalasekera(1995).

The x-component of the momentum equation can be defined by considering all the surface and body forces acting on a fluid element. This equation is written as:

$$\rho\frac{Du}{Dt}=\frac{\partial(-p+\tau_{xx})}{\partial x}+\frac{\partial\tau_{yx}}{\partial y}+\frac{\partial\tau_{zx}}{\partial z}+S_{MX} \qquad (3.3)$$

where p is the pressure acting on a fluid element and is negative due to its compressive nature. τ_{ij} are surface stresses, acting on a surface normal to the i direction, and acting in the j direction. S_{MX} is a source term and includes the body forces. Similar expressions may be found for both the y and z components of the momentum equation. The special derivative operator D/Dt represents the 'substantial derivative' or 'derivative following the fluid' and involves both the local unsteady and convectional accelerations.

In equation(3.3) it can be seen that the viscous stress components, τ_{ij}, have been introduced. These viscous stresses represent unknowns, and in order

to continue with the analysis, a methodology needs to be developed which allows these viscous stresses to be modelled.

One such model assumes the fluid to be Newtonian and the individual viscous stresses to be proportional to the rate of change of deformation of a fluid element. Considering the x-component of momentum, the viscous stresses can be written for an incompressible fluid as:

$$\tau_{xx} = 2\mu\frac{\partial u}{\partial x} \tag{3.4}$$

$$\tau_{yx} = \mu\left(\frac{\partial u}{\partial y} + \frac{\partial v}{\partial x}\right) \tag{3.5}$$

$$\tau_{zx} = \mu\left(\frac{\partial \mathrm{u}}{\partial \mathrm{z}} + \frac{\partial \mathrm{w}}{\partial \mathrm{x}}\right) \tag{3.6}$$

where μ is the dynamic viscosity of the fluid. Equation(3.4) represents the effects of linear elongation deformation and equations(3.5) and (3.6) represent the effects of linear shearing deformation.

The substitution of equations(3.4), (3.5) and (3.6) into the x-momentum equation(3.3) produces the Navier-Stokes equation for the x-component of a Cartesian co-ordinate system for an incompressible fluid as:

$$\rho\frac{\mathrm{Du}}{\mathrm{Dt}} = -\frac{\partial \mathrm{p}}{\partial \mathrm{x}} + \frac{\partial}{\partial \mathrm{x}}\left[2\mu\frac{\partial \mathrm{u}}{\partial \mathrm{x}}\right] + \frac{\partial}{\partial \mathrm{y}}\left[\mu\left(\frac{\partial \mathrm{u}}{\partial \mathrm{y}} + \frac{\partial \mathrm{v}}{\partial \mathrm{x}}\right)\right] + \frac{\partial}{\partial \mathrm{z}}\left[\mu\left(\frac{\partial \mathrm{u}}{\partial \mathrm{z}} + \frac{\partial \mathrm{w}}{\partial \mathrm{x}}\right)\right] + \mathrm{S_{MX}} \tag{3.7}$$

The x-component of the Navier-Stokes equation(3.7) for an incompressible, Newtonian fluid can be re-written as:

$$\frac{\partial \mathrm{u}}{\partial \mathrm{t}} + \mathrm{div}(\mathrm{u}\mathbf{u}) = -\frac{1}{\rho}\frac{\partial \mathrm{p}}{\partial \mathrm{x}} + \upsilon\,\mathrm{div\ grad\,u} + \mathrm{S_{MX}} \tag{3.8}$$

where υ is the kinematic viscosity μ/ρ and the substantial derivative Du/Dt has been split into a local unsteady acceleration $\partial u/\partial t$ and a convective

acceleration div(ρ**u**). Similar expressions can be found for the y and z components of the Navier-Stokes equations.

The introduction of Newton's law of viscosity into equation(3.3) has generated four equations, namely, the mass conservation equation and the three components of Navier-Stokes equations, which can be solved for the four unknowns. The procedure has now resulted in a mathematical equation for a general flow regime that can be solved directly for laminar flow.

The analysis throughout this chapter concentrates solely on the derivation of the Navier-Stokes equations based on a Cartesian (x, y, z) co-ordinate system. However the computational model for the pump applied the Navier-Stokes equations based on a cylindrical polar(r, θ, z) co-ordinate system of equations. This was due to the cylindrical nature of the grid and the rotation of the impeller.

For completeness the r(radial), θ(circumferential) and z(axial) Navier-Stokes equations are quoted here.

$$\frac{\partial(v_r)}{\partial t}+\frac{1}{r}\frac{\partial(rv_r^2)}{\partial r}+\frac{1}{r}\frac{\partial(v_r v_\theta)}{\partial \theta}+\frac{\partial(v_z v_r)}{\partial z}-\frac{v_\theta^2}{r}$$
$$=-\frac{1}{\rho}\frac{\partial p}{\partial r}+\nu\left(\frac{\partial^2 v_r}{\partial r^2}+\frac{1}{r^2}\frac{\partial^2 v_r}{\partial \theta^2}+\frac{\partial^2 v_r}{\partial z^2}+\frac{1}{r}\frac{\partial v_r}{\partial r}-\frac{2}{r^2}\frac{\partial v_\theta}{\partial \theta}-\frac{v_r}{r^2}\right) \quad (3.9)$$

$$\frac{\partial(v_\theta)}{\partial t}+\frac{1}{r}\frac{\partial(rv_r v_\theta)}{\partial r}+\frac{1}{r}\frac{\partial(v_\theta^2)}{\partial \theta}+\frac{\partial(v_z v_\theta)}{\partial z}-\frac{v_r v_\theta}{r}$$
$$=-\frac{1}{\rho r}\frac{\partial p}{\partial \theta}+\nu\left(\frac{\partial^2 v_\theta}{\partial r^2}+\frac{1}{r^2}\frac{\partial^2 v_\theta}{\partial \theta^2}+\frac{\partial^2 v_\theta}{\partial z^2}+\frac{1}{r}\frac{\partial v_\theta}{\partial r}+\frac{2}{r^2}\frac{\partial v_r}{\partial \theta}-\frac{v_\theta}{r^2}\right) \quad (3.10)$$

$$\frac{\partial(v_Z)}{\partial t} + v_r\frac{\partial(v_Z)}{\partial r} + \frac{v_\theta}{r}\frac{\partial(v_z)}{\partial \theta} + \frac{\partial(v_z)}{\partial z} = -\frac{1}{\rho}\frac{\partial p}{\partial z} + \nu\left(\frac{\partial^2 v_z}{\partial r^2} + \frac{1}{r}\frac{\partial v_z}{\partial r} + \frac{\partial^2 v_z}{\partial z^2} + \frac{1}{r^2}\frac{\partial^2 v_z}{\partial \theta^2}\right) \quad (3.11)$$

where v_r is the component of velocity in the radial direction, v_θ is the component of velocity in the circumferential direction, v_z is the component of velocity in the axial direction and r is the radial position.

The right hand side for both equations(3.9 and 3.10) can now be written in a more compact form. For the radial Navier-Stokes equation this gives:

$$\frac{\partial(v_r)}{\partial t} + \mathrm{div}(v\mathbf{v}) - \frac{v_\theta^2}{r} \quad (3.12)$$

and for the circumferential Navier-Stokes equation(3.10):

$$\frac{\partial(v_\theta)}{\partial t} + \mathrm{div}(v\mathbf{v}) - \frac{v_r v_\theta}{r} \quad (3.13)$$

The term v_θ^2/r in equations(3.9 and 3.12) and represents the centrifugal force and the term $v_r v_\theta/r$ in equations(3.10 and 3.13) represents the Coriolis force. Both these terms are added as body forces to the right hand side of their respective equations.

3.2.3 Rotating Reference Frame

The sliding mesh model contains two reference frames both sharing the same coordinate origin.

One frame contains the impeller and rotates with an angular velocity, ω about the z-axis. This is similar to the rotating reference frame models described in Chapter 2.

The other reference frame is stationary with respect to an absolute frame and contains the volute and diffuser.

When the equations of motion are written with respect to the rotating , non-inertial, coordinate system additional body force terms must be included so that the overall accelerations are correct in the absolute frame. It may be shown that if the relative coordinate system rotates about the z-axis at constant angular velocity, as in the pump model, the additional acceleration terms are:

$$-2\omega_z w_\theta - \omega_z^2 r \tag{3.14}$$

in the radial direction and

$$2\omega_z w_r - \omega_z^2 r\theta \tag{3.15}$$

in the circumferential direction.

The terms w_r and w_θ are the relative velocities in the radial and circumferential directions respectively. A derivation is given in Appendix B.

Hence the equations of motion in terms of the relative velocities in the rotating frame may written as:

$$\frac{\partial w_r}{\partial t} + \mathrm{div}(ww) - \frac{w_\theta^2}{r} - r\omega_z^2 - 2\omega w_\theta = -\frac{1}{\rho}\frac{\partial p}{\partial r} + \nu\left(\frac{\partial^2 w_r}{\partial r^2} + \frac{1}{r^2}\frac{\partial^2 w_r}{\partial \theta^2} + \frac{\partial^2 w_r}{\partial z^2} + \frac{1}{r}\frac{\partial w_r}{\partial r} - \frac{2}{r^2}\frac{\partial w_\theta}{\partial \theta} - \frac{w_r}{r^2}\right) \tag{3.16}$$

$$\frac{\partial w_\theta}{\partial t} + \mathrm{div}(ww) + 2\omega_z w_r - \omega_z^2 r\theta + \frac{w_r w_\theta}{r} = -\frac{1}{\rho r}\frac{\partial p}{\partial \theta} + \nu\left(\frac{\partial^2 w_\theta}{\partial r^2} + \frac{1}{r^2}\frac{\partial^2 w_\theta}{\partial \theta^2} + \frac{\partial^2 w_\theta}{\partial z^2} + \frac{1}{r}\frac{\partial w_\theta}{\partial r} + \frac{2}{r^2}\frac{\partial w_r}{\partial \theta} - \frac{w_\theta}{r^2}\right) \tag{3.17}$$

3.3 Turbulence Modelling

3.3.1 Introduction

In principle, the unsteady Navier-Stokes equations give a complete description of the physics of fluid flows, whether laminar or turbulent. However, the direct solution of the Navier-Stokes equation(3.7) for

turbulent flow is possible only at research level as it is outside the capability of most computers. This is not a serious limitation as engineering problems only require information regarding the time-averaged properties of the flow, and not details about each individual eddy. Fluent is therefore able to solve the Navier-Stokes equations by modelling the time-averaged effects of the turbulence.

This section of work first explains the purpose of a turbulence model and then provides a brief account of the models supplied by Fluent v 4.4. In the final section a comparison is made of three turbulence models when applied to the centrifugal pump model.

Three turbulence models are offered by Fluent. These are the k-ε model, the Renormalization Group k-ε model (RNG k-ε) and the Reynolds Stress Model (RSM). The RSM however cannot be used in conjunction with the sliding mesh model, so could not be used for the full rotor-stator interaction in the present study.

During preliminary tests the RNG k-ε model in version 4.4 was found to cause rapid divergence when operating with the sliding mesh model. To overcome this problem Fluent supplied a Beta test version of its code, and this was used to obtain a solution for RNG k-ε model and the RNG k-ε model with swirl.

The following section of work considers the basic mathematics of turbulent flows.

The instantaneous velocity at a fixed point in the pump experiencing turbulent flow is composed of two components; a periodic component generated by the blade passing and an instantaneous fluctuation superimposed onto it. However, to simplify the analysis in this section the instantaneous velocity at a fixed point will be decomposed into two parts; a steady, mean velocity, with a fluctuating component(Figure 3.1).

This can be written mathematically as:

$$u(t) = \bar{u} + u'(t) \tag{3.18}$$

The mean flow is time averaged and is given as:

$$\bar{u} = \frac{1}{t_0}\int_0^{t_0} u\, dt \tag{3.19}$$

The turbulent fluctuations are random in nature with either positive or negative values of $u'(t)$ just as likely to occur. The time average of the turbulent component can be written as:

$$\bar{u'} = \frac{1}{t_0}\int_0^{t_0} u'(t)\, dt = 0 \tag{3.20}$$

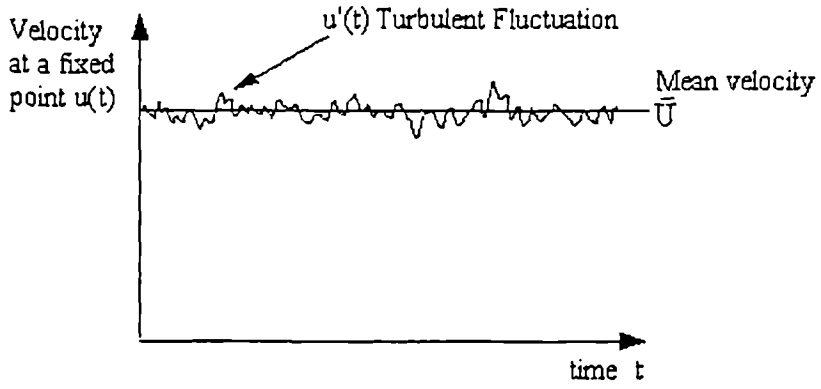

Figure 3.1 Velocity Measurement of a Turbulent Flow.

Information regarding the fluctuating part of the flow can be found using the root-mean square (rms) of the fluctuations or the turbulent kinetic energy.

To obtain the mean turbulent flow equations where mean and fluctuating components are combined the "Reynolds Rules of Averaging" have to be applied. These rules can be found in most CFD textbooks such as Versteeg and Malalasekera(1995).

To simplify the analysis only the x component of the two dimensional incompressible Navier-Stokes equation is considered. This can be written in Cartesian coordinates as:

$$u\frac{\partial u}{\partial x}+v\frac{\partial u}{\partial y}=-\frac{1}{\rho}\frac{\partial p}{\partial x}+\nu\left[\frac{\partial^2 u}{\partial x^2}+\frac{\partial^2 u}{\partial y^2}\right] \qquad (3.21)$$

where ρ is the density and ν is the kinematic viscosity.

Substituting equation (3.18) and applying the "Reynolds Rules of Averaging" to equation(3.21) generates the following time averaged instantaneous Navier-Stokes equation written as:

$$\bar{u}\frac{\partial \bar{u}}{\partial x}+\overline{u'\frac{\partial u'}{\partial x}}+\bar{v}\frac{\partial \bar{u}}{\partial y}+\overline{v'\frac{\partial u'}{\partial y}}=-\frac{1}{\rho}\frac{\partial \bar{p}}{\partial x}+\nu\left[\frac{\partial^2 \bar{u}}{\partial x^2}+\frac{\partial^2 \bar{u}}{\partial y^2}\right] \qquad (3.22)$$

and after substantial rearranging this gives:

$$\bar{u}\frac{\partial \bar{u}}{\partial x}+\bar{v}\frac{\partial \bar{u}}{\partial y}=-\frac{1}{\rho}\frac{\partial \bar{p}}{\partial x}+\frac{\partial}{\partial x}\left[\nu\frac{\partial \bar{u}}{\partial x}-\overline{u'^2}\right]+\frac{\partial}{\partial y}\left[\nu\frac{\partial \bar{u}}{\partial y}-\overline{u'v'}\right] \qquad (3.23)$$

Equation 3.23 is known as the time averaged Reynolds Stress Equation for an incompressible fluid. The quantities $\overline{u'^2}$ and $\overline{u'v'}$ can be interpreted as extra turbulent stresses, called the Reynolds stresses. Engineers have been able to discard the instantaneous fluctuating velocity components by concentrating on only the time-average flow quantities. However, the equations now contain unknowns due to the Reynolds stresses. It is the purpose of a turbulence model to predict these Reynolds stresses.

A full derivation of each of the turbulence models is beyond the scope of this thesis and only the salient points for each model will be presented. However, explanations and derivations can be found in Tennekes and Lumley(1972), Wilcox(1994) and Versteeg and Malalasekera(1995).

3.3.2 The *k*-ε Turbulence Model

The *k*-ε turbulence model is based on an eddy viscosity model. This assumes the Reynolds stresses in equation(3.23) are proportional to the mean velocity gradients with the constant of proportionality being the turbulent viscosity. This was first proposed by Boussinesq, and the relationship for a compressible fluid is stated in the Fluent Users' Manual (1996) as:

$$-\rho\overline{u'_i u'_j} = -\rho\frac{2}{3}k\delta_{ij} + \mu_t\left(\frac{\partial U_i}{\partial x_j} + \frac{\partial U_j}{\partial x_i}\right) \qquad (3.24)$$

when i or j = 1 corresponds to the x direction, i or j = 2 corresponds to the y direction and i or j = 3 corresponds to the z direction. ρ represents the fluid density, δ_{ij} is a Kronecker delta and μ_t is the turbulent viscosity. The turbulent kinetic energy, k is defined as:

$$k = \frac{1}{2}\left(\overline{u'^2} + \overline{v'^2} + \overline{w'^2}\right) \qquad (3.25)$$

The use of the *k*-ε turbulence model simplifies the computational modelling of turbulence by allowing the Reynolds averaged equations to be represented by the laminar momentum equations with the molecular viscosity replaced by an effective viscosity, given as:

$$\mu_{eff} = \mu + \mu_t \qquad (3.26)$$

The turbulent viscosity, μ_t is assumed to be proportional to the product of a turbulent velocity and length scale. The *k*-ε turbulence model defines the velocity and length scales from the turbulent kinetic energy, k, and the rate of dissipation of turbulent kinetic energy, ε. The velocity scale is defined as $k^{1/2}$, and the length scale is defined as $\frac{k^{3/2}}{\varepsilon}$. This enables the turbulent viscosity to be defined as:

$$\mu_t = \rho C_\mu \frac{k^2}{\varepsilon} \qquad (3.27)$$

where ρ is the density of the fluid and the value of the constant C_μ has been obtained empirically, and has a generally accepted value of 0.09.

The transport of the turbulent kinetic energy, k, and the rate of dissipation of turbulent kinetic energy, ε, are obtained from the following partial differential equations:

$$\frac{\partial(\rho k)}{\partial t} + div(\rho k \mathbf{U}) = div\left[\frac{\mu_t}{\sigma_k} grad k\right] + 2\mu_t E_{ij}.E_{ij} - \rho\varepsilon \qquad (3.28)$$

$$\frac{\partial(\rho \varepsilon)}{\partial t} + div(\rho \varepsilon \mathbf{U}) = div\left[\frac{\mu_t}{\sigma_\varepsilon} grad \varepsilon\right] + C_{1\varepsilon}\frac{\varepsilon}{k}2\mu_t E_{ij}.E_{ij} - C_{2\varepsilon}\rho\frac{\varepsilon^2}{k} \qquad (3.29)$$

where E_{ij} is the mean deformation of a fluid element and the constants found in the k-ε model have been obtained empirically and are widely accepted to be:

C_μ=0.09; σ_K=1.00; σ_ε=1.30; $C_{1\varepsilon}$=1.44; $C_{2\varepsilon}$=1.92;

Versteeg and Malalasekera(1995) described equations(3.28 and 3.29) in words as:

Rate of change of k or ε	+	Transport of k or ε by convection	=	Transport of k or ε by diffusion	+ production of k or ε	- destruction of k or ε

The transport equations (3.28 and 3.29) ensure that both the production and destruction of the turbulent kinetic energy is linked by making the dissipation equation proportional to the kinetic energy equation.

The main disadvantage of the k-ε turbulence model is its assumption that the normal Reynolds stresses are isotropic. This can be demonstrated by applying the Boussinesq equation(3.24) to an incompressible fluid. The first term on the right hand side of equation(3.24) for an incompressible fluid can be written as:

$$2\mu_t\left[\frac{\partial U}{\partial x} + \frac{\partial V}{\partial y} + \frac{\partial W}{\partial z}\right] = 2\mu_t div\mathbf{U} = 0 \qquad (3.30)$$

The normal stresses $-\rho(\overline{u'^2} + \overline{v'^2} + \overline{w'^2})$ for any flow are equal to twice the kinetic energy per unit volume($-2\rho k$). Therefore to ensure the equation(3.24) is physically realistic for incompressible flow, a second term on the right hand side allocates an equal third to each of the normal stresses.

This implies the normal Reynolds stresses are all equal and hence the turbulence is isotropic. The tangential Reynolds stresses are directly proportional to the mean strain rate. The k-ε turbulence model is therefore oblivious to the effects of rotation and streamline curvature.

Thus the basic model also has no mechanism to account for the rotational effects on the flow due to the centrifugal and Coriolis forces without ad-hoc corrections of the type suggested by Wilcox and Chambers(1977). More fundamentally, similar corrections are needed to model flow over curved surfaces.

Despite these disadvantages the k-ε model is used in industry for modelling a wide variety of turbulent flows. However, for flows that contain anisotropic turbulence Fluent suggests the use of the RNG k-ε model or the full Reynolds stress model.

3.3.3 The RNG k-ε Turbulence Model

The Renormalization Group (RNG) k-ε model was developed by Yakhot et al(1992) and uses Renormalization Group methods to model the transport of turbulence as opposed to the empirical methods used in the k-ε model.

RNG k-ε turbulence model systematically removes small-scale eddy motions allowing a modified Navier-Stokes equation to be calculated on relatively coarser grids and at higher Reynolds numbers.

The RNG k-ε model used by Fluent calculates the effective viscosity as:

$$\mu_{eff} = \mu_{mol}\left[1 + \sqrt{\frac{C_\mu}{\mu_{mol}}}\frac{k}{\sqrt{\varepsilon}}\right]^2 \qquad (3.31)$$

where μ_{mol} is the molecular viscosity and C_μ is a constant and equal to 0.0845.

The transport equations for k and ε are given in the Fluent Users' Manual (1996) and are similar to those found in the standard k-ε model, with the main difference occurring in the equation for the rate of dissipation, ε. It is claimed that the effect of this difference is to allow the RNG model to be responsive to changes in the rate of strain, which cannot be modelled in the standard dissipation equation used in the k-ε model.

Fluent's RNG k-ε model accounts for the effects of swirling flow by sensitising the constant C_μ in equation(3.31). The Fluent Users' Manual (1996) states the functional form of C_μ as:

$$C_\mu = C_{\mu o} f(\alpha_s, \Omega, \frac{k}{\varepsilon}) \qquad (3.32)$$

where $C_{\mu o} = 0.0845$ and α_S is a swirl constant and is dependent on how dominant the swirl is. Fluent suggests for mildly swirling flows α_S should be 0.05, however a higher value may be used for more strongly swirling flows. The characteristic swirl number Ω, is defined as the ratio of the axial flux of angular momentum to the axial flux of axial momentum.

The main advantage the RNG k-ε model has over k-ε model is its anisotropic treatment of the turbulent flow. In tests, Yakhot et al.(1992) found the model produced good results for recirculating flows. However, Versteeg and Malalasekera(1995) noted the model is only a "newcomer to turbulence modelling and still needs to be widely validated".

Although the RNG model may relax the assumption of isotropy inherent in the standard k-ε model, it has a similar inability to account for the rotational

body forces that occur when examining problems which contain flows in a rotating reference frame.

To overcome the problem of modelling rotational body forces, Fluent suggest using the Reynolds stress model. As noted earlier, the Reynolds stress model is currently not available for use when using the sliding mesh model.

3.3.4 Revnolds Stress Equation Model (RSM)

The previous analysis of both the *k*-ε and RNG *k*-ε turbulence models indicated some of the problems that occur when modelling swirling or rotating flows. The RSM model overcomes these problems by solving the transport equation for the individual Reynolds stresses therefore taking account of their directional effects. The RSM implemented by Fluent is as follows:

$$\underbrace{\frac{\partial}{\partial t}\left(\overline{u_i' u_j'}\right) + u_k \frac{\partial}{\partial x_k}\left(\overline{u_i' u_j'}\right)}_{\text{Convective Transport}} =$$

$$\underbrace{-\frac{\partial}{\partial x_k}\left[\left(\overline{u_i' u_j' u_k'}\right) + \overline{\frac{p}{\rho}\left(\delta_{kj} u_i' + \delta_{ik} u_j'\right)} - \nu \frac{\partial}{\partial x_k}\left(\overline{u_i' u_j'}\right)\right]}_{\text{Diffusive Transport}}$$

$$\underbrace{-\left[\overline{u_i' u_k'} \frac{\partial u_j}{\partial x_k} + \overline{u_j' u_k'} \frac{\partial u_i}{\partial x_k}\right]}_{\text{Production}} \qquad (3.33)$$

$$\underbrace{\overline{\frac{p}{\rho}\left[\frac{\partial u_i'}{\partial x_j} + \frac{\partial u_j'}{\partial x_i}\right]}}_{\text{Pressure-Strain}} \quad \underbrace{-2\nu\overline{\left[\frac{\partial u_i'}{\partial x_k}\frac{\partial u_j'}{\partial x_k}\right]}}_{\text{Dissipation}}$$

$$\underbrace{-2\Omega_k\left[\overline{u_j' u_m'}\varepsilon_{ikm} + \overline{u_i' u_m'}\varepsilon_{jkm}\right]}_{\text{Rotational Term}} + \underbrace{S_{ij} + D_{ij}}_{\text{Curvature Related Terms}}$$

where S_{ij} and D_{ij} are curvature-related source terms which are included when cylindrical coordinates are used. Thus the Reynolds Stress model does finally include terms to represent rotational and streamline curvature effects.

In order to mathematically close the equation (3.33) Fluent makes approximations for the diffusion, dissipation rate and pressure strain terms.

The dissipation rate, ε is found using the transport equation (3.29), and is the same equation used for the *k*-ε turbulence model.

RSM models can be potentially very accurate for modelling the mean flow and Reynolds stresses for both simple and complex problems. However, this increased accuracy also increases the cost in terms of computing time, because seven extra partial differential equations need to be solved. The RSM model is also relatively new and like the RNG *k*-ε model has not had the same level of validation as the standard *k*-ε model.

Compromises are thus inherent in the turbulence modelling for the present study, but similar compromises are routinely accepted in many of the reported applications of CFD. Turbomachinery workers in general have preferred to use still simpler, algebraic or "zero-equation" turbulence models, such as that of Baldwin and Lomax(1978), involving even greater approximations.

3.3.5 Near Wall Treatment of Turbulent Flows

The turbulence is damped near to the wall, with a thin region of laminar flow, known as the viscous or laminar sub-layer immediately adjacent to the wall. At the outer part of the near-wall region the turbulence increases greatly, due to the large gradient in the mean velocity.

The near wall region contains large velocity gradients and determines the shear stress boundary conditions for the flow calculation, and so it is

important to have an accurate representation of the flow in this region. Ideally, the grid near the wall should be fine enough to allow resolution of the laminar sub-layer, but in practice this is often not possible. A commonly used alternative is to use semi-empirical wall functions to bridge the region between the wall and the fully turbulent core flow, and this was the approach used in the present work. This technique is particularly popular in industry as it saves substantially on computing time and resources due to the fact that the near wall region does not have to be modelled.

The variation of velocity close to a flat plate wall is commonly described by plotting dimensionless velocity u^+ against dimensionless distance from the wall y^+ as in Figure 3.2 where:

$$u^+ = u/u_\tau \tag{3.34}$$

with u_τ being the so-called shear velocity $\sqrt{\tau_D/\rho}$ based on the wall shear stress and

$$y^+ = \frac{\rho u_\tau y}{\mu} \tag{3.35}$$

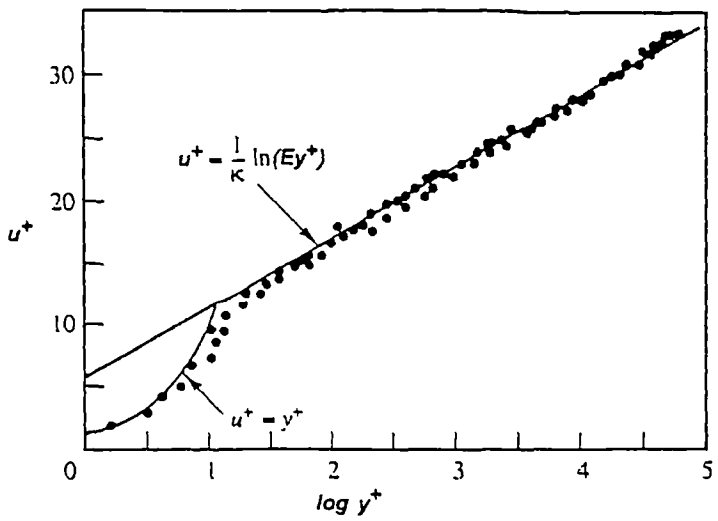

Figure 3.2 Near Wall Velocity Distribution. Versteeg and Malalasekera(1995).

Between the limits $11 < y^+ < 500$ the experimental data of Figure 3.2 is approximated by the empirical "law of the wall":

$$u^+ = \frac{1}{\kappa}\ln(Ey^+) \qquad (3.36)$$

where κ is Von Karman's constant equal 0.41, and E is an empirical constant equal 9.81.

Fluent uses a wall function based on equation(3.36), as first proposed by Launder and Spalding(1974). In equation(3.36) u^+ and y^+ are related to the values

y_P = displacement from wall,

k_p = turbulent kinetic energy,

and u_P = local mean velocity

all at a grid point P immediately adjacent to the wall boundary by:

$$u^+ = \frac{u_p C_\mu^{1/4} k_p^{1/2}}{\tau_o/\rho} \qquad (3.37)$$

$$y^+ = \frac{\rho C_\mu^{1/4} k_p^{1/2} y_p}{\mu} \qquad (3.38)$$

Provided the point P lies in the log-law region, that is $11 < y^+ < 500$, then equation(3.35) may be used to relate u^+ and y^+. The wall shear stress τ_o may be found from known data at adjacent grid point P.

3.4 Discretisation for the Finite Volume Method

The differential equations in conservation law form (3.1 and 3.3) must be converted into algebraic equations to allow a numerical solution to be obtained. Fluent achieves this conversion process using a discretisation method suggested by Patankar(1980).

Patankar's method involves integrating the differential conservation equations about a control volume. This produces a series of finite volume equations, each of which conserves a particular property about that control volume.

Fluent's control volumes are defined using the non-staggered, or co-located grid system suggest by Rhie and Chow(1983). The co-located grid system stores all the primitive variables at the cell centres. This is in contrast to the staggered grid method adopted by Patankar(1980) in which the computational grid is effectively split into two offset grids, where one is used for storing the velocities and the other is used for storing the pressures.

The following example from the Fluent Users' Manual (1996) is used to demonstrate the integration of the conservation equations about a control volume. A one-dimensional problem is illustrated in Figure 3.3.

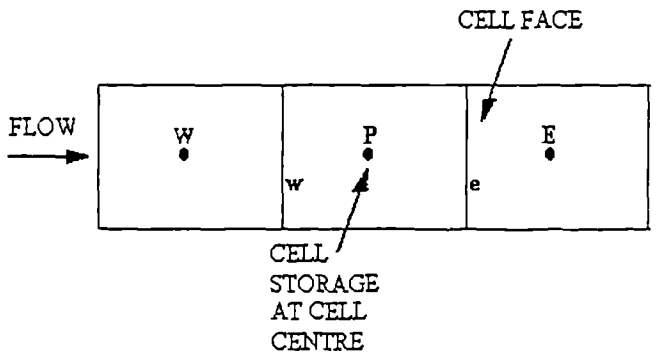

Figure 3.3 One-dimensional Control Volume Nomenclature.
Fluent Users' Manual (1996).

From Figure 3.3, the capital letters denote the cell centres with P representing the cell under investigation, W representing the cell centre to the left, or west cell, and E representing the cell to the right, the east cell. Lower case letters are used to indicate the cell faces.

The one-dimensional conservation equations for incompressible steady flow can be written as:

$$\frac{\partial u}{\partial x} = 0 \tag{3.39}$$

$$\frac{\partial}{\partial x}(uu) = -\frac{1}{\rho}\frac{\partial p}{\partial x} + \frac{\partial}{\partial x}\left[\upsilon\left(\frac{\partial u}{\partial x}\right)\right] + S \tag{3.40}$$

where υ is the kinematic viscosity and S is a source term. Equation(3.39) represents the continuity equation, while equation(3.40) represents the momentum equation.

These two equations can now be integrated over a control volume by applying the Divergence Theorem. This produces for the continuity equation(3.39):

$$\int_{volume,v} \frac{\partial u}{\partial x} dV = \int_{A} u.dA \tag{3.41}$$

where A is the area of a cell face.

Integrating equation(3.39) about the control volume displayed in Figure 3.3 gives :

$$(uA)_e - (uA)_w = 0 \tag{3.42}$$

where u is the velocity of the fluid and A the area of the cell. The lower case, 'e' and 'w' in equation(3.42) represent the east and west cell face of centre cell P.

Integration of the momentum equation(3.40) produces:

$$\left(u^2 A\right)_e - \left(u^2 A\right)_w = -(p_e - p_w)\frac{A}{\rho} + \left(\upsilon\left[\frac{u_E - u_p}{\Delta x}\right]A\right)_e - \left(\upsilon\left[\frac{u_P - u_W}{\Delta x}\right]A\right)_w + F\Delta V \tag{3.43}$$

where the A in the pressure term is the x-normal area at the centre of cell P. This can be written as:

$$J_e u_e - J_w u_w = -(p_e - p_w)\frac{A}{\rho} + \upsilon\left[\frac{1}{\Delta x_e}(u_E - u_P) - \frac{1}{\Delta x_w}(u_P - u_W)\right]A + F\Delta V \tag{3.44}$$

Equations(3.43) and (3.44) can be solved provided an interpolation scheme can be used which can relate both the pressures (p_e and p_w) and the fluxes (J_e and J_w) at the cell faces to the value at the cell centre. The method used by Fluent is based on the work by Rhie and Chow(1983) as further improved by Majumdar(1988).

Fluent has several schemes available that can be used to determine the face values of the convective quantities. These include Power Law, blended Second Order Upwind/Central Difference scheme and QUICK. However, when using the sliding mesh technique, only the Power Law scheme is currently available.

The Power-Law scheme interpolates for the values at the cell faces using a one-dimensional convection-diffusion equation. The one-dimensional equation used by Fluent Users' Manual(1996) describes the flux of a general conserved quantity ϕ as:

$$\frac{\partial}{\partial x}(\rho u \phi) = \frac{\partial}{\partial x}\Gamma\frac{\partial \Phi}{\partial x} \tag{3.45}$$

where ρu and Γ are constant across a control volume, δx. Equation(3.45) can be integrated to produce an equation that describes how the property ϕ varies with x. This is given as:

$$\frac{\phi(x) - \phi_0}{\phi_L - \phi_0} = \frac{\exp(Pe\frac{x}{l}) - 1}{\exp(Pe) - 1} \tag{3.46}$$

where ϕ_0 is the value of the flux at x=0, ϕ_L is the value of the flux at x=L and Pe is the Peclet number. This number describes the relative strength of the convection and diffusion terms and is defined as:

$$Pe = \frac{\rho u L}{\Gamma} \tag{3.47}$$

The variation of $\phi(x)$ between x=0 and x=L is given in the Fluent Users' Manual (1996) and is also displayed in Figure 3.4. The graph shows for high Peclet number flows, where the flow is dominated by convection effects, the value of ϕ at x=L/2 is virtually equal to the upstream value.

For problems with no flow, the Peclet number is equal to zero, and therefore pure diffusion is used and the value of ϕ may be found from linear interpolation.

The main disadvantage of the Power Law scheme is that it is only first order accurate in terms of Taylor series truncation error for Peclet numbers over about six, as noted by Leonard and Mokhtari(1990). Typical Peclet numbers encountered in the present work are around eight, so the spatial accuracy is only first order.

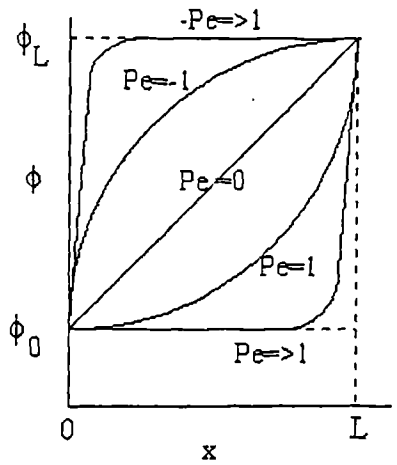

Figure 3.4. Variation of a variable ϕ, between x=0 and x=L for the Power Law scheme. Fluent Users' Manual (1996).

3.5 Pressure-Velocity Coupling using SIMPLE

For a three-dimensional problem, the continuity and three momentum equations allow the velocities and pressures to be determined. These four

equations can be solved as a set of simultaneous equations to obtain the values of the four unknowns. However, this method is computationally intensive and would limit the size of problem that could be tackled on a particular computer system. To solve this problem an iterative solution method that solves each of the four equations sequentially has been developed. For this iterative method to be successful a procedure needs to be developed which allows the pressure to be updated, as this is not explicitly available through any of the conservation equations.

By default Fluent uses the SIMPLE (Semi-Implicit Pressure Linked Equations) algorithm originally suggested by Patankar and Spalding(1972). The pressure-velocity coupling is therefore obtained by recasting the continuity equation in terms of a pressure correction.

The one-dimensional momentum equation(3.40) can be written as:

$$A_P u_P = \sum_{NB} A_{NB} u_{NB} + (p_w - p_e)A + S \qquad (3.48)$$

where A_P and A_{NB} are coefficients containing the convection and diffusion contributions of the momentum equation, A is the area of the cell and NB refers to neighbour points. For the one-dimensional problem, Figure 3.3, the neighbour points would be E and W. S is defined as a source term.

When interpolating the momentum and pressure for the cell faces, using the SIMPLE algorithm on the co-located grid system, care needs to be taken to prevent pressure velocity de-coupling. Fluent uses the scheme originally developed by Rhie and Chow(1983) and Peric(1985) which prevented this pressure-velocity de-coupling at a cell centre. Fluent's scheme also incorporates further improvements due to Majumdar(1988), which removes the dependence on under-relaxation factors found in the earlier work of Rhie and Chow(1983) and Peric(1985).

The first stage involves using a guessed pressure field p* taken as the pressure at the last iteration level, to calculate an approximate velocity field u* written as:

$$A_P u_P^* = \sum_{NB} A_{NB} u_{NB}^* + (p_w^* - p_e^*)A + S \qquad (3.49)$$

The continuity equation will only be satisfied by the u* field if the correct pressure field has been applied. For a pressure field that does not satisfy continuity it is necessary to define pressure and velocity corrections p' and u' by:

$$p = p^* + p'$$

$$u = u^* + u' \qquad (3.50)$$

so that p and u are the corrected fields which should satisfy Continuity.

The formula used to generate pressure correction is given as:

$$PA_p p'_p = PA_E p'_E + PA_W p'_W + b \qquad (3.51)$$

where PA_P, PA_E and PA_W represents the pressure correction coefficients for the central, east and west cells respectively and b represents a pressure source term and is related to the continuity equation.

It is given as:

$$b = \rho\left((u^* A)_e - (u^* A)_w\right) \qquad (3.52)$$

where ρ is the density and is assumed to be a constant. An under-relaxation factor is then applied to the values of the pressure-correction to aid stability.

The velocity correction equation may be found by subtracting equation(3.48) from equation(3.49). The equation generated from this subtraction is simplified by neglecting the off diagonal terms, $\sum_{NB} A_{NB} u'_{NB}$ making the algorithm semi-implicit.

The equation for the velocity correction is given as:

$$u_P = u_P^* + \frac{1}{A_P}(p'_w - P'_e)A \qquad (3.53)$$

where A_p is the coefficient at the central node.

The next stage is to update the pressure field, and obtain the new velocity field. This new velocity field can then used to update the general transport equations, such as the turbulence transport equations for the kinetic energy, k and the rate of dissipation ε.

A convergence criterion is then used to determine if the equations have been solved to an acceptable level of accuracy. If the equations are not yet converged then the newly calculated pressures and velocities are set equal to the guessed values and the whole procedure is completed again.

A summary of the SIMPLE algorithm when applied to a co-located grid is shown in Figure 3.5.

The SIMPLE algorithm is used as the standard pressure-velocity coupling method for all the computational models generated in this study.

3.6 Unsteady Flows

3.6.1 Introduction

The computational model used in this investigation will generate a time-dependent solution, due to the rotation of the impeller within the volute. Consequently this study differs from previous investigations in which a single blade passage has been modelled, allowing a steady state solution to be generated.

The following section considers the techniques Fluent applies for solving time-dependent, unsteady flows.

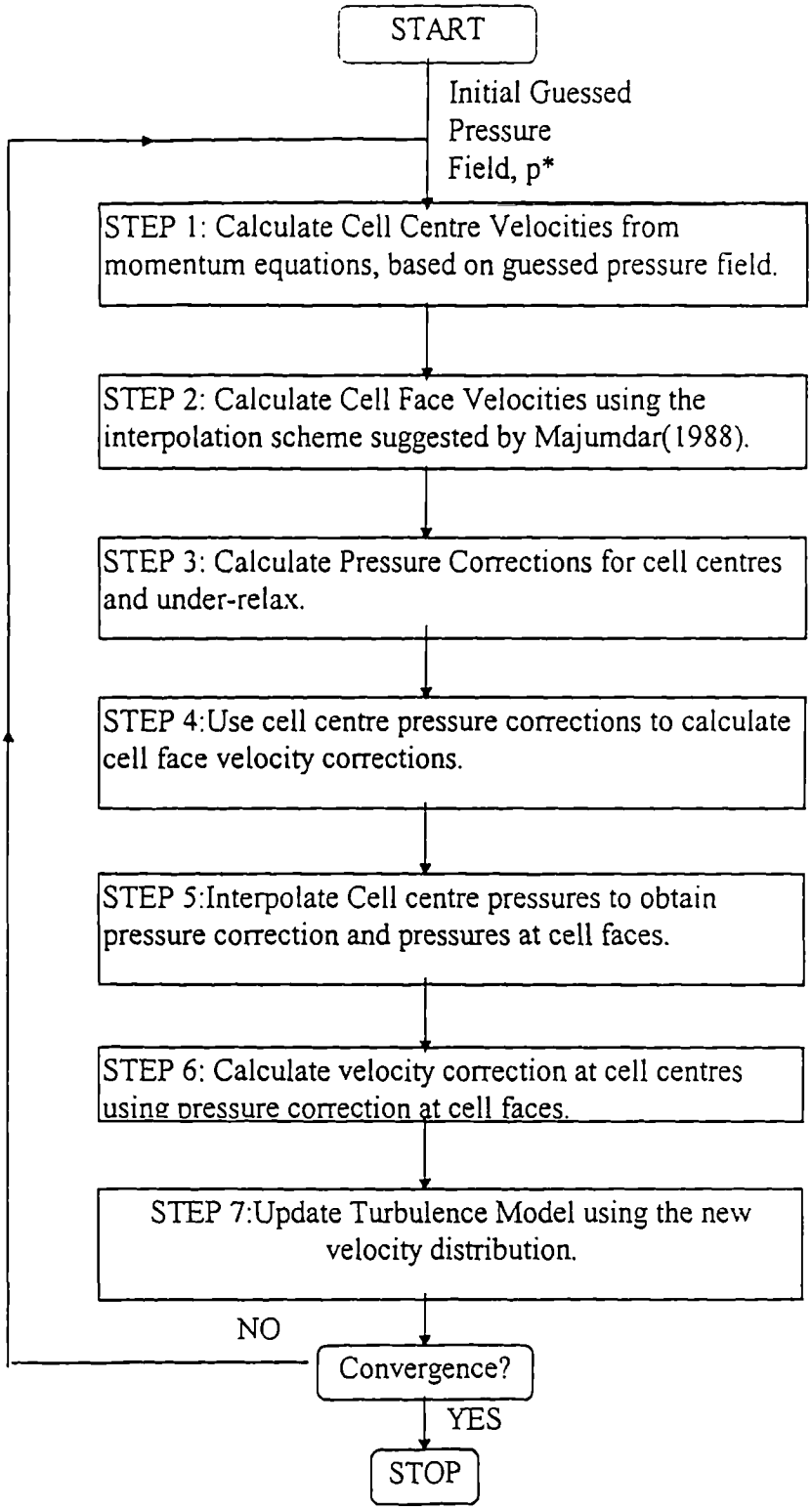

Figure 3.5. SIMPLE Algorithm for Colocated Grid.

For a transient problem the integration of the conservation equations is required over both a control volume and a finite time step. For a general conserved quantity the transient term is given as:

$$\int_{t}^{t+\Delta t} \frac{\partial(\rho\phi)dt}{\partial t} = (\rho\phi)^1 - (\rho\phi)^0 \qquad (3.54)$$

where ϕ is the conserved quantity, 1 indicates the value at time $t-\Delta t$ and 0 indicates the value at time t.

If other terms in the conservation equations are to be integrated assumptions need to be made regarding the variation of the conserved quantity from time t, to time, t+Δt. For example, consider the convection term, ρuϕ.
Integration over a time-step gives:

$$\int_{t}^{t+\Delta t} (\rho u\phi)dt = \left[f(\rho u\phi)^1 + (1-f)(\rho u\phi)^0\right]\Delta t \qquad (3.55)$$

If f=0 an explicit scheme is generated in which values of ρuϕ are calculated only from values of ρuϕ from the previous time level. Fluent uses a fully implicit method in which f=1. This assumes the new value of ρuϕ prevails over the new time step interval. Both the explicit and implicit methods are first order accurate in time, so small time steps are required to ensure accurate results. The main advantage of the fully implicit method is its unconditional stability due to the fact that all its coefficients are positive.

3.7 Sliding Mesh Model

3.7.1 Introduction

Fluent allows the simulation of problems involving impeller volute interaction, using the sliding mesh technique. This was first developed by Rai(1985) and then applied to Fluent by Perng and Murthy(1993). The method entails splitting the grid into two separate grids, one of which moves with the impeller, while the other is stationary and is fixed to the volute. The grid which contains the impeller is allowed to "slide" relative to the stationary grid. The interaction between the two grids takes place along a

slipping plane or surface and the values of the flow variables across this slipping surface are calculated using a conservative interpolation scheme.

Perng and Murthy(1993) presented the conservation equations in Cartesian tensor form for an incompressible fluid operating in a moving mesh as:

$$\frac{D}{Dt}\rho + \frac{\partial}{\partial x_j}\rho(u_j - v_j) = 0 \qquad (3.56)$$

$$\frac{D}{Dt}\rho u_i + \frac{\partial}{\partial x_j}\rho(u_j - v_j)u_i = -\frac{\partial p}{\partial x_i} + \frac{\partial}{\partial x_j}(\tau_{ij} + \tau_{ij,t}) + S \qquad (3.57)$$

where ρ is the density,

u_j is the flow velocity,

v_j is the velocity component due to the movement of the grid,

τ_{ij} is the molecular stress tensor,

$\tau_{ij,t}$ is the Reynolds Stress tensor,

S is a source term.

Equation(3.56) represents the mass conservation equation and the equation(3.57) represents the momentum equation. The expression D/Dt is the total derivative and expresses the time rate of change of a particular variable in the moving reference frame.

3.7.2 The Calculation of Interface Fluxes

The following analysis uses the notation developed in sections 3.4 and 3.5 for the discretized momentum equation. For a two-dimensional Cartesian grid in which the centre cell, P, has four neighbouring cells denoted as E, W, N and S the discretized momentum equation(3.48) can be written as:

$$a_P u_p = a_e u_E + a_w u_W + a_s u_S + a_n u_N + b \qquad (3.58)$$

where a represents the coefficient and u the velocity component.

The approach of Perng and Murthy(1993), as used by Fluent, involves the creation of fictitious cells on both sides of the slip plane. Figure 3.6 displays a section of a two-dimensional Cartesian grid in which one of the

zones moves relative to the other. The centre cell, P, is bordered by four neighbour cells, W, N, E, and S. The north cell, N, however is a fictitious cell formed from two cells in zone 2 that overlap the centre cell, P, in zone 1.

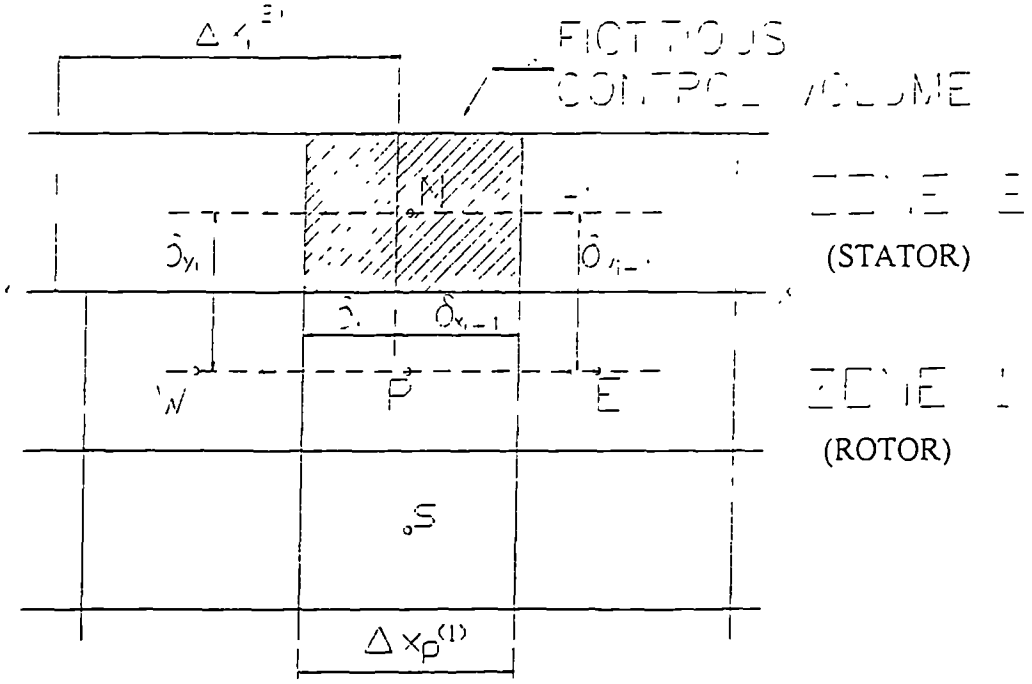

Figure 3.6 Interfacial Interpolation. Perng and Murthy(1993).

Fluent calculates the flux contribution to cell P from the West, South and East cells using the method described in section 3.4. The procedure used to calculate the value from the fictitious North cell is outlined now.

From Figure 3.6 the overlapping areas of the fictitious north cell, are denoted by δ_{xi} and δ_{xi+1}. It is assumed that the mass flux south from zone 2 is known, and these mass fluxes (mass flow per unit area) are denoted by $m_i^{(2)}$ and $m_{i+1}^{(2)}$ for the i and i+1 cells.

The mass flux acting on the north face of cell P in zone 1 is calculated using linear interpolation and this is given as:

$$m_P^{(1)} = (m_i^{(2)}\delta x_i^{(2)} + m_{i+1}^{(2)}\delta x_{i+1}^{(2)}) / \Delta X_P^{(1)} \qquad (3.59)$$

This equation ensures that mass conservation is conserved over the entire slip plane. The calculated flux is used to find the convective flux from the North cell in zone 2.

The diffusive flux is found by using linear interpolation of a diffusion operator, $\Gamma/\delta y$ given by Perng and Murthy(1993) as:

$$(\Gamma/\delta y)_P^{(1)} = \left((\Gamma/\delta y)_i^{(2)}\delta x_i^{(2)} + (\Gamma/\delta y)_{i-1}^{(2)}\delta x_{i-1}^{(2)}\right)/\Delta Y_P^{(1)} \qquad (3.60)$$

The north coefficient from equation(3.58) can now be determined using the Power law scheme described in Section 3.4. Having obtained this coefficient the discrete momentum equation(3.58) can be written as:

$$a_P u_P = a_e u_E + a_w u_W + a_s u_S + b + a_n u_N^* \qquad (3.61)$$

where the velocity u_N^* is the velocity at the fictitious north cell centre.

A fully implicit solution technique is used to solve for a particular flow field. The first stage of this solution is to calculate the flow in the rotor. The velocity u_N^* from the fictitious north cell N, is found from linear interpolation of the most recent values at stator cells i and i+1. The flow field in the stator grid is then solved in a similar fashion, also using the prevailing values. The velocity u_N^* can then be updated from the stator solution, and the rotor flow is solved again. This procedure is repeated until the value of u_N^* stabilises.

3.7.3 Boundary Conditions

It is important that cyclic boundaries are applied to each end of the circumferential plane when using the sliding mesh model. The impeller blades are then able to rotate around the computational grid, allowing them to pass through one cyclic boundary and enter at the other. To enable the rotor blades to pass from one cyclic plane to the other, it is imperative that the corresponding cells in the cyclic planes are identical.

3.8 Grid Creation & Sensitivity

3.8.1 Grid Generation

The following section describes how the computational grids were created. It then presents a grid sensitivity study to determine the effect the grid resolution has on the final solution.

The computational grids used in this investigation were created using two pre-processing packages supplied by Fluent. The first package, called PreBFC, created the geometry of the pump. This package was able to perform both the geometry and grid generation, however in this investigation it was used only to create the geometry.

The required geometry was created by manually entering the coordinates of the points that defined it. These points were then joined together by defining curves through them. Figure 3.7 displays a two-dimensional slice of the curves from the geometry data created from PreBFC.

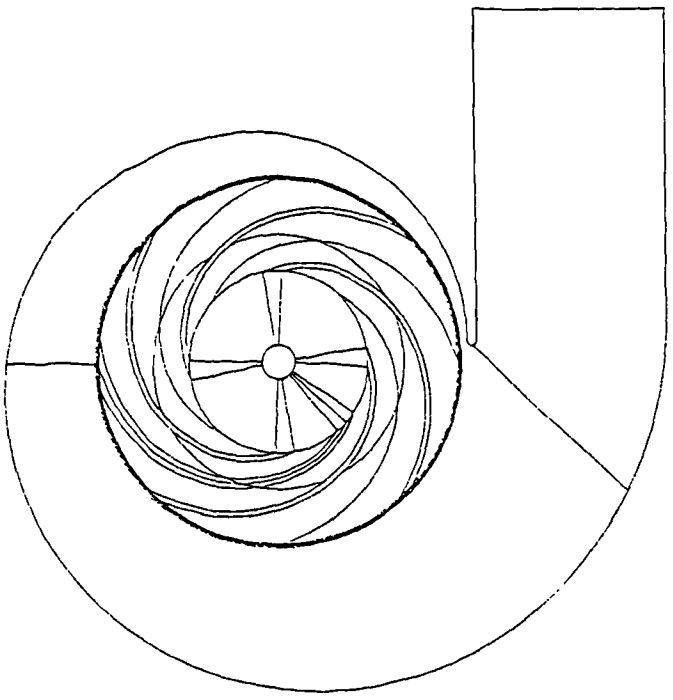

Figure 3.7 Geometry of Pump Created in PreBFC.

After the geometry had been defined, the pre-processor P-CUBE, which is contained in Fluent's GEOMESH package, was used to create the grid.

Fluent uses a numerical coordinate transformation to map the physical grid of Figure 3.7 onto a rectangular computational grid for solution of the governing fluid dynamic equations. Figure 3.8 shows the form of the computational grid.

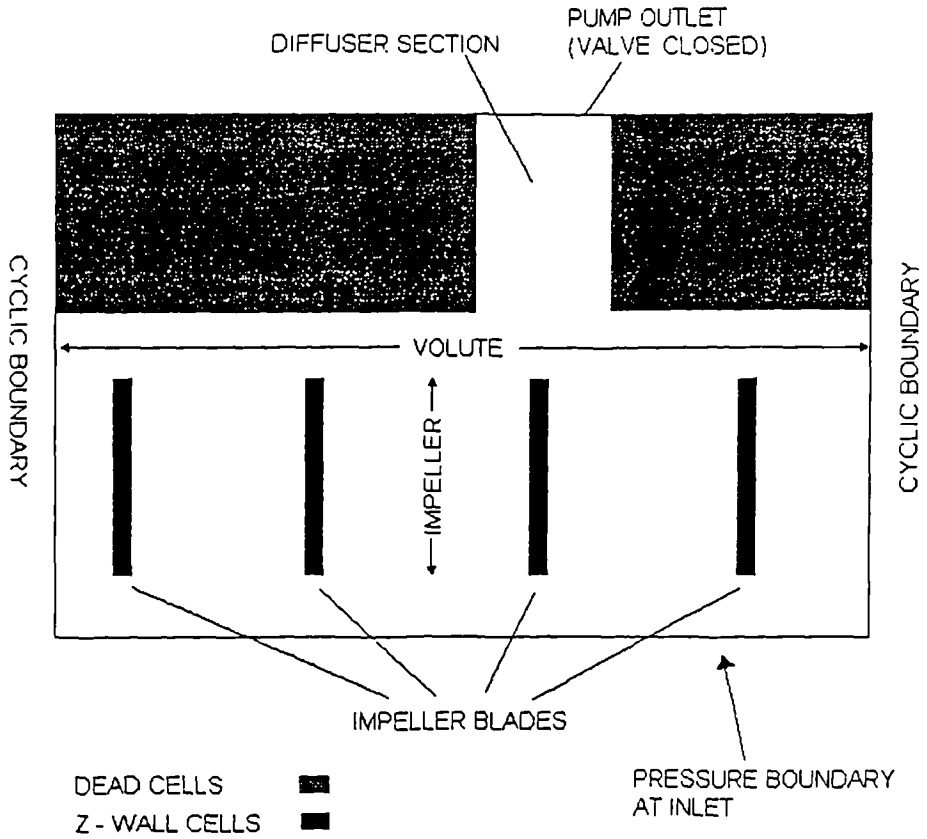

Figure 3.8. Representation of the Computational Grid Generated by Fluent.

The grid generation process involved three distinct processes. First blocks were attached to the domain, with each of the blocks connected to one another. This allowed the topology of the problem to be defined.

The second stage was called Bunching and involved determining the number of nodes and their distribution for each of the blocks in the computational model. P-CUBE forced the creation of legitimate grids by

defining edges as either masters or slaves. A series of topologically connected edges would therefore contain one master with all other edges defined as slaves. The slaves contained the same number of nodes as the master.

After completing the Bunching process, the next step was to create the grid itself. In this investigation three grids were created: a medium, a refined and a fine grid. Having defined the topology by connecting blocks together, the grids could easily be created by changing the bunching set on each of the master edges.

The medium grid had the lowest discretisation with 180 cells circumferentially (one every two degrees) and 44 cells radially in the impeller and volute. The refined grid also had 180 cells circumferentially, but had 58 radial cells in the impeller and volute. The fine grid had 360 cells circumferentially around the impeller (one every degree) with 64 cells radially in the impeller and volute.

Table 3.1 below displays the relative distribution of cells within the volute and impeller for each of the three grids.

	MEDIUM GRID	REFINED GRID	FINE GRID
No. of Circumferential cells	180	180	360
No. of Radial Cells in Impeller	34	34	49
No. of Radial Cells in Volute	10	24	25

Table 3.1 Distribution of Cells in each of the three grids used.

The three final grids were then checked for skewness and negative volumes using LEO, which is a program contained within GEOMESH used for

validating grids. In all the grids no cells were found having negative volumes i.e. each cell was properly defined.

LEO found a high degree of skewness particularly in the impeller, although no bad cells were found anywhere in the domain. This high degree of skewness was unavoidable with a structured grid, due to the log-spiral nature of the impeller blades.

3.9 Case Files & Solution Procedure

3.9.1 Introduction

After creating the grid file, the next stage was the generation of a CASE file. CASE files are created in Fluent and contain boundary conditions, physical properties of the working fluid and the solution models to be used. The next section describes various data inputs used in the creation of the CASE file and also describes the solution technique.

3.9.2 Boundary Conditions & Physical Properties

It is important when comparing any computational model with experimental data that the boundary conditions for the model are similar to those found on the actual test rig.

In this study, the experimental rig was designed specifically to help in the prescription of the boundary conditions for the computational model.

The outer walls of the volute and diffuser were set using standard wall cells. The impeller blades were defined as Z-Wall cells. These cells tell Fluent to rotate the blades with the angular velocity of the sliding mesh.

At the inlet to the pump a pressure boundary was set to represent the atmospheric pressure boundary found on the actual test rig.

Air was used as the working fluid and Fluent allowed the user to input both the density and viscosity for this fluid. The density of air was fixed at

1.23kg/m^3 as Fluent does not allow compressible flow to be solved in conjunction with the sliding mesh model, and for the velocity levels encountered the flow may be considered to be incompressible.

The viscosity of the air was also set constant at 1.7×10^{-5} kg /ms.

3.9.3 Linear equation solver & Under-Relaxation Parameters

Due to the implementation of the sliding mesh model, Fluent's standard multi-grid solver could not be used for the pressure correction equation. Instead the Line Equation Solver (LES) was used to solve for the pressure, as well as for velocities and turbulence parameters.

Fluent allows the user to set the number of sweeps performed by the LES for each of the solution parameters. In all the investigations these were set as follows:

Pressure = 20 Sweeps

Axial Velocity = 1 Sweep

Radial & Circumferential Velocity = 5 Sweeps

Energy (Turbulent) = 5 Sweeps

Dissipation (Turbulent) = 5 Sweeps

Under relaxation is used for two purposes in CFD; firstly to prevent divergence and secondly to speed up the solution's convergence.

The pressure correction equation is susceptible to divergence as the correction can sometimes be too large for stable computation. To prevent this instability only a fraction of the pressure correction is actually applied.

The under-relaxation parameters can also be used to speed up convergence, especially when dealing with a 'well-behaved' solution in which the residuals constantly fall. In this situation under-relaxation can be used to increase the rate of convergence by reducing the amount of iterations required per time step. However, care needs to be taken when increasing

the under-relaxation parameter for one variable to improve its convergence as this can cause another variable to become unstable. The values of the under-relaxation factors used at the start of this investigation are given as:

Pressure = 0.5

Velocities = 0.2

Viscosity = 0.2

Energy (Turbulent) = 0.2

Dissipation (Turbulent) = 0.2

3.9.4 Solution Procedure

The same solution procedure was applied to all cases in this study. This procedure comprised of four distinct phases, as follows:

Stage 1 - Establishing Initial Flow Field

The first stage involved obtaining a first guess for the flow field found in the pump. This was achieved by allowing the sliding grid to rotate a large number of grid cells per time step, without convergence being achieved for each individual time step. Allowing the grid to rotate a large number of grid cells was valid for this investigation as it is the periodic nature of the flow that is of interest and not the start up transient flow field.

The initial flow field was established by allowing the grid to rotate six grid cells (12 degrees for the Refined Grid) per time step with the number of solution iterations at each time step limited to 10. The number of time steps which were performed at this stage of the solution depended on the fall of the residuals and could be monitored in two ways. The first method involved monitoring the time history of a selection of solution variables at different points within the computational domain. The second method involved analysing the values of the residuals for each time step to determine the convergence of the solution.

After obtaining an initial solution the next three phases of the solution procedure were concerned with obtaining a converged solution at each time step.

Stage 2 - Reducing Time Step

The next stage of the solution procedure involved halving the number of grid cells moved per time step to three (grid rotating six degrees per time step for the refined model). This had a dramatic effect on reducing the residuals and moving closer to convergence. The number of time steps completed at this stage of the solution procedure was again determined by analysing the residuals.

Stage 3 Further Reduction of Time Step

The number of grid cells moved was reduced to one grid cell per time step (grid rotating two degrees per time step for the refined model). This was supplemented by the increase in the number of iterations per time step from ten to twenty. This had the effect of convergence being achieved for most time steps. The number of actual time steps completed at this stage was again determined by the analysis of the residuals.

Stage 4 Manual Time Step

The purpose of this final stage was to ensure that a converged periodic solution had been obtained. This was achieved by applying a manual time step so that the grid rotated at only half a degree (quarter of a grid cell for the refined grid). The under-relaxation of the radial and circumferential velocities was also increased to 0.5. At this stage of the solution every time step converged.

To ensure a periodic final solution had been obtained, ten random cells within the impeller, volute and diffuser were chosen and the time histories of the pressure and the radial and tangential velocities were found. The Fluent Users' Manual (1996) states that a converged periodic solution is achieved when the change from one period to the next is less than five

percent. This standard Fluent rule was used to ensure that each of the final solutions was converged and periodic.

3.10 Computational Studies

The following section of work presents three studies that were used in the generation of the final computational model. In section 3.10.1 the various turbulence models are considered. In section 3.10.2 the time dependence of the solution is examined and in section 3.10.3 the grid sensitivity is considered.

3.10.1 Turbulence Model Study

The following study compares three turbulence models, the k-ε model, the RNG- k-ε model and the RNG k-ε model with swirl. A solution of the pump shut-off flow using each turbulence model was obtained using the same solution parameters and grid (Refined Grid see Figure 3.18).

Comparisons were made at a number of radial intervals across the volute passage at Windows 1, 3, 5 and 7 (see Figure 5.1). At each position the results were obtained using the three turbulence models for the tangential and radial velocities and pressure and were averaged over one blade passing period. The object of the study was to determine the influence the turbulence model had on the computed flow patterns.

A selection of results is shown in Figure 3.9 through 3.12. Both the mean tangential velocities and pressures predicted by the RNG and RNG Swirl models gave practically identical solutions.

At virtually all the positions considered the k-ε model under predicted the values obtained using the RNG models, though the velocity results were very similar in each case.

The differences between the k-ε model and the RNG models for the prediction of the velocity were not significant, with qualitative agreement obtained at all positions and quantitative agreement at most.

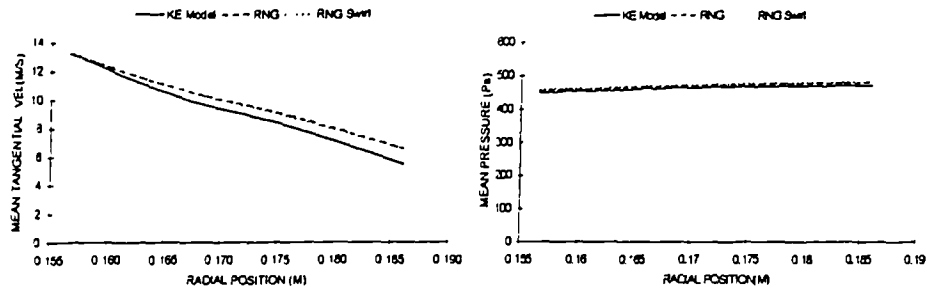

Figure 3.9 Comparison of Turbulence Models. Window 1 Passage-Averaged Results for Mean Tangential Velocity and Pressure.

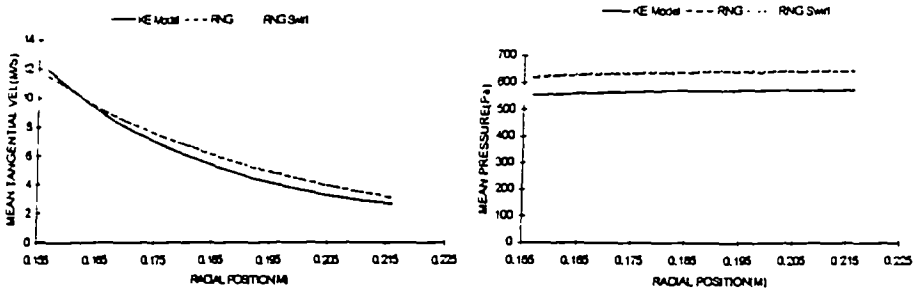

Figure 3.10 Comparison of Turbulence Models. Window 3 Passage-Averaged Results for Mean Tangential Velocity and Pressure.

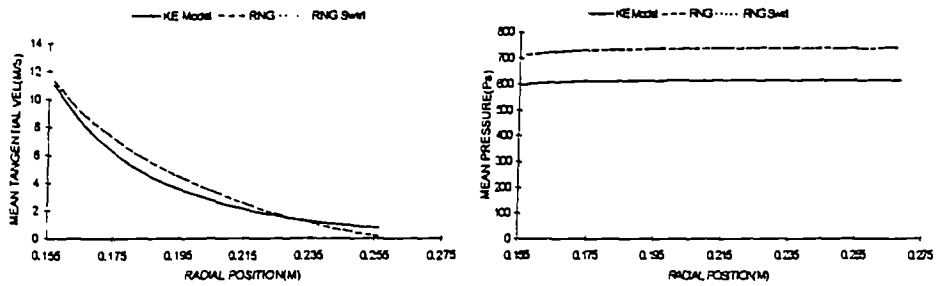

Figure 3.11 Comparison of Turbulence Models. Window 5 Passage-Averaged Results for Mean Tangential Velocity and Pressure.

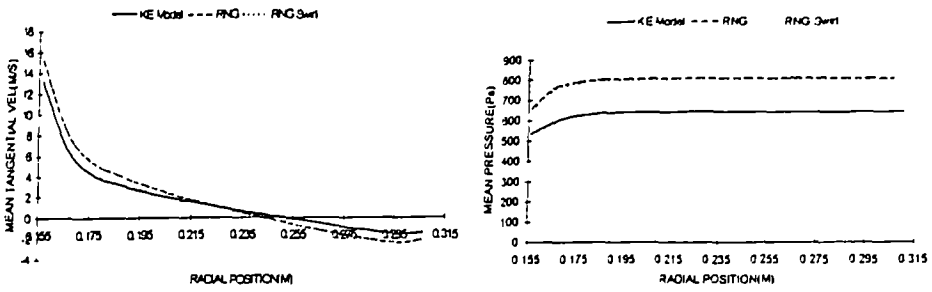

Figure 3.12 Comparison of Turbulence Models. Window 7 Passage-Averaged Results for Mean Tangential Velocity and Pressure.

The above figures show that with an increase in circumferential angle around the volute, the *k*-ε model under predicts the pressure found by the RNG models. However, the RNG models have not had the same level of validation as the *k*-ε model, and as will be shown later the *k*-ε model gives the best agreement with the experimental measurement.

In conclusion, the rest of the calculations will be made using the *k*-ε model. The reasons for this are:

1) Both the *k*-ε model and the RNG *k*-ε models do not take into account the body forces produced by a rotational reference frame, so no benefit is gained when modelling the impeller flow from either model.
2) The time taken to obtain a solution using the *k*-ε model is a lot shorter when compared to the RNG *k*-ε models (these models took nearly twice as long to converge). This makes the *k*-ε model much more appealing when having to perform multiple runs.
3) The *k*-ε model is tried and tested, and its limitations are well documented. The RNG model's extension to swirling flows is a relatively new advancement and Fluent suggest any results be validated against the Reynolds Stress Model, which is currently not available for sliding mesh problems. Also the confidence in the RNG models were not high due to the failure of Fluent and the subsequent use of the beta test code supplied by Fluent.

3.10.2 Time Dependence Study

The following study determines the way in which the length of the time step effects the computational solution for the mean velocities and pressures. As noted in the previous section, the accuracy of a solution using the fully implicit method, which is only first order accurate, can be strongly dependent on the length of time step used. For computational economy it is therefore important to determine the longest time step possible, which produces a time-step independent solution.

In this investigation three lengths of time step were used. These corresponded to the impeller grid moving 0.25 degrees per time step, 0.5 degrees per time step and 1 degree per time step. All the results were taken using the Refined Grid (Figure 3.18) and the k-ε turbulence model. Each different length of time step was run from the same starting point. A check was also made to ensure that each solution generated had a converged periodic solution.

The smaller the value of the time step, the more time steps will be required to complete a period. However, fewer iterations are required to obtain a converged solution for each time step. A larger time step would cause the impeller to rotate further and therefore cause a bigger disturbance to the flow field, requiring more iterations per time step to obtain a converged solution. Therefore there is a compromise between calculating more time steps with less iterations or performing fewer time steps but with more iterations.

A selection of mean velocity and pressure profiles is shown in Figure 3.13 through 3.16. These results show that the 0.25deg and 0.5deg time steps give approximately the same results for the mean velocities and pressures. The larger time step of 1.0deg, however, produces different results from the other two time steps, especially for the mean radial velocities and pressures across the volute.

From this analysis it is therefore possible to conclude that:

- ◊ The 1.0 degree per time step does not produce an independent solution.
- ◊ Both the 0.5degree and the 0.25degree solutions agree closely with each other, with 0.5degree solution within ±5% of the 0.25degree solution for virtually all of the positions considered. It is therefore possible to assume that both these solutions are independent of the size of the time step.

The 0.5degree time step is used for all future calculations as it generates a solution that is independent of the time step with the best computational efficiency.

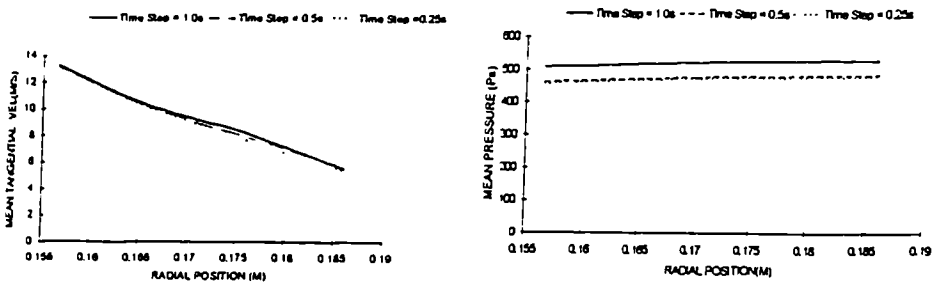

Figure 3.13 Comparison of Size of Time Step. Window 1 Results for Mean Tangential Velocity and Pressure, Averaged over One Blade Passing Period.

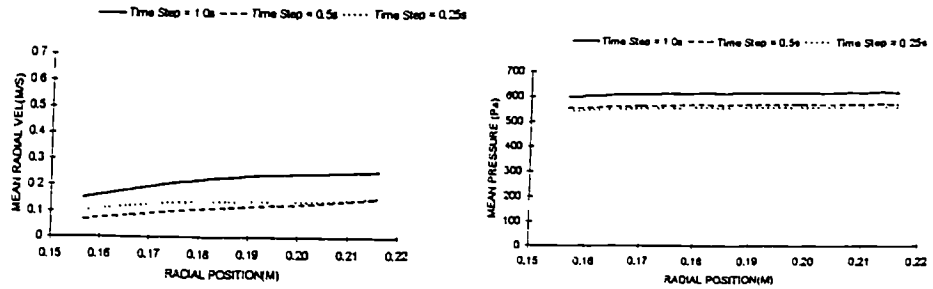

Figure 3.14 Comparison of Size of Time Step. Window 3 Results for Mean Radial Velocity and Pressure Averaged over One Blade Passing Period.

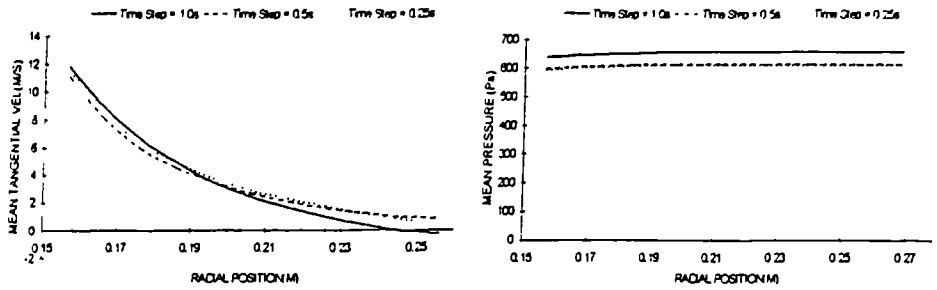

Figure 3.15 Comparison of Size of Time Step. Window 5 Results for Mean Tangential and Pressure Averaged over One Blade Passing Period.

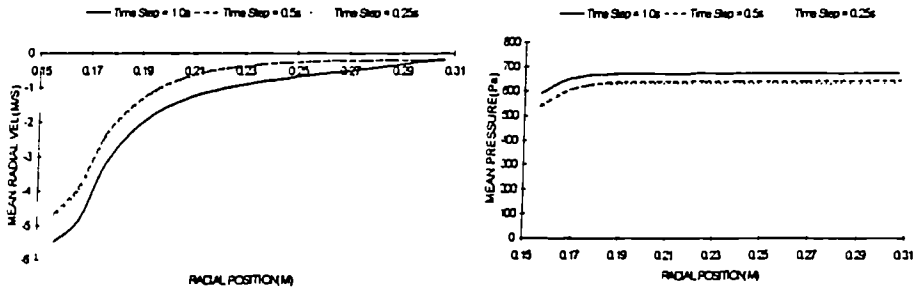

Figure 3.16 Comparison of Size of Time Step. Window 7 Results for Mean Radial and Pressure Averaged over One Blade Passing Period.

3.10.3 Grid sensitivity study

The medium, refined and fine grids are displayed in Figures 3.17 through 3.20. Following the generation of the grids in GEOMESH and then their subsequent validation in LEO, the grids were then converted to Fluent compatible grid files. These grid files could then be read into Fluent v4.4 and converted into Fluent CASE files for solution.

The following study was completed to determine the effect the grid discretisation had on the final solution. It was anticipated that the numerical solution obtained would be dependent on the number of cells used. As the number of cells increased, however, so did the computational run times, making it less attractive to industry.

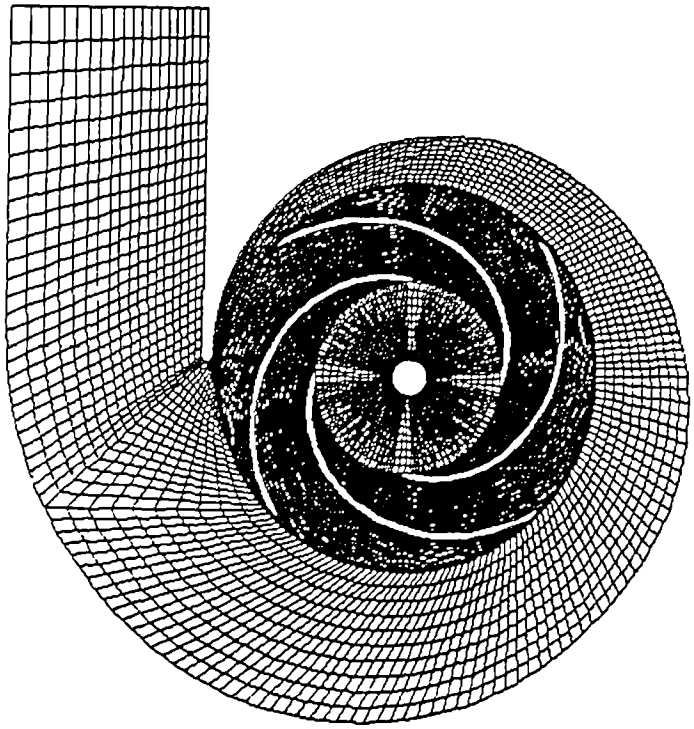

Figure 3.17 Medium Grid (182x89x3 cells).

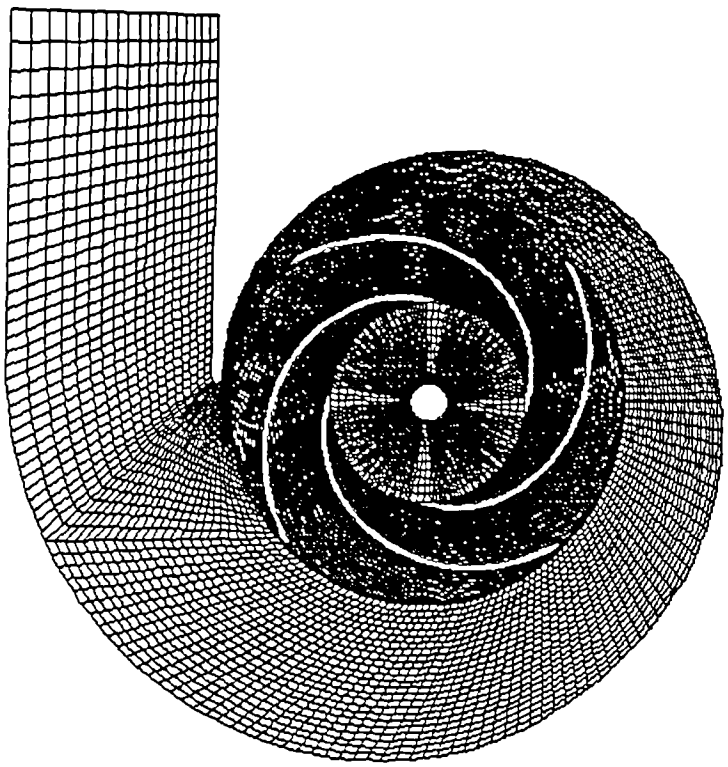

Figure 3.18 Refined Grid (182x109x3 cells).

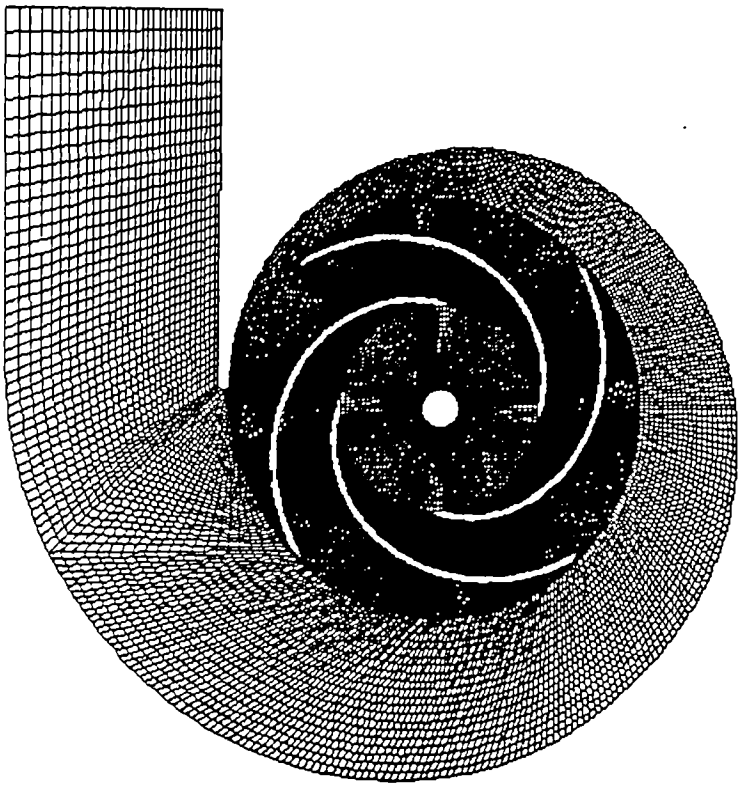

Figure 3.19 Fine Grid (362x137x3 cells).

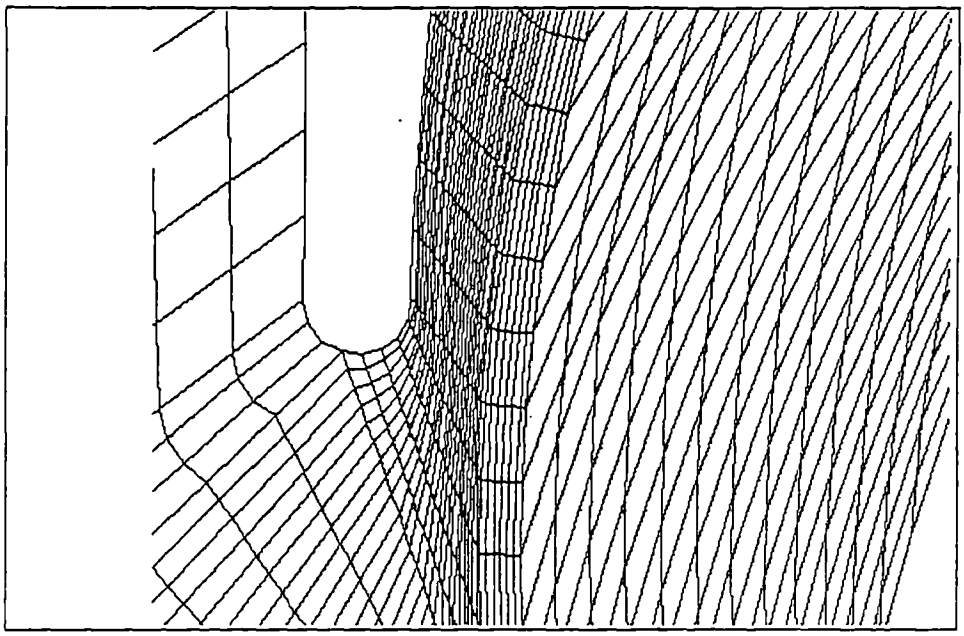

Figure 3.20 Close up of Refined Grid Near Tongue.

The study was performed on three grids, medium, refined and fine to determine a minimum level of grid discretisation that would enable a grid independent solution to be obtained.

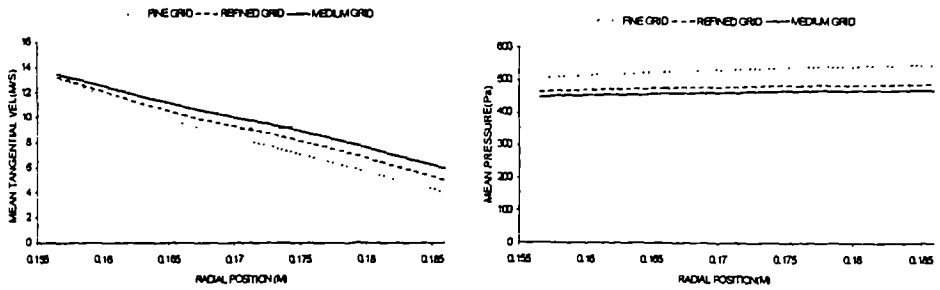

Figure 3.21 Grid Sensitivity Study. Window 1 Passage-Averaged Results for Mean Tangential and Pressure.

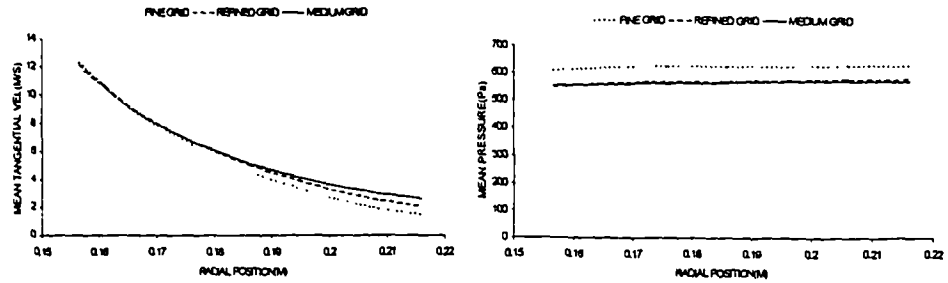

Figure 3.22 Grid Sensitivity Study. Window 3 Passage-Averaged Results for Mean Tangential and Pressure.

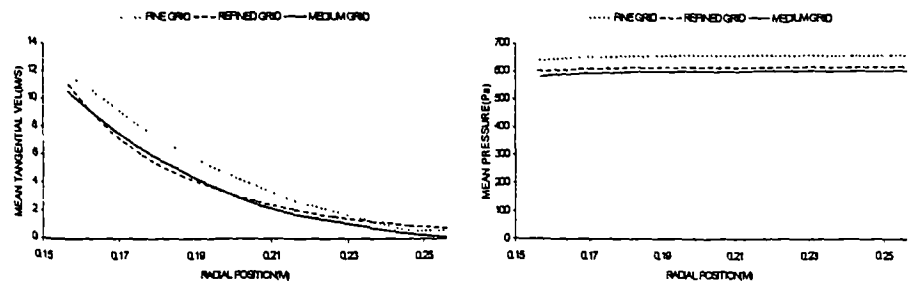

Figure 3.23 Grid Sensitivity Study. Window 5 Passage-Averaged Results for Mean Tangential and Pressure.

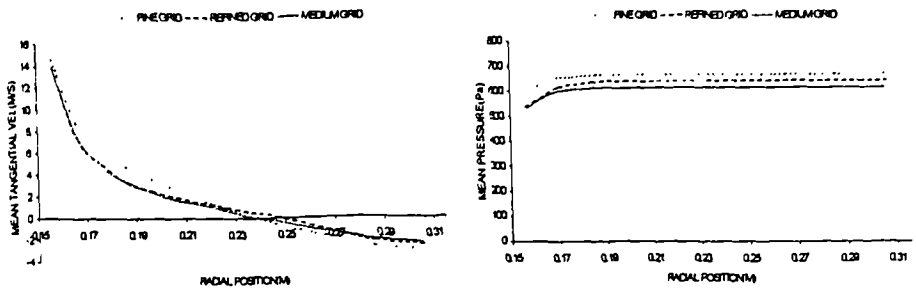

Figure 3.24 Grid Sensitivity Study. Window 7 Passage-Averaged Results for Mean Tangential and Pressure.

From the above graphs the following conclusion can be made:

- ◊ The above figures show that quantitative agreement was obtained for all the positions considered for both the mean pressure and velocity.
- ◊ The fine grid predicted consistently higher mean pressures than the refined and medium grids.
- ◊ The mean pressure calculated using the refined grid was within 10% of the mean pressure calculated using the fine grid at all positions.
- ◊ For the mean velocities, the refined grid agrees at all positions to within approximately 15% of the results obtained using the fine grid. The medium grid agrees to within approximately 20%.

The purpose of this study was to determine the level of grid discretisation required that would allow a grid independent solution to be obtained with the best computation efficiency.

The time required to obtain a solution for the fine grid was approximately twice that required for the refined grid. The medium grid however did not produce significant improvements in the solution time over the refined grid.

The results show the refined grid produced good agreement with the fine grid at most positions but had the benefit of much shorter run times. Therefore for all other investigations, the refined grid will be used as it produces the right balance of accuracy and computational efficiency.

CHAPTER 4:
EXPERIMENTAL APPARATUS

4.1 Introduction

This chapter describes the design of the test rig and the measuring techniques used to obtain the experimental data.

The first section discusses the design of the impeller and volute for the experimental rig. It looks at the constraints, both computational and experimental, which need to be considered in order to obtain experimental measurements.

The second section outlines the basic parts of the LDA system and describes their interaction. It also considers the requirements of the system in terms of seeding and frequency shifting.

The third section describes the equipment set-up for the microphone system used. It looks at the operation of a condenser microphone and the apparatus required to make a successful pressure measurement. It also considers both the static and dynamic calibrations of the microphone.

The final section discusses the errors encountered from both microphone and LDA systems.

4.2 Experimental Rig

4.2.1 Introduction

The experimental test rig was built to enable measurements to be obtained, in order that they could be compared with predicted data from the computational model. To enable a good comparison between the two sets of data, the limitations imposed on the computational model needed to be explored.

The following section considers these restrictions:

◊ Due to limitations of computing resources and time, only a pseudo three-dimensional computational model will be generated. This is in essence a slice of live computational cells, sandwiched between two symmetry planes. In using a pseudo three-dimensional model it is assumed there will be no axial variation in the flow. The experimental rig therefore will have to reflect the absence of axial flow in the computational model.

◊ By implementing the pseudo-three dimensional model, both inlet pipe recirculation observed by Peacock and Goulas(1985), and leakage flow from the impeller outlet back to the inlet, will be eliminated. The experimental rig must therefore take account of this to enable similarity between the two sets of results.

The design of the experimental rig was subject to only a few design constraints. These are as follows:

◊ Air was used as the working fluid instead of water. The use of air reduced the stresses and forces in the experimental rig. The lack of experimental work at shut-off conditions is due to the excessive vibrations and noise that occur when operating at this condition. The detrimental effect of noise and vibrations was significantly reduced when air was used.

The second chapter demonstrates that dynamic similarity could be obtained between results using air and those using water.

Using air also simplifies the sealing requirements due to lower pressures in the rig and it eliminates the need for flow loops, which are essential in supplying water at constant conditions to the rig.

◊ Both the LDA system and the condenser microphones placed restrictions on the design of the test rig. The LDA system required optical access to the volute to allow velocity data to be collected. A microphone holder had to be designed to allow the microphone to be positioned within the volute at different measuring points.

The final design of the test rig is now discussed, with reference to available literature. Miner et al.(1988 and 1989) used a simplified centrifugal pump rig to obtain two-dimensional velocities in the impeller and volute. Miner and co-workers' results showed the axial profile for the tangential velocity to be uniform. However, axial variation did occur for the radial velocity, which was distorted by the ninety-degree turn made by the flow as it moved from the inlet pipe into the impeller.

If the inlet flow and pipe were eliminated, then a pump design based on Miner's could be implemented to produce an experimental two-dimensional flow field. This would provide the similarity required between the computational and experimental results.

This could be achieved by removing the inlet pipe and leaving only a small gap between the hub and a blanking plate to allow a small amount of flow into the pump to replace leakage flow. This small gap at inlet could be modelled computationally using a pressure boundary set at ambient conditions at the inlet to the pump.

As discussed in Chapter 2, an investigation by Barrand et al(1984) demonstrated the use of air as the working fluid in experimental pump test rigs. The investigation demonstrated that dynamic similarity existed between water and air tests, with Reynolds number independence, so long as the Rotational Reynolds, Re was greater than $5x10^5$. This requirement places a restriction on the size of the impeller and its rotational speed.

The leakage flow was reduced by the implementation of tight clearances between the shroud of the impeller and the volute, and the use of a liquid ring seal. This type of seal is used in steam turbine design and uses the centrifugal force developed by the rotation of the impeller to generate a water seal.

4.2.2 Impeller and Volute Design

The design of the experimental pump was based on that used by Miner et al(1988 and 1989). However, this design was adapted to enable air to be used as the working fluid, with further design modifications made to eliminate inlet pipe and leakage flow.

An existing motor and belt drive assembly fixed the angular velocity of the impeller to 188rad/s. In order to obtain dynamic similarity, the dimensions of the diameter of the impeller are defined by the rotational Reynolds number, given as:

$$Re_{ROT} = \frac{\rho \Omega D_t^2}{2\mu} \qquad (4.1)$$

where ρ is the density of the fluid, Ω is the angular velocity of the impeller, D_t is the diameter of the impeller and μ is the viscosity of the fluid.

In this study, air is the working fluid with a μ viscosity of 18×10^{-6} kg/ms and a density, ρ of 1.293kg/m^3. As noted above, the rotational speed is set at 188rad/s.

Figure 4.1 demonstrates the variation of Rotational Reynolds number with an increase in the diameter of the impeller. Using the graph the impeller diameter was set at 0.3m, which gave a Reynolds number of 6.08×10^5. A larger diameter impeller was not considered due to the increase in cost and weight.

The final impeller design is shown in Figure 4.2. The impeller was shrouded with four 16-degree log-spiral blades. The diameter at outlet was set to 0.3m and the inlet diameter was obtained using the same radius ratio as that implemented in Miner's pump.

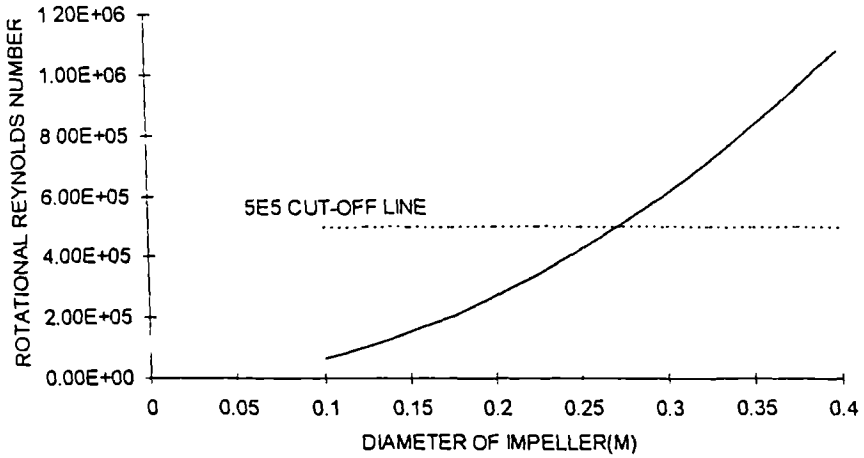

Figure 4.1. Variation in Rotational Reynolds Number with Change in Impeller Diameter.

The impeller had constant width, from inlet to exit, which although unconventional in industrial pump design, prevented any three-dimensional flow effects. The width of the test impeller was obtained using the same width ratio as that used in Miner's pump design.

The volute design is based on than used in Miner's pump using a log-spiral shape, so that at design conditions constant tangential velocity is maintained.

In centrifugal pump design the volute tongue clearance is set typically to be 5%-10% of the impeller radius, leading to clearances of between 7.5mm to15mm. In this investigation a tongue clearance of 9mm was used. This

value was obtained using Miner's tongue ratio, given by, r_2 / r_t where r_2 is the impeller radius and r_t the tongue radius.

The same volute angle of 83^0 applied by Miner was used. This together with the tongue clearance allowed the volute shape to be defined as:

$$R_{VOL} = 0.159e^{0.115(\theta - 0.1145)} \qquad (4.2)$$

where θ is the angle measured around the pump and R_{VOL} is the radius of the volute measured in metres.

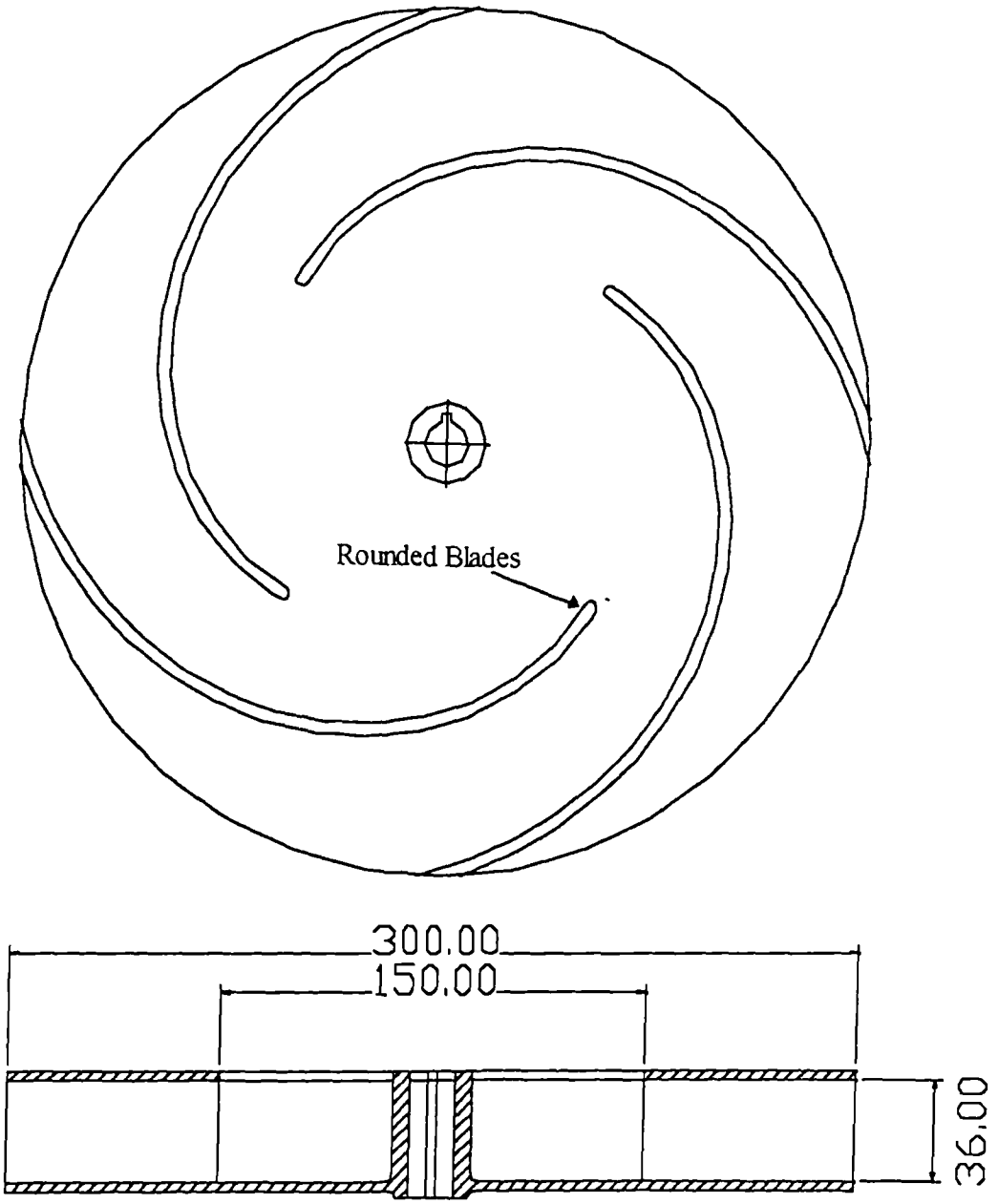

Figure 4.2 Impeller Design Used In Test Rig.

The volute design used in this investigation is displayed in Figure 4.3.

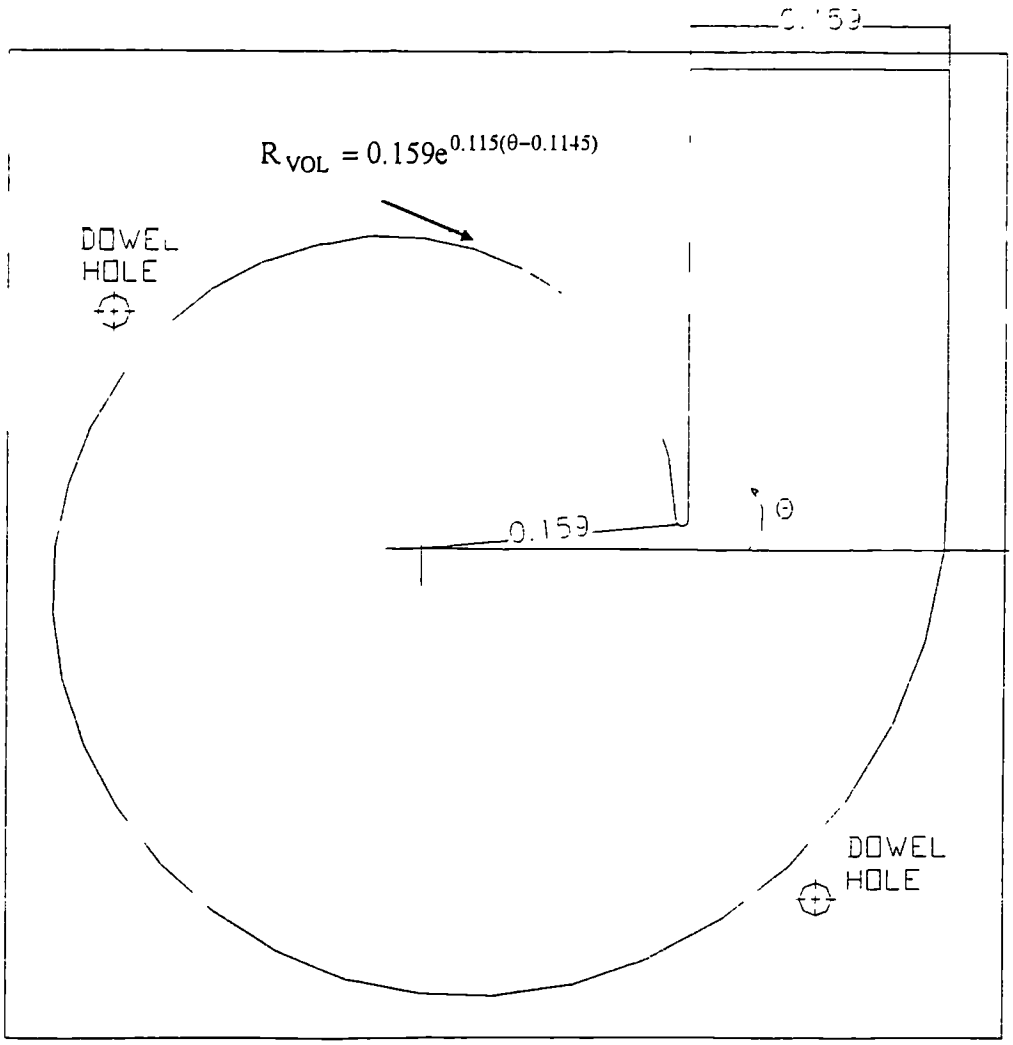

Figure 4.3 Volute Dimensions.
(All Dimensions in m)

The volute was designed with parallel walls at the same width as the impeller to eliminate any three-dimensional flow effects.

Figure 4.4 shows the assembly of the test rig. The rig was constructed in three sections. The first section was an aluminium back plate that bolted onto the bearing housing of an existing fan rig. The back plate provided support for the other sections.

The second section contained the volute's log spiral profile (Figure 4.3). This was manufactured from medium density fibre (MDF). The use of MDF kept both the weight and cost of the experimental rig down. The volute profile was CNC machined and the inside volute profile was coated with a cellulose varnish to seal the MDF. The volute was then bolted to the back plate.

The third section contained the front plate. This front plate was changed depending on whether LDA or microphone measurements were required.

For LDA measurements a sheet of 8mm clear acrylic was bolted to the back plate, sandwiching the volute section. This allowed the required optical access to the volute for the laser.

An aluminium front plate was used for the pressure measurements. Like the acrylic front plate this was bolted onto the back plate, thus sandwiching the volute section. The aluminium front plate had tapped holes positioned around the volute to allow a microphone holder to be placed. These holes were filled by specially manufactured screws when not in use by the microphone holder.

The final part of the assembly was the liquid ring seal. The outer housing of the seal was connected to the front plate and the seal impeller was attached to the pump impeller. The purpose of the liquid ring seal was to eliminate leakage flow from the pump impeller.

The seal design is based on that used in older low pressure steam turbines, as described by Kearton(1973) which uses a liquid ring seal to form a barrier between the impeller outlet and inlet flows.

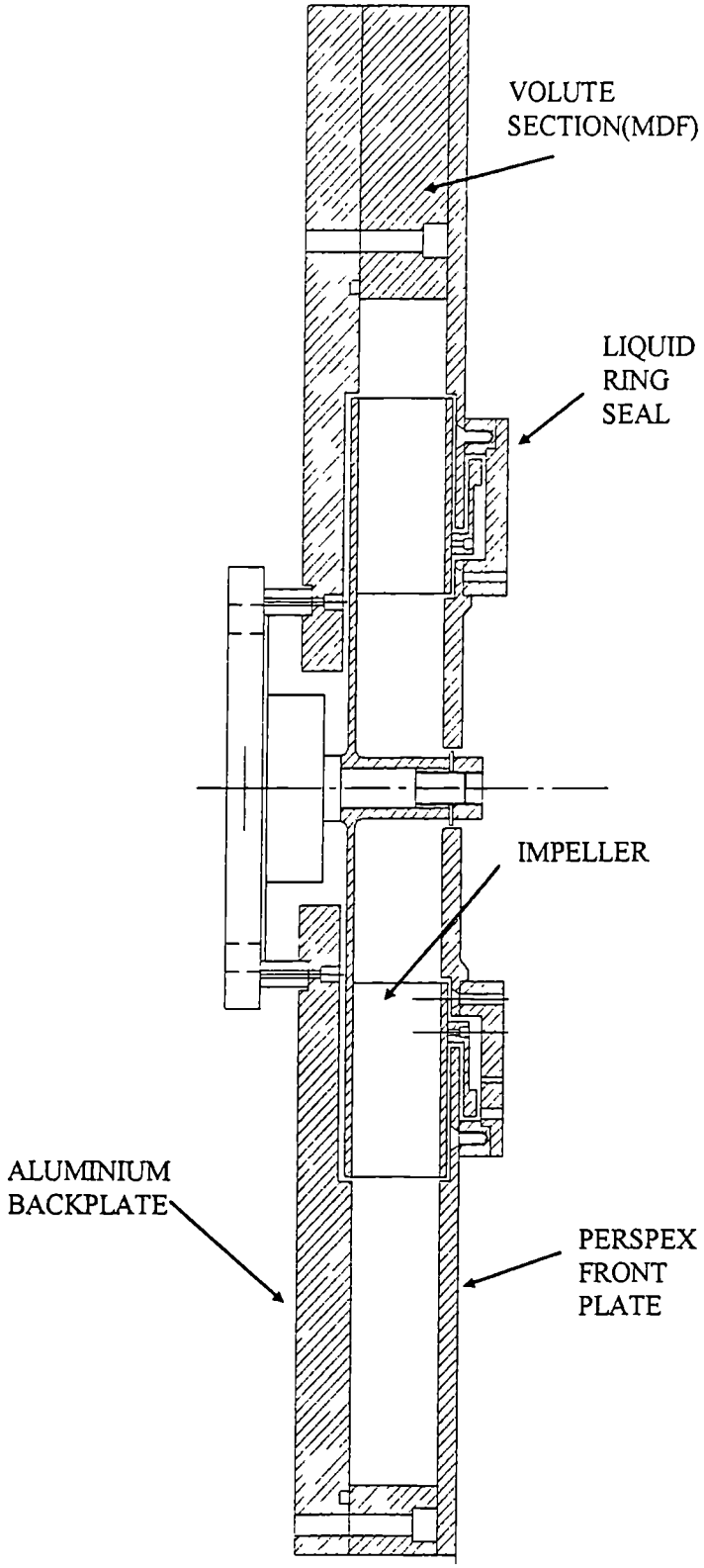

Figure 4.4. Test Rig Assembly for LDA Measurements.

4.3 LDA System

4.3.1 Introduction

The following section gives a brief introduction of the operation of the LDA system. Further detailed information regarding LDA can be found in Drain(1986) and Jenson(1988).

The LDA system employed in this investigation uses the differential Doppler technique displayed in Figure 4.5, taken from Drain(1986). Two beams from a single laser are focused to a point so that the beams cross each other. This crossing of the beams generates a pattern of light and dark fringes. These fringes form what is called the probe volume.

As a seeding particle moves through the probe volume, light is scattered from it and is modulated in intensity by the fringes. A photo detector receives the light and passes it through an amplifier to a signal processor. The processor then uses details of the fringe spacing to calculate the Doppler frequency and then the velocity of the particle.

4.3.2 The LDA System

As mentioned previously, the LDA system takes a measurement when a seeding particle passes through the probe volume and is validated. In the LDA system used in this investigation, the Doppler frequency of a particle is obtained, then the signal processor determines the angular position of the impeller from a shaft encoder. Both the Doppler frequency of the valid particle and the angular position of the impeller are then stored together.

A single-component LDA system operated in back-scatter mode was used for this investigation. The equipment set-up for the LDA readings is shown in Figure 4.6 and the following section considers each of the individual parts of the system.

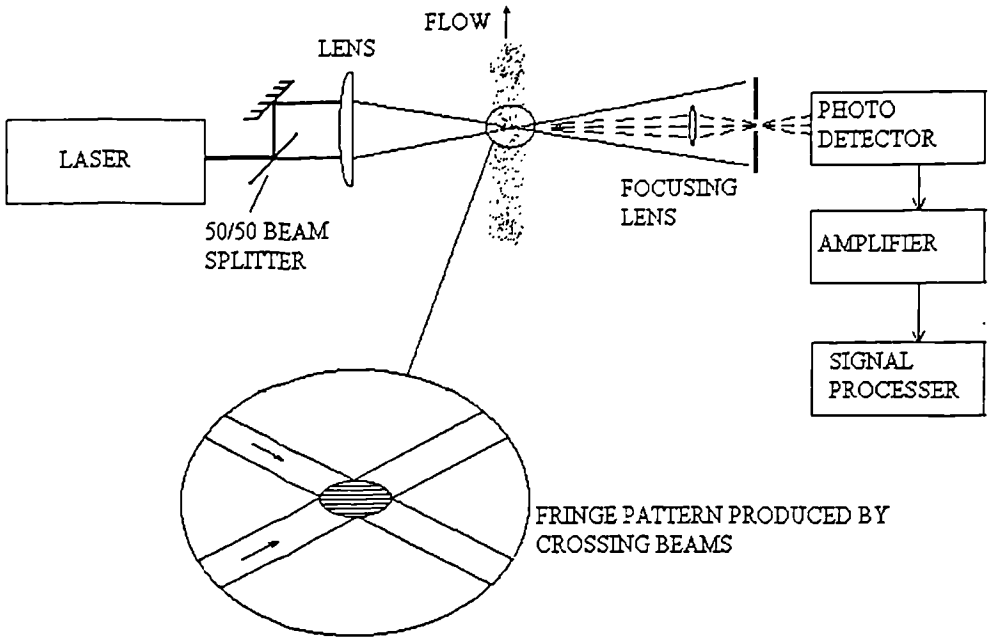

Figure 4.5. Differential Doppler technique, Drain(1986).

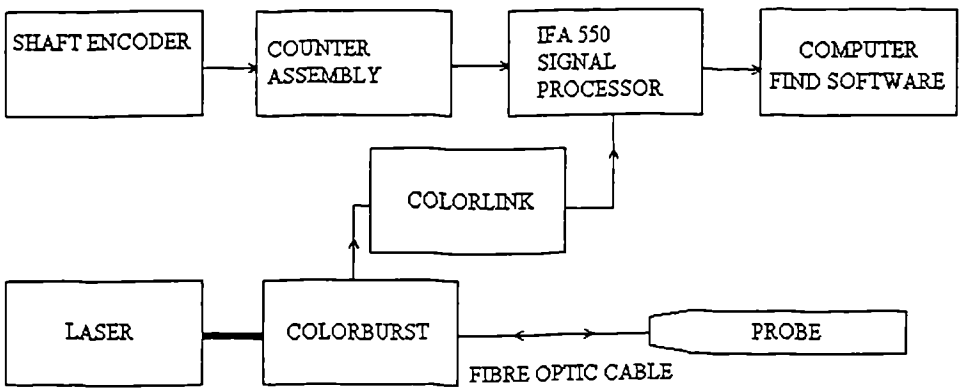

Figure 4.6 Set-up of LDA Apparatus.

A Hohner 85 series incremental hollow shaft encoder was used to determine the position of the impeller shaft. This encoder sends two pulses to the counter assembly box, a once per revolution pulse, and a pulse every half a degree, giving 720 pulses per revolution.

The half-degree pulse is used to increment a counter in the encoder interface unit, which may be read by the IFA550, via the C-bus, whenever a

valid laser measurement is taken. The once per revolution pulse is used to reset this counter to zero after each complete revolution. Thus the position of the impeller is constantly available to an accuracy of ±0.5 degree.

IFA 550(Intelligent Flow Analyser) provides the signal processing for the LDA system and its operation is described in detail by Jenson et al.(1988). The IFA performs two tasks, first to search for a particle and then to validate that particle. The search function obtains a Doppler signal and then passes it to a validation function which determines whether the signal is valid or noise.

A valid particle's Doppler frequency is obtained by the IFA 550 when it passes through sixteen contiguous fringes, within a fixed time period. If a particle meets this criteria, the time taken for it to traverse the fringes is passed as a valid measurement. If the particle fails at any of the fringes, its measurement is aborted and the IFA searches for a new particle.

In this investigation an MI 550 card was installed in the IFA 550 which enabled the information regarding the impeller angle from the shaft encoder to be stored with a velocity measurement.

An Elonex 386 personal computer with 8Mb of RAM was used to store the data files generated in this study. The computer ran TSI's analysis software FIND, Flow Information Display. FIND forms the interface between the user and the system hardware. It also allows diagnostic checks to be made to ensure the hardware is operating correctly.

FIND includes two important programs, the Data Acquisition and the Statistical Analysis Program. The Data Acquisition Program provides the means to set-up both the hardware, such as filters and the frequency shift, and the software, such as the data file management for a particular point. It also controls the hardware when taking the experimental measurement.

A most important function of the Data Acquisition Program is its ability to display a real time histogram of current velocity or frequency measurements. This provides a check that the system is set up correctly and valid measurements are being obtained.

The Statistical Analysis Program performed an analysis of the raw data file generated by the Data Acquisition Program. Following this analysis two files were generated: a statistics file and a velocity file. The statistics file contained statistical information regarding the raw data file, such as the number of points measured, the mean velocity and the standard deviation of the velocity data. The velocity file contained the velocities converted from the raw data file, with no processing of the impeller angular position information.

To determine both the velocity and angle information for a particular point, the velocity file created by the Statistical Analysis Program was processed by another program supplied by TSI called FINDVEL. This program outputted each raw velocity measurement together with a corresponding impeller angle. However, the output from the file was not ordered and the data appeared in the sequence in which it was obtained.

A final piece of analysis software written by Dr I. Potts read each of the files generated by FINDVEL and then averaged the velocities for each impeller angular position. The program reduced the angular discretisation of the shaft encoder from every half-degree to every degree, therefore reducing the amount of data required for manipulation.

For this investigation one hundred revolutions worth of data was collected in six raw data files, each 12 Kilobytes in size, for each measuring position. For evenly distributed flow this would represent one hundred measurements at every half-degree position. These one hundred measurements were then

ensemble averaged together to eliminate noise, leaving only the periodic signal.

An examination of a sample of velocity files was undertaken to determine the number of measurements being collected at each angular position. This examination showed a fairly even spread of data with most positions being within 100±20 velocity measurements per half degree position.

The laser used in this study was a Lexel 2Watt Argon-Ion Laser operated at a nominal power of 0.75Watts. The laser produced a beam of light in the range of wavelengths between 457.9nm to 528.7nm.

The light from the laser was sent to the COLORBURST where it was split into three colours: green, cyan and blue. For this single channel system only green light at a wavelength of 514.5nm, was transmitted down to the probe via a fibre optic cable. The COLORBURST enabled the laser to be aligned to the fibre optic cable using Fibre couplers.

The probe itself combined both the focusing and receiving optics and was portable to allow the operator to position the measurement volume without having to move the whole LDA system.

The COLORLINK received the light scattered by particles in the flow through a fibre optic cable. It then used a Photomultiplier tube to convert the scattered light into an electric signal. This electrical signal was then amplified and filtered before being passed to the signal processor. The Colorlink also performs the important task of providing frequency shift which is discussed in section 4.3.4.

The probe was traversed from point to point using a Puma 560 robot arm. A connection plate was designed to allow the probe to be mounted directly to the wrist of the robot. A number of programs were written using the robot's controller language VAL to move the probe to each of the specified

measurement points. This allowed positioning of the probe to an accuracy of ±1mm in three-dimensional space, together with known angular positioning about the probe axis.

The measurement of the radial and tangential velocity components, using the single channel system, was achieved by rotating the probe through ninety degrees about its axis. The unfortunate drawback of this technique is that it is not possible to measure the fluctuations in each component simultaneously, so precluding measurement of the Reynolds stresses and detailed velocity bias compensation.

Photographs displaying the experimental rig in operation can be found in Appendix C.

4.3.3. Seeding

In order that the Doppler frequency and hence a velocity measurement could be obtained from the LDA system seeding particles must be present to generate scattered light.

In the study of liquid flows, particles which occur naturally can be adequate for LDA measurements, however, when using air, seeding particles need to be artificially added.

Drain(1986) and Agarwal and Johnson(1981) stated the requirements for seeding particles as:

1) They must follow the flow sufficiently closely.
2) They must scatter enough light to give an acceptable signal to noise ratio under the conditions of the experiment and produce the required data rate.
3) They must survive the environment.
4) They must not be prohibitively expensive.

For this investigation a smoke generator was successfully used to produce seeding particles from a mixture of smoke oil and paraffin. The generator produced neutrally buoyant smoke particles that were sub micron in size.

The response of a particle to fluctuations in the velocity field was presented by Drain(1986). He presented the following criterion based on viscous drag which estimates the maximum diameter of a particle for a given frequency of fluctuation. The formula is given as:

$$a^2 < 0.1\frac{\mu}{f_u \rho_p} \qquad (4.3)$$

where a is the radius of a particle, μ the viscosity of the fluid (1.8×10^{-5} kg m^{-1} s^{-1}), f_U is the frequency of fluctuations and ρ_P is the density of the particle (900 kg m^{-3}).

The blade passing frequency in this investigation is 30Hz, however to determine the frequencies of the major fluctuations an investigation was made by connecting a condenser microphone to an F.F.T. frequency analyser. The results of the investigation showed frequencies up to 1500Hz would capture all major fluctuations.

To satisfy the criterion presented in equation(4.3) particles must have a diameter of less than 2 microns. Therefore the smoke particles would respond to any significant flow fluctuations found in this investigation. The ability of the smoke particles to scatter light and thus produce an adequate data rate was determined experimentally. Tests were performed to determine the velocity at various positions in the volute and outlet duct. At all the positions considered the data rate was good, and varied between a minimum of 100Hz to over 12KHz.

The previous investigation already demonstrated the ability of the particle to survive the environment inside the pump test rig and generate a good data

rate. However, due to the smoke condensing on the front plate, the rig had to be stripped down and cleaned periodically.

The smoke particles were introduced into the pump through the gap formed between the hub and front plate. Therefore any flow distortion error generated by the injection of particles was negligible and is not considered further in this study.

4.3.4 Frequency Shift

In an LDA system without frequency shifting the fringes in the control volume would be stationary and thus would generate the same frequency modulation on the back-scattered light from particles moving in the forward or reverse flow directions. This ambiguity is eliminated by shifting the velocity-frequency curve, using a frequency shift on one of the beams, thus enabling positive and negative flows to be measured; see Figure 4.7. This ability to measure both forward and reverse flows is one of the major advantages LDA has over other experimental methods such as hot-wire anemometry.

One of the advantages of frequency shift is to increase the number of fringes within the measurement volume therefore increasing the probability a valid measurement can be made.

The increase in the number of fringes due to frequency shifting also reduces the effects of fringe bias. This is the relationship between the particle's direction of travel and the probability of a measurement being obtained. The maximum probability of a measurement occurs when a particle travels perpendicular to the fringes, with zero probability occurring if the particle moves parallel to the fringes.

A study by Whiffen(1976) demonstrated that a minimum frequency shift of twice the Doppler frequency of the particle significantly reduced the effects

of directional sensitivity. However, using an even higher frequency shift can eliminate the effects of fringe bias.

Frequency shift can also enable the measurement of a small velocity component in the presence of a larger mean flow. This is of particular importance when attempting to measure the small radial velocity component in the presence of the much larger tangential velocity.

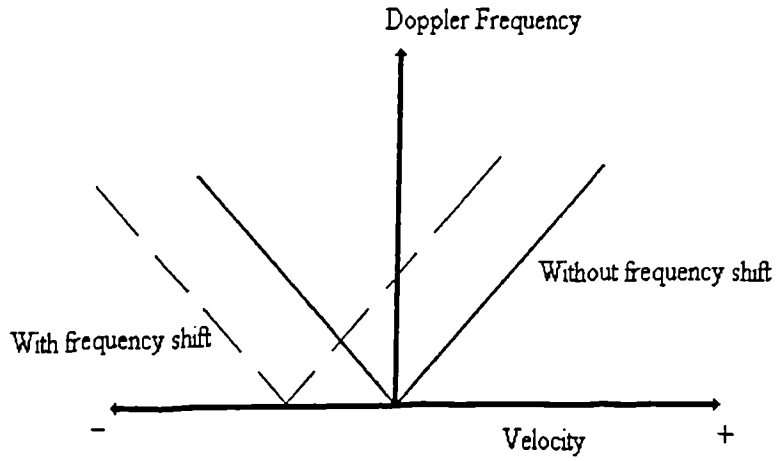

Figure 4.7. Using Frequency Shifting to Eliminate Directional Ambiguity TSI Model 9230 COLORLINK Multicolour Receiver Manual(1994).

The amount of frequency shift which is added is, however, limited by the range of the filters on an LDA system. Using a large frequency shift in a system with a high mean velocity can cause data representing high velocities to be lost. Using the real time histogram facility provided by TSI's FIND software and then reducing the frequency shift if necessary can prevent this problem. Generally a 5MHz frequency shift was used in this study.

Table 4.1 displays the probe volume specifications, which were used to determine the frequency shift and its effect. Figure 4.8 displays a section through the probe volume. From table 4.1 it may be seen that even a

stationary particle in the measurement volume would generate fifty-eight fringe crossings, compared to the sixteen required for a valid sample, when a 5MHz shift is present. Thus measurement of small radial velocities is possible despite the presence of much larger tangential velocity component.

Minimum number of complete cycles required by signal processor (N_m) - (16 fringe crossings)	8
Fringe spacing (d_f)	3.6 μm
Diameter of measurement volume (d_m)	117 μm
Number of fringes (N_f)	32
Typical tangential velocity within pump (V)	10m/s
Doppler Frequency of a particle Calculated as ($V\ d_f$)	2.78 MHz
Transit time of particle Calculated as (d_m/V)	11.7 μs
Effective frequency shift selected	5 MHz
Flow Movement	Against Fringes
No. of fringes crossing measurement volume in transit time	58
Total number of fringe crossings for typical particle travelling at 10m/s (N_f + Additional fringes due to frequency shift)	90

Table 4.1 Probe Volume Specifications.

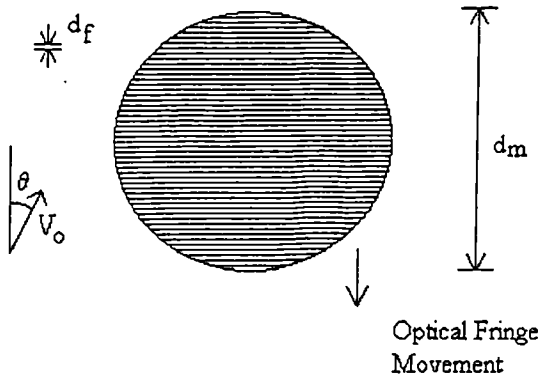

Figure 4.8 Definition of Probe Volume Measurement.

4.4 Microphone System

4.4.1 Introduction

The basic construction of a condenser microphone comprises an air gap enclosed by a diaphragm, usually a thin stretched piece of metal, and an insulating material containing an electrode (Figure 4.9). A voltage is then applied across the diaphragm and electrode causing the diaphragm to be attracted inwards.

A force, due to a fluctuating pressure field on the diaphragm, causes a change in distance between the diaphragm and electrode that in turn changes the capacitance of the microphone.

The Oscillator consists of a Clapp oscillator and a tuned circuit that converts the microphones change in capacitance to a change in frequency. This change in frequency is then converted to a voltage by the reactance converter.

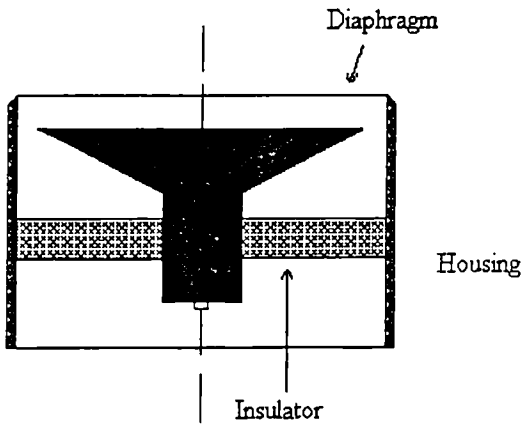

Figure 4.9 Basic Components of a Condenser Microphone. DISA(1970).

4.4.2 Apparatus set-up for Microphone Measurements

The equipment used to obtain and record the fluctuating pressure measurements is displayed in Figure 4.10 and the following section describes its operation.

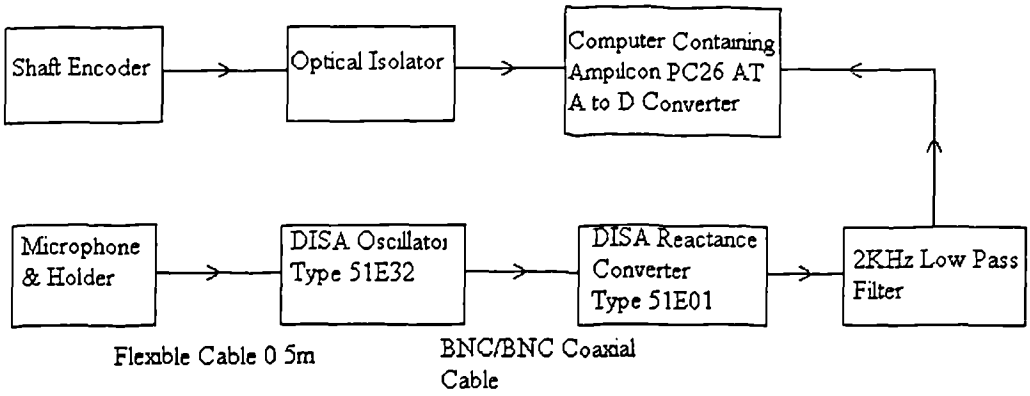

Figure 4.10. Equipment Assembly for Pressure Fluctuations.

This investigation used a quarter inch Brüel & Kjær Type 4135 condenser microphone which had been adapted by DISA for use with their Capacitive Measuring System.

The microphone was placed in a specially designed holder. This holder performed two important tasks:

- ◊ It enabled the microphone to be easily positioned within the volute at the various measuring positions.
- ◊ It was specially designed to ensure that the response of the microphone was not altered for the frequencies of interest therefore allowing accurate measurements of the fluctuating pressure to be made.

The microphone and holder together form a Helmholtz Cavity. The frequency response of this cavity determines the range of frequencies that can be accurately measured.

Richardson(1953) gave the resonant frequency for a Helmholtz Cavity as:

$$n = \frac{a}{2\pi}\sqrt{\frac{s}{lv}} \qquad (4.4)$$

where a is speed of sound, s is the area of the tapping, l is the length of the tapping and v is the volume of the cavity. Using a spreadsheet, values for resonant frequency of the cavity were calculated taking into account the

blade passing frequency and manufacturing capabilities. This led to a design of cavity that had a resonant frequency of 3750Hz allowing pressure fluctuations to be measured safely up to 1500Hz.

The final microphone holder was designed by Dr. I. Potts and the results of the frequency analysis of the microphone and holder is shown in section 4.4.3.

The DISA Capacitive Measuring System comprised the DISA Oscillator and Reactance Converter. The Oscillator contained four tuning circuits that allowed the range of pressures measured to be changed. In this investigation the 0.1pF tuned circuit was employed which allowed the measurement of pressures between ±70mm H_2O.

The Reactance Converter first amplifies the oscillator signal before it is sent to a frequency sensitive detector that rectifies the signal. The final output from the Converter is a voltage variation that is related to the pressure on the microphone.

This voltage variation is then passed through a second order, low pass filter with a 2KHz bandwidth to remove unwanted higher frequencies and noise.

After the analogue signal had been filtered it was then converted into a digital signal using an Amplicon PC 26 AT card operating in an Elonex 486 PC. The PC 26 AT card was a sixteen channel Analogue to Digital conversion card with 12-bit resolution on a ±10Volt scale and a conversion time of 10μs.

The shaft encoder used to determine the angular position of the impeller for the pressure measurements was the same as that used for the LDA measurements. That is, a Hohner 85 series rotary incremental shaft

encoder. This generated two pulses, one every half degree and one every revolution.

During experimental testing the signal from the encoder was found to be contaminated with noise from the electric motor driving the impeller. Feeding the signal generated by the encoder through an optical isolator, IL74, to remove the noise solved this problem.

The program that controlled the taking of the data was written by D.Glennie. This program averaged one hundred revolutions worth of voltage measurements for each of the 720 angular positions with the average voltage stored with its respective angular position in a data file.

The conversion from voltage to pressure was achieved using equation(4.5) obtained from the static calibration of the microphone. This equation provided a relationship between pressure and voltage for the microphone arrangement.

4.4.3 Static Calibration of Microphone

The static calibration enabled the voltages generated from the microphone to be converted into pressures. Figure 4.11 displays the pressure vessel arrangement used to perform the static calibration.

The microphone was attached to the pressure vessel using an adapter, and was then connected to a digital voltmeter through the DISA Capacative Measuring System. A Betz manometer capable of measuring pressures to an accuracy of 0.1mm of H_2O was also connected to the pressure vessel.

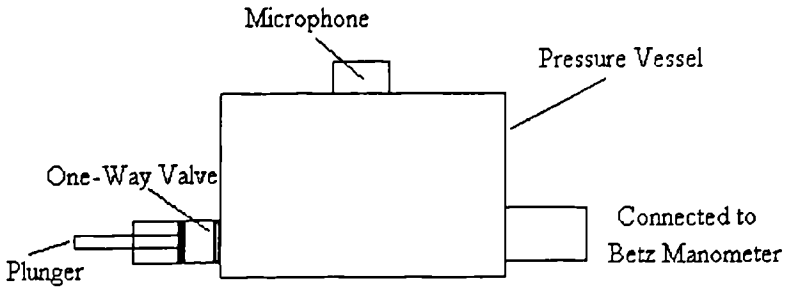

Figure 4.11 Apparatus used for Static Pressure Calibration.

The plunger was then used to generate increasing pressures within the vessel. The pressures measured from the Betz manometer and the voltages taken from the voltmeter were then recorded. The results from the calibration were then plotted, Figure 4.12. An equation was then fitted to the data to obtain the relationship between the pressure and the voltage.

This relationship is given as:

$$Pressure\ (PA) = -0.54v^2 + 104.04v \qquad (4.5)$$

where v is the voltage measured in volts.

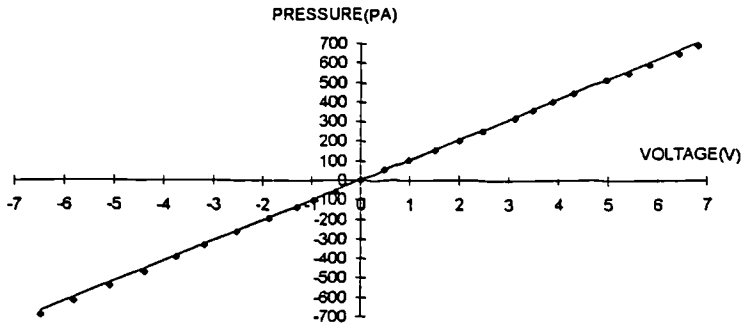

Figure 4.12 Static Calibration Curve

4.4.4 Dynamic Calibration of Microphone

The frequency response of the microphone and holder was obtained to ensure that, for the fluctuations of interest, resonance did not occur. The calibration followed that presented by Kacker(1973).

The test involved positioning the horizontal axis of a loudspeaker 0.35m from the surface of a bench. At a distance 0.60m from the speaker a ¼" microphone was positioned so that the whole face of the microphone could receive the sound radiation from the speaker. The microphone holder was positioned 25mm from the first microphone.

The loudspeaker was then energised by an oscillator and the ratio of the outputs from the two microphones, in response to the same sound wave, was plotted as a function of frequency.

Figure 4.13 shows the ratio of the magnitudes from the microphones with a varying frequency. The graph shows the microphone holder has a resonant frequency of approximately 3750Hz, similar to the predicted value given by Richardson(1953).

The response curves show the holder can be used safely up to 1500Hz. Figure 4.13 displays the ratio of the magnitudes being constant and approximately equal to unity up to 1500Hz. Figure 4.14 shows the ratio of the phase angles being constant and approximately equal to zero up to 1500Hz.

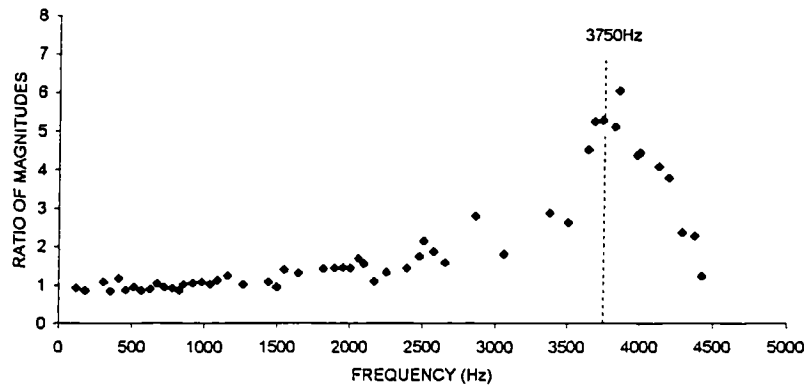

Figure 4.13 Ratio of Magnitudes for
Microphone Holder /Direct Reading Microphone.

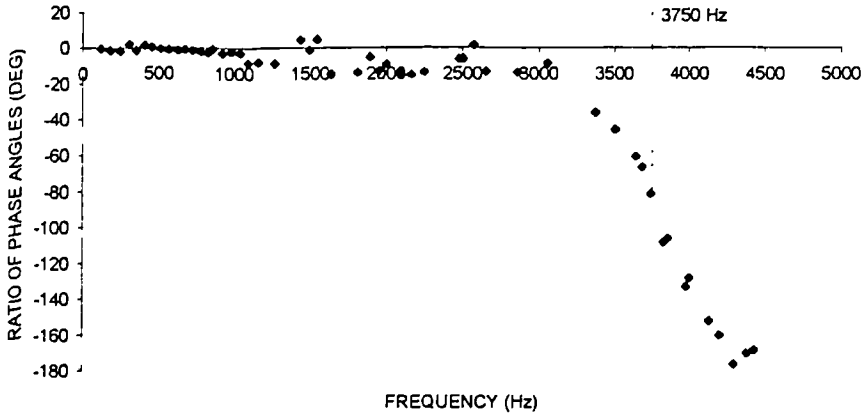

Figure 4.14 Ratio of Phase Angles For
Microphone Holder /Direct Reading Microphone.

4.5 Error Analysis

This section of work considers the experimental errors encountered when measuring either the velocities or pressures.

4.5.1 Laser Measurement Errors.

The following section of work considers the experimental errors that occurred during the measurement of the velocities when using the LDA system.

Errors induced from the seeding of the flow

The injection of the seeding particles into the flow can distort the main flow field. Particles from the smoke generator discharged against the hub of the impeller and were then induced into the pump due to the low pressure that existed there. This prevented any disturbance to the main flow field. Further evidence that the main flow field was not disturbed can be found from the lack of any axial velocity variation.

Particle lag bias

Particle lag bias occurs when the particles are too large to follow the flow accurately. However, by using the analysis presented previously, a correct

size of particle, able to respond to the fluctuations in the flow, was selected. Therefore any error due to particle lag bias will be negligible.

Errors due to the geometrical parameters of the probe volume

These errors tend to be small with the most common type being frequency broadening. This error occurs when the laser beams do not intersect at the beam waist and result in non uniform spacing of the fringes. However, the use of fibre couplers and fibre optic cables ensure the location of the beam waist is optimised.

Velocity Bias

Velocity bias is an error that can cause the mean velocity measured to be higher than the actual mean velocity of the flow. It is not always correct to assume the mean velocity of the flow is the average of all valid measurements, as particles with a higher velocity are more likely to pass through the measurement volume in a given time.

There are two conventional methods that correct for this bias. The first method involves measuring the radial and tangential velocity components simultaneously. The second method determines the transit time of each valid velocity reading and then weights the mean velocity accordingly.

The LDA system used has a single component so it would be impossible to measure both velocity components simultaneously. Also the IFA 550 does not calculate the transit time of each valid measurement.

Nevertheless, it was possible to manually calculate the transit times for the tangential flow. The analysis of some sample positions showed the weighted mean velocity was almost identical as the averaged value, showing any error introduced was negligible for this particular study.

Electronic effects

This type of error is concerned with the internal processing by the IFA and is impossible to quantify. However, ensuring both repeatability of results together with a good data rate can minimise any electronics errors.

Probe Volume Location Uncertainty

The probe was traversed using a Puma 560 robot arm. This allowed extremely accurate positioning and repeatability of the probe volume within the pump. The uncertainty in the axial and radial positioning is estimated as ±0.5mm. The angular rotation error of the probe is estimated at ±0.5degree.

The overall error for the LDA measurements is difficult to determine due to a lack of available information. However, an examination of the scatter from the passage averaged data shown in Figure 5.3 can provide an insight. The overall error therefore can be estimated as ±0.2m/s for the radial velocity component and ±0.4m/s for the tangential velocity component.

4.5.2 Pressure Measurement Errors.

The formula used to determine the fluctuating pressure exerted on the microphone is given by equation(4.5). The voltmeter used had an uncertainty of ±0.01v. Using the rules of the propagation of errors from Barry(1978) an overall error for the pressure measurements can be obtained. Representative values of these uncertainties are shown in Table 4.2.

Voltage(V)	Pressure(Pa)
1	103.5 ± 1.03
2	205.92 ± 1.02
3	307.26 ± 1.01
4	407.52 ± 1.00
5	506.70 ± 0.99
6	604.80 ± 0.98
7	701.82 ± 0.96

Table 4.2 Uncertainties in Pressure Measurements.

CHAPTER 5:
COMPARISON OF COMPUTATIONAL AND LDA RESULTS

5.1 Introduction

In this chapter a comparison is made between the computational results generated using Fluent and experimental data obtained using LDA. The investigation examined the radial and tangential velocity components within the volute, and the horizontal and vertical components in the outlet duct.

Data for the study was collected at points across the volute at forty-five degree intervals. Figure 5.1 displays the location of the measurement points within the volute and outlet duct and Appendix D gives a full listing of the locations used.

Each of the forty-five degree intervals were labelled as windows, with Window one at the twelve o'clock position. The experimental data was obtained in a plane at mid axial position within the volute. A further study was made to determine if any axial variation occurred.

Data was also taken around the circumference of the impeller at angular locations 22.5deg apart. This data was used to estimate the impeller leakage flow.

Further measurements were taken of the vertical and horizontal velocity components, across two horizontal traverse lines, within the outlet duct. All the data was collected at shut-off flow condition only.

The data is presented in two forms. The first shows the radial and absolute tangential velocity as a function of the blade position with respect to the stationary LDA's probe volume. The second shows the variation radially across the volute passage of the mean radial and tangential velocity, averaged over one blade passing period.

5.2 Passage Averaged Data

The experimental data used for comparison with the computational results is passage averaged raw data. This method assumes the flow pattern for all four blade passages to be identical allowing them, therefore, to be averaged together. To verify this assumption an investigation was made to examine the periodic nature of the flow measured.

Figure 5.2 displays the raw data for a complete revolution, that is, four periods, at Window 3, R=0.156m, (1.04 x rotor tip radius). Each data point represents approximately one hundred data samples, for the same rotor position, averaged together.

Figure 5.3 displays a comparison of each of the four passages together with the passage averaged data. This investigation demonstrates that there was very little variation in either the radial or tangential profile from passage to passage. It is therefore valid to assume passage averaged data is representative of the overall flow structure and this process will be applied to all further measurements.

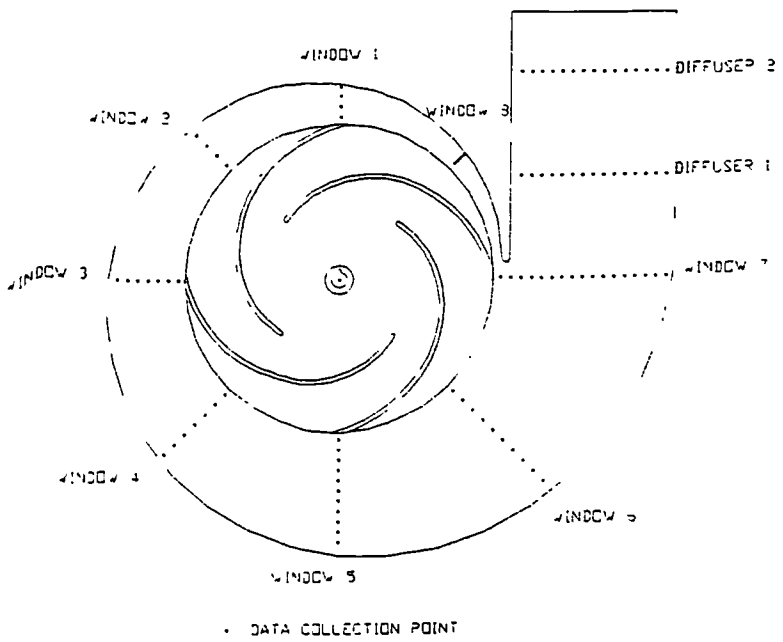

Figure 5.1 Position Used For Comparison of LDA and Fluent Data.

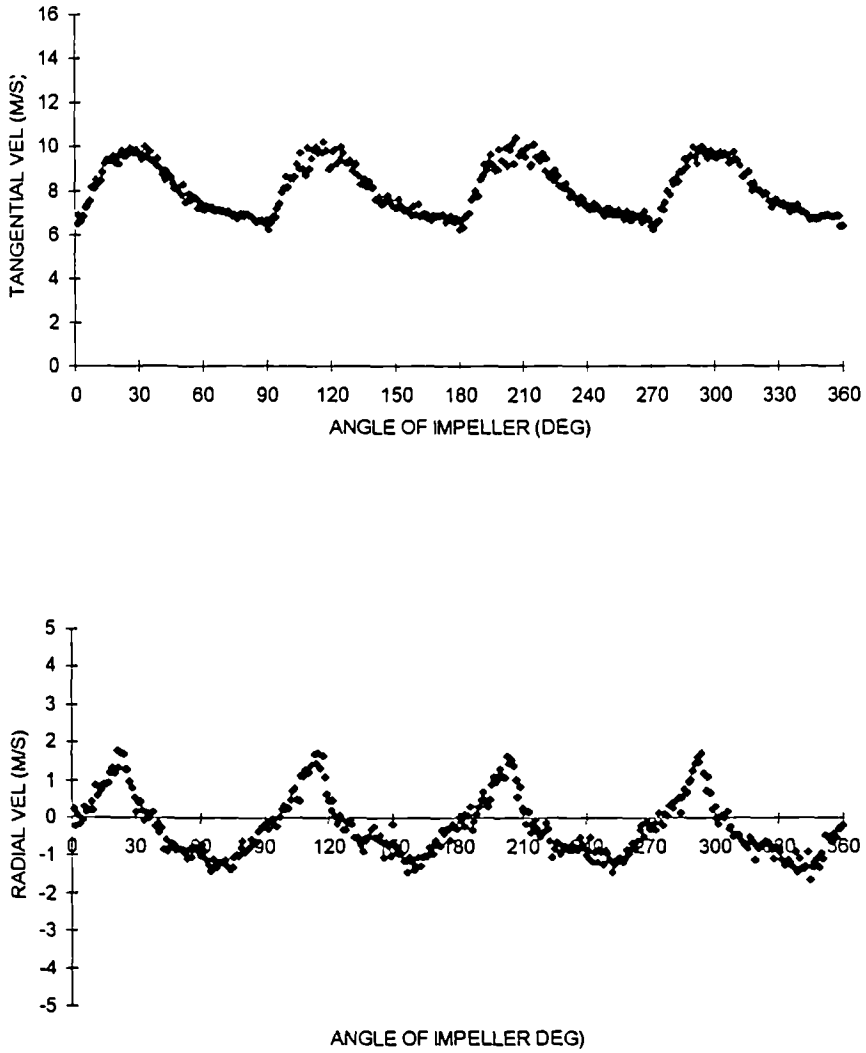

Figure 5.2 LDA Raw Velocity Data For One Revolution, Window 3, R=0.156m. (Based on average of approx. 100 samples at each position).

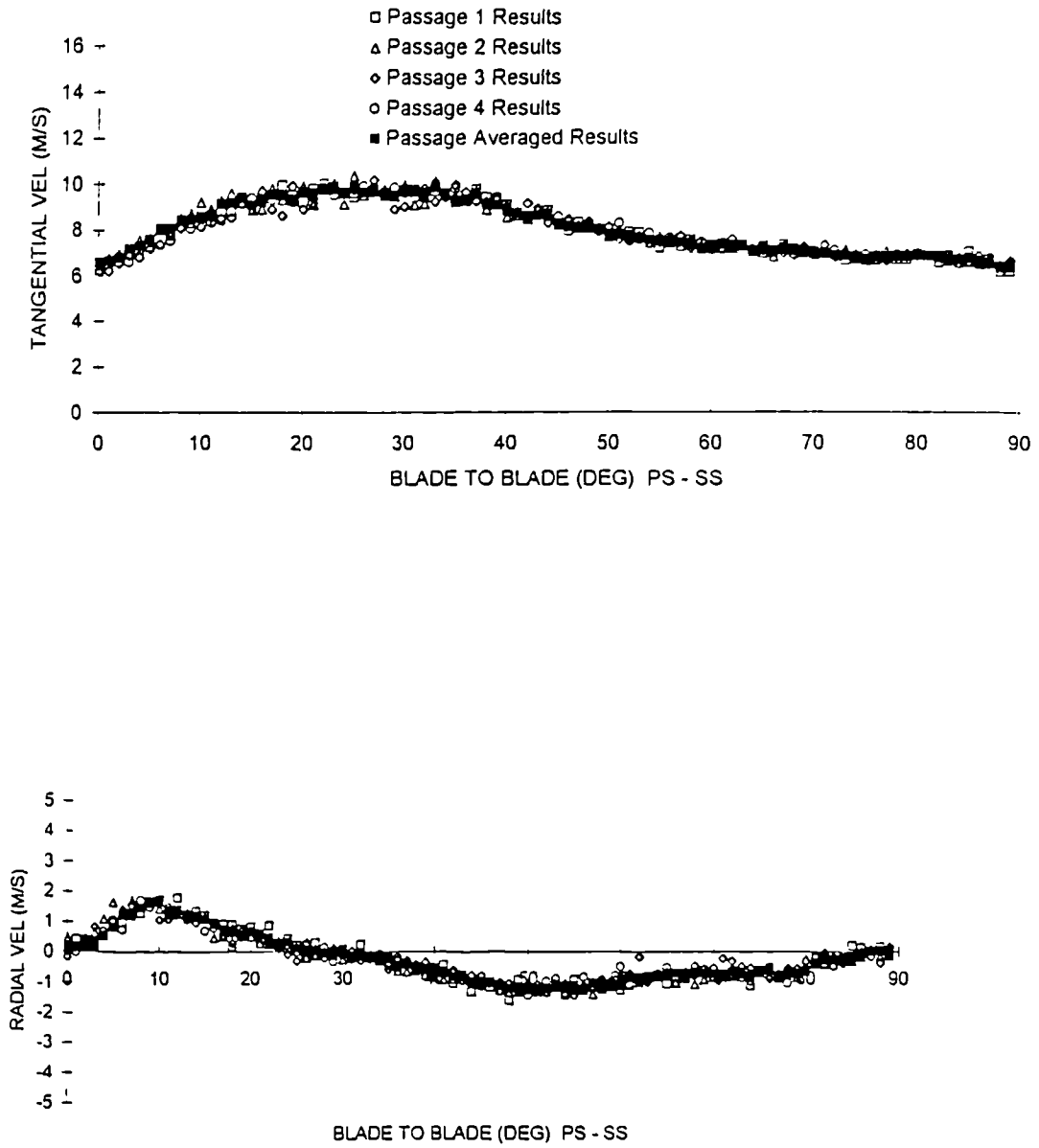

Figure 5.3 Comparison of Four Passages At Window 3, R=0.156m.

5.3 Axial Variation

The experimental rig was designed to give a two dimensional flow field suppressing any three dimensional flow effects as far as possible. To determine whether this had been achieved, an axial traverse was made at Window three, R=0.156m. The axial dimension of the volute ran from +18mm from the centreline at the shroud or inlet side, to -18mm to the hub or shaft side. However, measurements were only possible between -8mm and +12mm because of reflections from both the impeller shroud and the wall of the volute.

Figure 5.4 shows the axial positioning used for this study and Figure 5.5 shows the axial variation in the tangential and radial velocity profile. The data was presented as a function of the blade position. Both traverses show some variation in the axial profile. The axial variation in the tangential velocity is within ± 12 % of the centreline data whereas the radial velocity is within 30% of the centreline radial velocity.

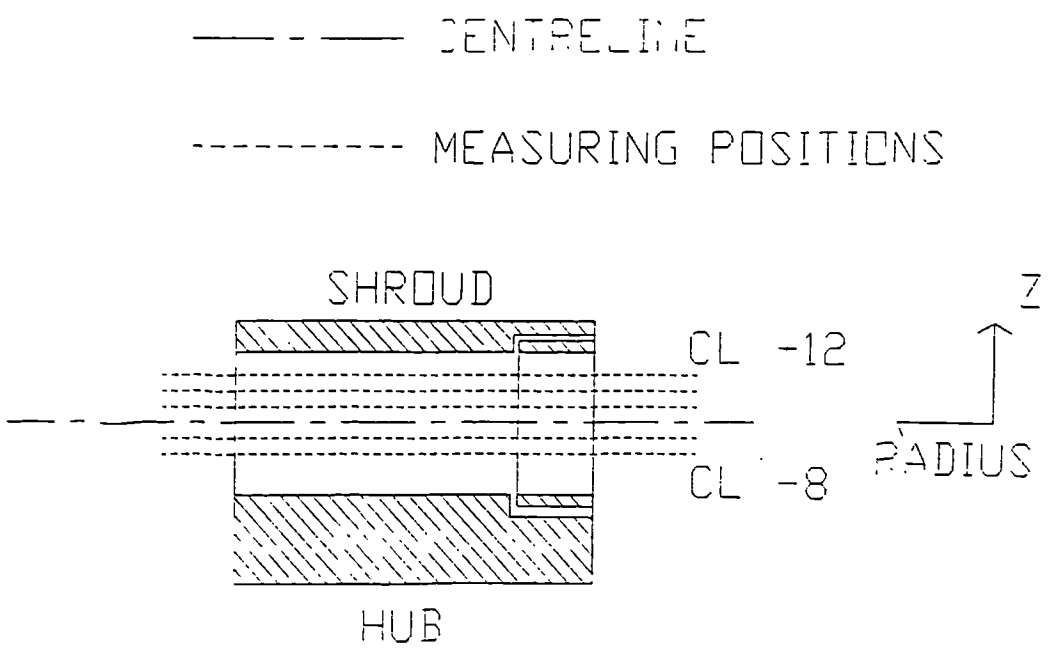

Figure 5.4 Axial Measuring Positions in Volute.

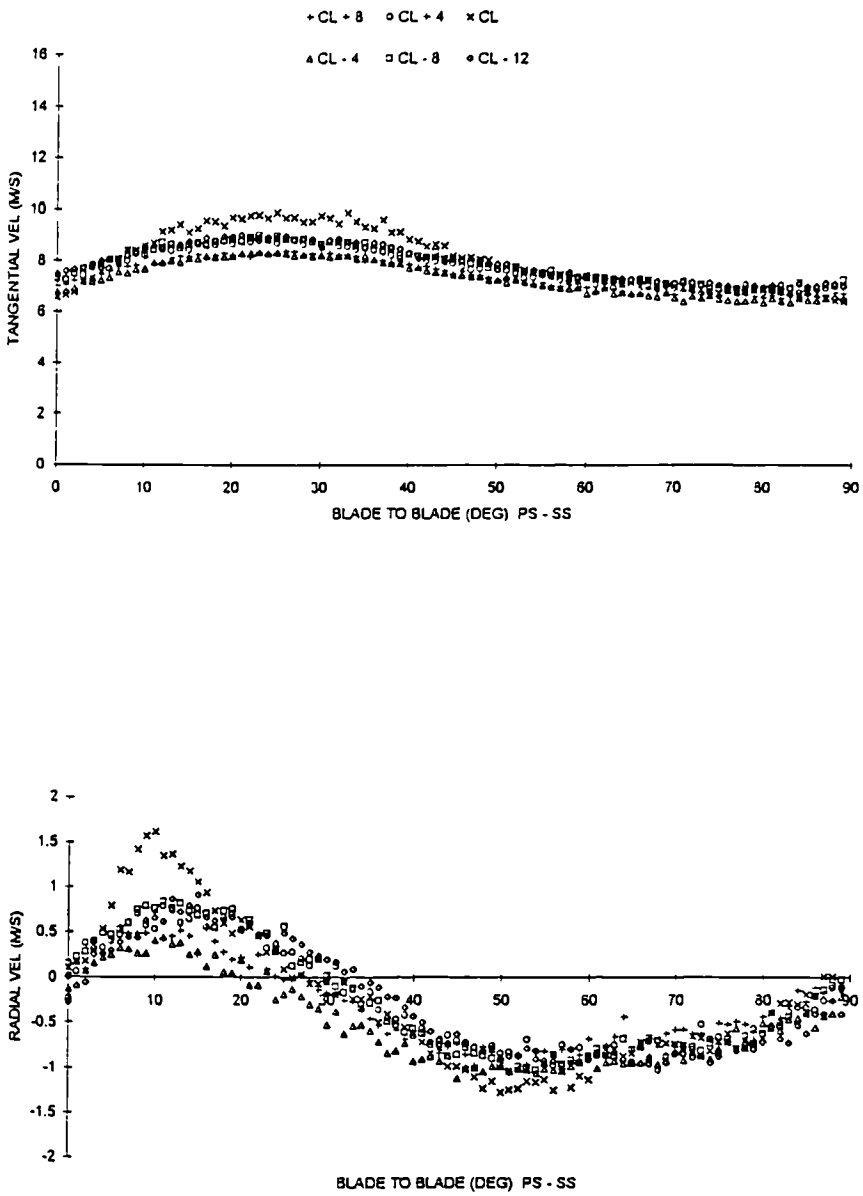

Figure 5.5 Axial Variation at Window 3, R = 0.156m.

A plot of the axial variation of the mean tangential velocity is shown in Figure 5.6. This shows that despite the blade to blade variation shown in Figure 5.5, the bulk mean tangential flow shows only a small axial variation.

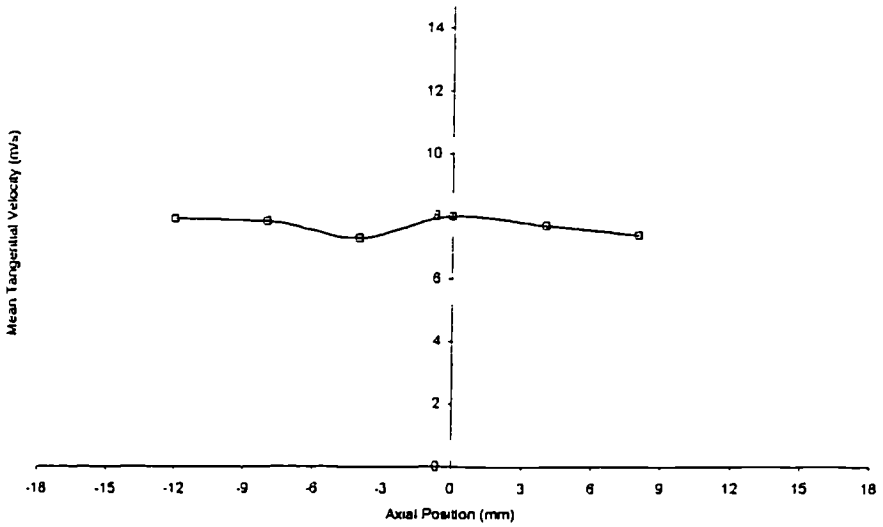

Figure 5.6 Axial Variation in Mean Tangential Velocity at Window 3, R=0.156m.

5.4 Comparison of Velocity Profiles Around Volute At Shut-Off

This section of work compares the results obtained from Fluent with the experimental LDA measurements for the volute flow.

The results for Window 1 are shown in Figures 5.7 through 5.10. The predicted tangential velocity profiles agreed well with the experimental data, with good qualitative agreement at all positions. The best agreement occurred at the inner radius, R=0.156m, where the prediction was within ±5% of the experimental profile for the majority of the blade passage.

Figure 5.11 displays the comparison of mean tangential velocities across the volute passage. The experimental results show the mean tangential velocity reduced slowly across the volute, dropping only 3m/s from the inner to the outer radius of the volute passage. This represented an approximate twenty percent drop in the mean tangential velocity. Fluent however predicted a

sixty percent reduction in the mean tangential velocity across the volute passage.

A general feature of the computational model was the under prediction of the mean tangential velocities across the volute passage. This trend is also exhibited at Windows 2, 3, and 4, see Figures 5.16, 5.24 and 5.32.

The measured radial velocity profiles for Window 1 exhibit a jet like structure in the centre of the blade passage at radii, R=0.166m and R=0176m. A small jet like structure was also predicted by Fluent, but this was situated at the pressure side of the blade passage.

Figure 5.11 demonstrates that both the experimental and computational results show a mean radial flow out of the impeller at Window 1. Fluent predicted a flat mean radial velocity profile across the volute, whereas the experimental measurements peak towards the middle of the volute passage. At all positions Fluent under predicted the mean radial velocity by at least 0.6m/s.

This discrepancy was investigated by repeating the experimental measurements to ensure the data was reliable. The second set agreed to within experimental tolerance of the original data.

Another general feature of the computational model was the flat mean radial velocity profiles it predicted across the volute. This was also found for Windows 2, 3 and 4 together with an under prediction of the measured value at all radii considered, see Figures 5.16, 5.24 and 5.32.

Figure 5.12 through 5.16 presents the comparison for Window 2. The predicted tangential velocity was found to agree within ±1.5m/s of the values measured for R=0.156m and R=0.170m. However, at the last two

radial positions, Fluent under predicted the measurements of tangential velocity by over 3m/s.

The measured and predicted radial velocity profile at R=0.156m and R=0.170m, display a relatively strong outflow at the pressure side of the blade passage. At first sight, this would suggest the recirculatory flow pattern caused by a relative eddy, cf. Lennemann and Howard(1970). However, a relative eddy, would rotate in an opposite direction to that of the impeller, thus causing outflow at the suction surface.

Both the computational model and the experimental measurements predict outflow along the pressure surface, thus suggesting that the flow pattern is not caused by the recirculation of a relative eddy, but by another flow pattern.

Evidence to substantiate this 'other' flow pattern is found in Figure 5.12 and Figure 5.13 in which the experimental measurements show there is no flow into the impeller. This inflow would be an essential part of a recirculatory flow pattern.

For all the radial positions at Window 2, good qualitative agreement was obtained, all predictions being within ±1m/s of the measured values. The results demonstrate that Fluent tends to under predict the radial velocity at most radial positions across the blade passage.

Figures 5.17 through 5.24 display the tangential and radial velocity profiles at Window 3. At all positions the computational model gives qualitative agreement with the experimental measurements.

Near the impeller, R=0.156m, the computational model over predicted the tangential velocity by approximately 4m/s across the blade passage. At the centre of the volute passage, between R=0.166m to R=0.186m, the

computational model gives excellent agreement with experimental data to within approximately ±1m/s.

Towards the outer wall of the volute, the computational model under predicted the tangential velocity, continuing the trend found at Windows 1 and 2. At the outer-most position, R=0.216m, the computational model under predicted the tangential velocity by 3.5m/s, giving a computed profile which is approximately a third of the measured value.

The radial velocity prediction, produced by the computational model for Window 3, gives good qualitative and quantitative agreement at all positions. At the inner radius, R=0.156m, both methods predict outflow at the pressure side of the impeller passage and inflow at the suction side, exhibiting a similar trend to that found at Window 2.

However, a difference was found between the experimental measurements taken at R=0.156 for Windows 2 and 3. At Window 2 the measurements indicated no inflow (Figure 5.12), but at Window 3 (Figure 5.17) inflow was measured towards the suction surface.

The mean radial flow across the volute passage, Figure 5.24, shows the model predicting flow out of the impeller, however the experimental data shows the mean radial flow is into the impeller. As the radius increases, both the prediction and experimental data display a mean radial velocity out of the impeller.

Figures 5.25 through 5.32 display the tangential and radial velocity profiles at Window 4. For all radial positions at this window the computational model gives good qualitative agreement with the experimental data for both tangential and radial velocities.

At the exit of the impeller, R=0.156m, Fluent over predicted the tangential velocity across the blade passage, by +4.5m/s. At mid passageway, between R=0.170m and R=0.197m, the experimental and measured values agree within ±1m/s. Towards the volute wall the computational model under predicted the tangential velocity by approximately 1.5m/s over the blade passage. The computational model agrees with the measurements for mean tangential velocity within ±1.6m/s for all radial positions with the exception of the first radial position, R=0.156m.

The predicted radial velocity profiles at Window 4 give good qualitative agreement with the measurements at all radial positions. At the impeller exit, R=0.156m, both the model and experimental results show a flow out of the impeller passage towards the pressure surface of the blade. Flow into the rotor is predicted and measured over the suction side of the blade passage cf. Windows 1, 2 and 3.

The computational model over predicted the strength of the maximum velocity of outflow, at the impeller exit, by 1.5m/s and under predicted the maximum velocity of the inflow by 0.5m/s.

At all other radial positions the computational model agrees well with the experimental data and to within approximately ±0.75m/s of the radial velocity between the blades.

The data collected at Window 5 is displayed in Figures 5.33 through 5.44. The tangential velocity profile shows excellent qualitative and quantitative agreement at all positions. The only discrepancy in the comparison occurs at the inner radius, R=0.156m, where the computational model over predicted the tangential velocity by approximately +3.6m/s over the blade passage.

For all other radial positions, the tangential velocity predicted by the model across the blade passage, agreed to within ±1.5m/s of the experimental results. The computed mean tangential velocity profile agreed to within ±0.5m/s for the majority of the measured values.

The predicted radial profile at Window 5 gave good qualitative agreement at all positions. The biggest discrepancy occurred at the two radial positions close to the impeller, R=0.156m and R=0.166m. At these two positions, the model predicted a jet of outflow near the pressure surface and a region of inflow into the impeller, covering just over fifty percent of the blade passage.

The experimental measurements show that virtually all the radial flow across the blade passage is into the rotor. As the radius increases, the effect of the blades on the impeller flow diminishes, and the prediction improves to within approximately 0.6m/s over the blade passage.

The model and experimental data both predict a mean radial flow into the impeller. Close to the impeller, R=0.156m and R=0.166m, Fluent under predicts the mean radial velocity by 1.5m/s.

Figures 5.45 through 5.55 display the data collected at Window 6. The predicted tangential velocity gives excellent qualitative agreement at all positions and good quantitative agreement when compared with the experimental measurements.

The model exhibits similar trends to those found in the previous windows. At the inner radius, R=0.156m, the computational model over predicted the tangential velocity by approximately 4m/s, similar to Windows 2, 3, 4 and 5.

As the radius increases, the predicted tangential velocity agrees more closely with the measured value, to within approximately ±1m/s across the

blade passage for radii between R=0.170m and R=0.282m. This is clearly demonstrated in Figure 5.55 which displays the comparison between the predicted and measured mean tangential velocities.

The computed radial velocity profile at Window 6, displays good qualitative agreement at all radial positions. However, Fluent fails to predict the significant reversed net inflow near the rotor (Figure 5.55).

At R=0.156m, the computational model and the experimental data predict a similar flow pattern to that found in previous windows.

This flow pattern is characterised by outflow at the pressure surface of the blade and inflow across the rest of the blade passage. The results from the computational model, Figure 5.45, predict outflow over a greater area, and with a higher maximum velocity, than the measured profile. The rest of the blade passage displays inflow. However, the computational model under predicts the magnitude of the inflow by approximately 2m/s.

The results show that as the radius increased across the volute, the agreement of the model with the experimental data improves significantly. From R=0.198m to R=0.282m, the model agrees within approximately ±0.4m/s. From R=0.240m to the outer wall both the prediction and measured results show the blades have very little effect on the flow.

Fluent predicts a flat mean radial velocity profile at Window 6, this flat profile being similar to those found in all previous windows. The measurements however, display a high amount of inflow close to the impeller, which reduces as the radius increases towards the volute wall.

The results for Window 7 are displayed in Figures 5.56 through 5.73. A comparison of the tangential velocity profiles shows very good qualitative

agreement at all positions, with quantitative agreement being obtained at most positions.

The most significant discrepancy between the model and the experimental measurements for tangential velocity at Window 7 occurs at the first radial position, R=0.1565m. Here Fluent over predicts the mean tangential velocity by approximately 2m/s. This is clearly demonstrated in Figure 5.73 which displays a comparison of the mean tangential velocity profile.

At all other radial positions, R=0.166m to R=0.316m, the model predicted the mean tangential velocity and the blade passage tangential velocities to within approximately ±0.8m/s for Window 7.

The measured mean tangential velocity shows that the centre for the recirculation in the outlet duct occurs at R=0.235m. The model, however, predicted the centre of recirculation at a slightly higher radius of R=0.250m.

The predicted radial velocity profiles for Window 7 give good qualitative and quantitative agreement at all radial positions in the volute.

Both the model and the measurements show, at Window 7, that there is a large amount of flow into the impeller (Figure 5.72). At R=0.156m, the computational model under predicted the flow into the impeller, by approximately 1.5m/s on the mean radial velocity. For all other radial positions, R=0.166m to R=0.316m, the computational model predicted the radial velocity profile to within ±0.8m/s of the experimental data (Figure 5.72).

For radial positions greater than R=0.216m, both the model and experimental data show the radial and tangential velocities are unaffected by the blade passing. The blade passing effects are less significant at these radial positions because of the dissipation caused by the viscous effects of

the flow cf. Window 5, Figure 5.39 through 5.44, Window 6 Figure 5.50 through 54.

The results for Window 8 are displayed in Figures 5.74 through to 5.78. As the data has been collected at radial positions 2mm apart only the results at R=0.156m, 0.160m, 0.164m and 0.168m are displayed together with the mean velocity profiles.

At Window 8 the model and the experiment results produce poor qualitative and quantitative agreement for both the tangential and radial velocities.

The best correlation between the experimental measurements and the model for the blade passage tangential velocity was obtained at R=0.156m where agreement was within ±1m/s. As the radius increases so the under prediction increases from 5m/s at R=0.160m to 7m/s at R=0.166m.

The experimentally measured mean tangential velocity across the volute varied only ±1.5m/s from its own mean value. The computational model, however, predicts a continuously falling mean velocity profile, decreasing by 4m/s from R=0.156m to R=0.166m.

The radial blade passage velocity profile significantly under predicted the experimental measurements, by approximately 4m/s, for all radial positions at Window 8.

Fluent predicted a flat mean radial velocity profile across the volute passage at Window 8. However, it under predicted the experimental mean radial velocity by approximately 3m/s over the volute passage (Figure 5.78).

5.5 Comparison of Velocity Profiles in Outlet Duct at Shut-Off.

The vertical and horizontal mean velocity components at outlet duct plane 1 are displayed in Figure 5.79. The computational results give qualitative and

quantitative agreement with the experimental data for both the vertical and horizontal velocities.

The computed vertical velocities agreed with the experimental data to within approximately ±0.5m/s. The model also predicted the centre of the recirculation to within two millimetres.

The horizontal velocities were predicted by the computational model to within approximately ±0.35m/s of the experimental data. The model, however over predicted the magnitude of the horizontal velocity and under predicted the magnitude of the vertical velocity at all positions for outlet duct plane 1.

The results for outlet duct plane 2 are displayed in Figure 5.80. Agreement at this position was not as good as outlet duct 1. The computational model did, however, give good qualitative measurements at all positions for both vertical and horizontal velocity.

For outlet duct plane 2, the vertical velocities were predicted to within approximately ±1.2m/s, with the model under predicting the magnitude of the vertical velocity at all positions. The centre of the recirculation region is predicted within eight millimetres.

The computational model under predicted the horizontal velocities to within 0.75m/s of the experimental values at all positions.

5.6 Circumferential Variation of Radial Velocity

The circumferential variation of the mean radial velocity at R=0.156m is displayed in Figure 5.81 and Table 5.1. From the graph and table an estimation was made of the amount of leakage in the experimental rig. It was important to determine the amount of leakage flow in order to ascertain whether it would have an effect on the overall flow. The experimental rig

was specifically designed with small clearances, which are not normally found in centrifugal pumps, to reduce the leakage flow.

Table 5.1 compared the mean radial velocities obtained using Fluent with those measured experimentally. Measurements were made at 22.5^0 intervals around the volute.

The results suggest a maximum leakage flow of $0.023m^3/s$ in the experimental rig, and this represented a leakage flow rate of 39% through the pump, based on the design flow rate.

It should be noted that the computational model also had a leakage flow of 8.5% based on the design flow. This value obtained for Fluent should theoretically be zero, but the use of a finite number of circumferential measurement positions has resulted in a small error. A similar error would also be introduced into the experimental rig measurements. The experimental leakage flow value should therefore be treated with caution.

5.7 Summary

The following section summarises the findings of a comparison between Fluent and the measurements taken using LDA.

One of the most significant results was the discovery of the flow patterns at the exit of the impeller at shut-off. Previous flow visualisation studies have suggested the existence of a relative eddy at the exit of the impeller, Lennemann and Howard(1970). It was believed that this eddy provided a momentum interchange mechanism between the impeller and volute flows. Both the computational model and the experimental results showed no signs of a relative eddy at the exit of the impeller.

WINDOW	ANGLE (DEG)	LASER MEAN RADIAL VELOCITY(M/S)	FLUENT MEAN RADIAL VELOCITY(M/S)
1	0	0.548	1.187
	22.5	0.244	0.604
2	45	0.342	0.435
	67.5	0.246	0.537
3	90	0.151	-0.247
	112.5	0.097	-0.954
4	135	-0.007	-1.233
	157.5	-0.102	-2.023
5	180	-0.174	-1.888
	202.5	-0.276	-2.496
6	225	-0.323	-2.07
	247.5	-0.744	-2.930
7	270	-5.477	-6.727
	292.5	1.460	1.568
8	315	0.934	3.99
	337.5	0.741	1.256
AVERAGE OF RADIAL VELOCITIES		**-0.687**	**-0.147**
LEAKAGE FLOW (M^3/S)		**-0.023**	**-0.005**

Table 5.1 Comparison Between Fluent and Experimental Measurements Displaying Circumferential Variation In Mean Radial Velocities.

The computational and experimental results show momentum interchange does take place however the mechanism is different to that discussed by Lennemann and Howard(1970) and is discussed in Chapter 7.

The present measurements suggest that, if a relative eddy does exist, it is contained within the impeller and does not directly effect the volute flow. The results do show, however, a surprising blade passage radial flow pattern at the impeller exit, with inflow at the suction surface and outflow at the pressure surface. The result was somewhat unexpected, and a further examination of the computational model revealed that flow first entered the impeller at the suction surface, then followed a path approximating a chord across the impeller exit, before leaving at the impeller's pressure surface. Further details of this flow pattern can be found in chapter 7.

The results at Window 7 and the outlet duct display a recirculatory flow pattern that rotates to fill the outlet duct. This type of recirculatory flow pattern had been assumed to exist by Frost and Nilsen(1991) in their shut-off head prediction method. Yedidiah(1985) also discovered a similar recirculatory flow pattern in the outlet in his flow visualisation study taken at shut-off flow condition.

Both the model and the experimental results displayed high velocities at the entrance of the volute. However, despite this, no separation effects were apparent at the end of the high acceleration region around the tongue, either in the computational or experimental data, and the flow appeared to remain attached to the volute wall.

An examination of the mean tangential velocity profiles at each window highlights trends which exist between the Fluent and the experimental measurements. The best agreement between the model and the experiment for the mean tangential velocity occurred at Windows 5, 6 and 7 (Figures 5.44, 5.55 and 5.73 respectively).

At these three windows Fluent predicted the flow pattern across the volute passage very accurately, producing both very good qualitative and quantitative agreement. The only discrepancy occurred in the prediction of the flow at the exit of the impeller, and this was a trend which existed at virtually all circumferential positions.

The best prediction of the mean tangential flow at the impeller exit, R=0.156m, was at Windows 8, 1 and 2, the first three circumferential positions measured after the tongue. Here the flow was strongly influenced by a low pressure region which caused a high acceleration of the flow into the volute.

At all circumferential positions near the exit of the impeller, R=0.156m, the mean tangential flow displayed a significant amount of slip, with its value being far less than the tip speed of the impeller blades.

This dispels the notion, which has been the foundation of many of the shut-off head prediction methods, that the flow in the impeller moves with solid body rotation.

A further study of both the measured and the computational blade passage tangential velocities at the impeller exit showed the flow at the exit demonstrated none of the characteristics of solid body rotation. Both the prediction and experimental results show a complex pattern of flow entering and exiting the impeller. A discussion of the computed impeller flow can be found in chapter 7.

At Windows 4, 5, 6 and 7 the computational model over predicted the tangential velocity at the impeller's exit, R=0.156m. This over prediction was quite significant, being approximately 4m/s at these windows.

The measurements displayed a flat mean tangential velocity profile across the volute passage at Windows 3 and 8, with a gradually decreasing profile at Windows 1,2 and 4. The computational model, however, predicted a more rapid decrease in the mean tangential velocity between the impeller exit and the volute wall.

A flat mean radial velocity profile was predicted across the volute passage at all the windows, except Window 7. However, the experimental mean radial velocity profiles varied with changes in radial position for all the windows considered. At Window 7, where the flow was dominated by the large amount of inflow into the impeller, Fluent's prediction produced both good qualitative and quantitative agreement.

The predicted mean radial velocity fell between approximately ±0.5m/s for all the circumferential positions except Windows7 and 8. At these two windows unusually high values for radial flow into and out of the impeller were found.

The computational model has produced some very encouraging results for the flow at shut-off within a centrifugal pump, giving both qualitative and quantitative agreement. However, there were discrepancies and inaccuracies between the model and the experimental results. These can be attributed to the following factors:

◊ The k-ε turbulence model used here assumes an isotropic flow structure, which is clearly not the case for the pump that contains significant swirl and secondary flows in the impeller, volute and outlet duct. In addition, the k-ε model does not account for rotational body forces occurring in the rotating impeller. All these effects help explain why better agreement was not obtained between the model and experimental data. The use of the RSM turbulence model and a three dimensional grid would be more suitable for modelling pump flows as this would enable both the

rotational body forces and the anisotropic nature of the turbulence to be modelled as well as any secondary flow effects. At present Fluent does not allow the use of the RSM model for sliding mesh calculations, and the computational model is only pseudo three-dimensional.

◊ When using the sliding mesh technique, Fluent restricts the type of models which can be used to obtain a solution, allowing only the standard power law scheme to be used. This differencing scheme is only first order accurate in space on the basis of a Taylor series truncation error. The high grid skewness in the impeller could introduce errors due to false diffusion, as the flow does not align exactly with the grid. Therefore a higher order scheme, such as QUICK, would help minimise the effects of the grid skewness enabling an improved computational solution to be generated.

◊ Only a first order accurate, fully implicit, time marching scheme is used by Fluent to model time dependency. As shown in Chapter 3 the solution shows some effects of time dependency. This could be improved by using a computational scheme with second order accuracy in time, such as a Crank-Nicholson scheme.

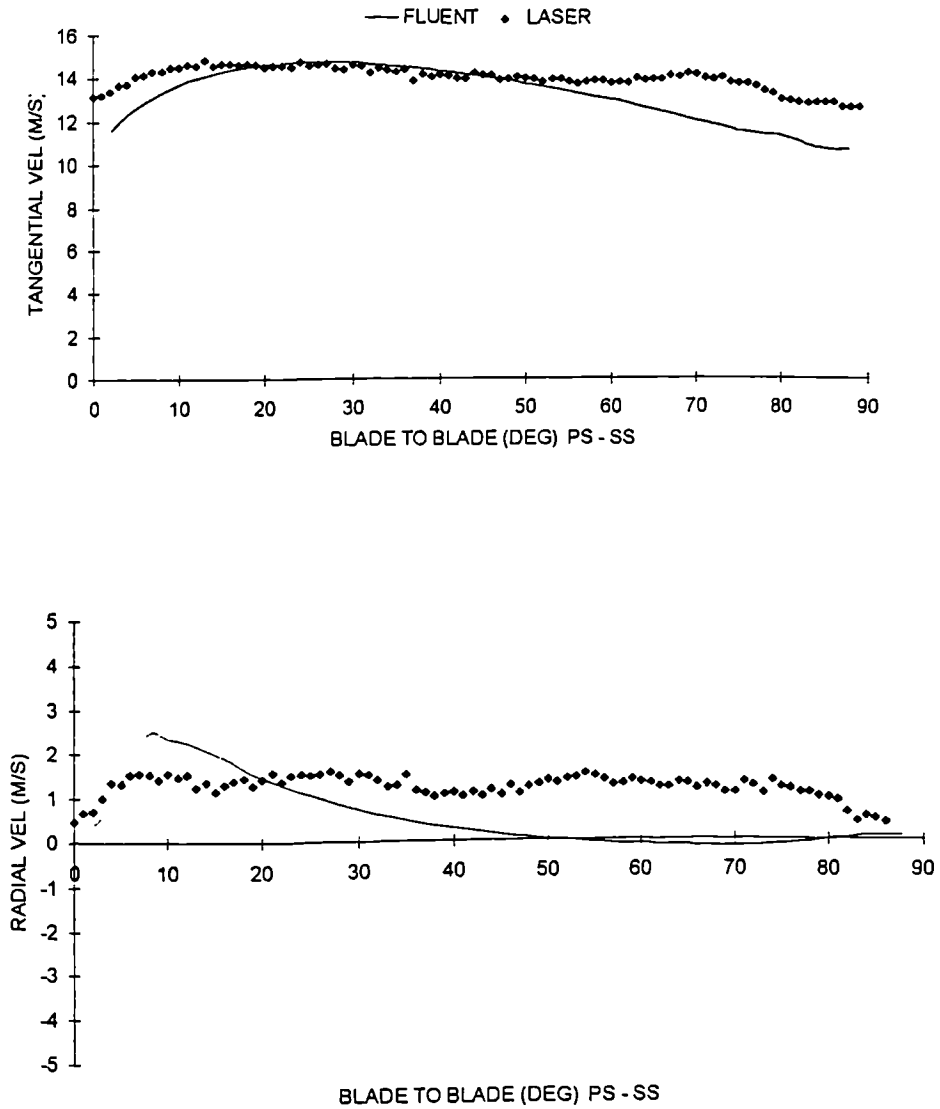

Figure 5.7 Comparison of experimental and computational velocity profiles, R=0.156m, Window 1.

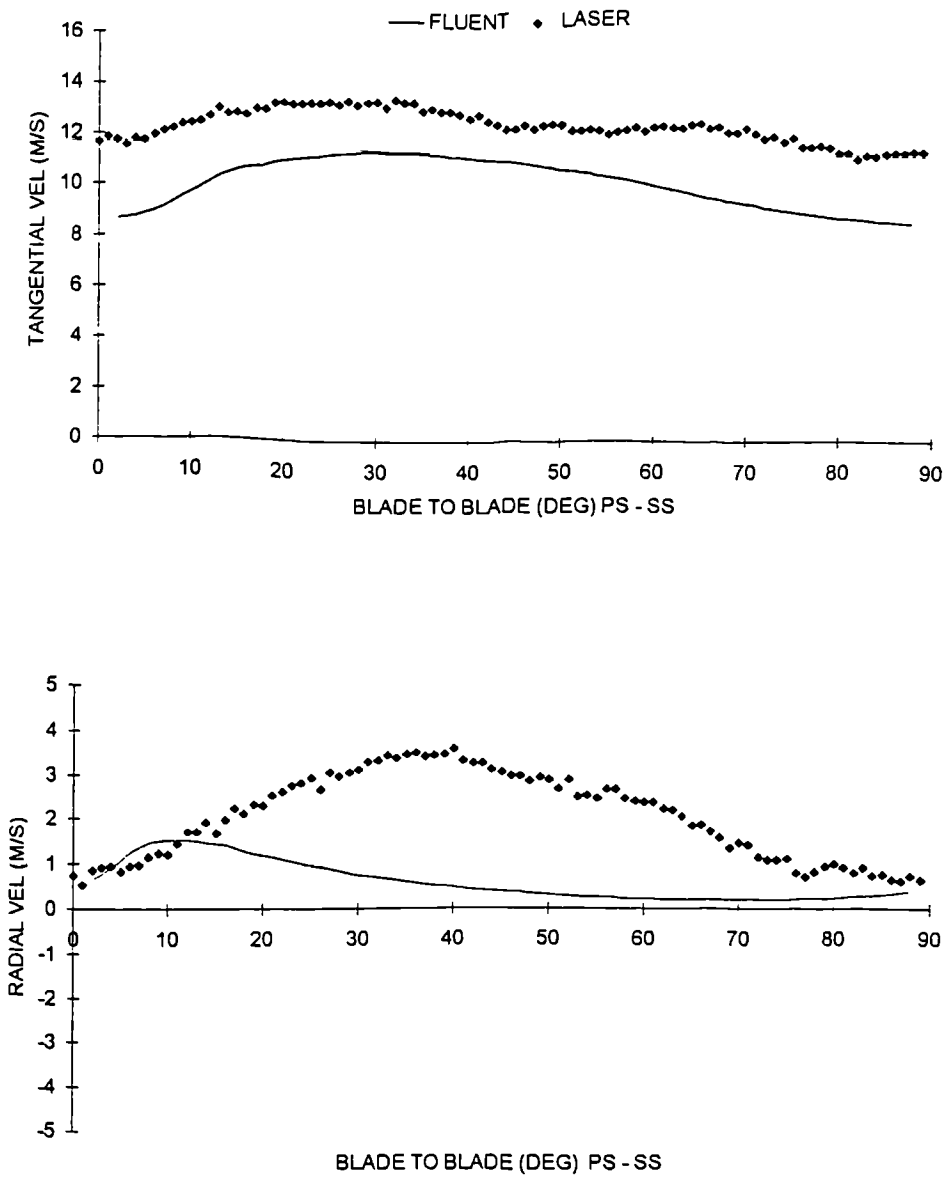

Figure 5.8 Comparison of experimental and computational velocity profiles, R=0.166m, Window 1.

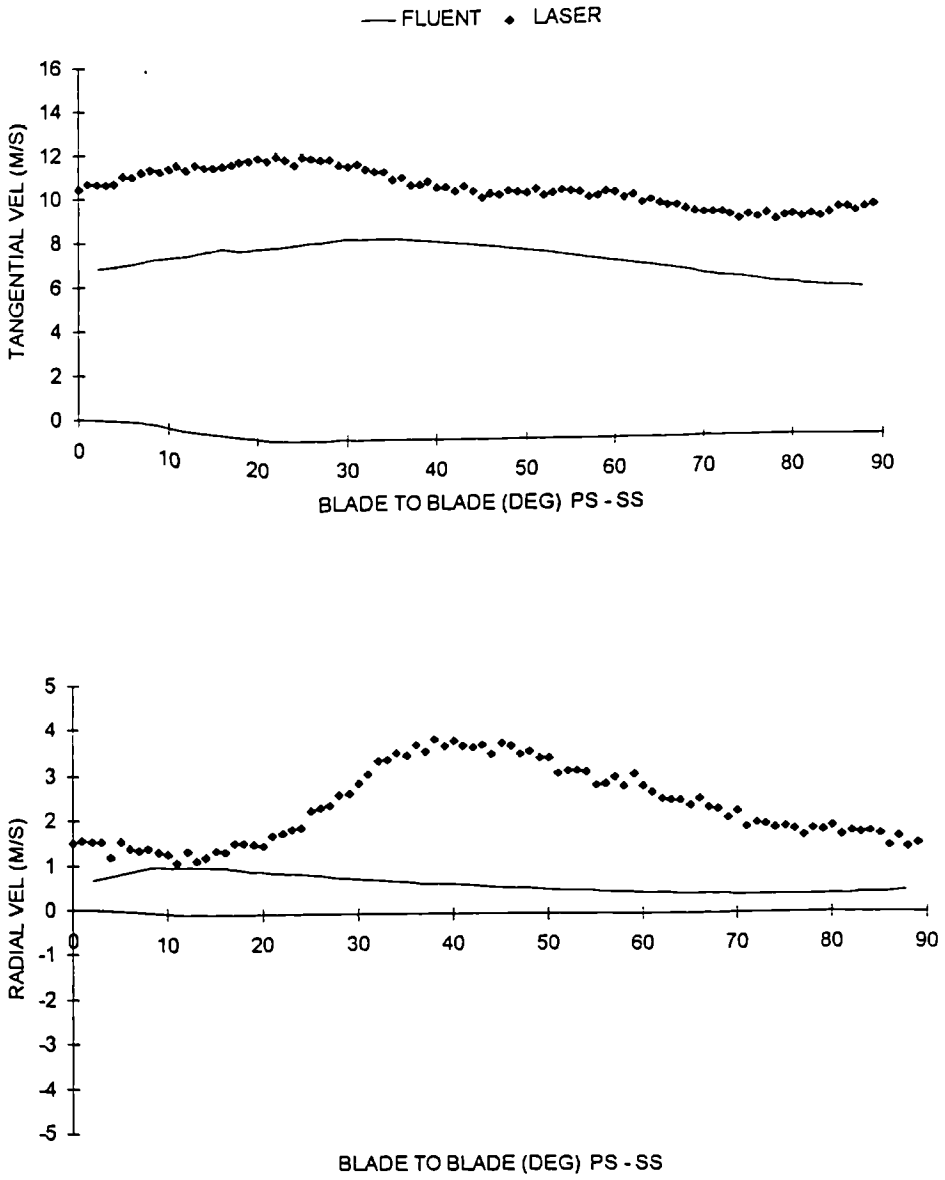

Figure 5.9 Comparison of experimental and computational velocity profiles, R=0.176m, Window 1.

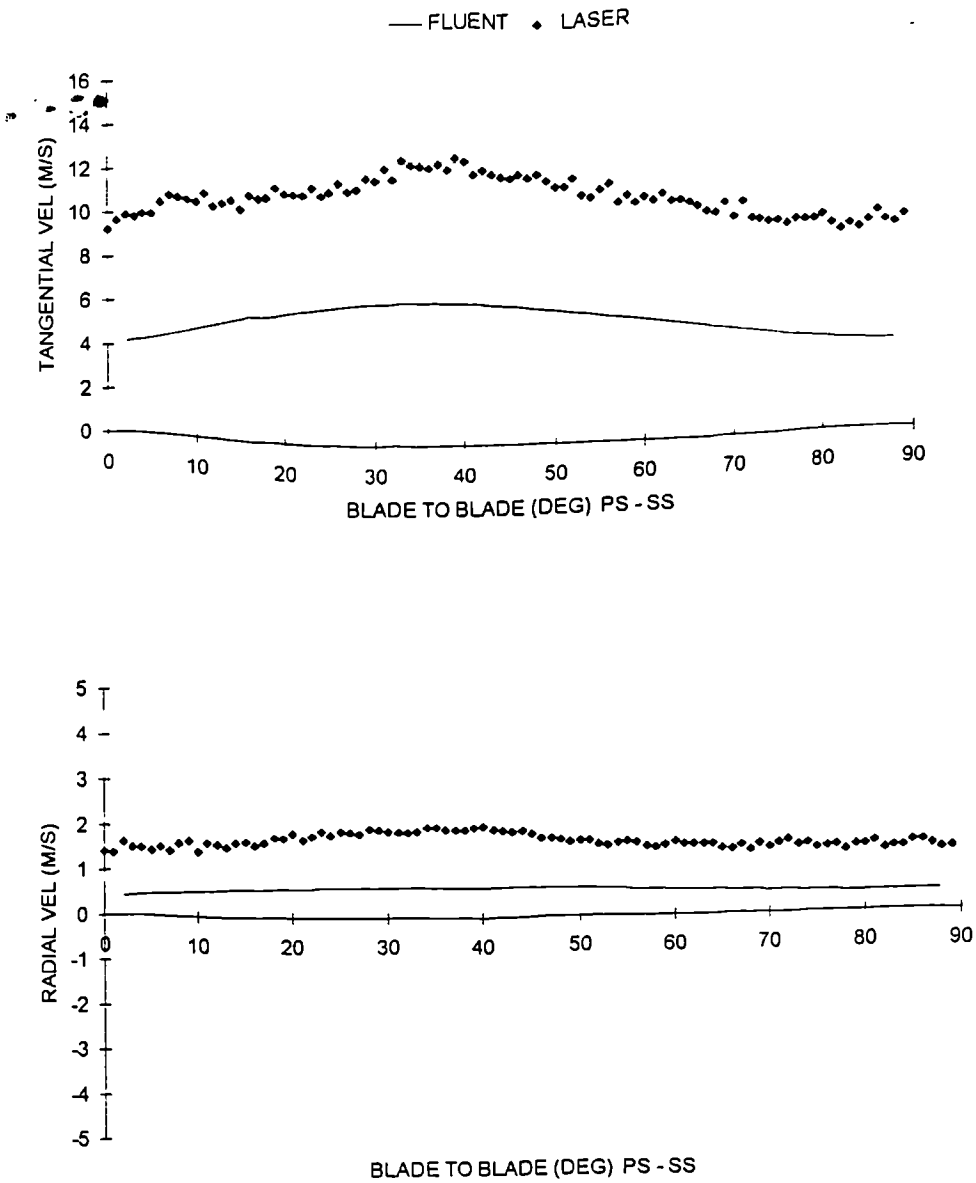

Figure 5.10 Comparison of experimental and computational velocity profiles, R = 0.186m, Window 1.

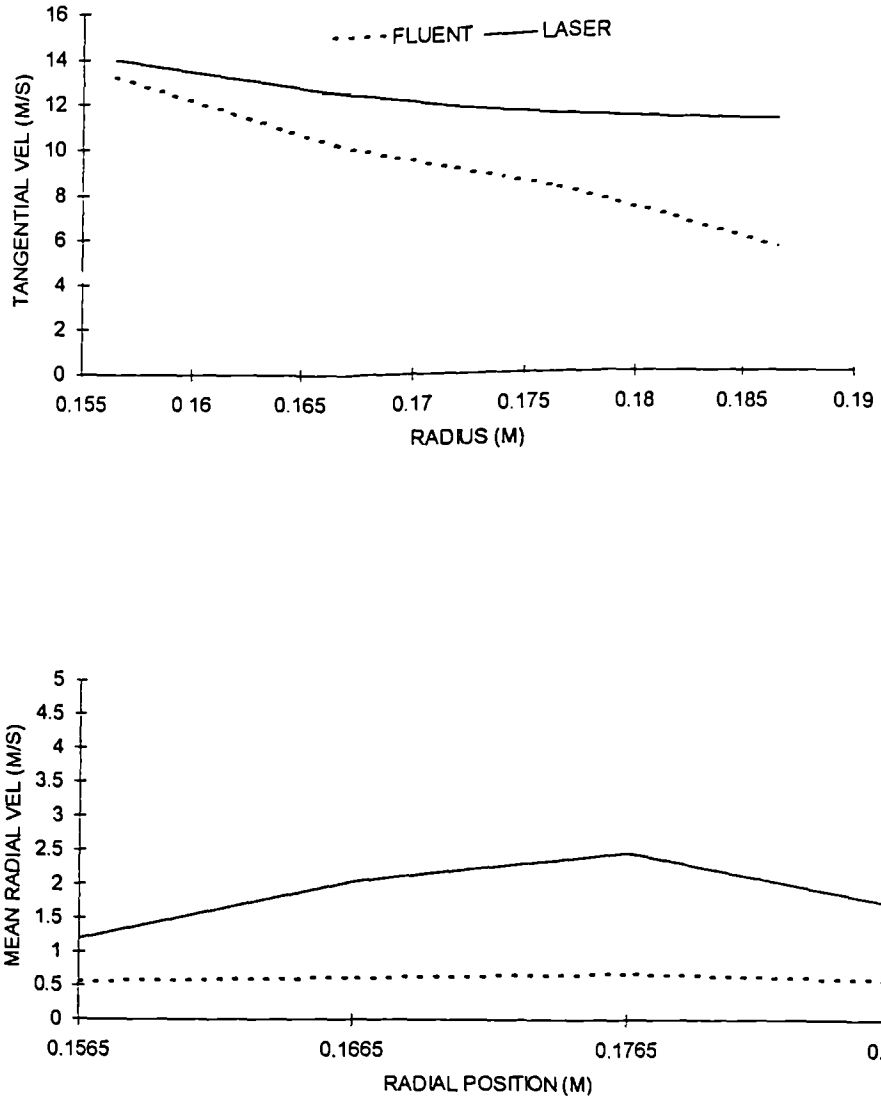

Figure 5.11 Mean Tangential and Radial Velocity Profiles Across the Volute, Window 1.

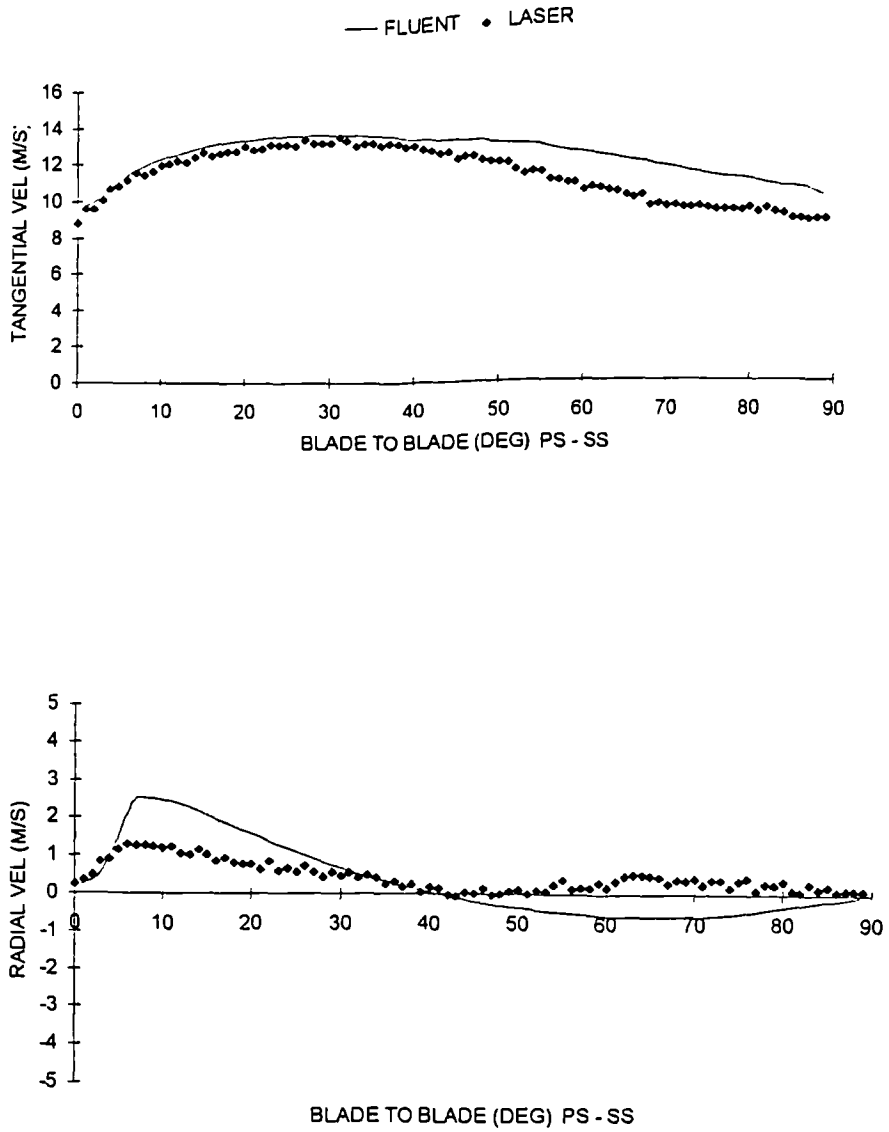

Figure 5.12 Comparison of experimental and computational velocity profiles, R = 0.156m, Window 2.

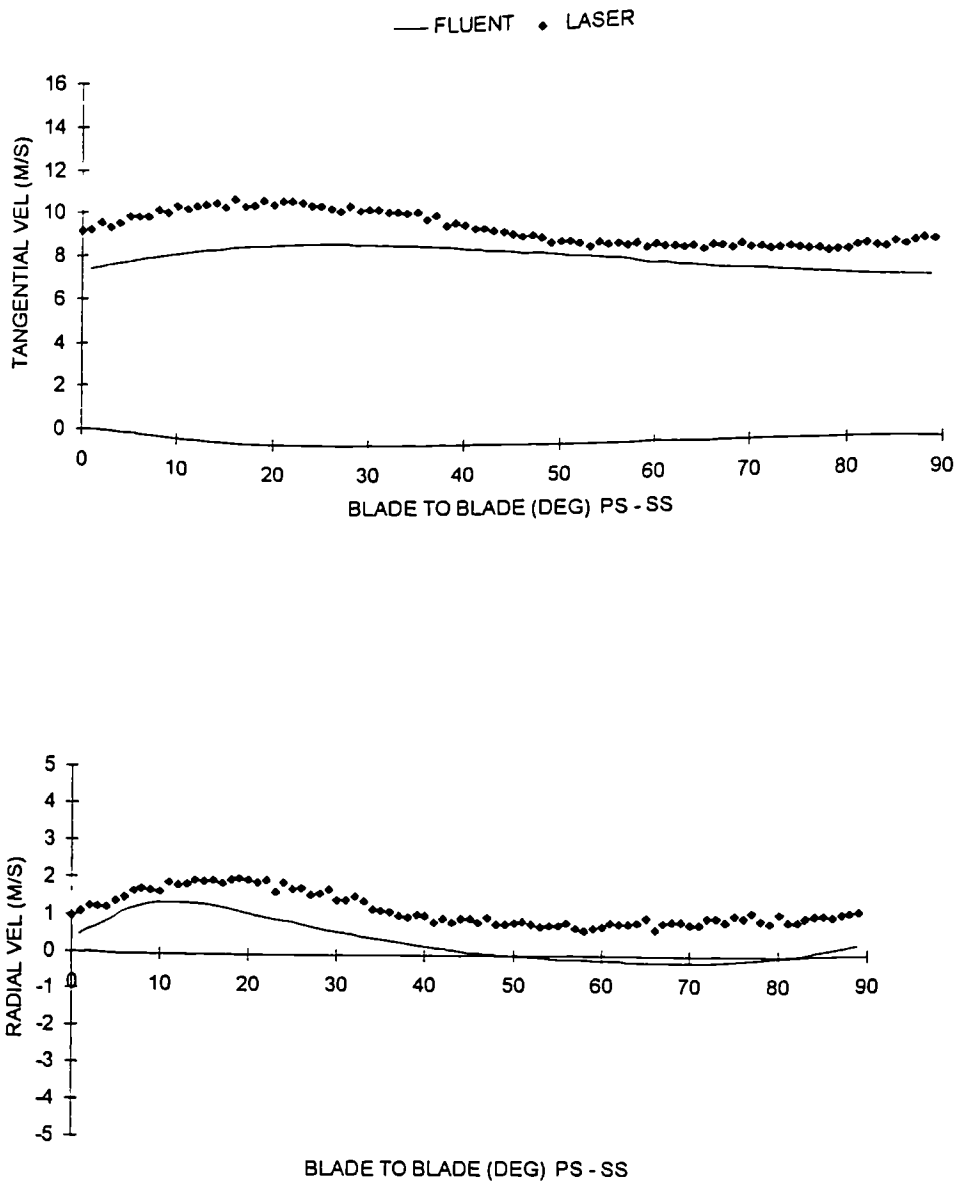

Figure 5.13 Comparison of experimental and computational velocity profiles, R = 0.170m, Window 2.

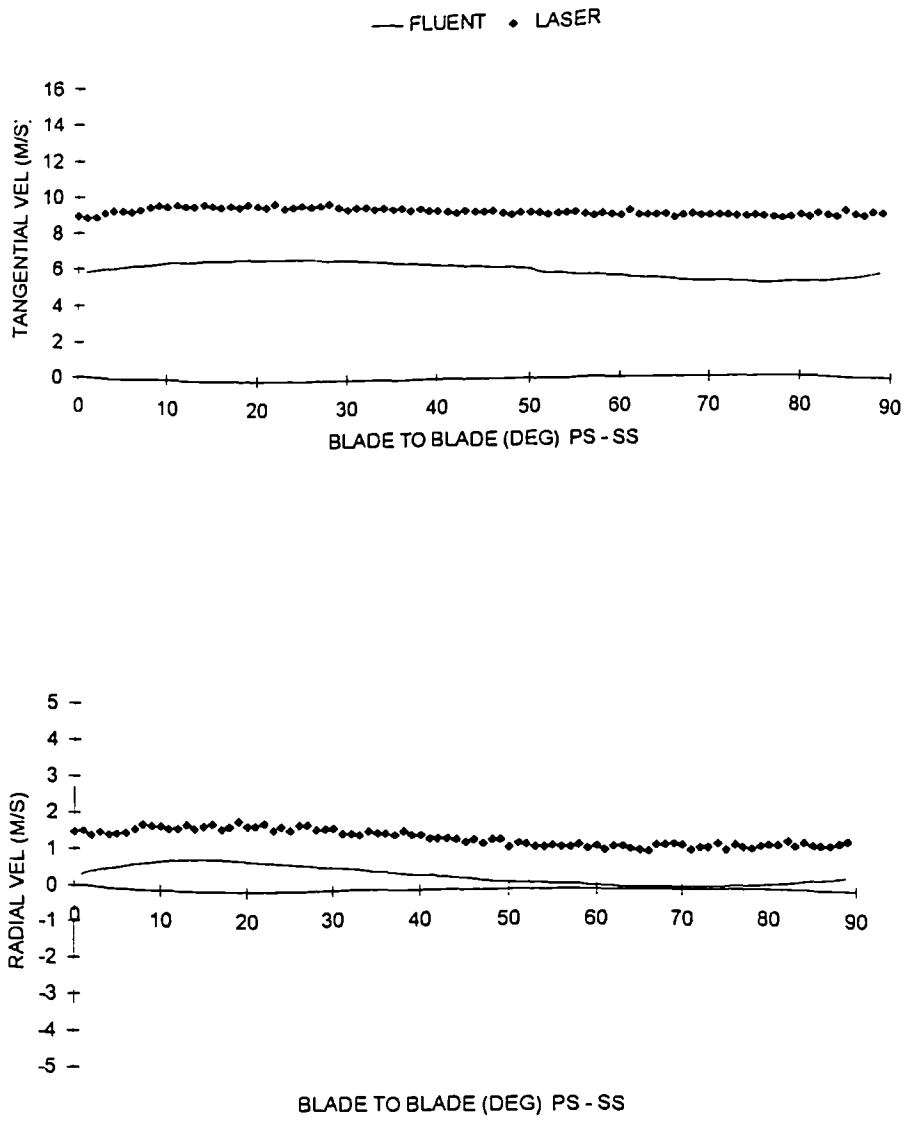

Figure 5.14 Comparison of experimental and computational velocity profiles, R = 0.184m, Window 2.

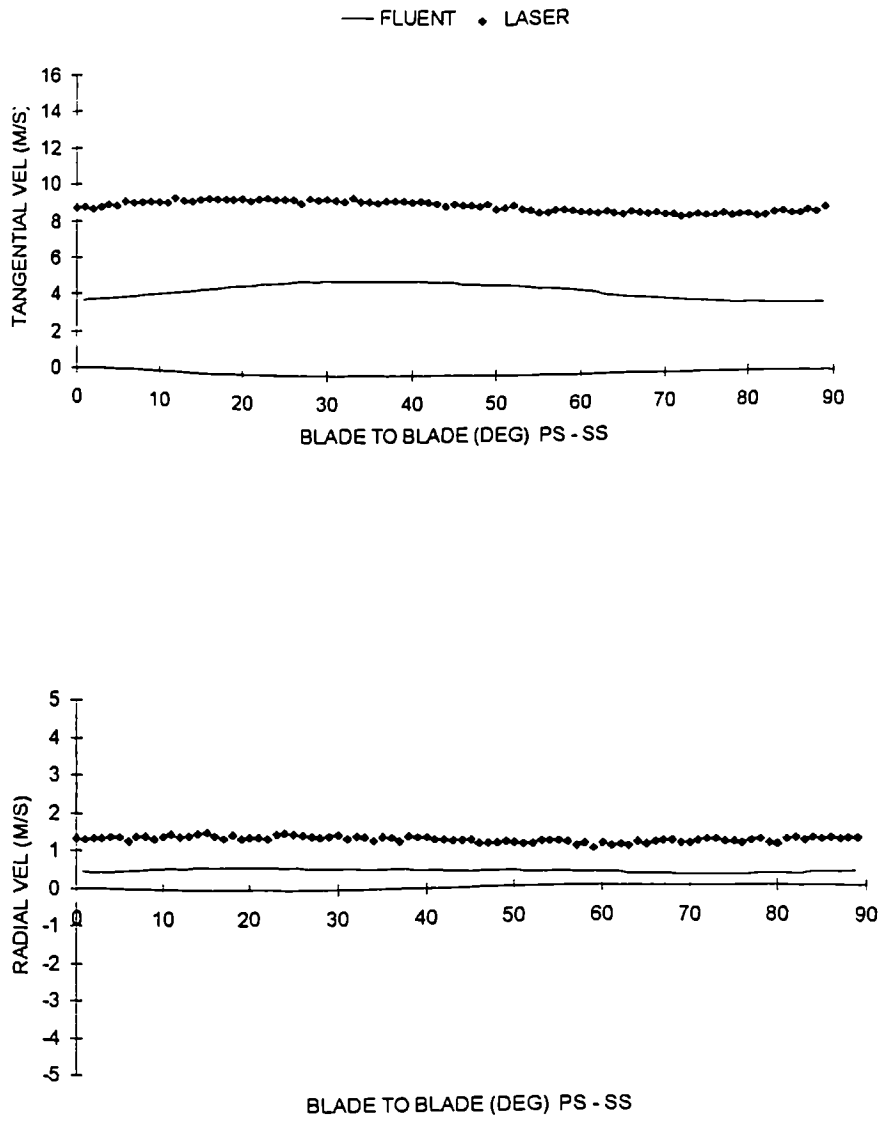

Figure 5.15 Comparison of experimental and computational velocity profiles, R = 0.198m, Window 2.

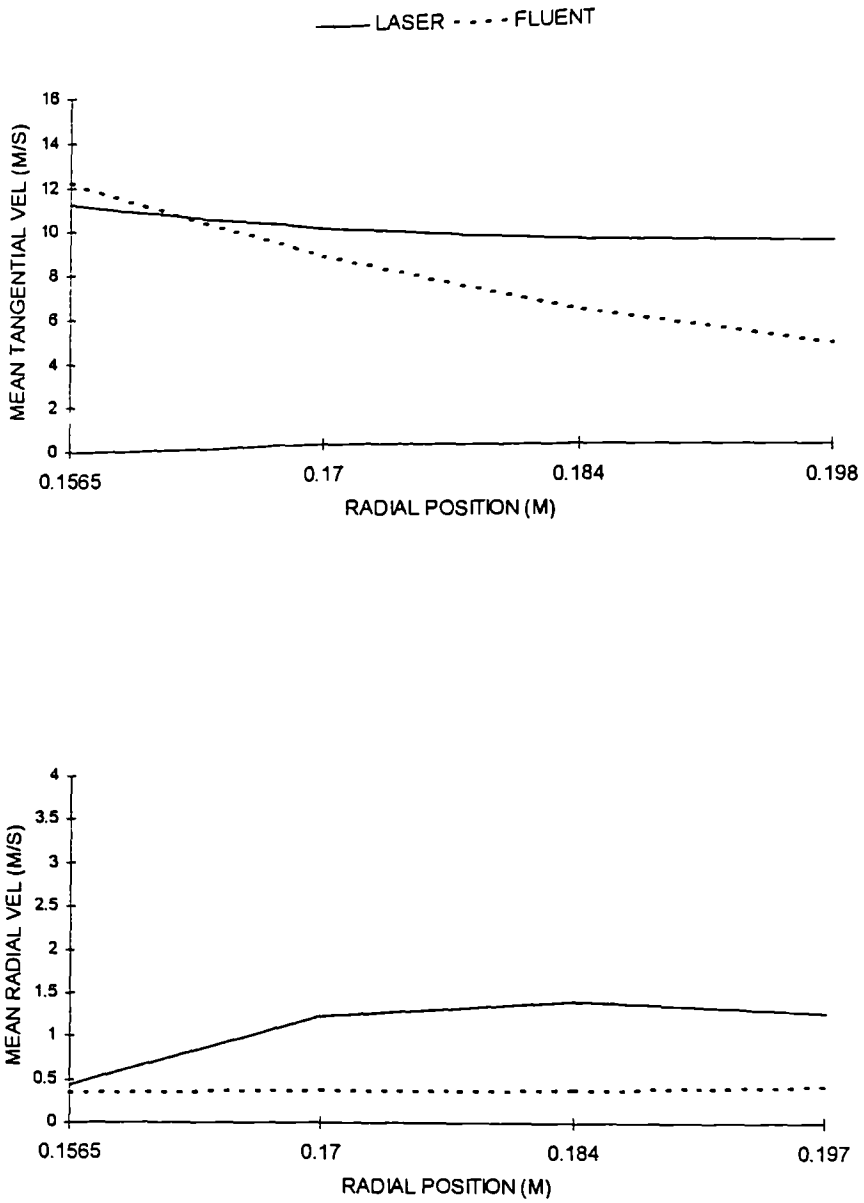

Figure 5.16 Mean Tangential and Radial Velocity Profiles Across the Volute, Window 2.

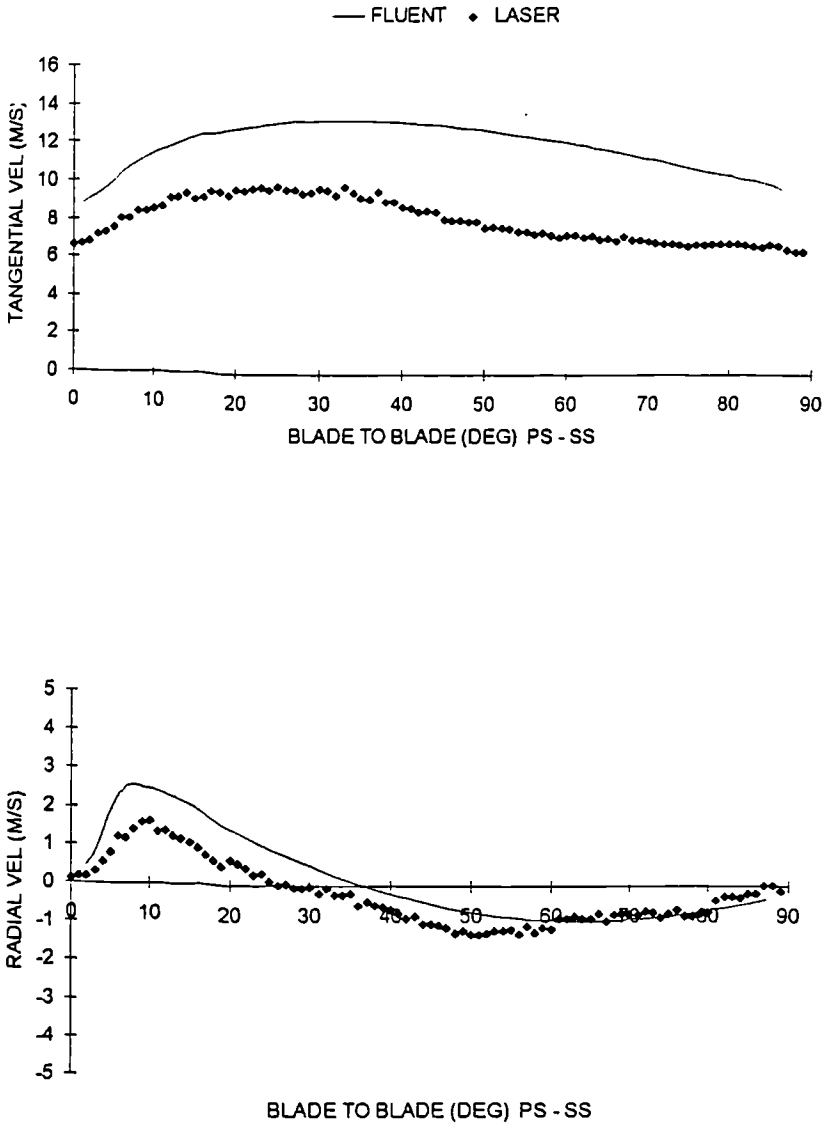

Figure 5.17 Comparison of experimental and computational velocity profiles, R = 0.156m, Window 3.

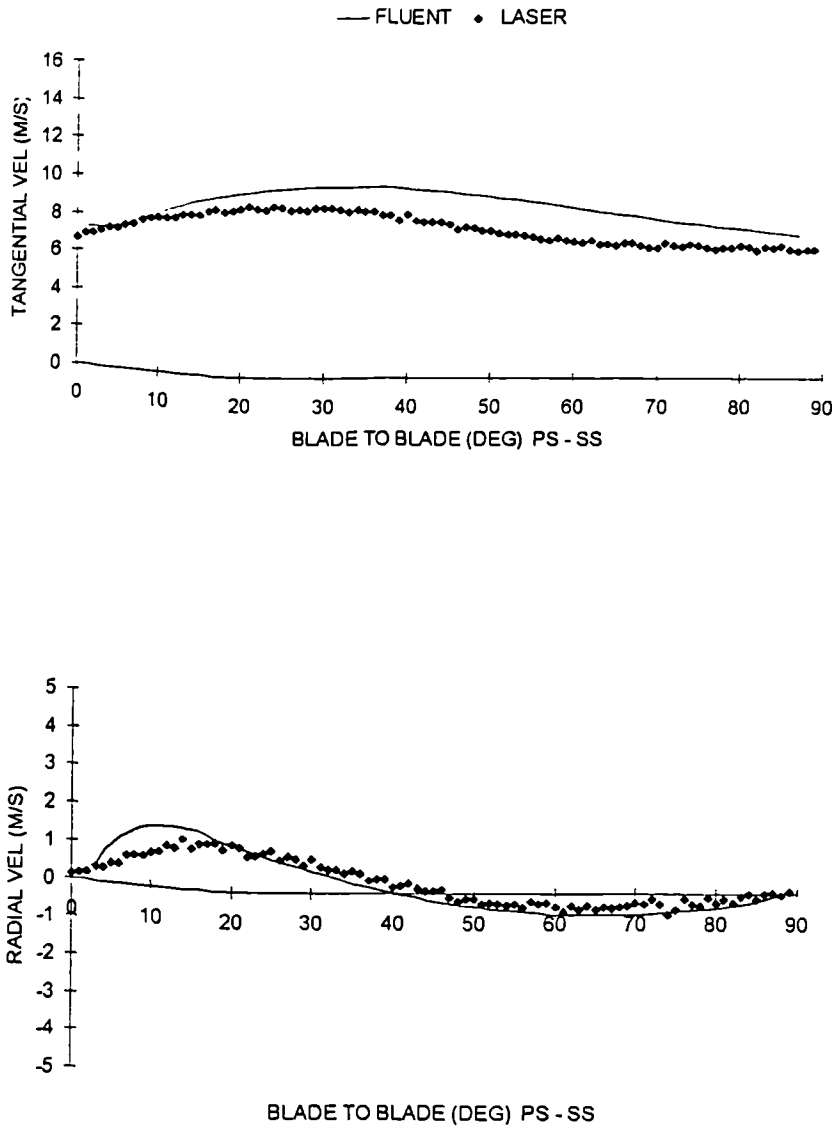

Figure 5.18 Comparison of experimental and computational velocity profiles, R = 0.166m, Window 3.

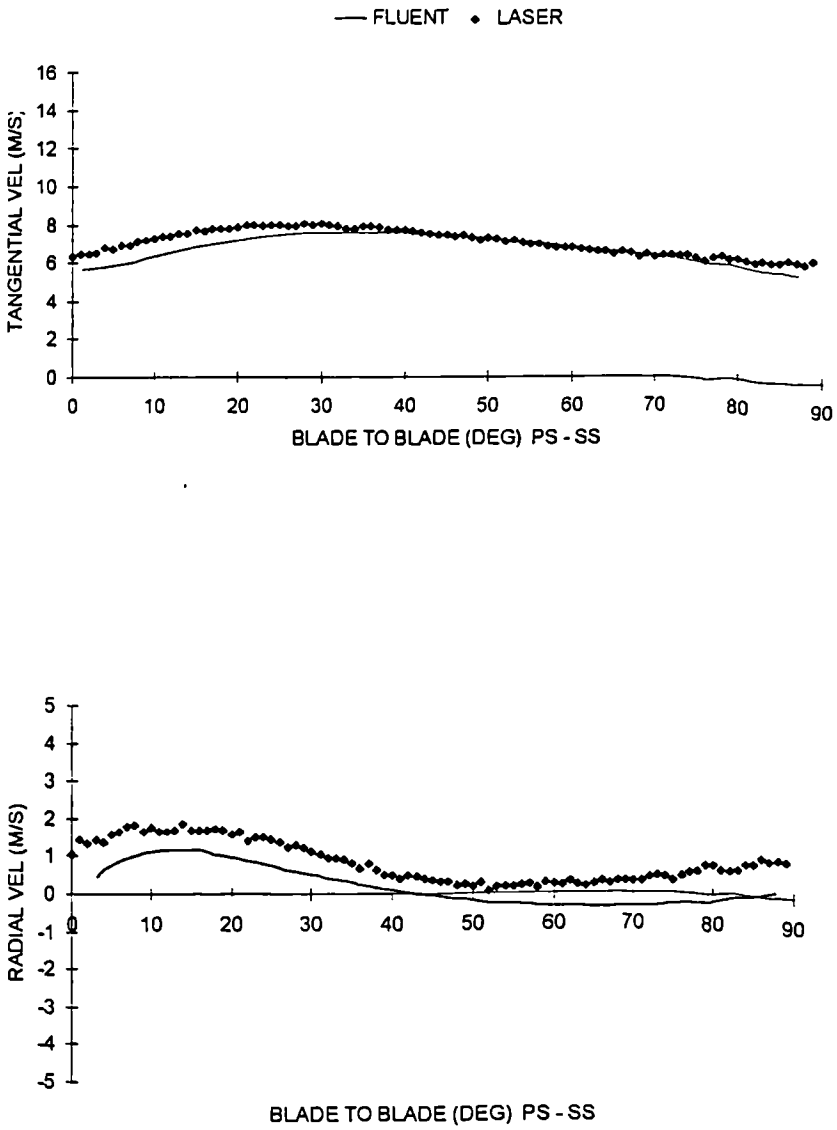

Figure 5.19 Comparison of experimental and computational velocity profiles, R = 0.176m, Window 3.

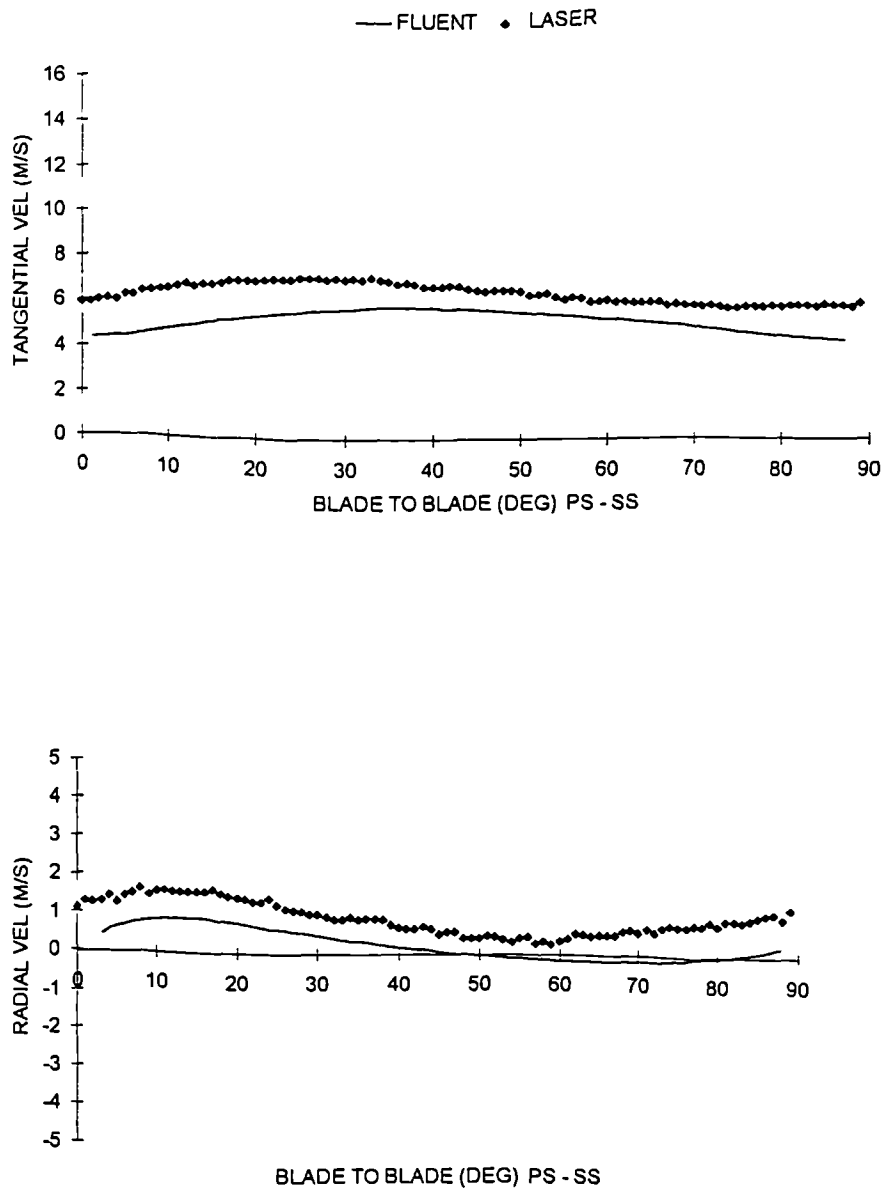

Figure 5.20 Comparison of experimental and computational velocity profiles, R = 0.186m, Window 3.

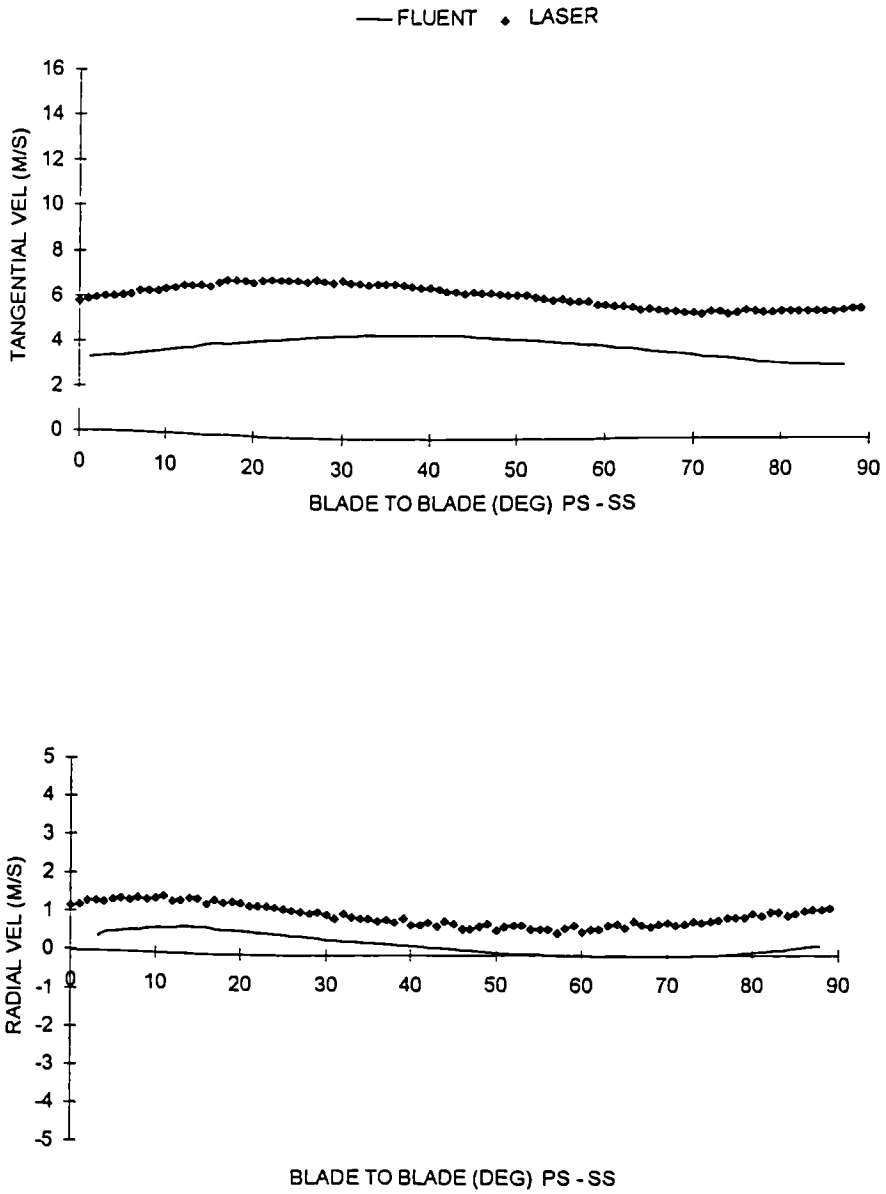

Figure 5.21 Comparison of experimental and computational velocity profiles, R = 0.196m, Window 3.

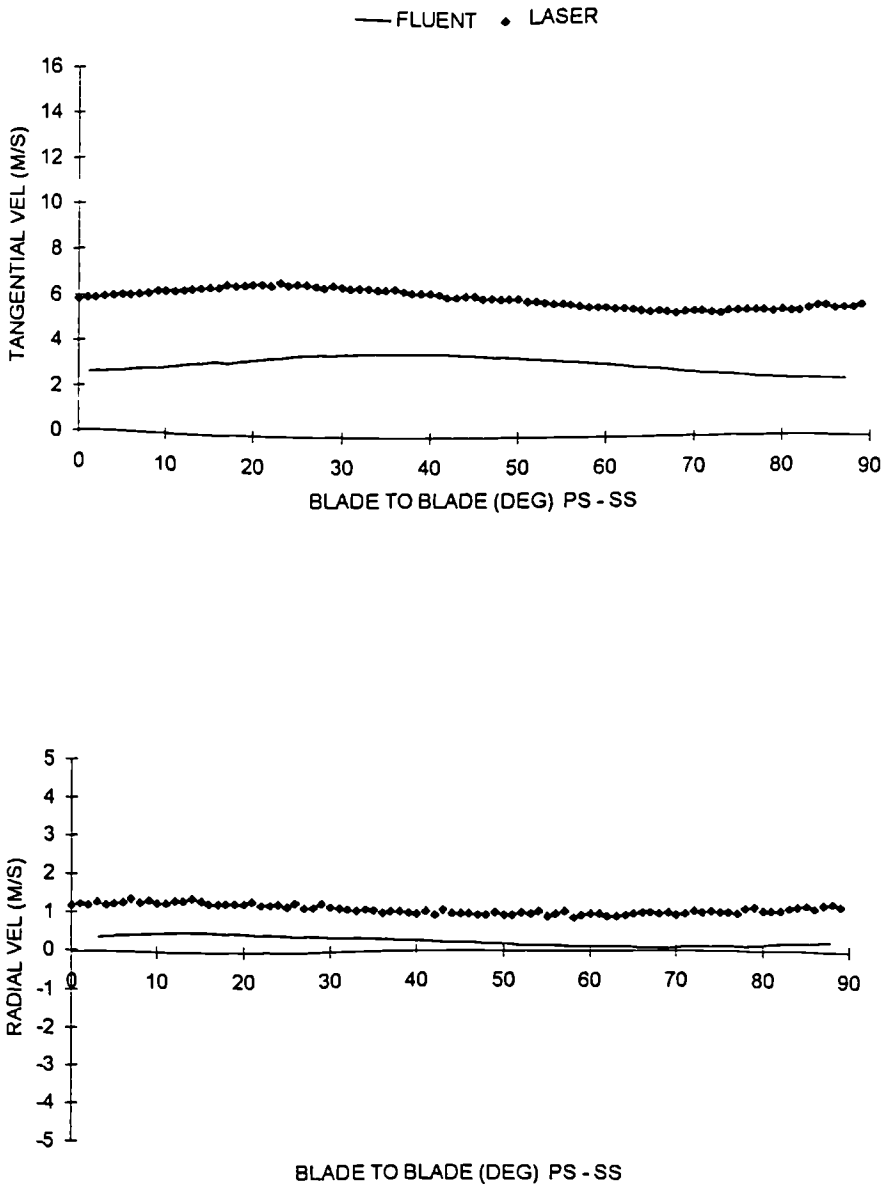

Figure 5.22 Comparison of experimental and computational velocity profiles, R = 0.206m, Window 3.

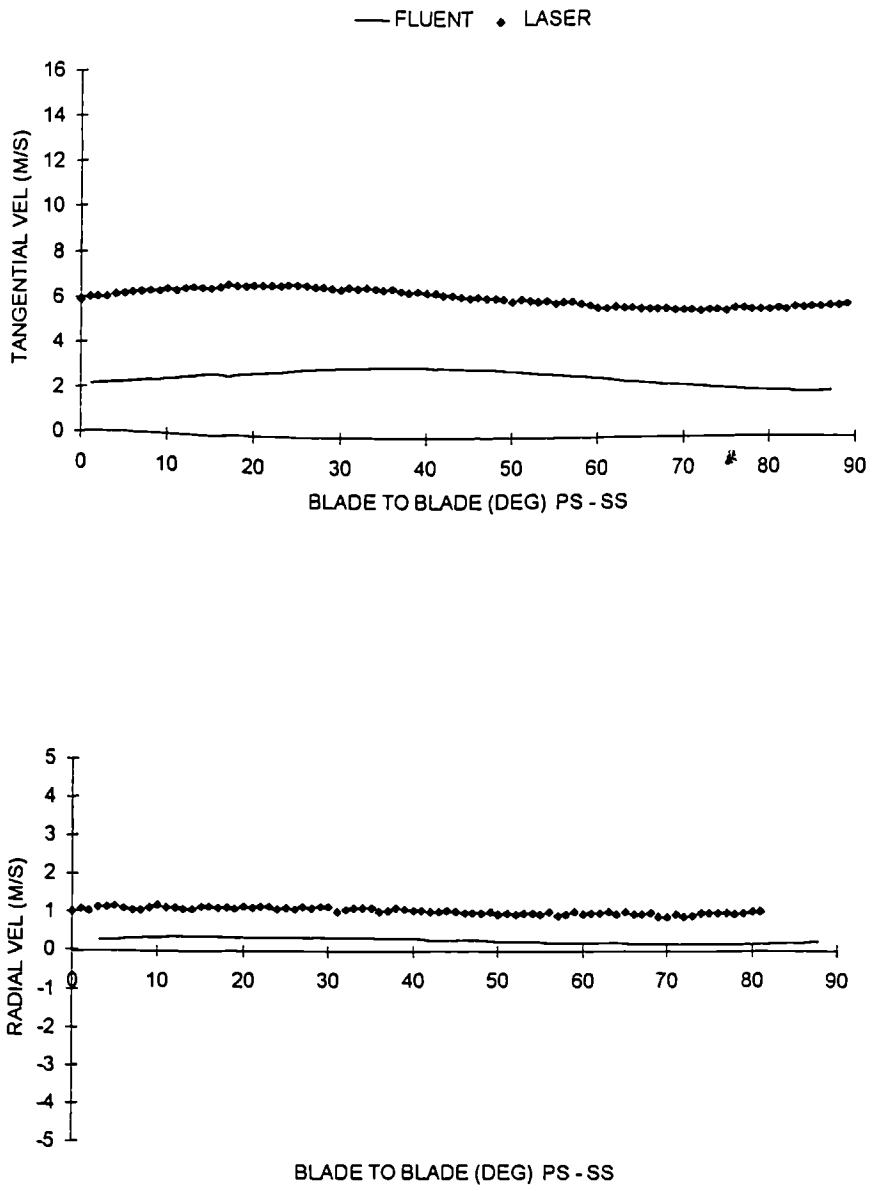

Figure 5.23 Comparison of experimental and computational velocity profiles, R = 0.216m, Window 3.

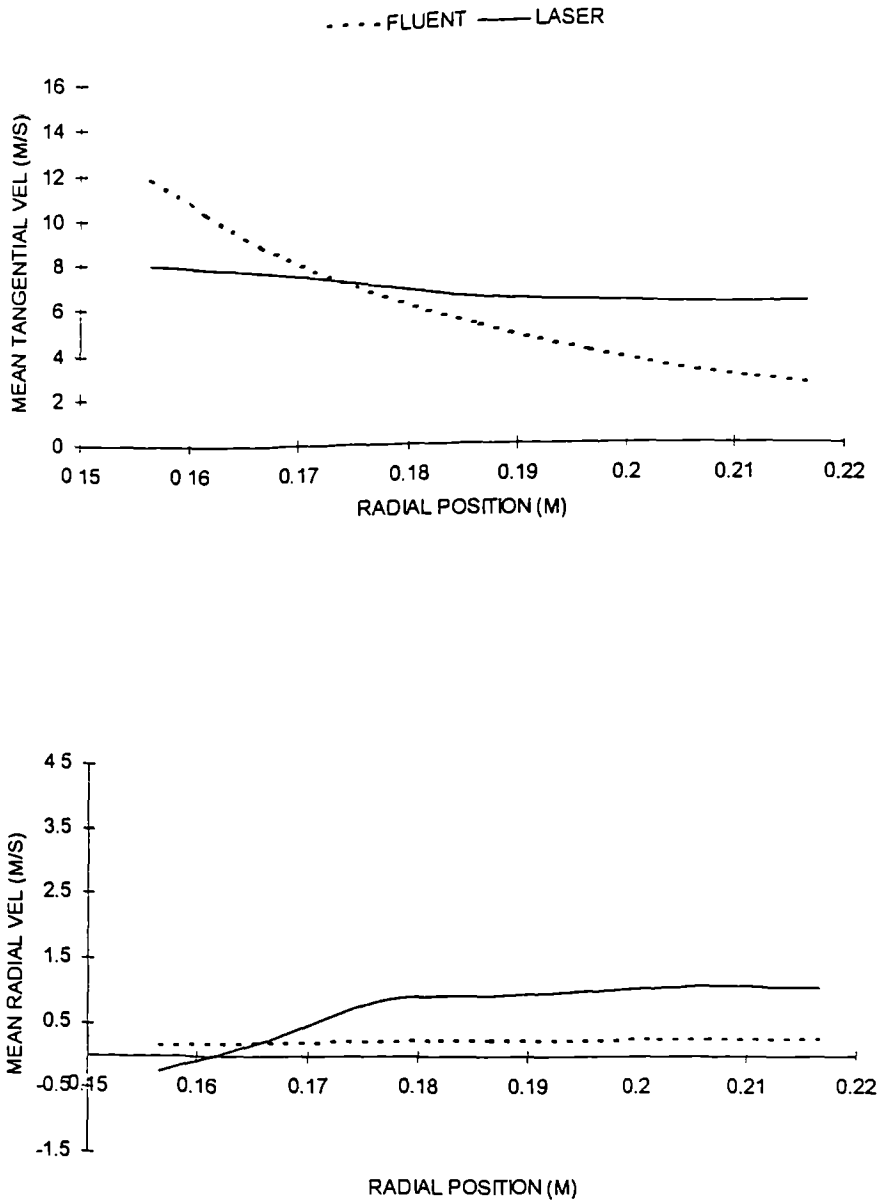

Figure 5.24 Mean Tangential and Radial Velocity Profiles Across the Volute, Window 3.

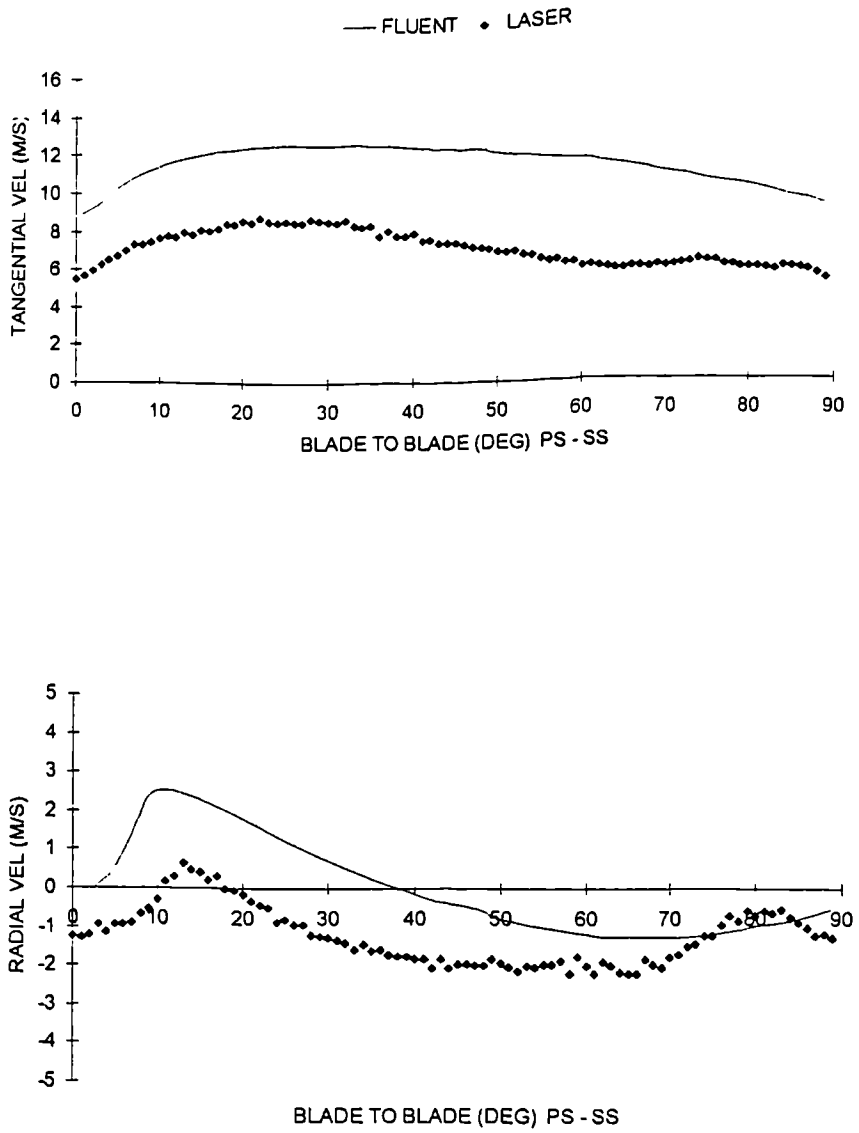

Figure 5.25 Comparison of experimental and computational velocity profiles, R = 0.156m, Window 4.

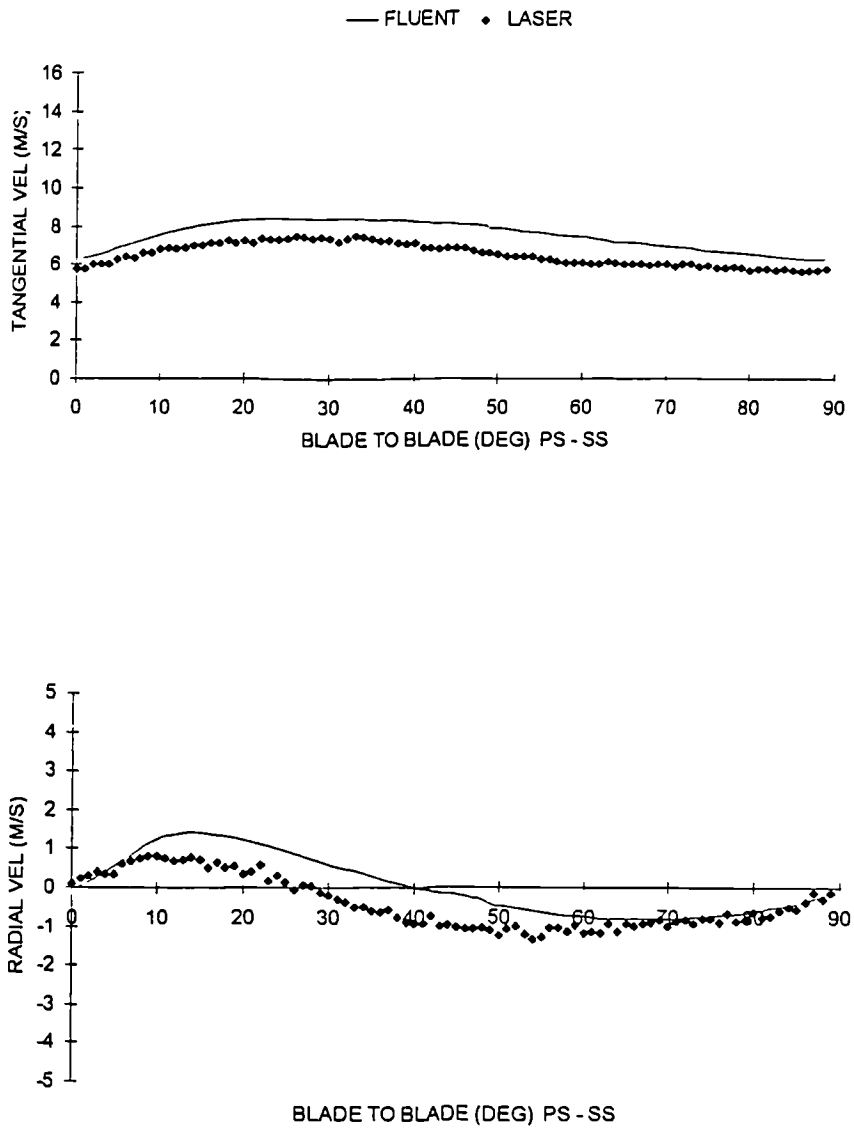

Figure 5.26 Comparison of experimental and computational velocity profiles, R = 0.170m, Window 4.

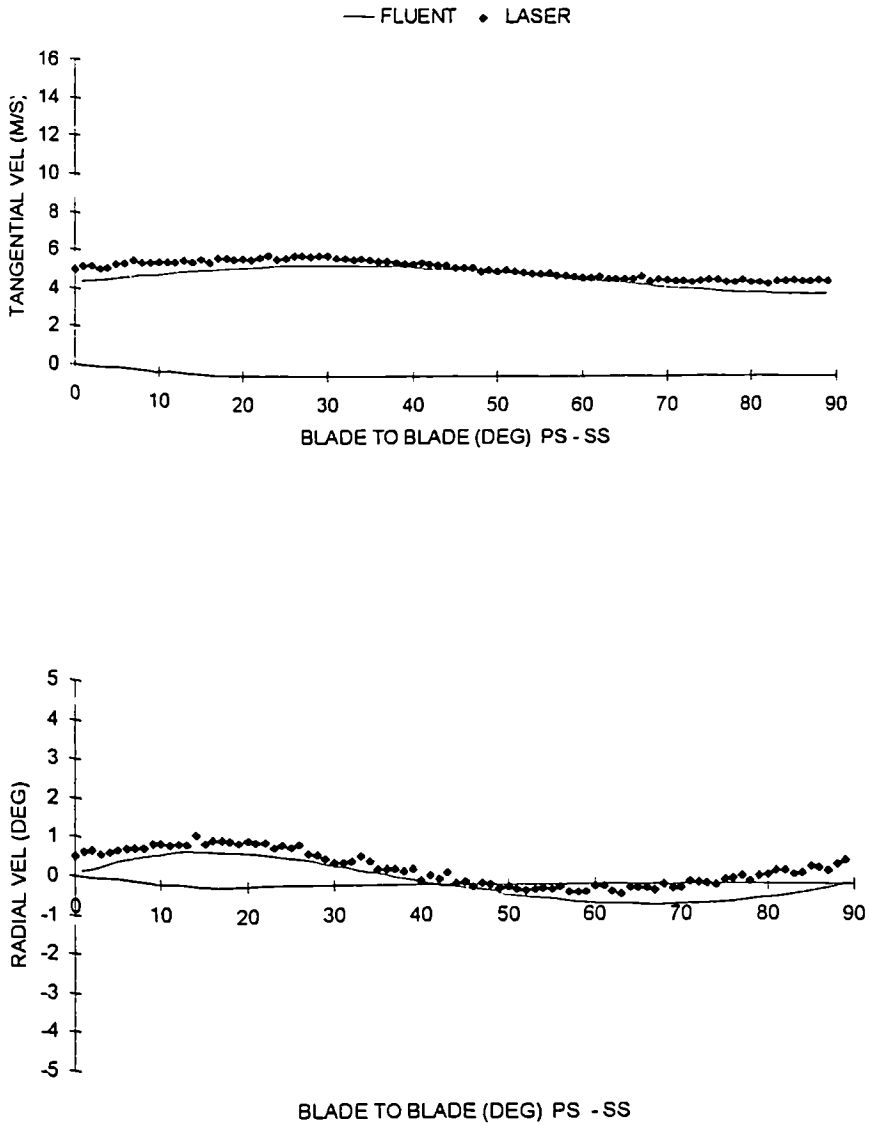

Figure 5.27 Comparison of experimental and computational velocity profiles, R = 0.184m, Window 4.

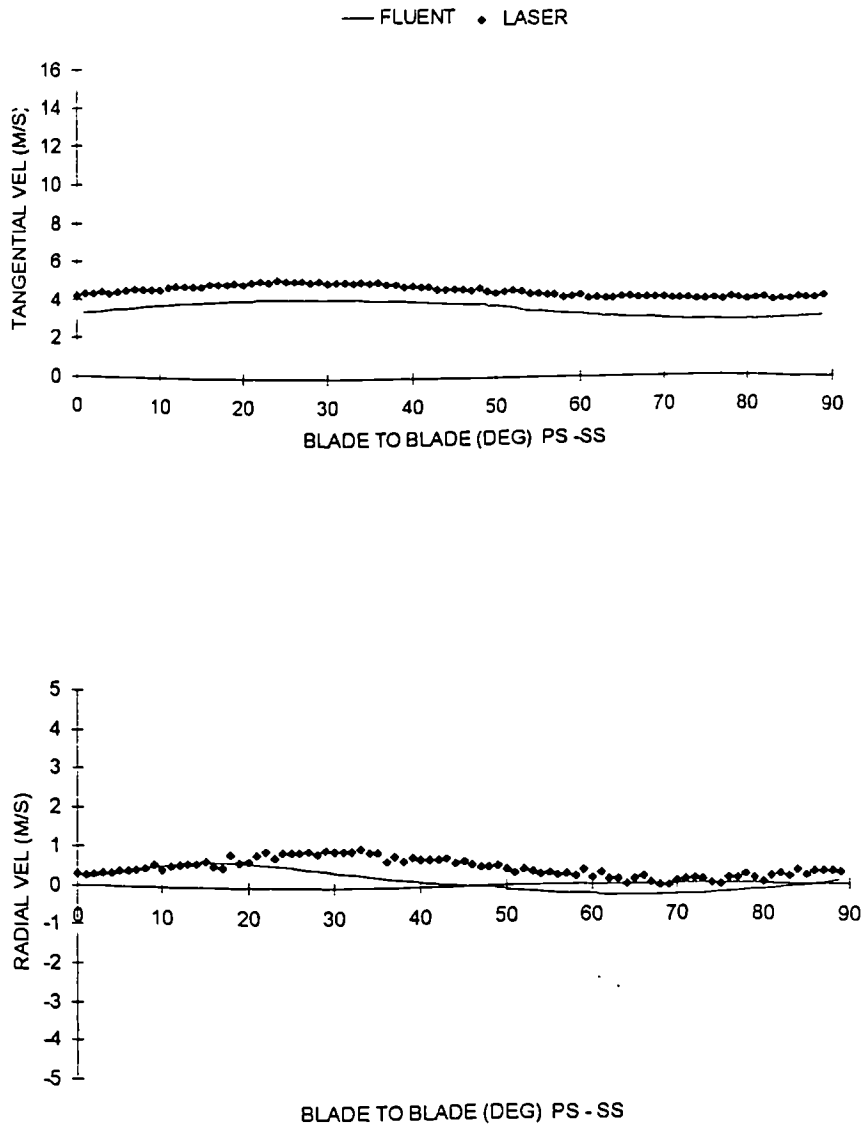

Figure 5.28 Comparison of experimental and computational velocity profiles, R = 0.198m, Window 4.

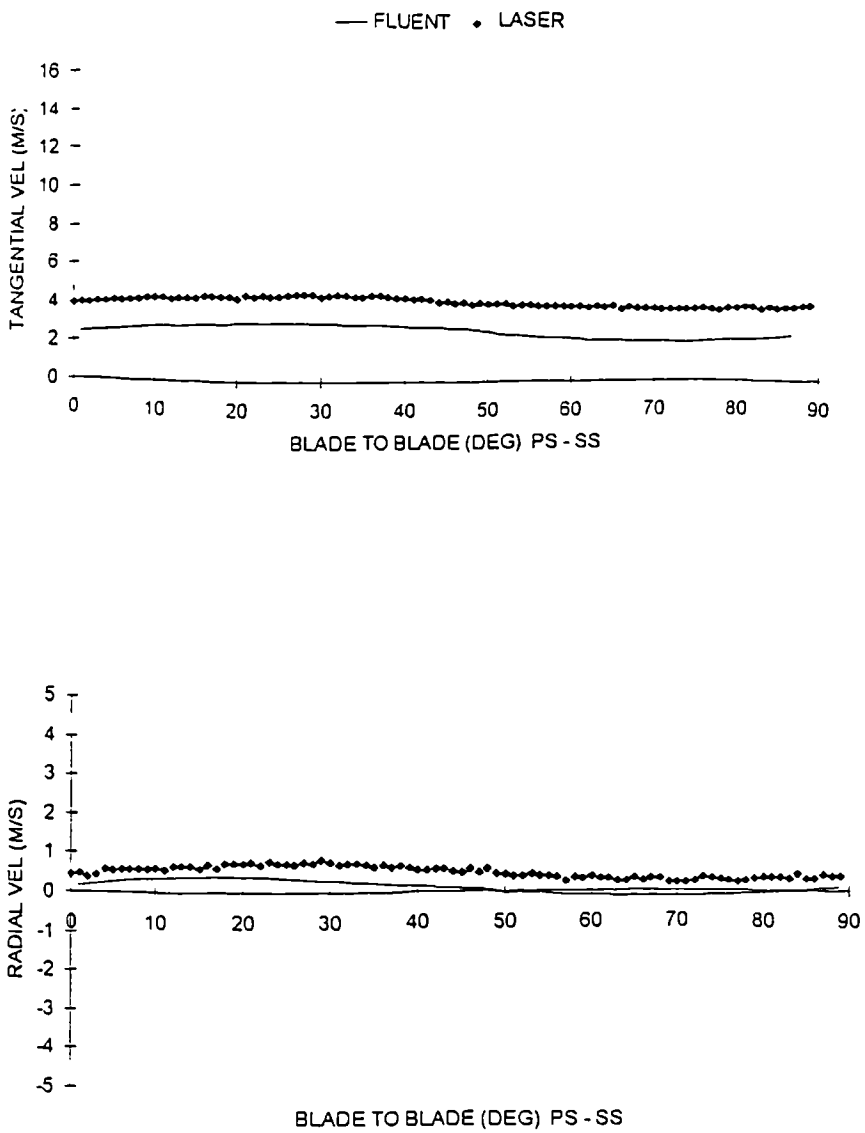

Figure 5.29 Comparison of experimental and computational velocity profiles, R = 0.212m, Window 4.

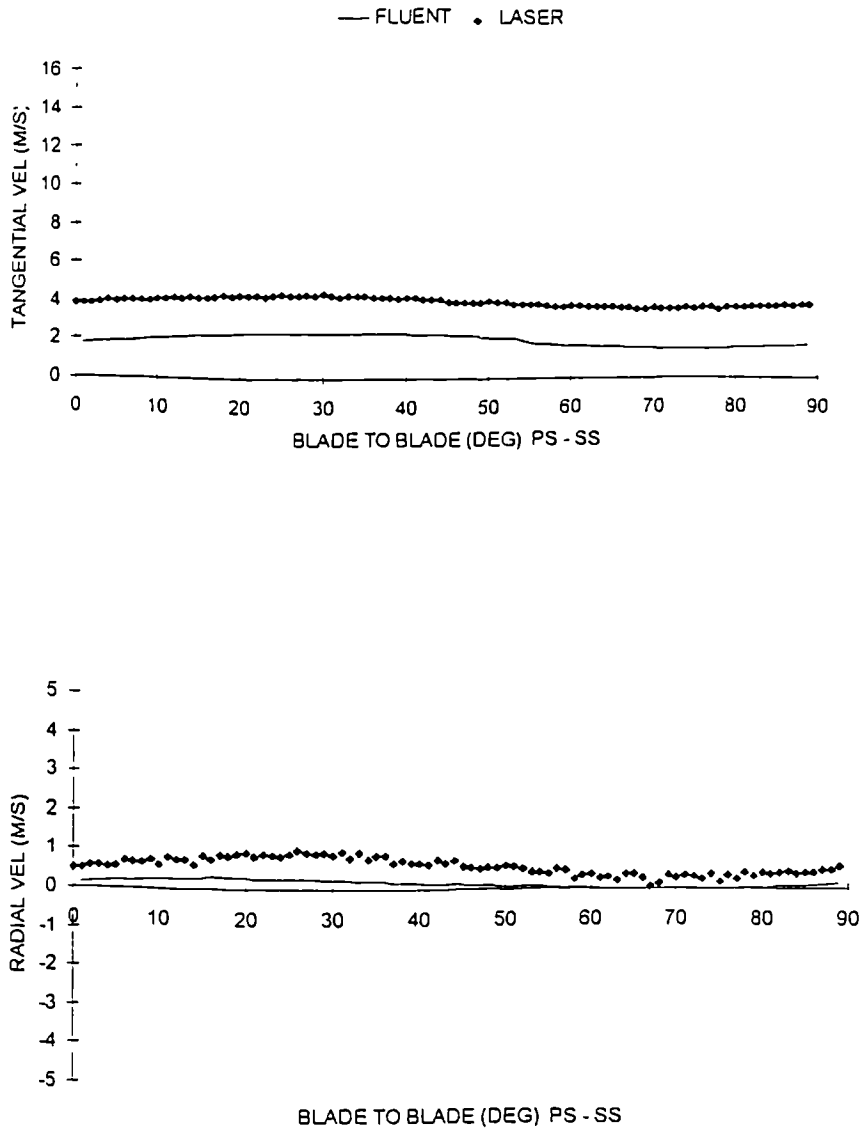

Figure 5.30 Comparison of experimental and computational velocity profiles, R = 0.226m, Window 4.

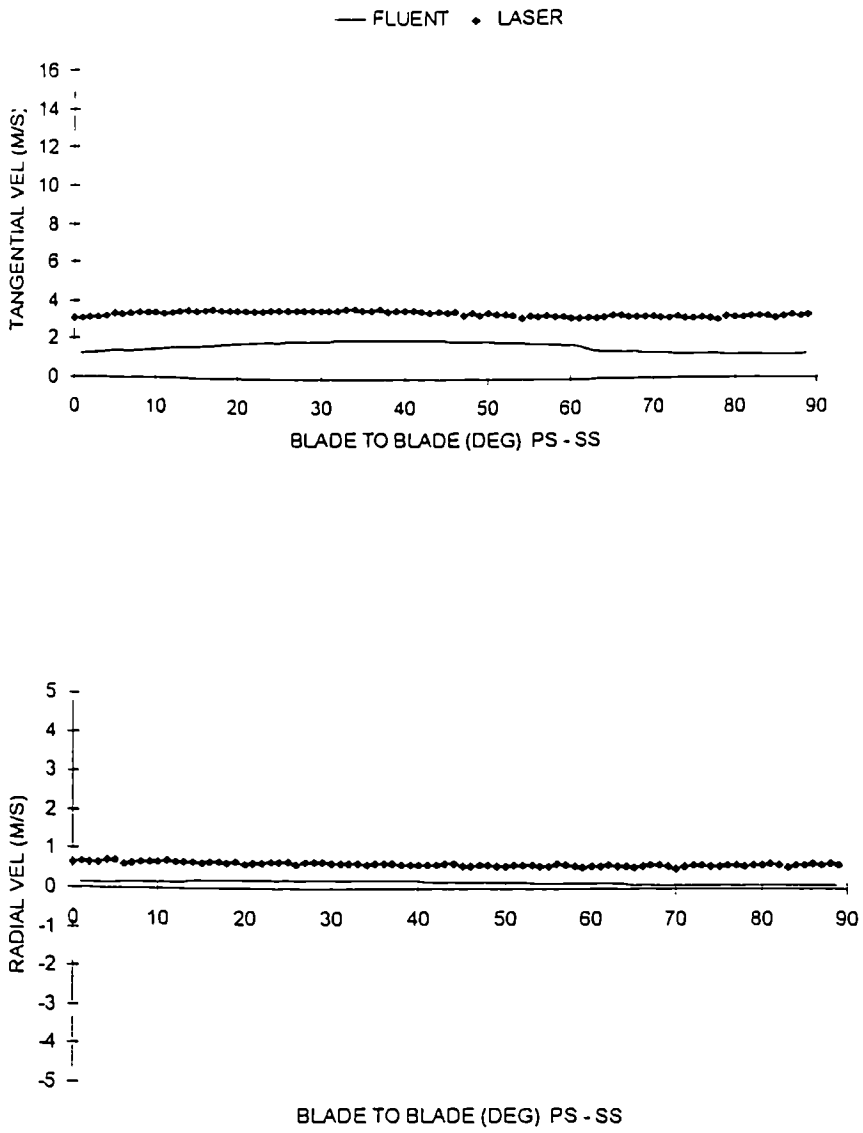

Figure 5.31 Comparison of experimental and computational velocity profiles, R = 0.240m, Window 4.

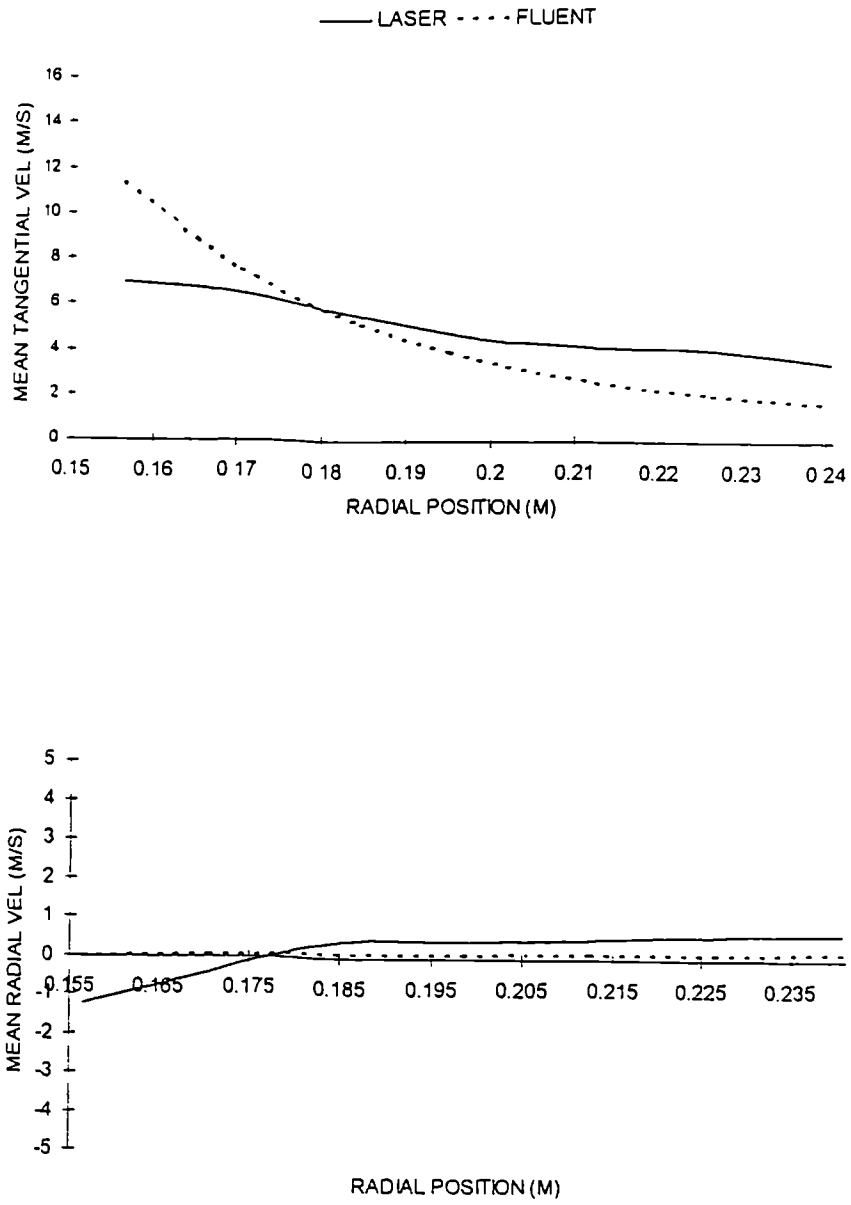

Figure 5.32 Mean Tangential and Radial Velocity Profiles Across the Volute, Window 4.

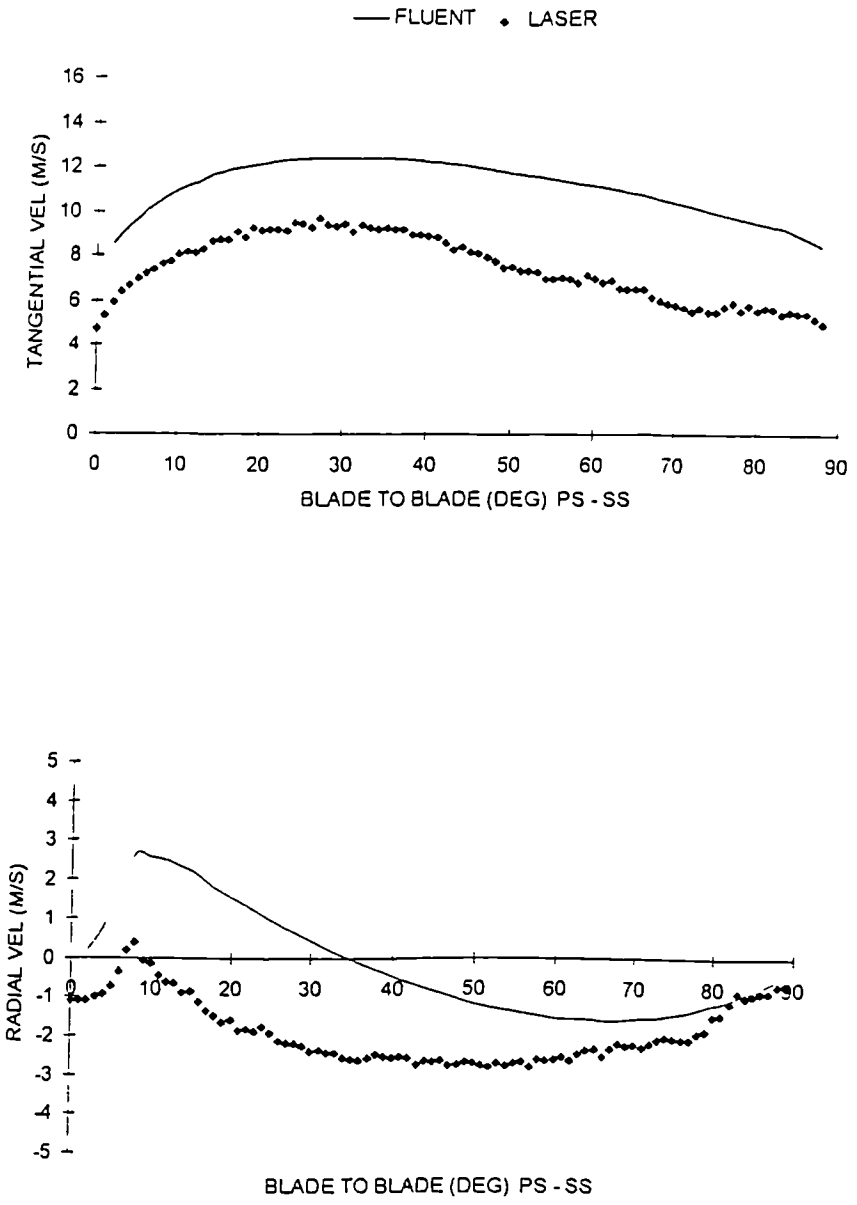

Figure 5.33 Comparison of experimental and computational velocity profiles, R = 0.156m, Window 5.

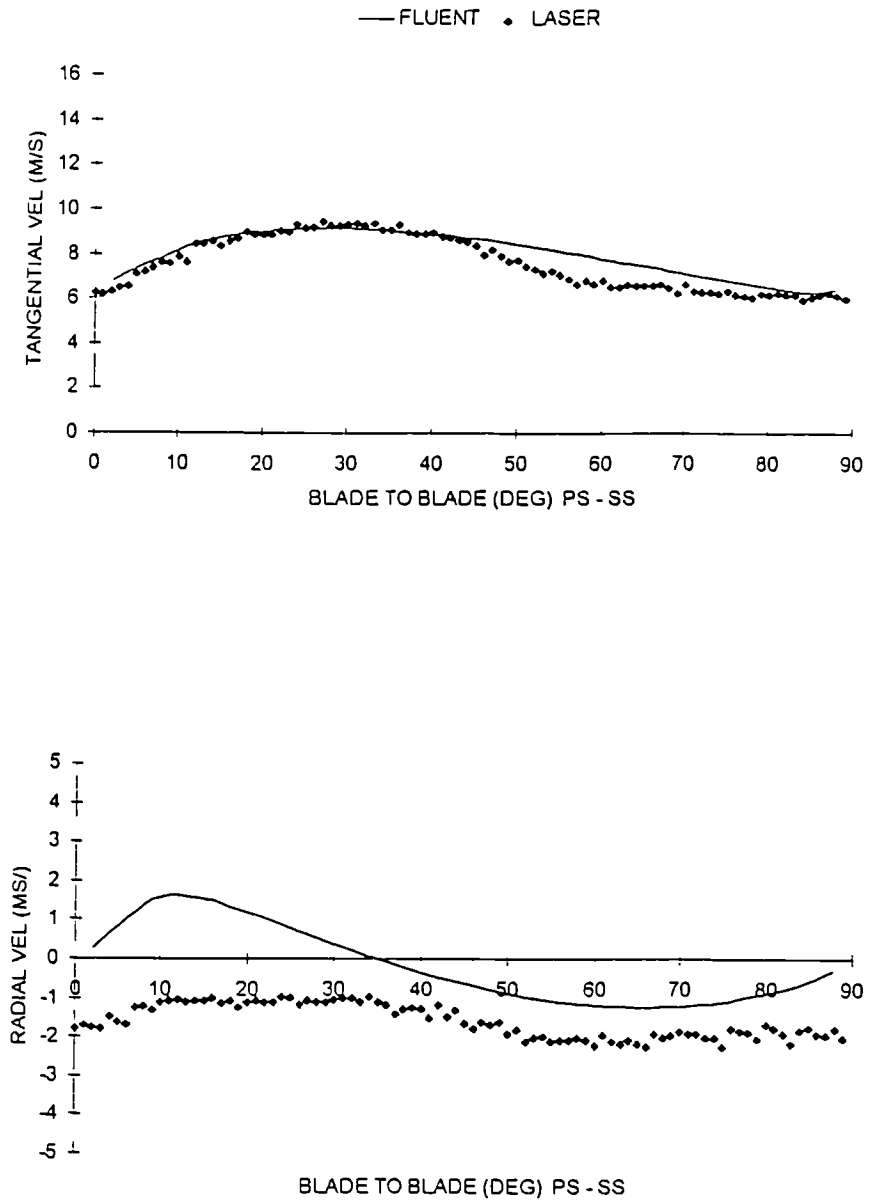

Figure 5.34 Comparison of experimental and computational velocity profiles, R = 0.166m, Window 5.

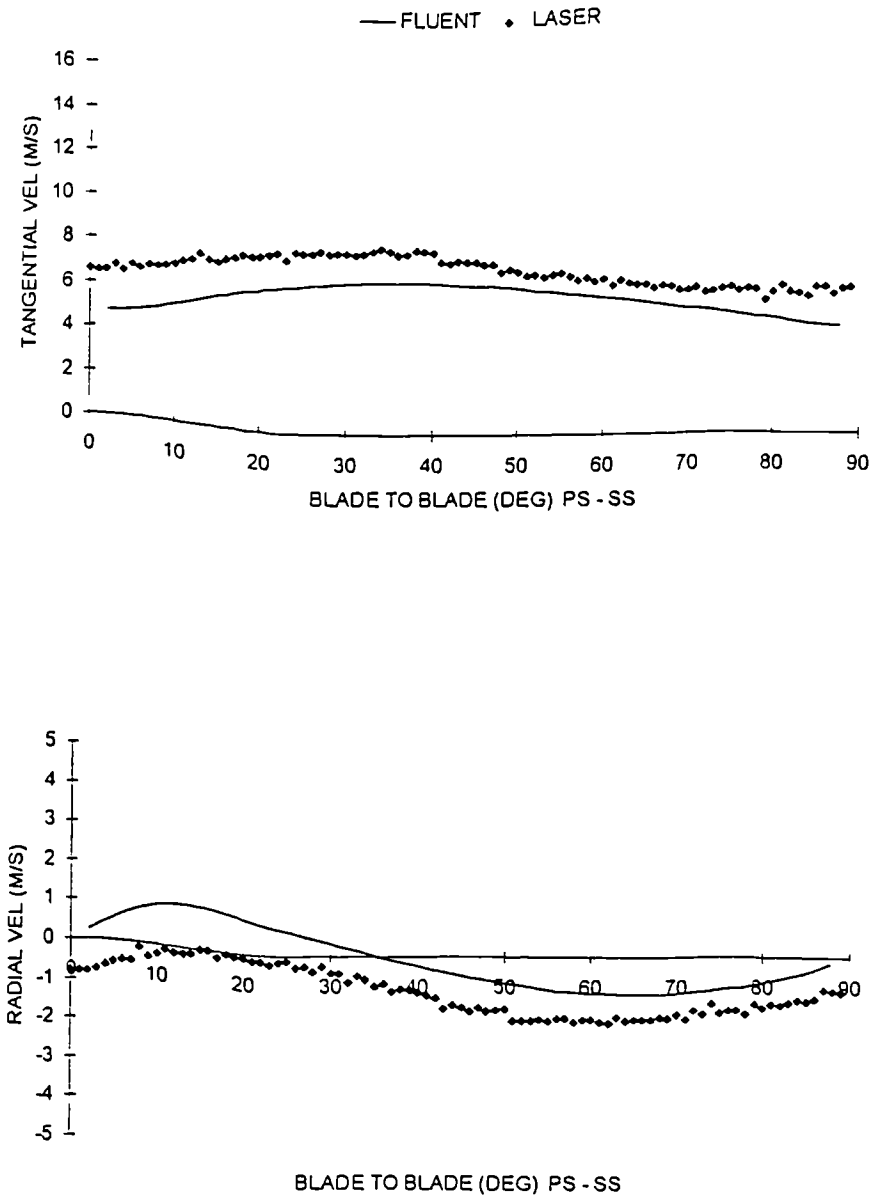

Figure 5.35 Comparison of experimental and computational velocity profiles, R = 0.176m, Window 5.

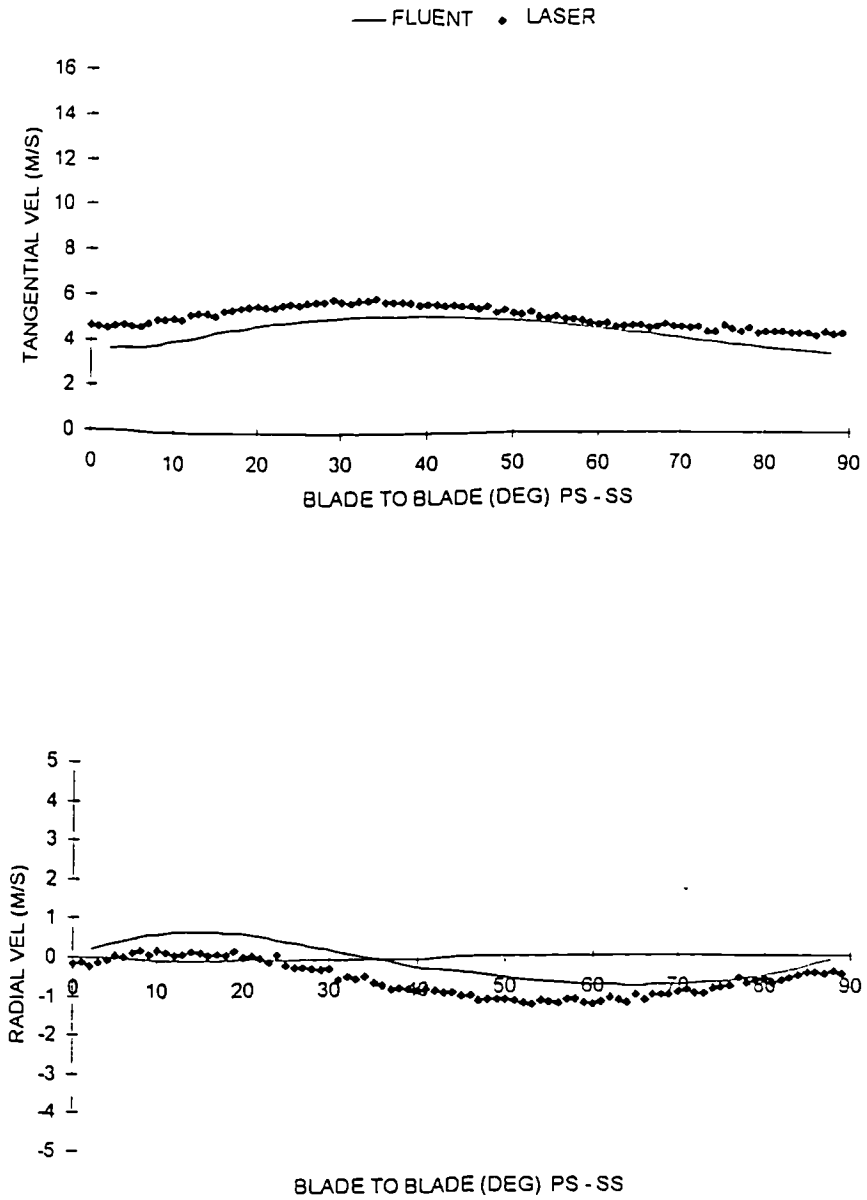

Figure 5.36 Comparison of experimental and computational velocity profiles, R = 0.186m, Window 5.

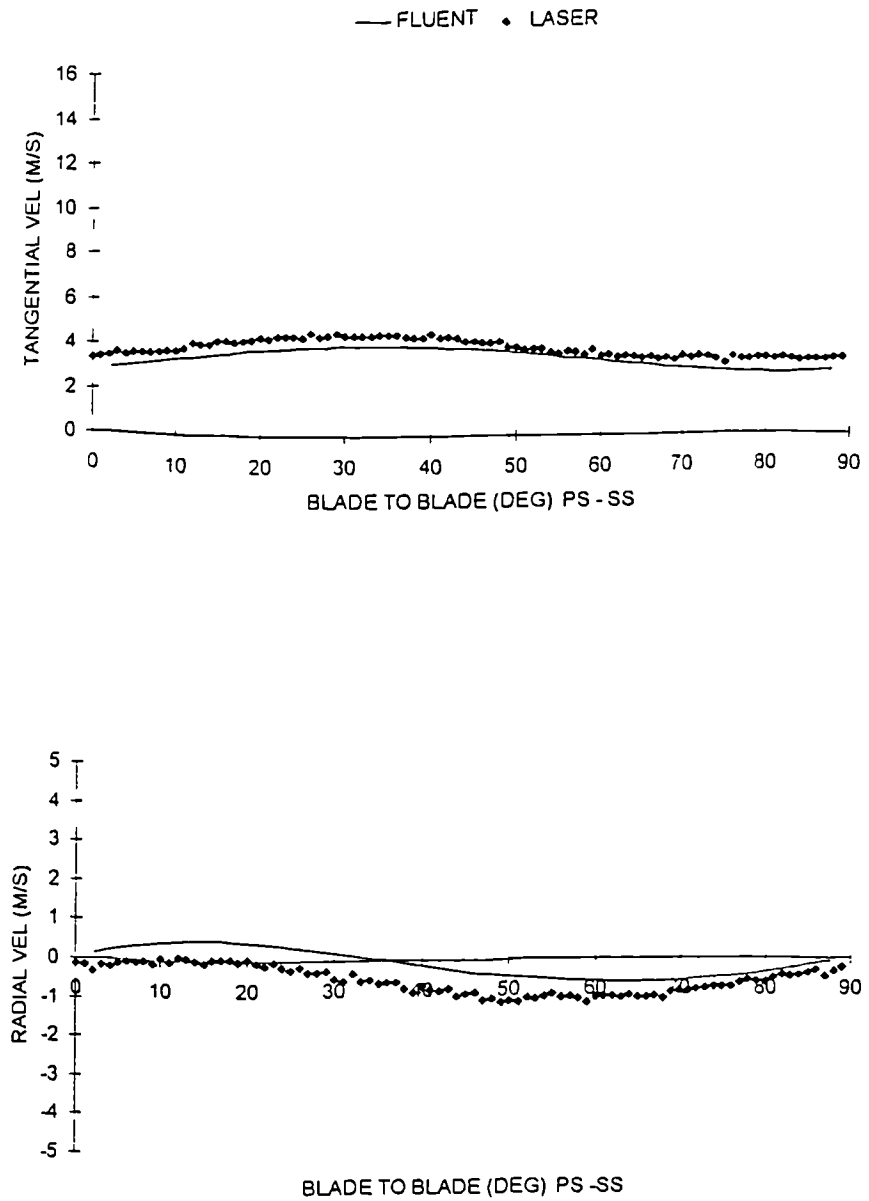

Figure 5.37 Comparison of experimental and computational velocity profiles, R = 0.196m, Window 5.

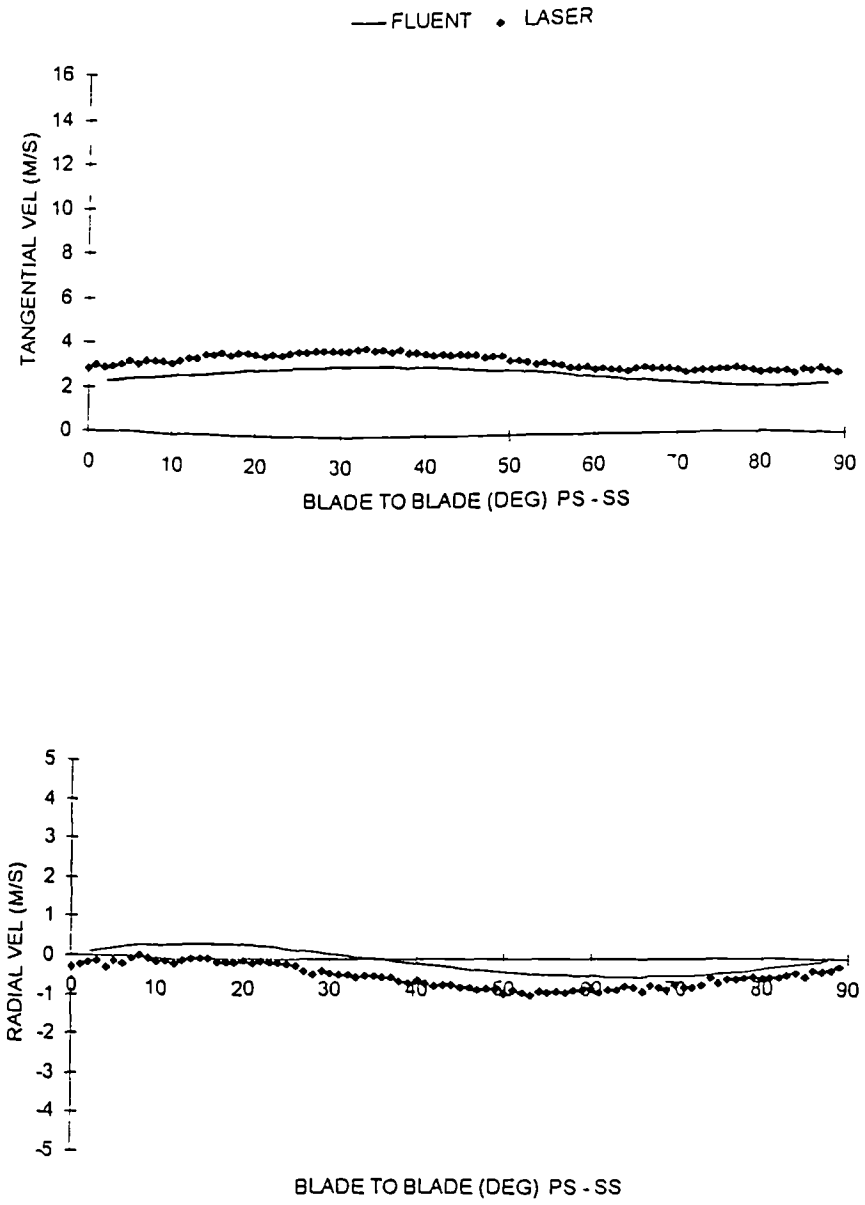

Figure 5.38 Comparison of experimental and computational velocity profiles, R = 0.206m, Window 5.

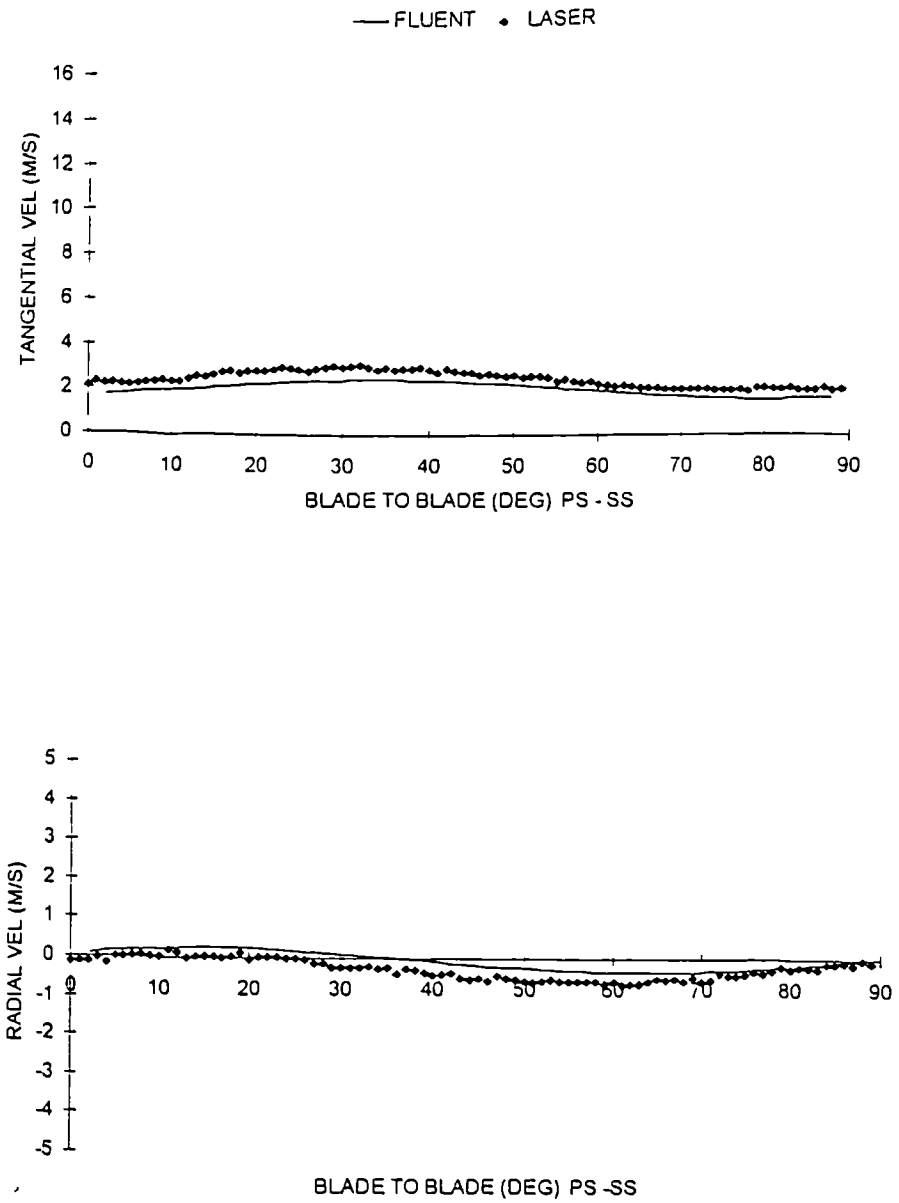

Figure 5.39 Comparison of experimental and computational velocity profiles, R = 0.216m, Window 5.

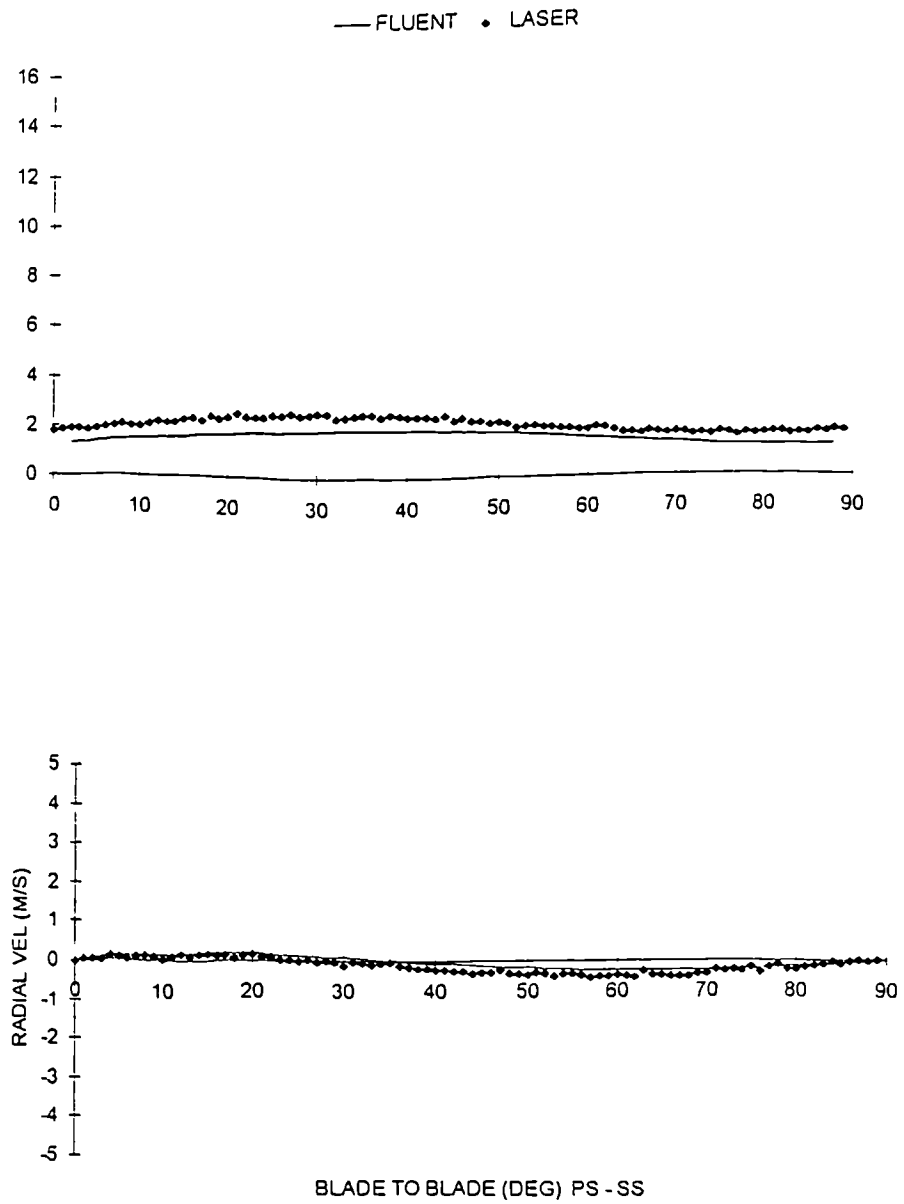

Figure 5.40 Comparison of experimental and computational velocity profiles, R = 0.226m, Window 5.

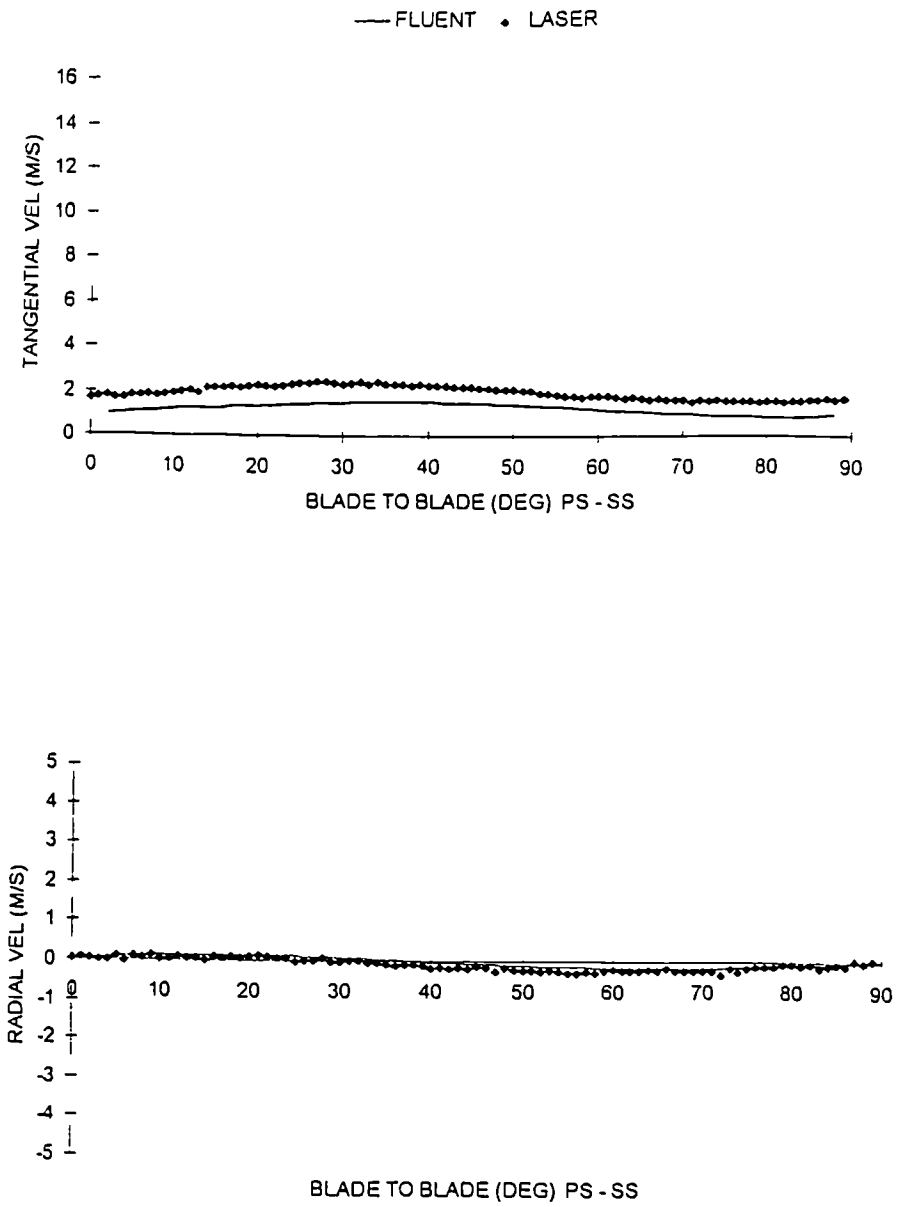

Figure 5.41 Comparison of experimental and computational velocity profiles, R = 0.236m, Window 5.

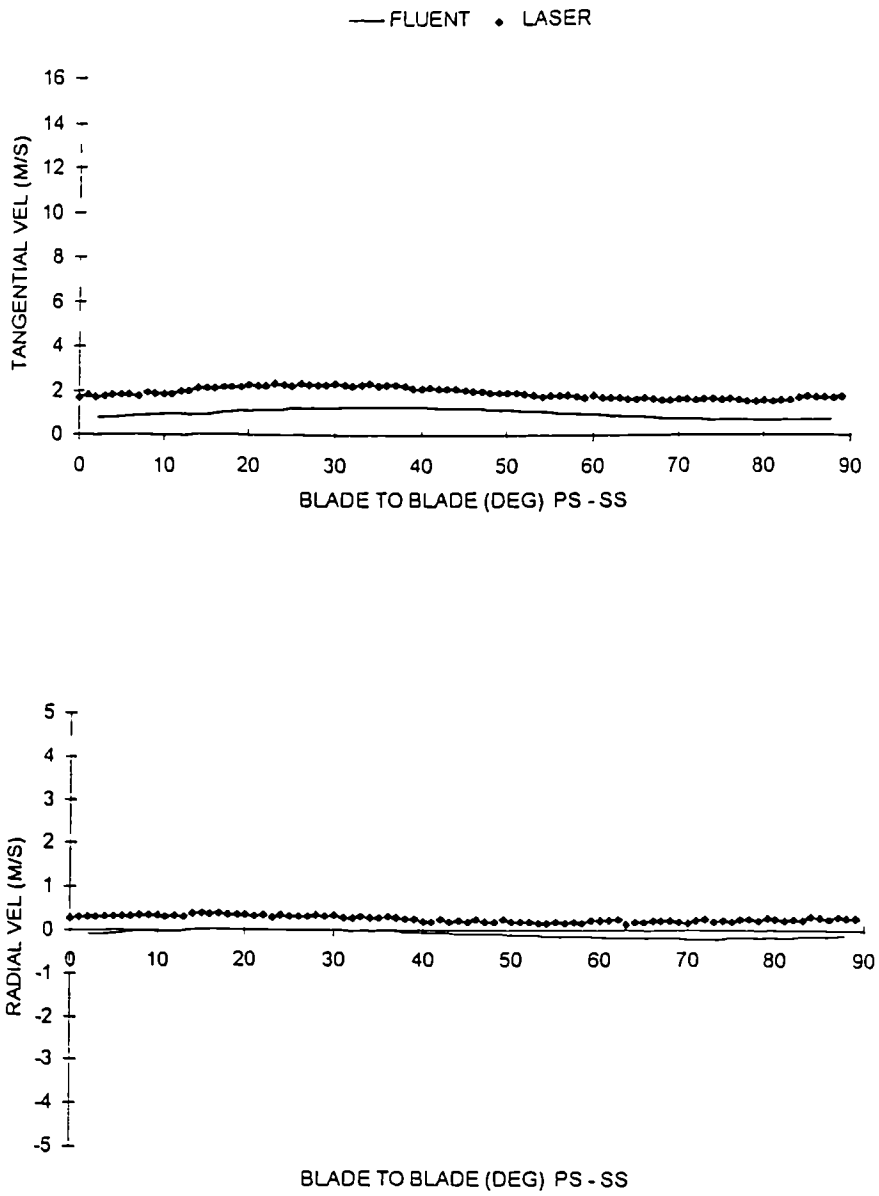

Figure 5.42 Comparison of experimental and computational velocity profiles, R = 0.246m, Window 5.

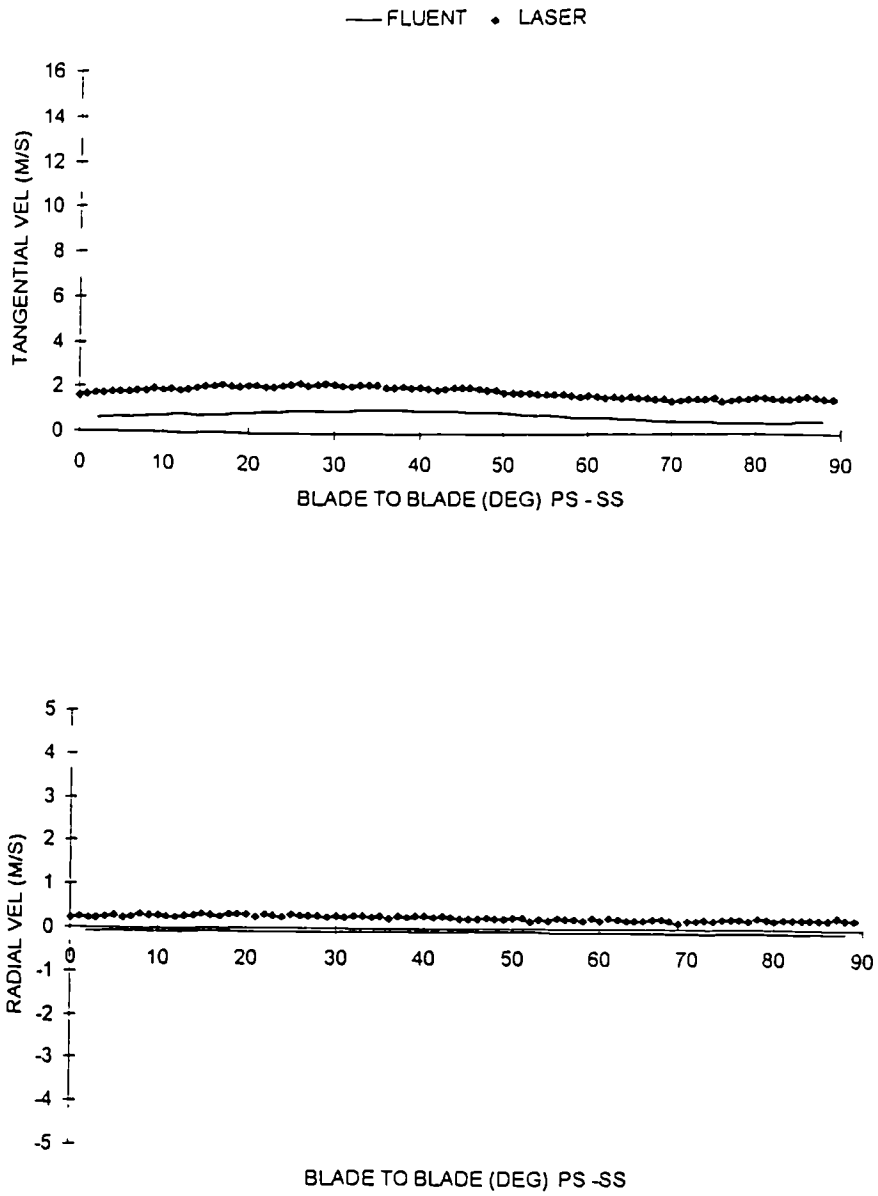

Figure 5.43 Comparison of experimental and computational velocity profiles, R = 0.256m, Window 5.

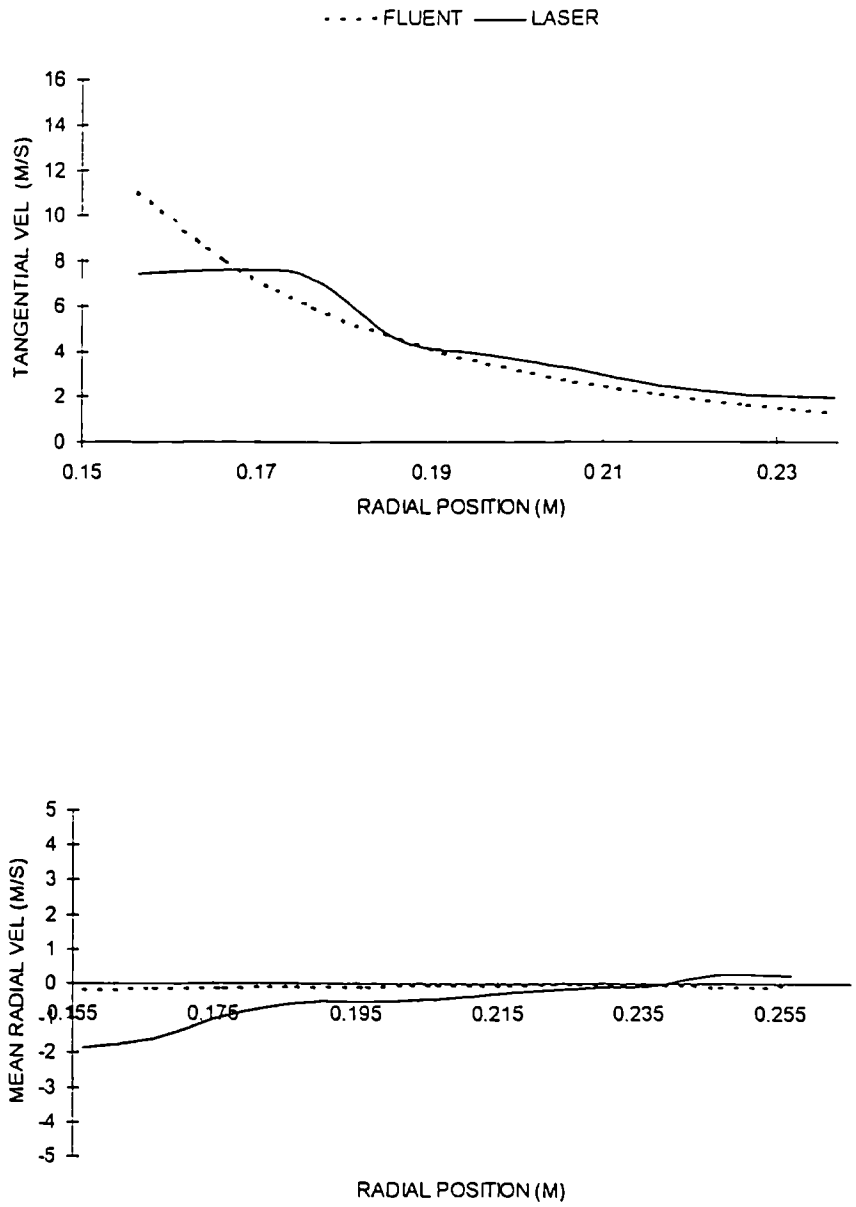

Figure 5.44 Mean Tangential and Radial Velocity Profiles Across the Volute, Window 5

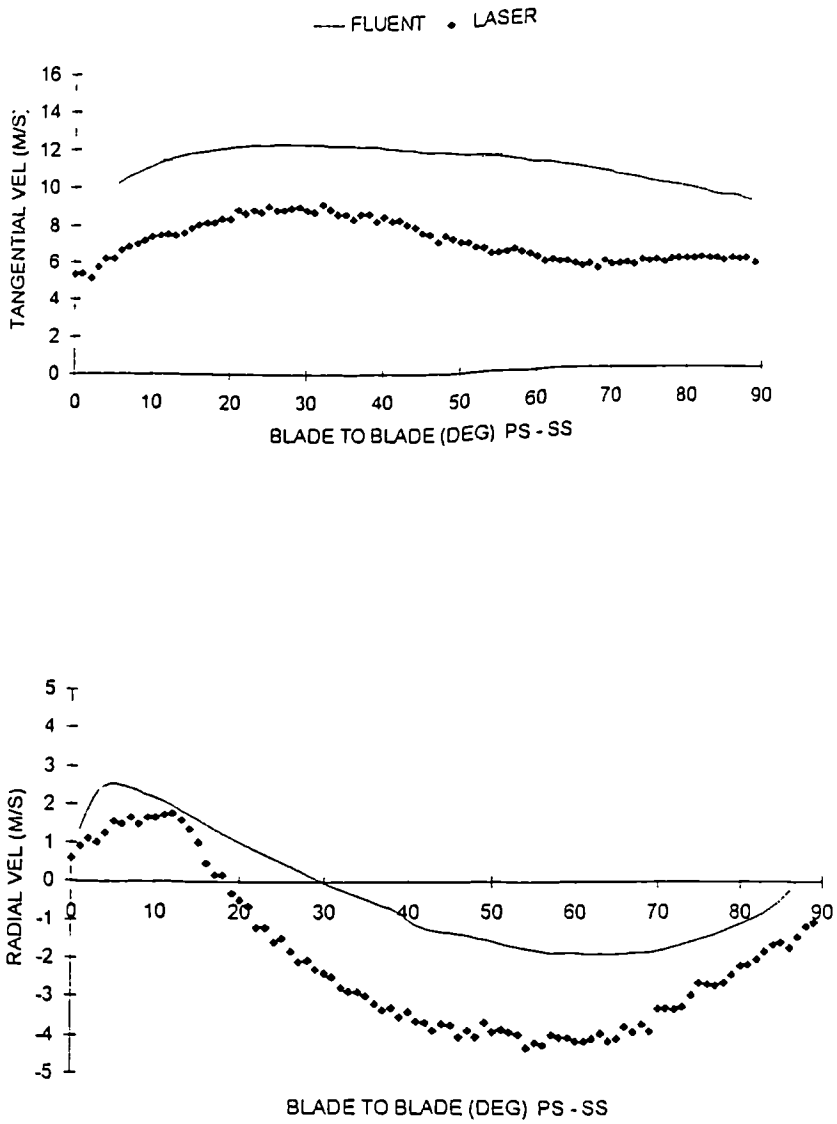

Figure 5.45 Comparison of experimental and computational velocity profiles, R = 0.156m, Window 6.

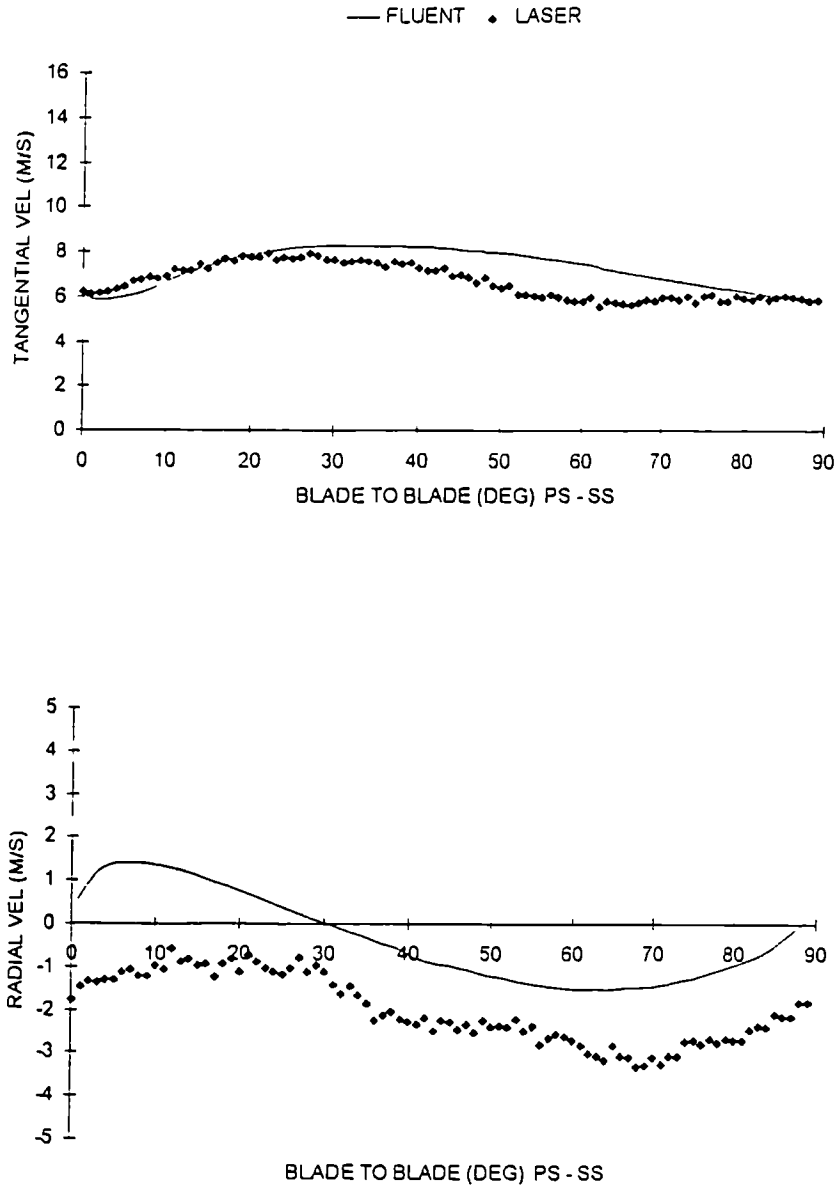

Figure 5.46 Comparison of experimental and computational velocity profiles, R = 0.170m, Window 6.

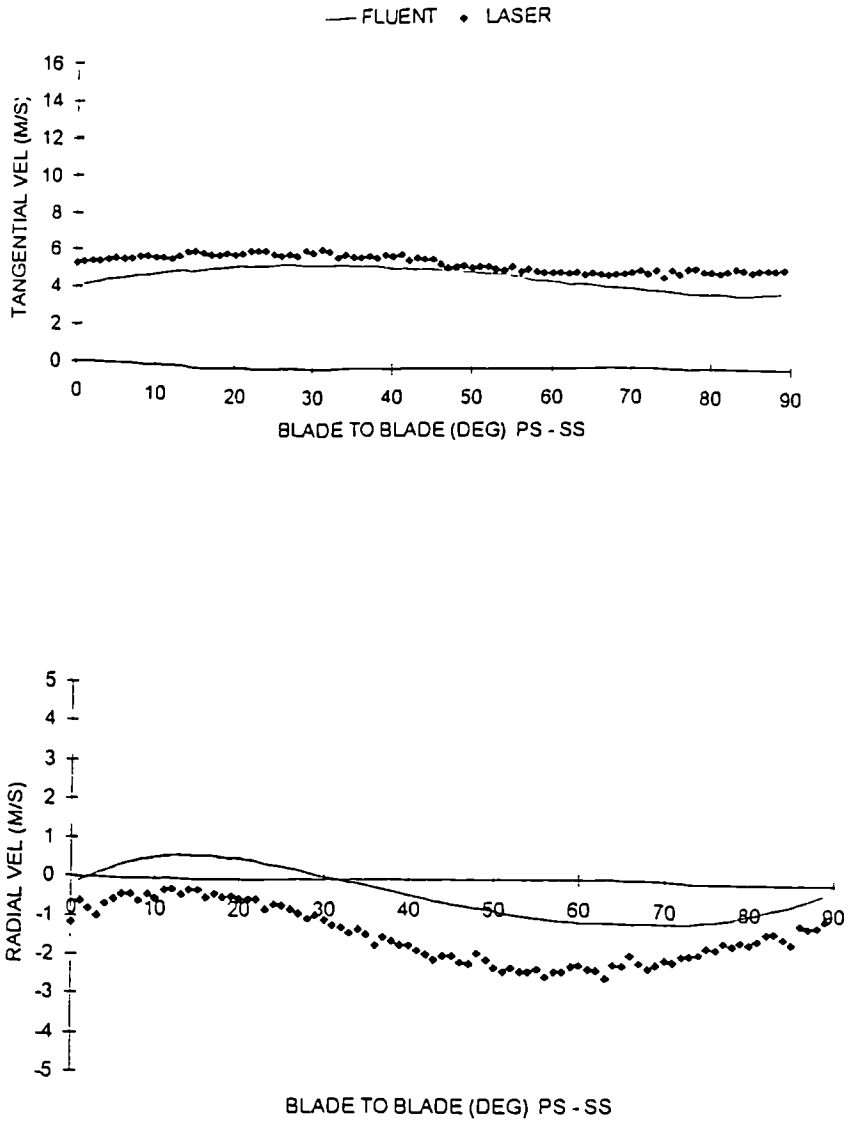

Figure 5.47 Comparison of experimental and computational velocity profiles, R = 0.184m, Window 6.

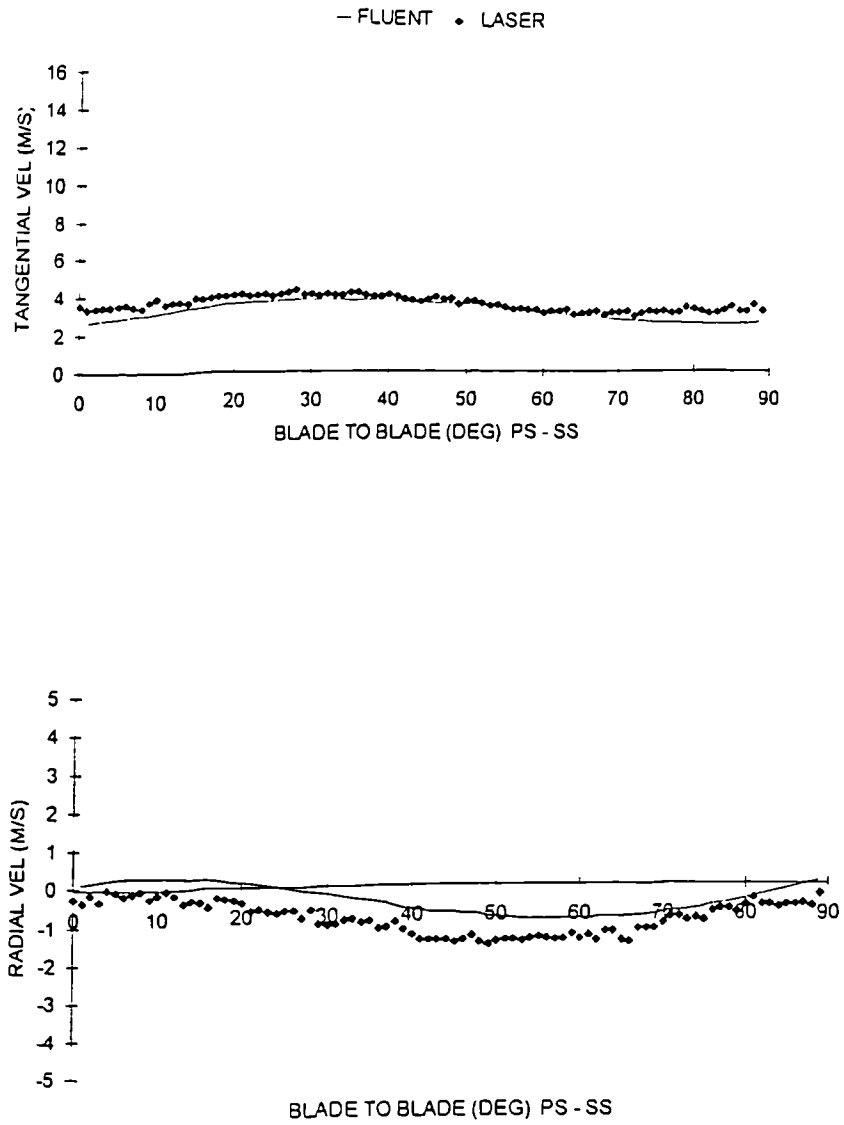

Figure 5.48 Comparison of experimental and computational velocity profiles, R = 0.198m, Window 6.

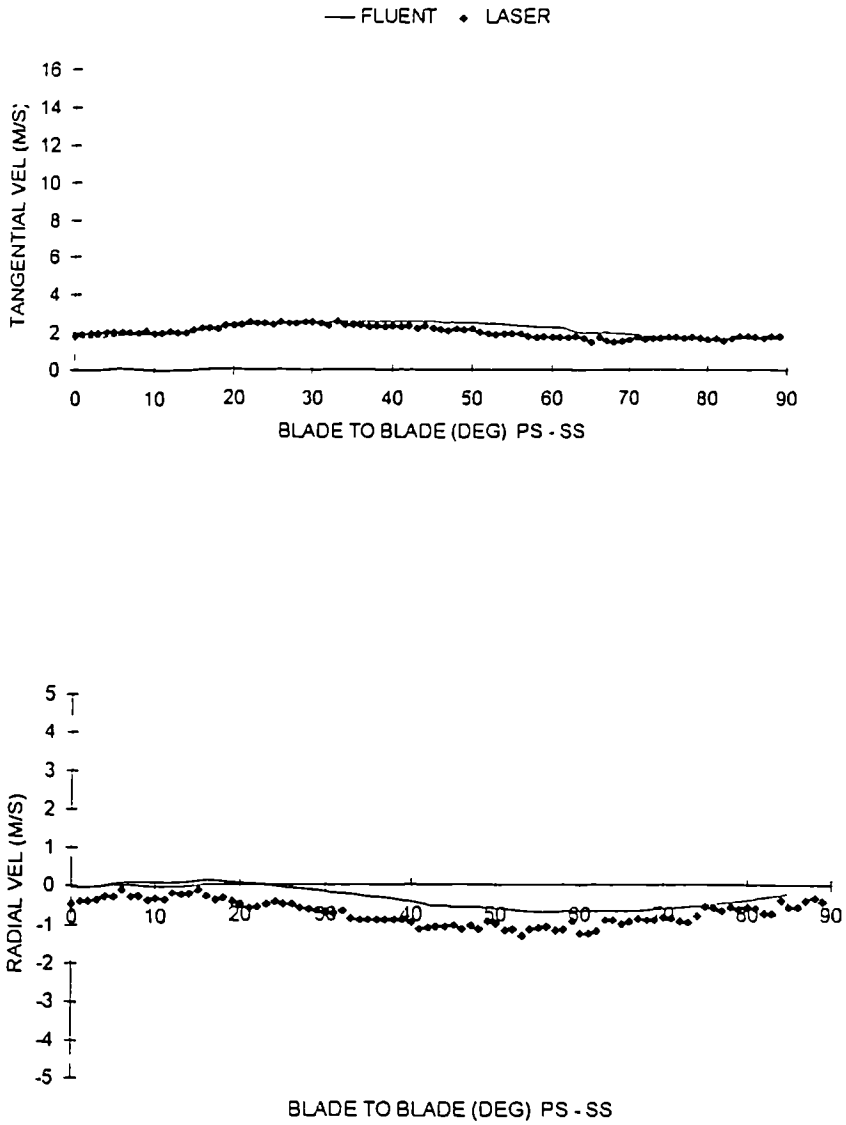

Figure 5.49 Comparison of experimental and computational velocity profiles, R = 0.212m, Window 6.

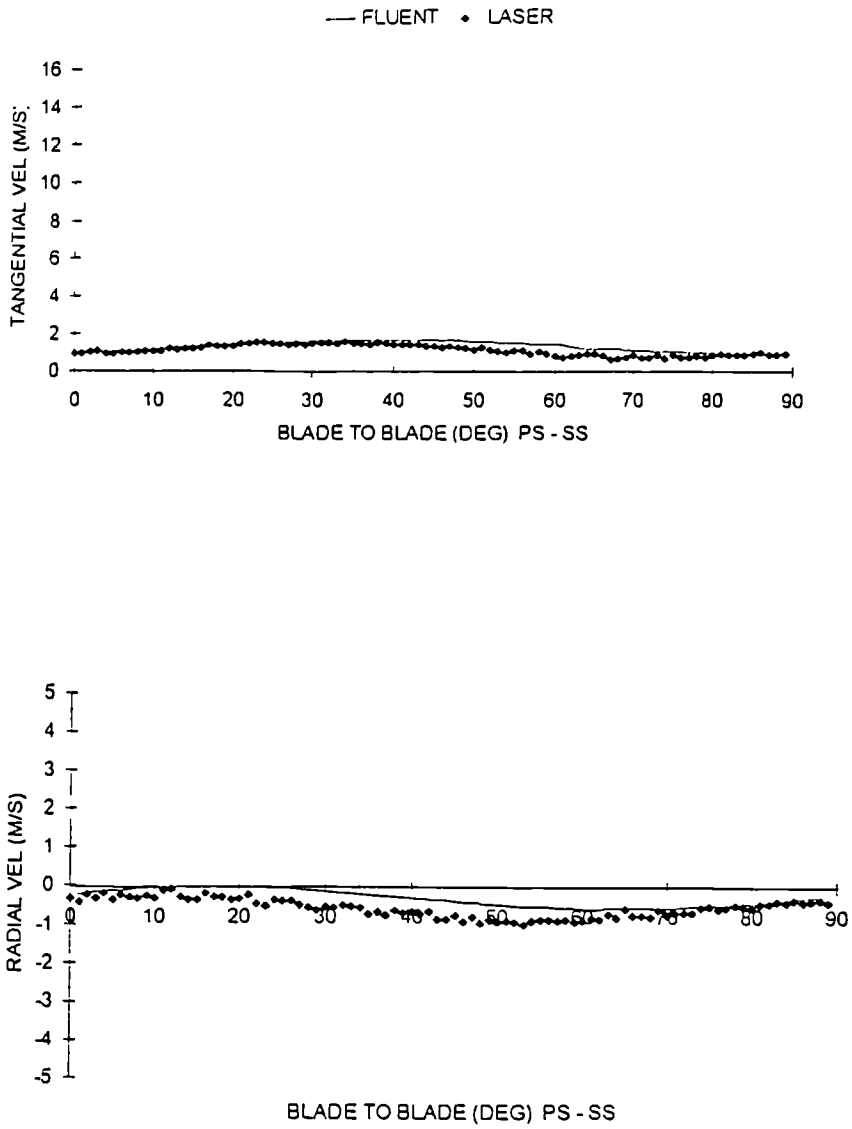

Figure 5.50 Comparison of experimental and computational velocity profiles, R = 0.226m, Window 6.

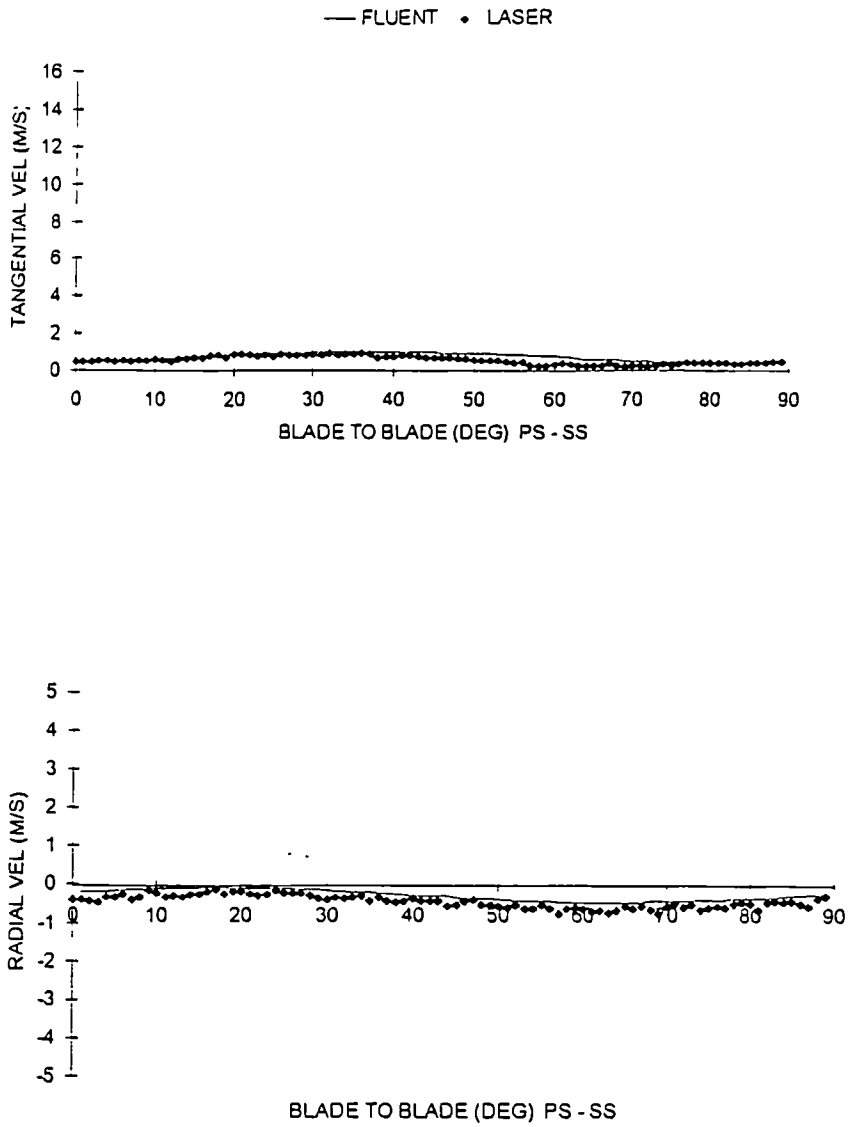

Figure 5.51 Comparison of experimental and computational velocity profiles, R = 0.240m, Window 6.

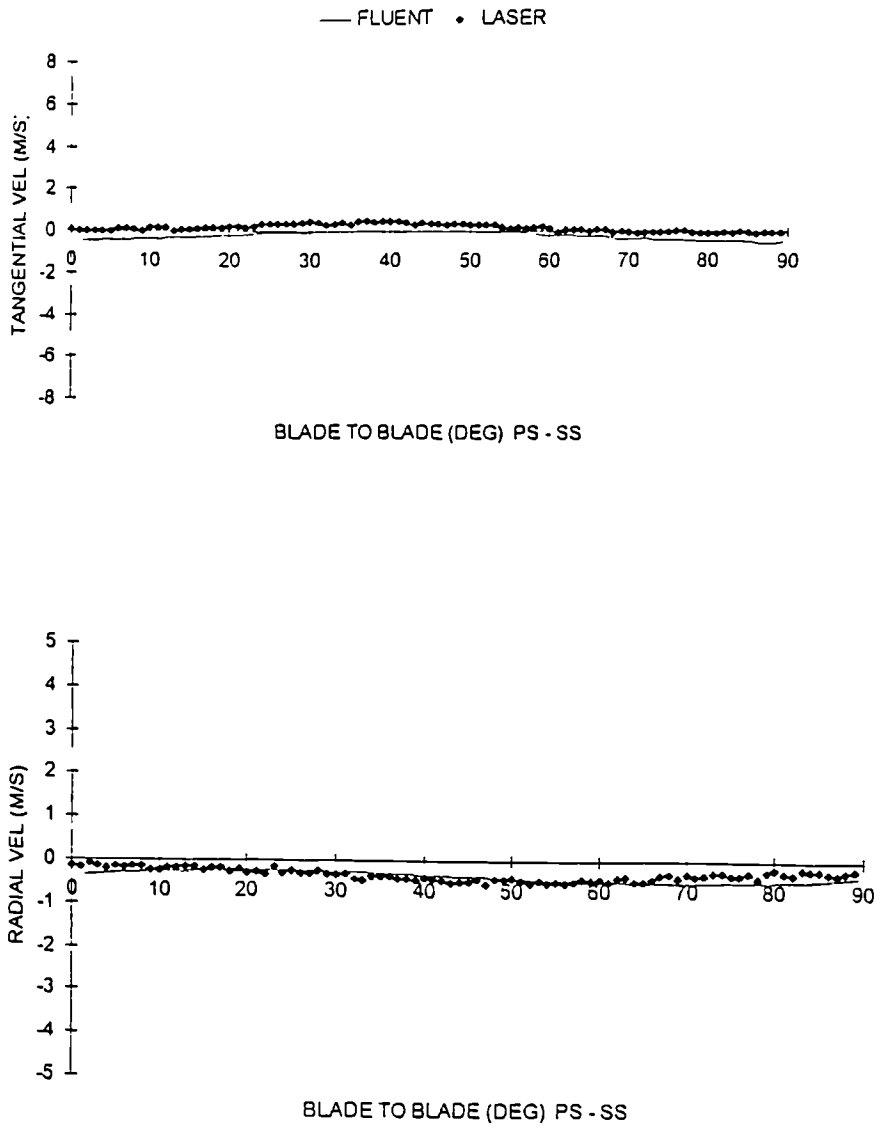

Figure 5.52 Comparison of experimental and computational velocity profiles, R = 0.254m, Window 6.

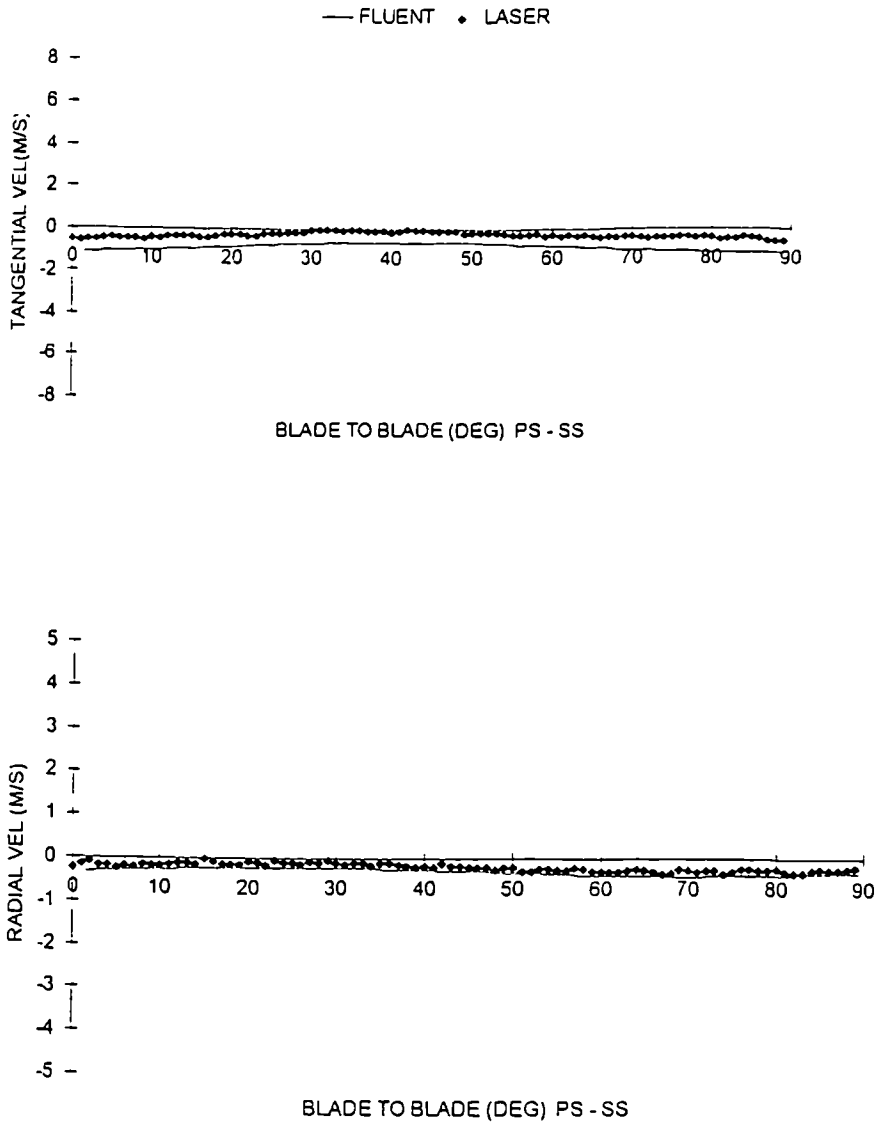

Figure 5.53 Comparison of experimental and computational velocity profiles, R = 0.268m, Window 6.

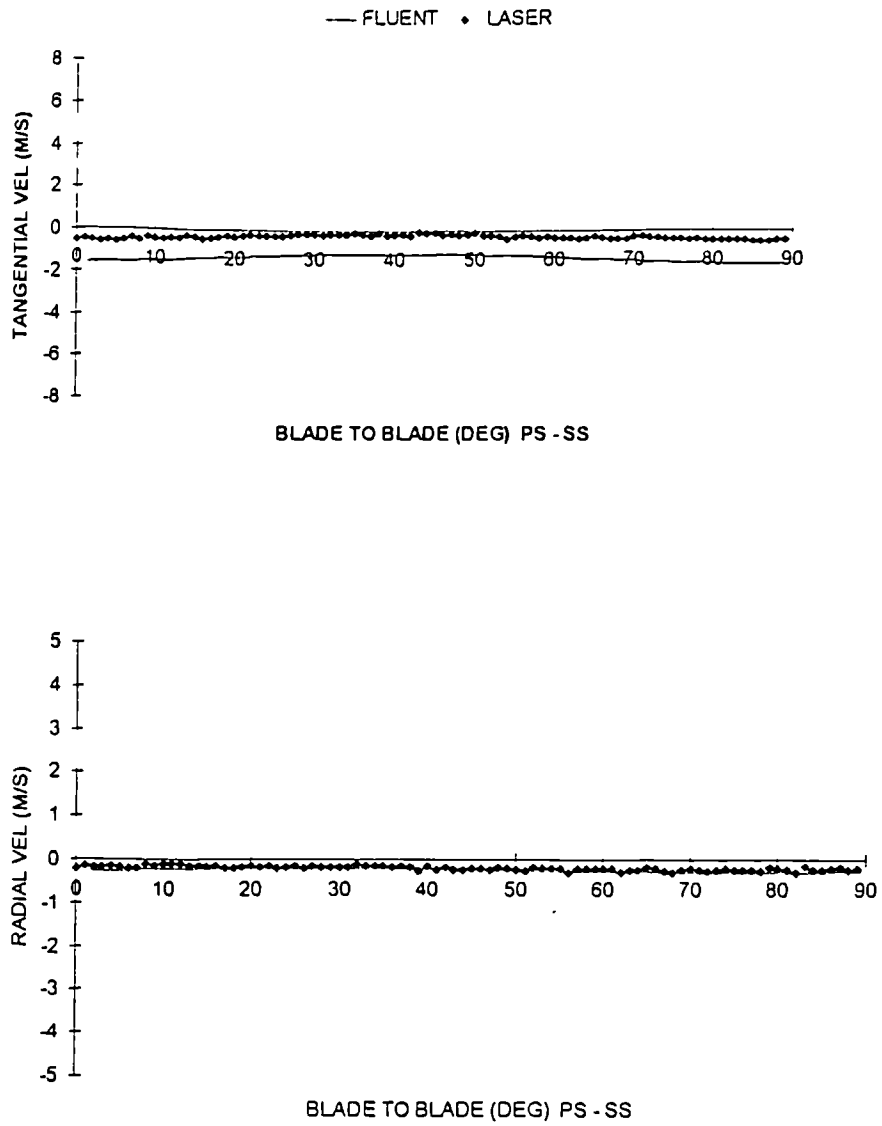

Figure 5.54 Comparison of experimental and computational velocity profiles, R = 0.282m, Window 6.

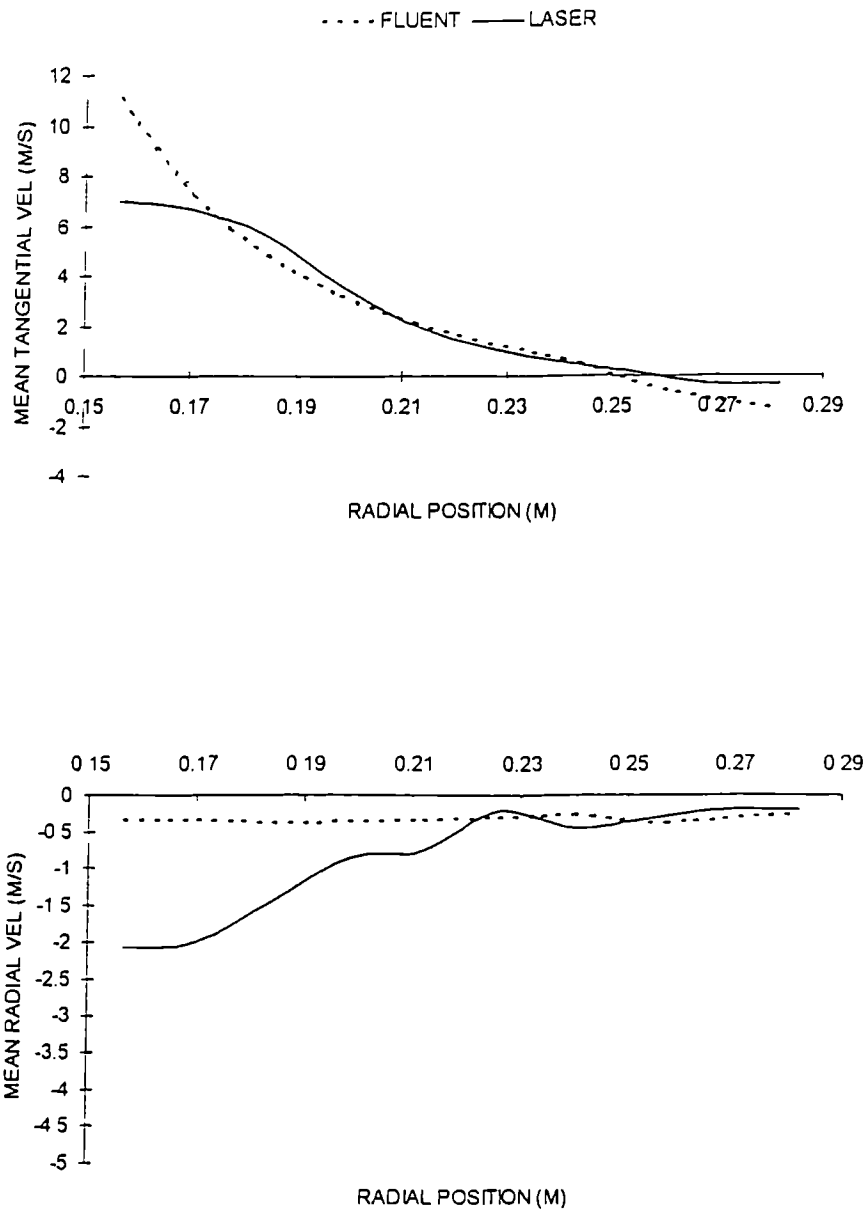

Figure 5.55 Mean Tangential and Radial Velocity Profiles Across the Volute, Window 6.

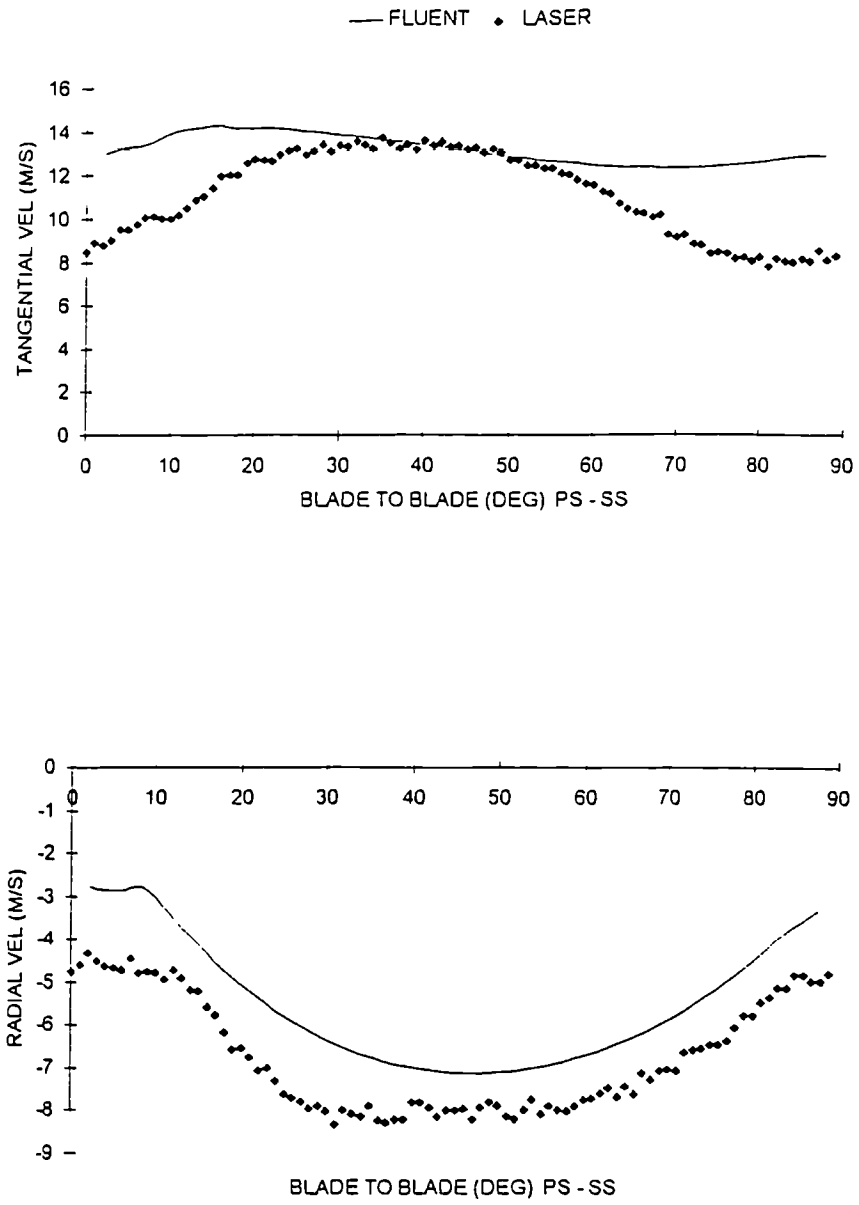

Figure 5.56 Comparison of experimental and computational velocity profiles, R = 0.156m, Window 7.

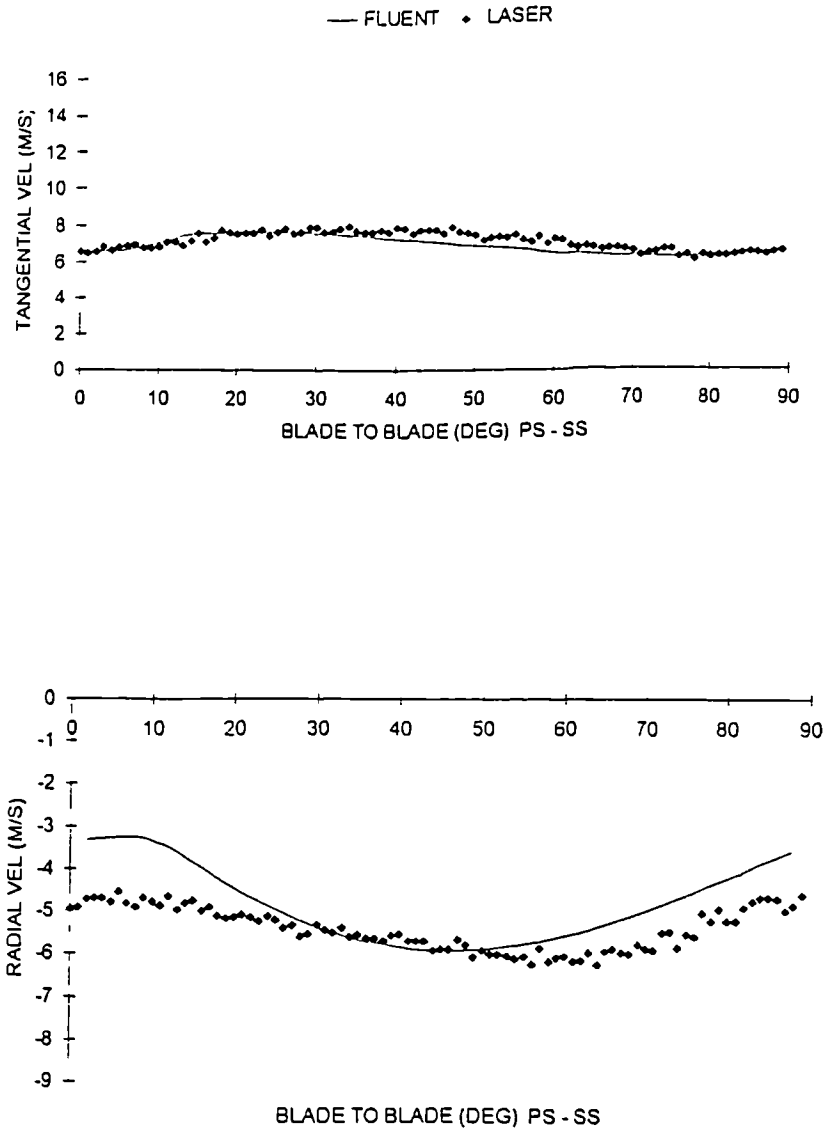

Figure 5.57 Comparison of experimental and computational velocity profiles, R = 0.166m, Window 7.

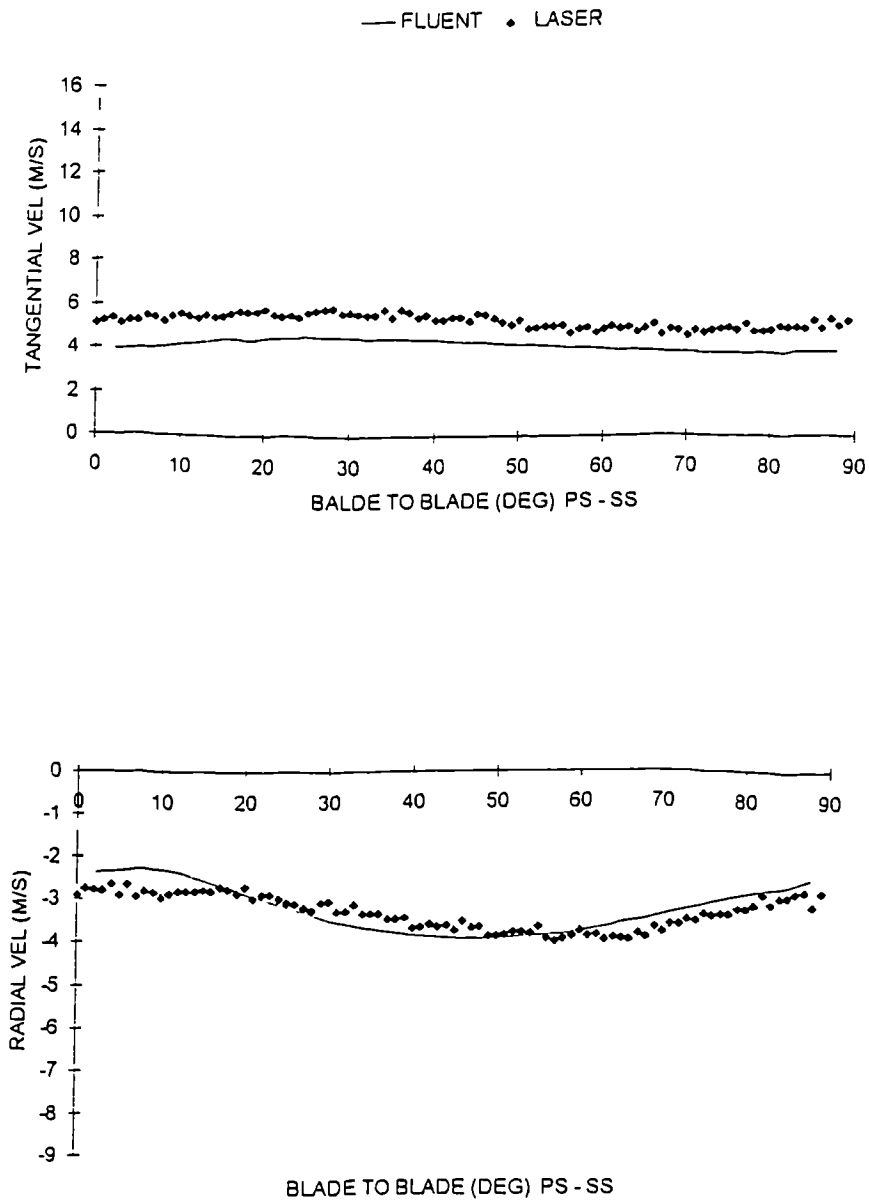

Figure 5.58 Comparison of experimental and computational velocity profiles, R = 0.176m, Window 7.

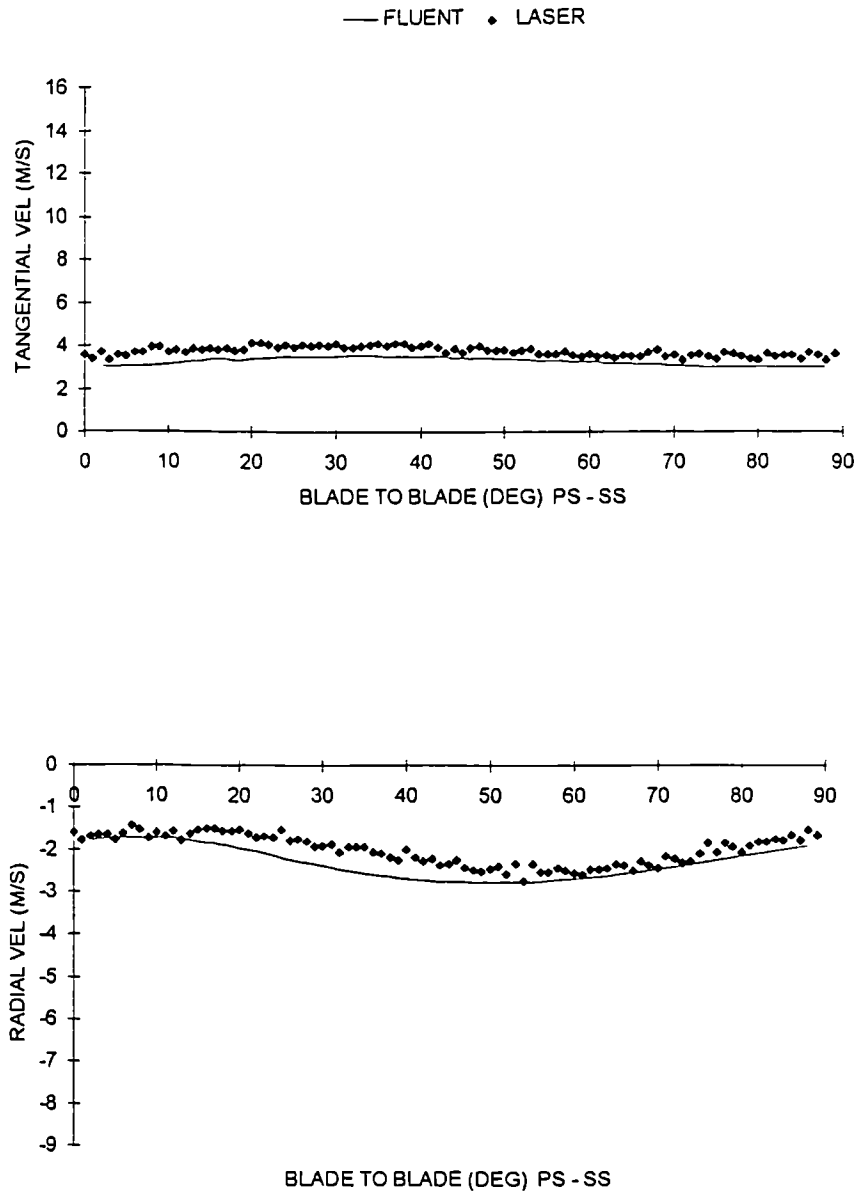

Figure 5.59 Comparison of experimental and computational velocity profiles, R = 0.186m, Window 7.

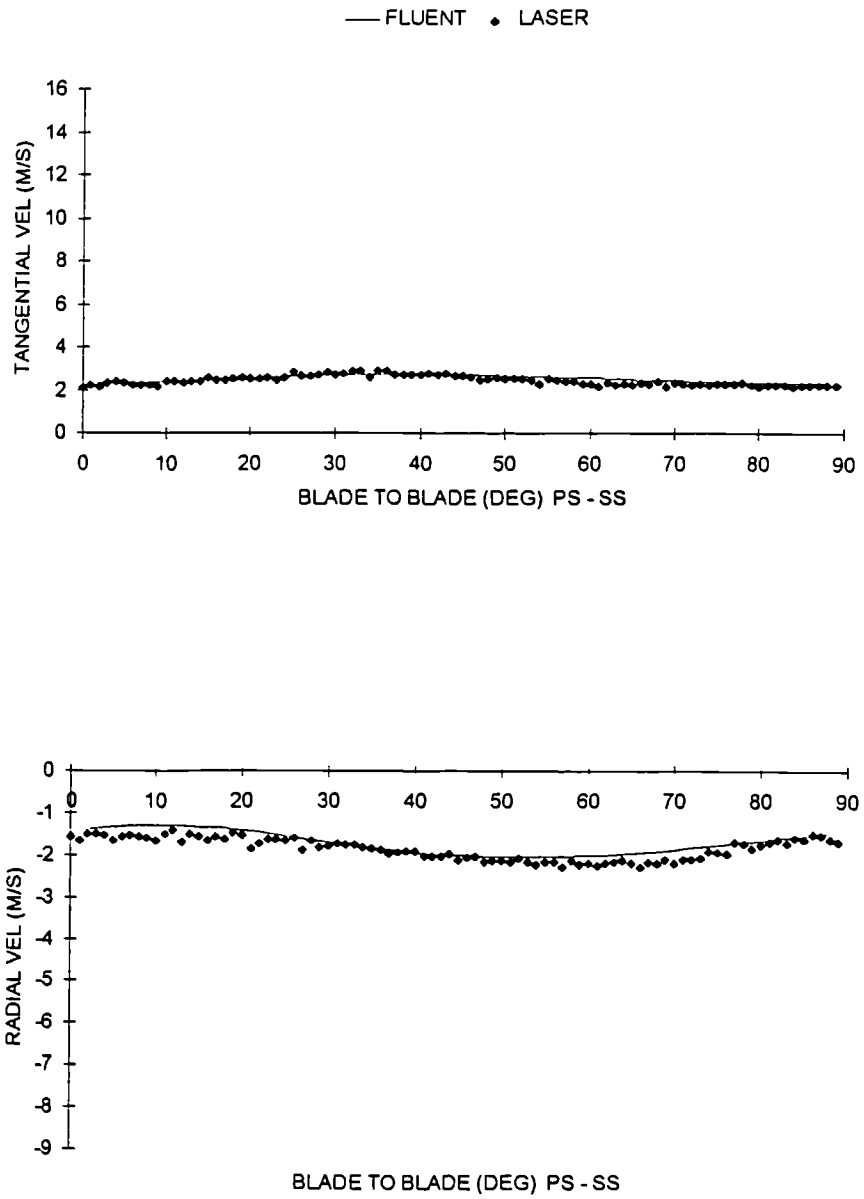

Figure 5.60 Comparison of experimental and computational velocity profiles, R = 0.196m, Window 7.

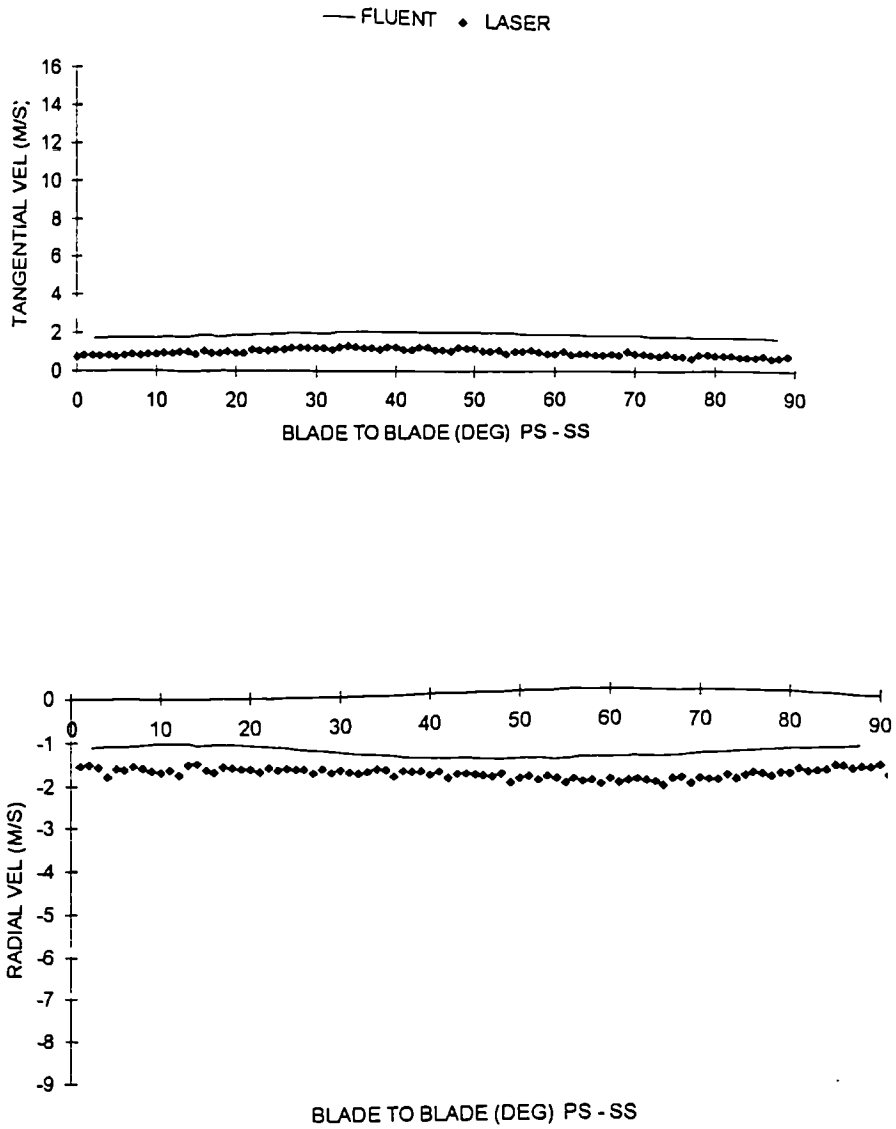

Figure 5.61 Comparison of experimental and computational velocity profiles, R = 0.206m, Window 7.

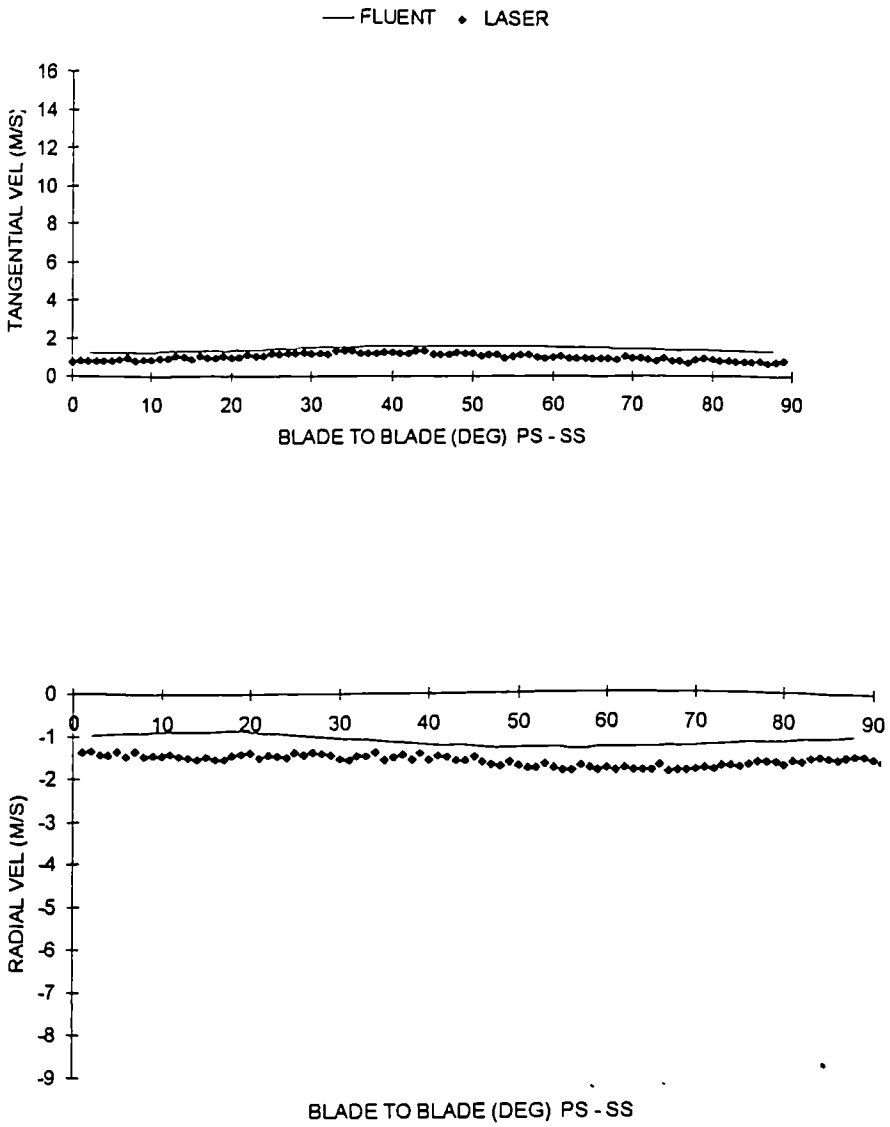

Figure 5.62 Comparison of experimental and computational velocity profiles, R = 0.216m, Window 7.

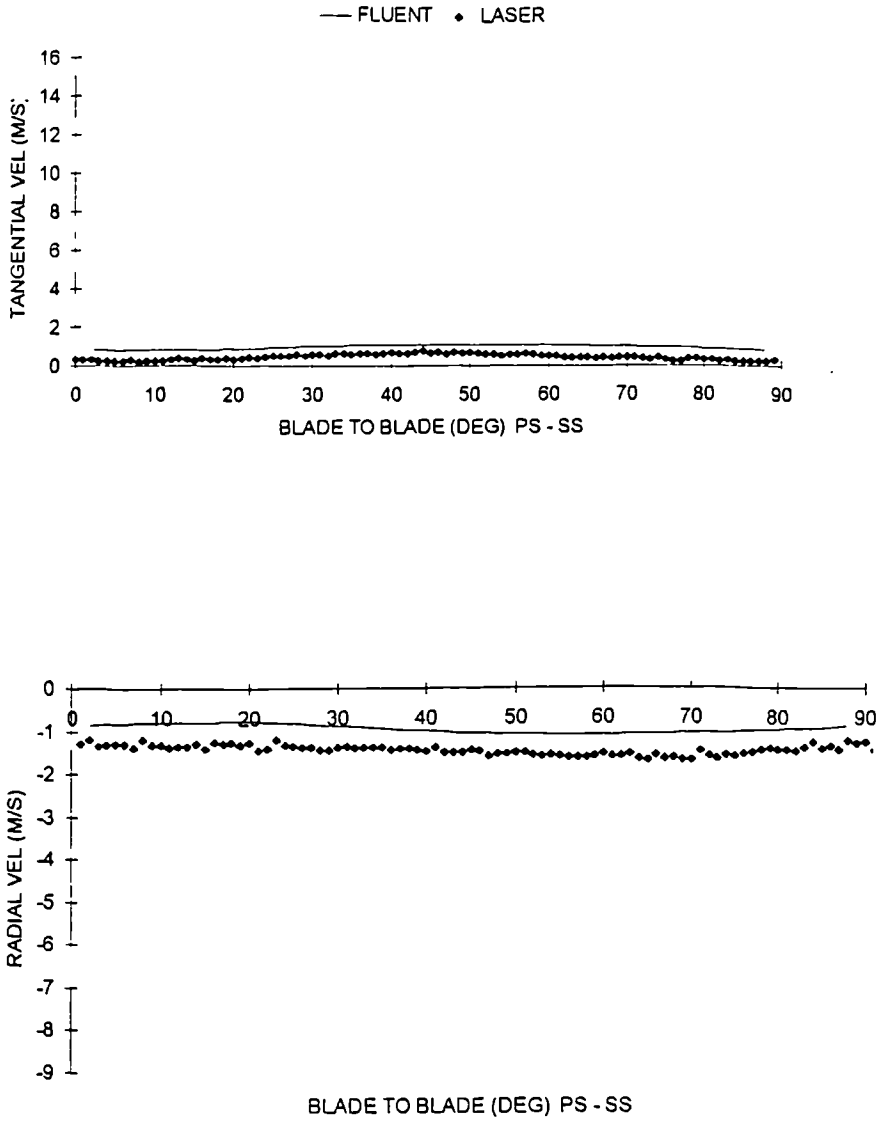

Figure 5.63 Comparison of experimental and computational velocity profiles, R = 0.226m, Window 7.

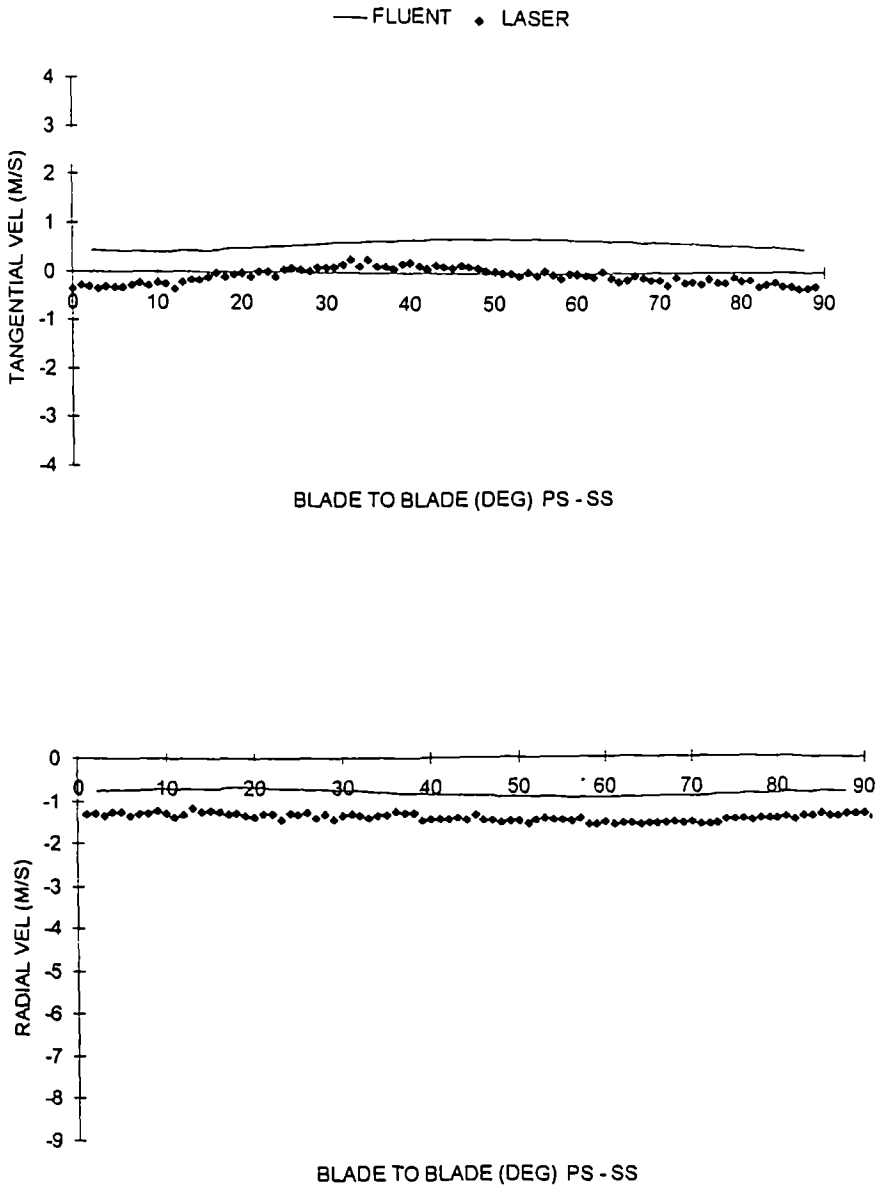

Figure 5.64 Comparison of experimental and computational velocity profiles, R = 0.236m, Window 7.

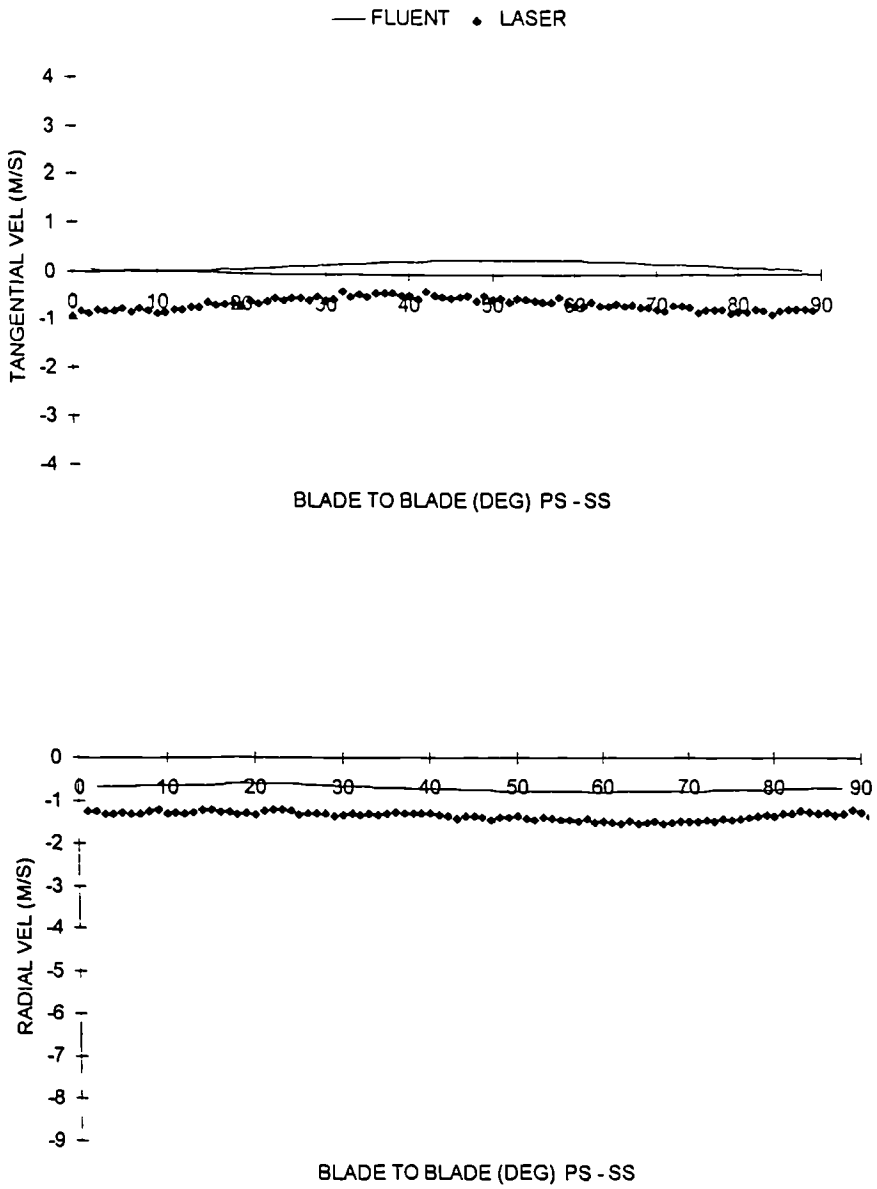

Figure 5.65 Comparison of experimental and computational velocity profiles, R = 0.246m, Window 7.

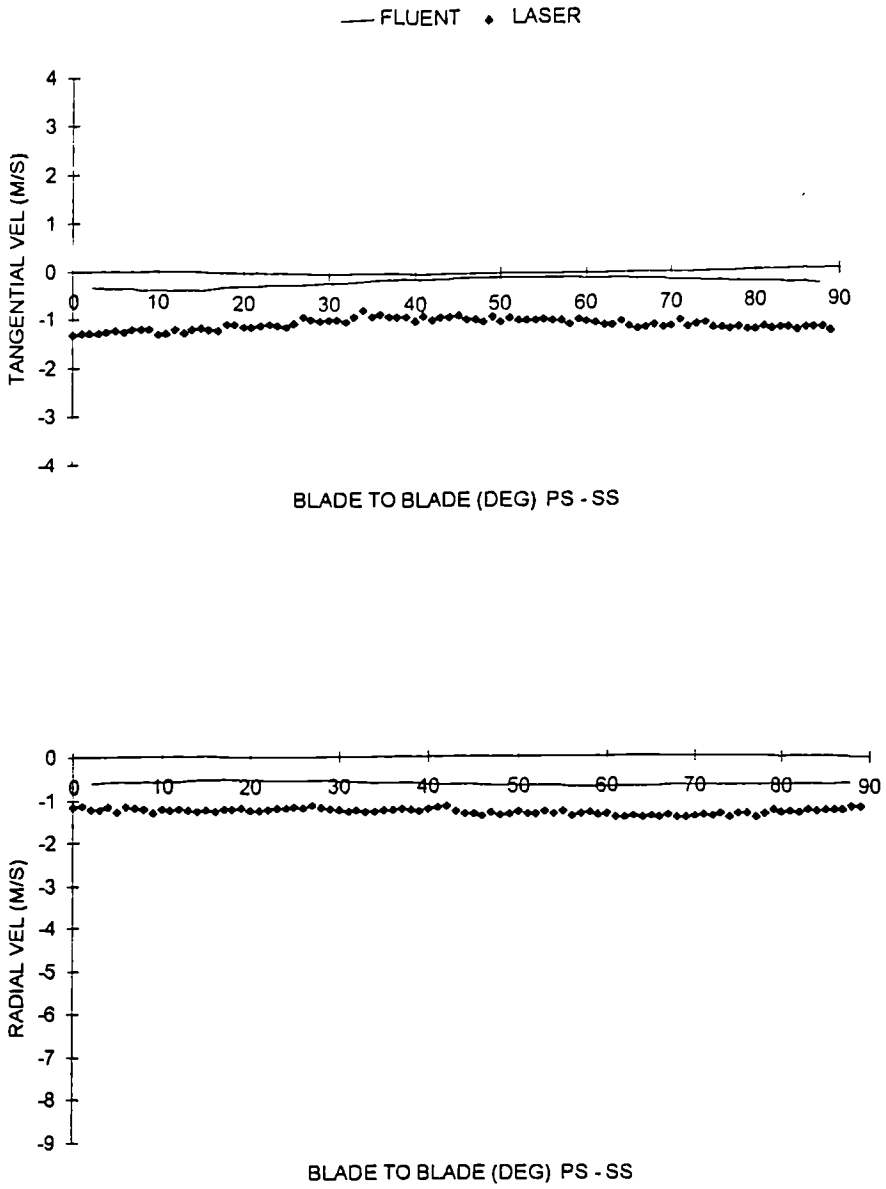

Figure 5.66 Comparison of experimental and computational velocity profiles, R = 0.256m, Window 7.

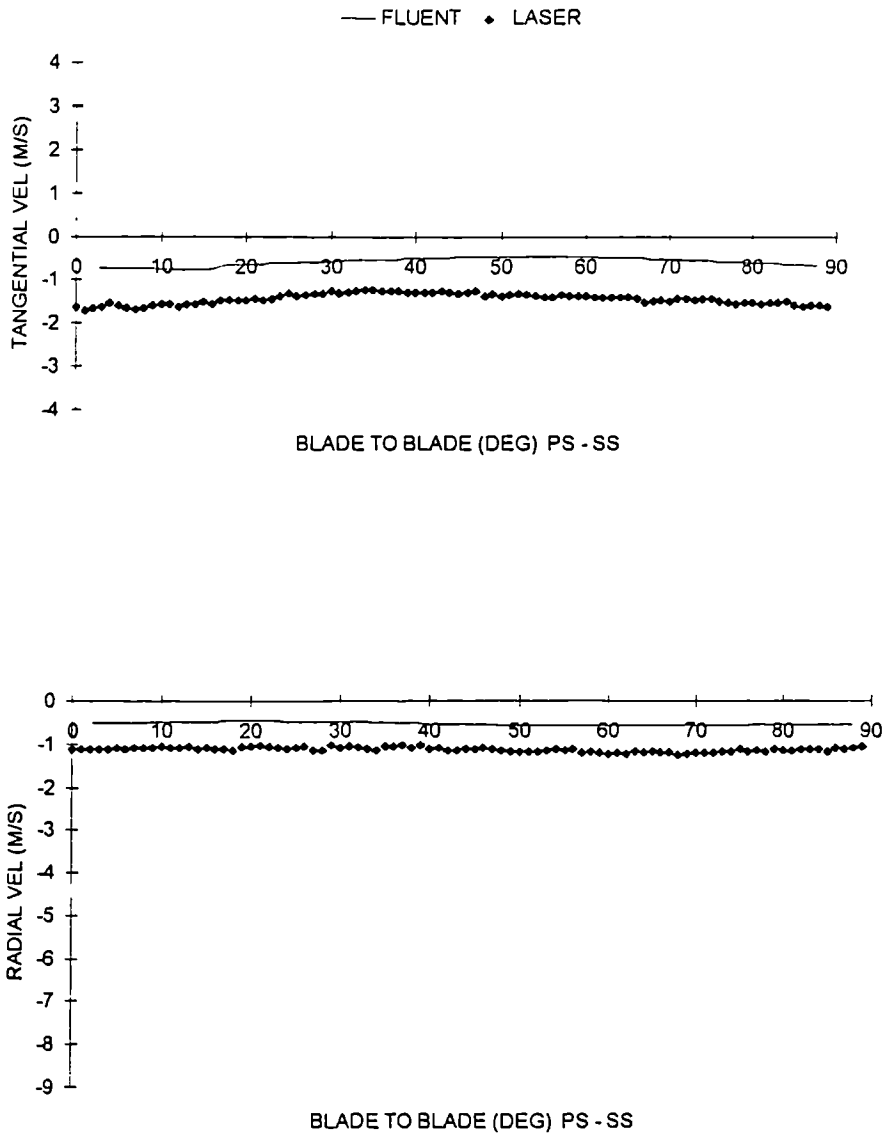

Figure 5.67 Comparison of experimental and computational velocity profiles, R = 0.266m, Window 7.

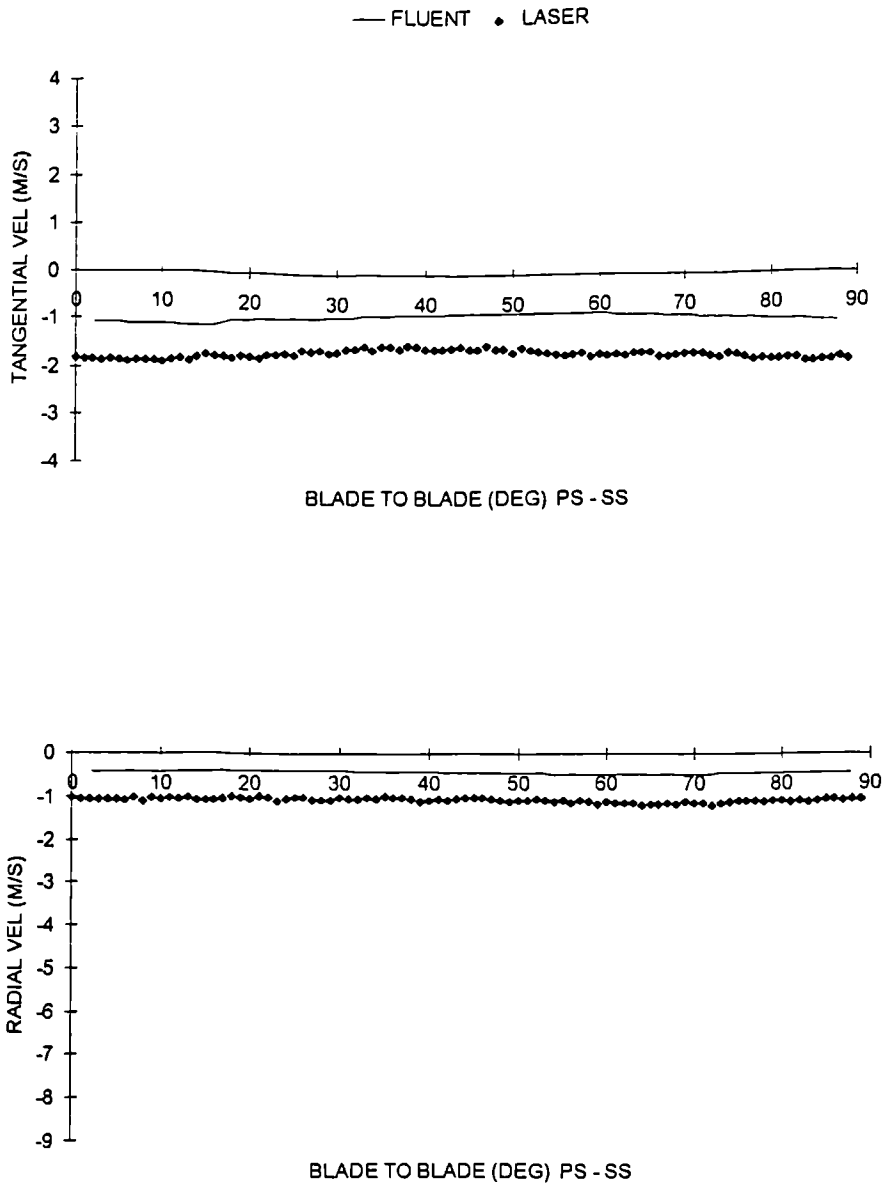

Figure 5.68 Comparison of experimental and computational velocity profiles, R = 0.276m, Window 7.

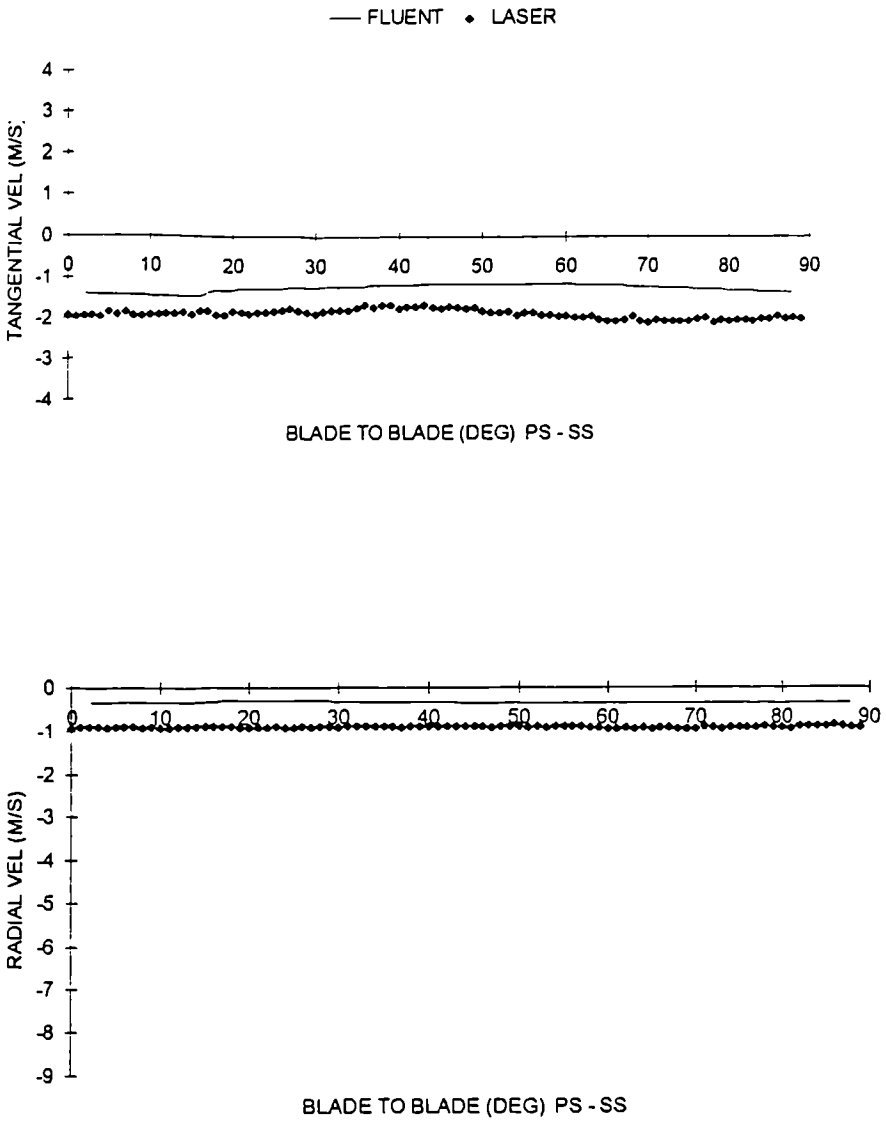

Figure 5.69 Comparison of experimental and computational velocity profiles, R = 0.286m, Window 7.

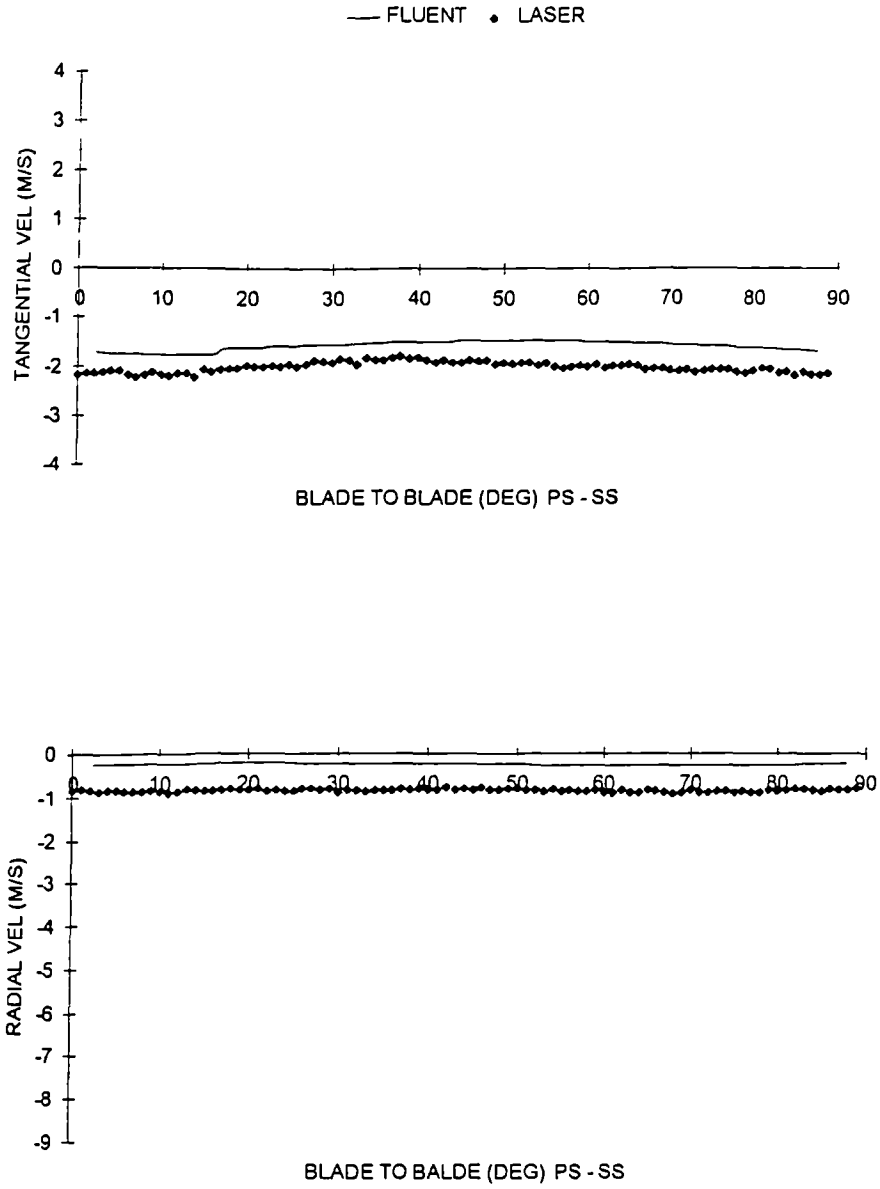

Figure 5.70 Comparison of experimental and computational velocity profiles, R = 0.296m, Window 7.

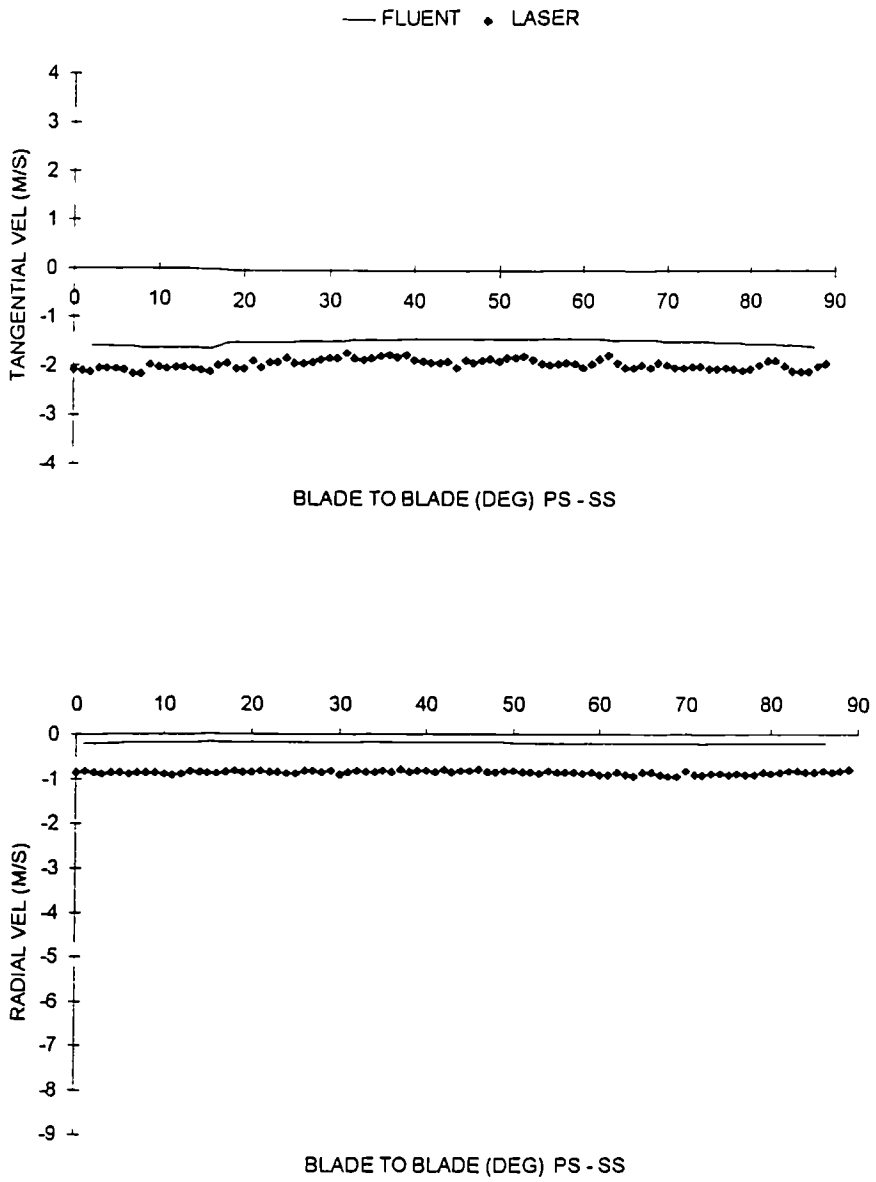

Figure 5.71 Comparison of experimental and computational velocity profiles, R = 0.306m, Window 7.

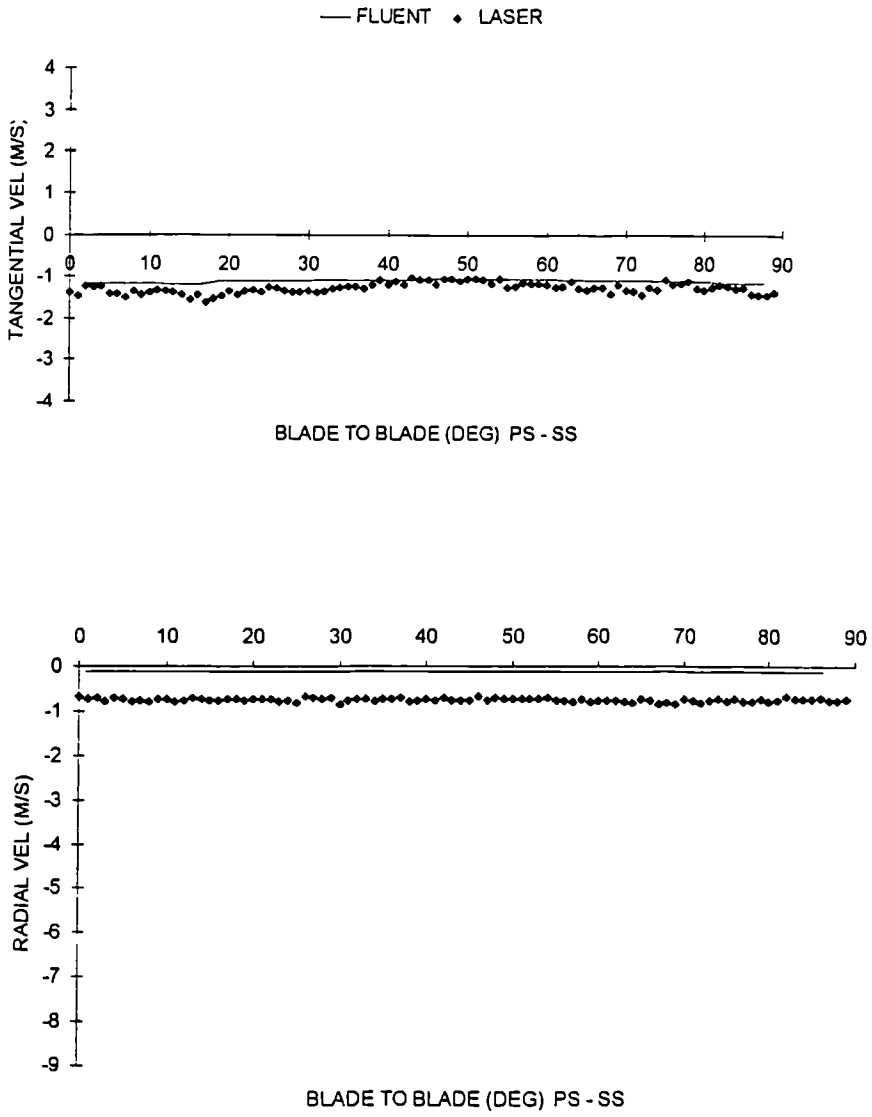

Figure 5.72 Comparison of experimental and computational velocity profiles, R = 0.316m, Window 7.

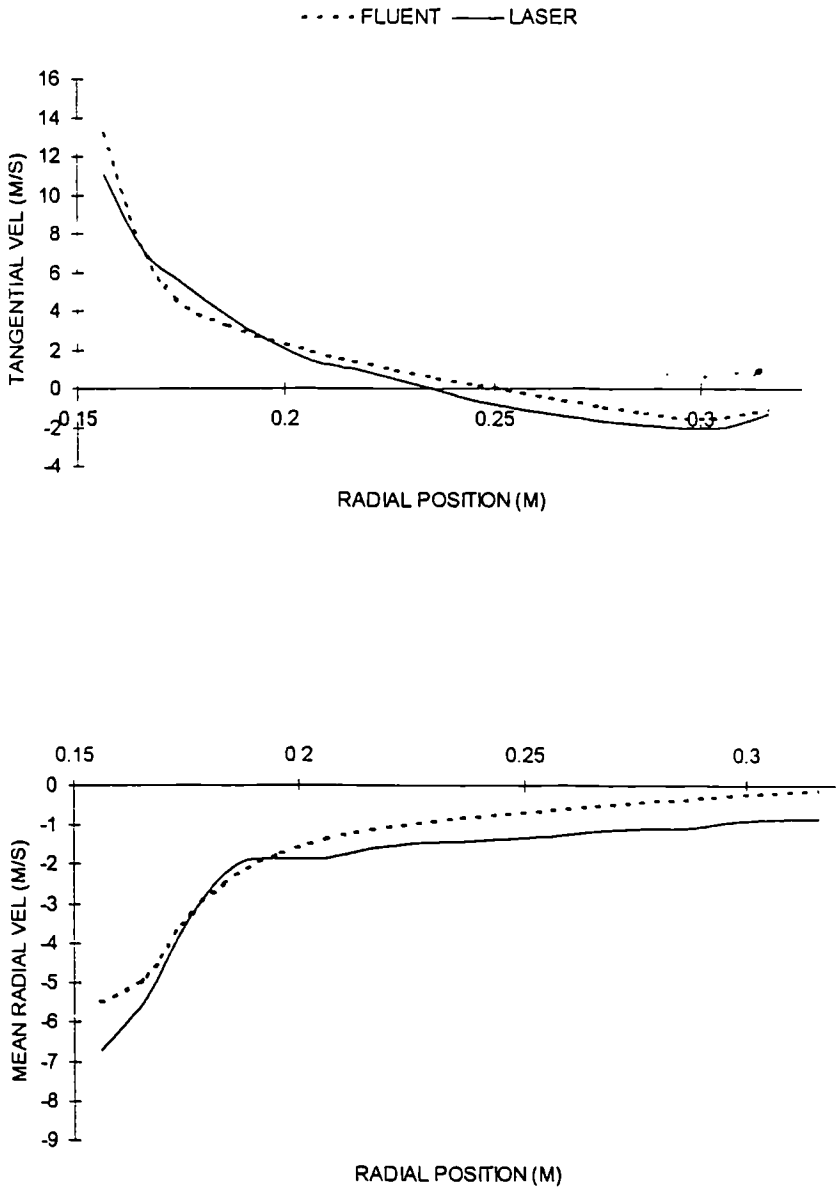

Figure 5.73 Mean Tangential and Radial Velocity Profiles Across the Volute, Window 7

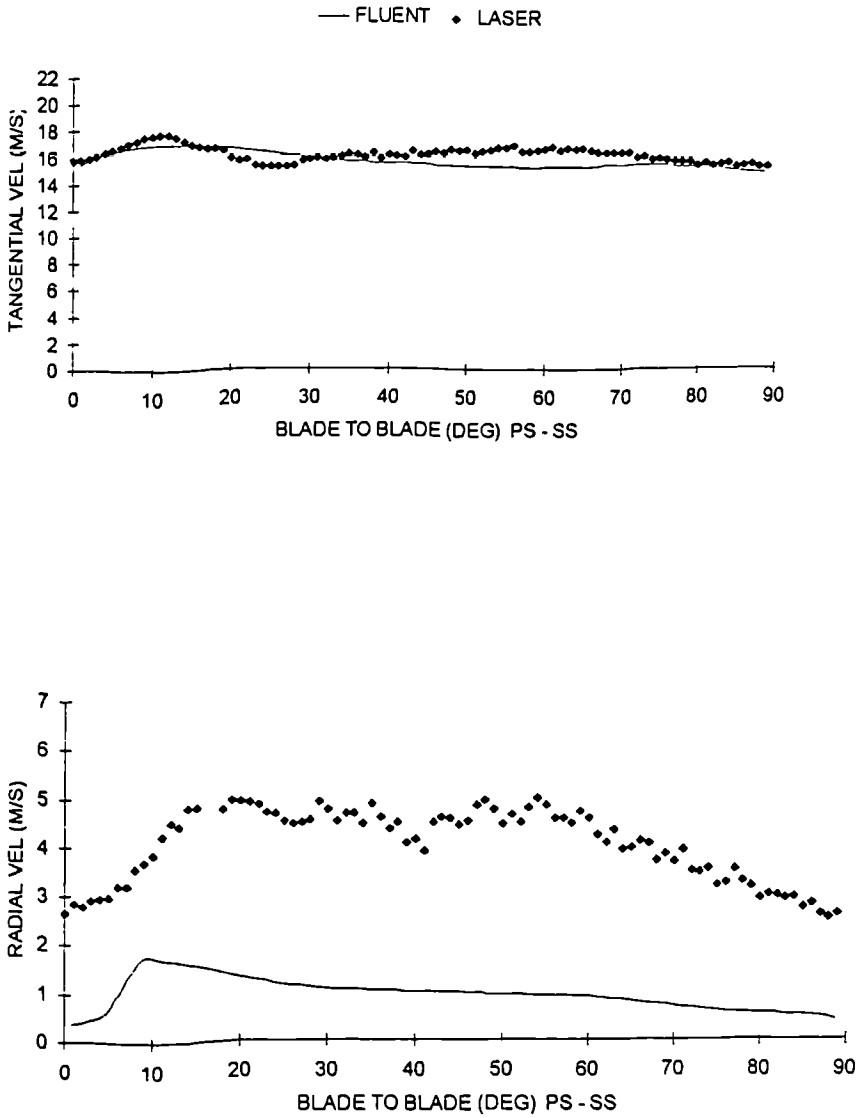

Figure 5.74 Comparison of experimental and computational velocity profiles, R = 0.156m, Window 8.

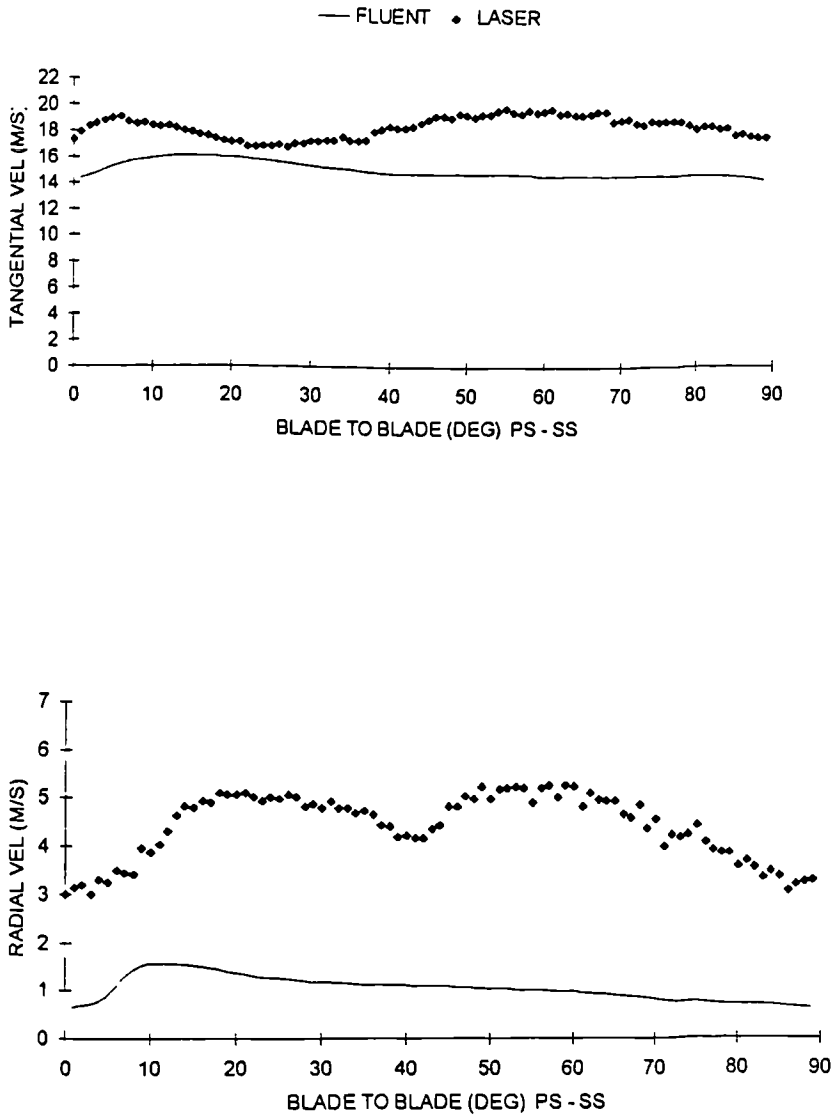

Figure 5.75 Comparison of experimental and computational velocity profiles, R = 0.160m, Window 8.

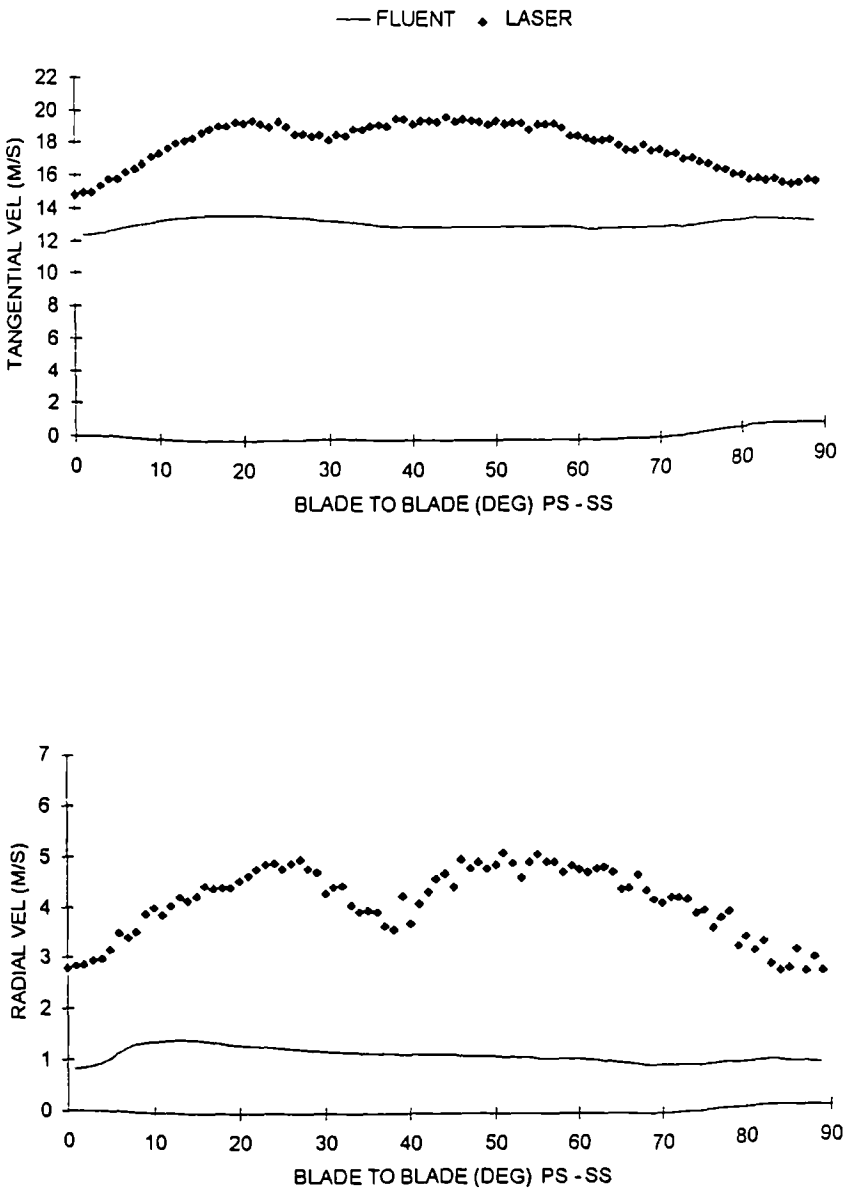

Figure 5.76 Comparison of experimental and computational velocity profiles, R = 0.164m, Window 8.

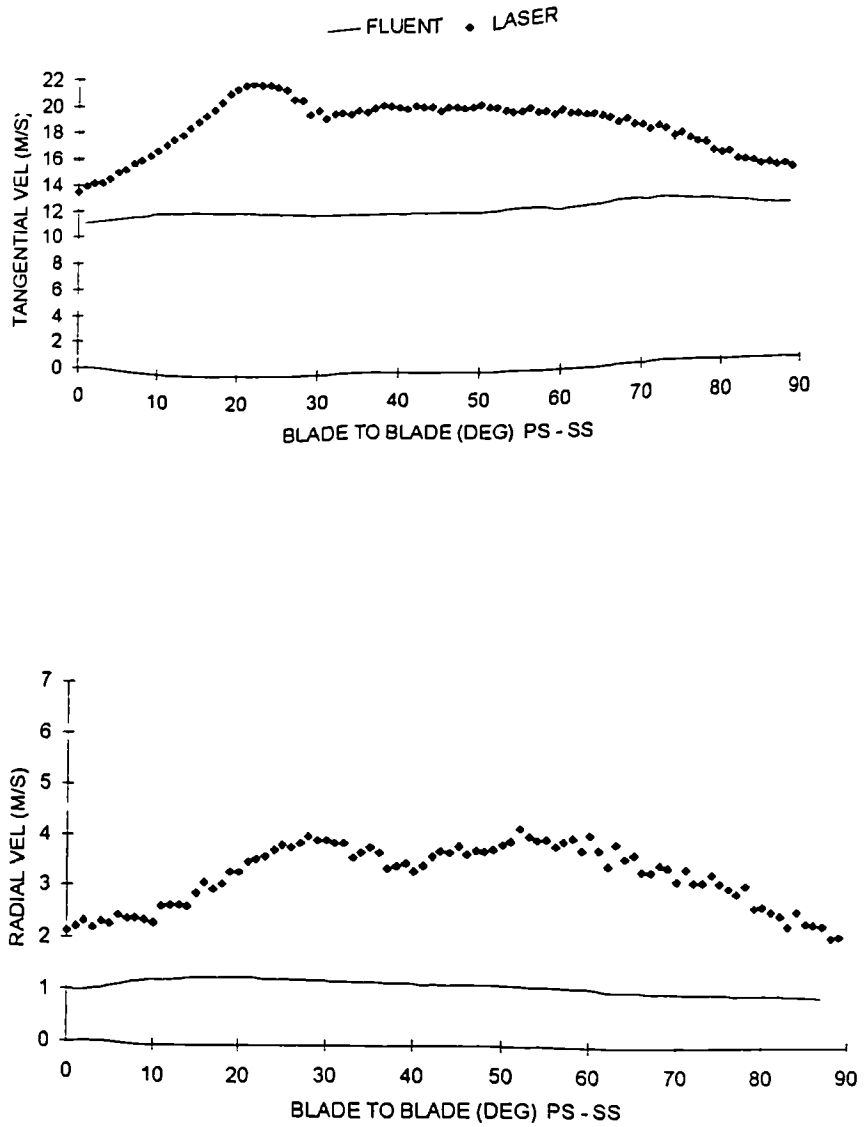

Figure 5.77 Comparison of experimental and computational velocity profiles, R = 0.168m, Window 8.

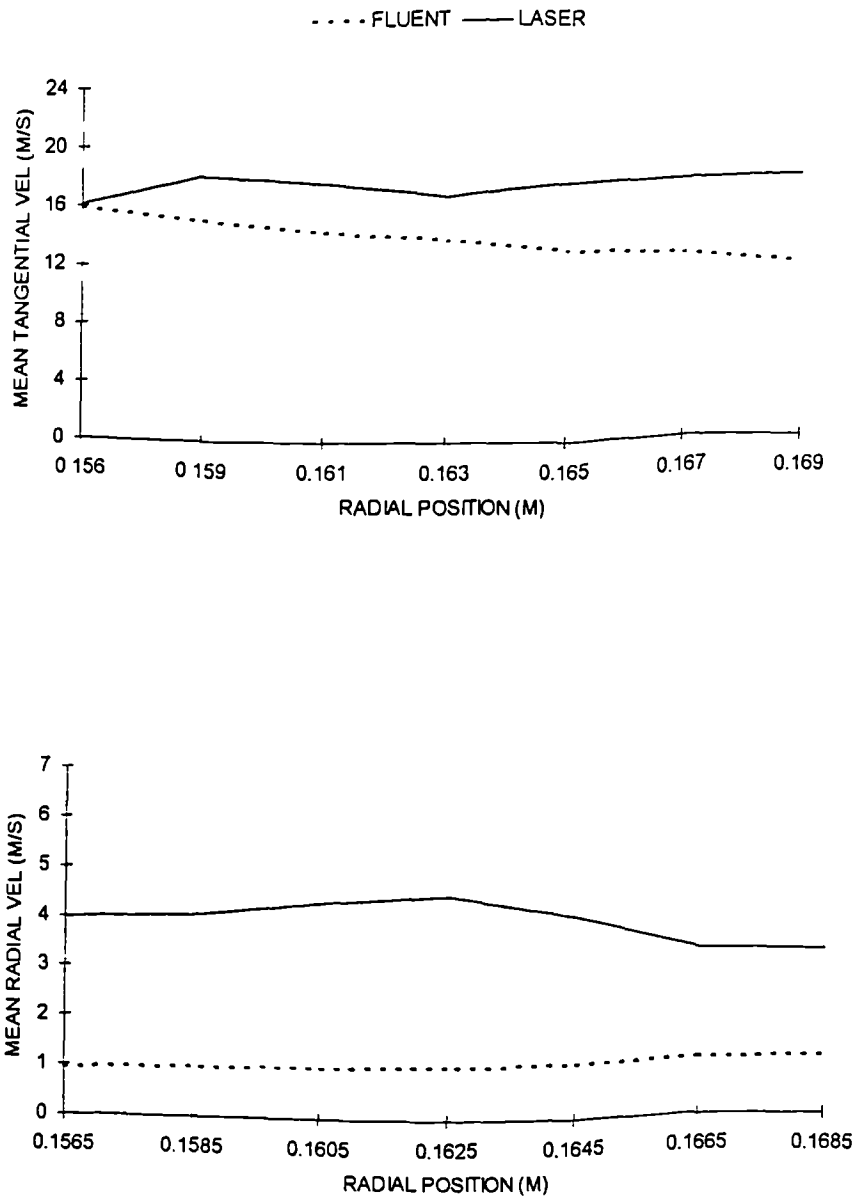

Figure 5.78 Mean Tangential and Radial Velocity Profiles Across the Volute, Window 8.

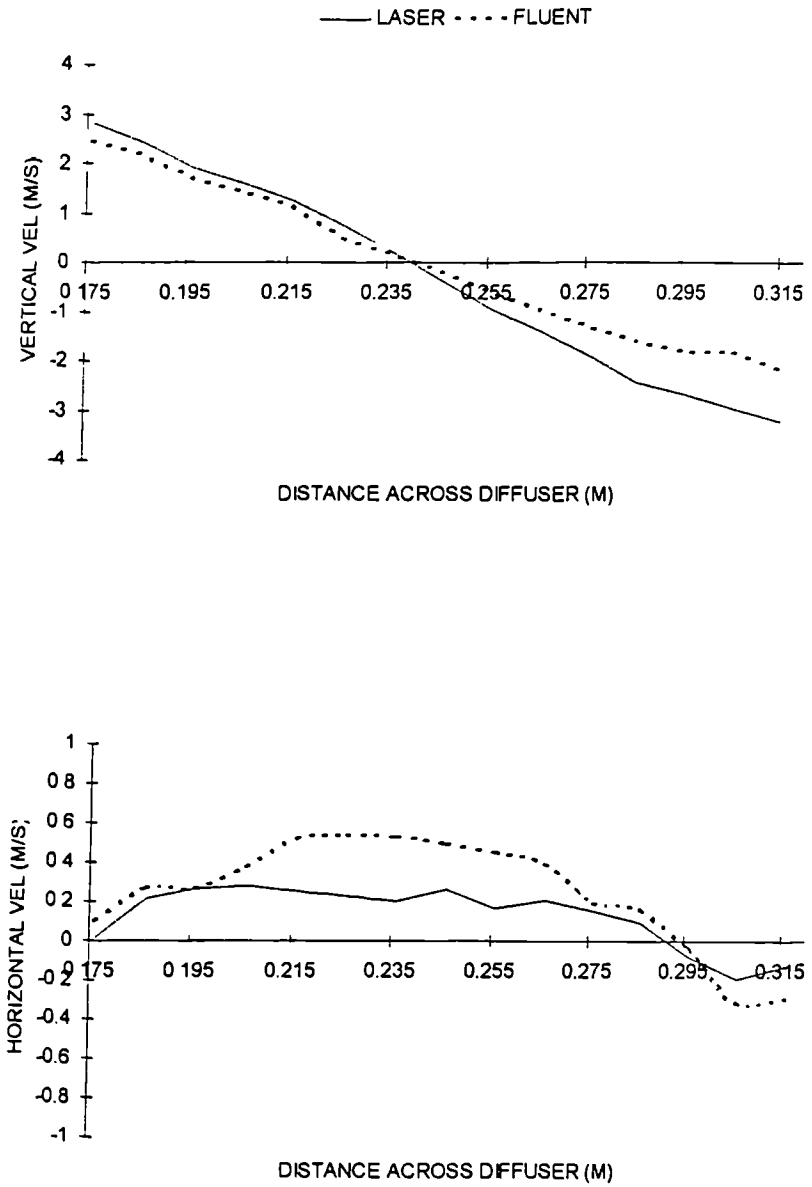

Figure 5.79 Mean Vertical and Horizontal Velocity Profiles Across Outlet Duct One.

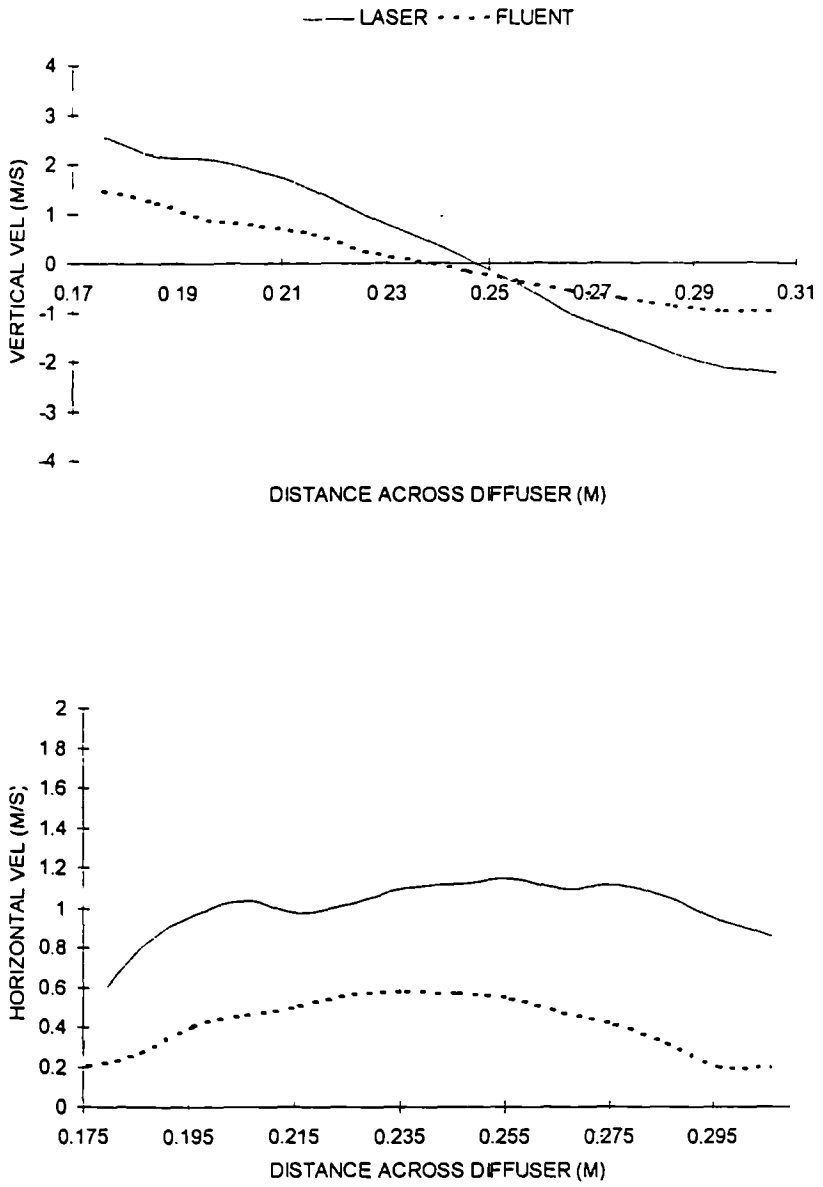

Figure 5.80 Mean Vertical and Horizontal Velocity Profiles Across Outlet Duct Two.

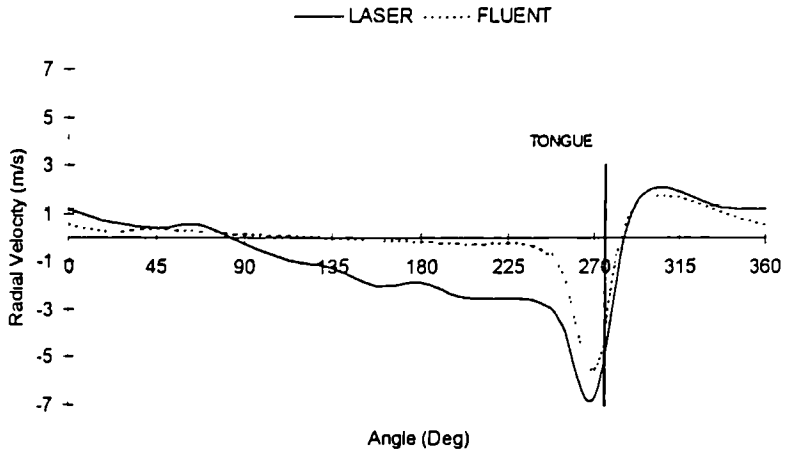

Figure 5.81 Circumferential Variation of the Mean Radial Velocity.

CHAPTER 6:
COMPARISON OF COMPUTATIONAL AND MICROPHONE RESULTS

6.1 Introduction

This chapter compares the computational results generated using Fluent with experimental data obtained using a condenser microphone. The investigation examined the unsteady, static pressure field in the volute and outlet duct of the two-dimensional centrifugal pump.

Pressure measurements were made at similar positions to those used to gather the LDA data, that is, at points radially across the volute at forty-five degree intervals. However extra points were positioned around the first ninety degrees around the volute from the tongue, as this was where the computational model predicted the biggest pressure rise. Figure 6.1 displays the location of the measurement points within the volute and outlet duct and Appendix D gives a full listing of the locations used.

The labelling of measurement positions for the pressure measurements was the same as that used for the LDA measurements, that is, each of the forty-five degree intervals were labelled as windows, with Window one at the twelve o'clock position. The experimental pressure data was obtained using static wall tappings on the volute.

Further measurements were also taken across two horizontal traverse lines within the outlet duct. All the data was collected at shut-off flow condition only.

6.2 Passage Averaged Data

As with the LDA measurements the experimental pressure data used for comparison with the computational results averaged together the phase locked average data from the individual passages. This method assumes the flow pattern for all four blade passages to be identical, thus allowing them

to be averaged. To verify this assumption an investigation was made to examine the periodic nature of the flow measured.

Figure 6.2 displays the raw pressure data for one complete revolution, that is, four periods, at Window 3, R=0.156m. Each data point represents one hundred constant phase data samples averaged together. The fake origin on the *y*-axis allows the fluctuations in the measured pressure field to be seen. These fluctuations occur within ±5% of the measured mean pressure and become unobservable when viewed on a *y*-axis with a true zero origin.

Figure 6.3 displays a comparison of the raw pressure data obtained for each individual passage together with the data averaged over the flow passages. This investigation shows that there was very little variation in the measured raw pressures from passage to passage. It would therefore be valid to assume the passage averaged data to be representative of each individual passage. This process of passage averaging is applied to all further measurements.

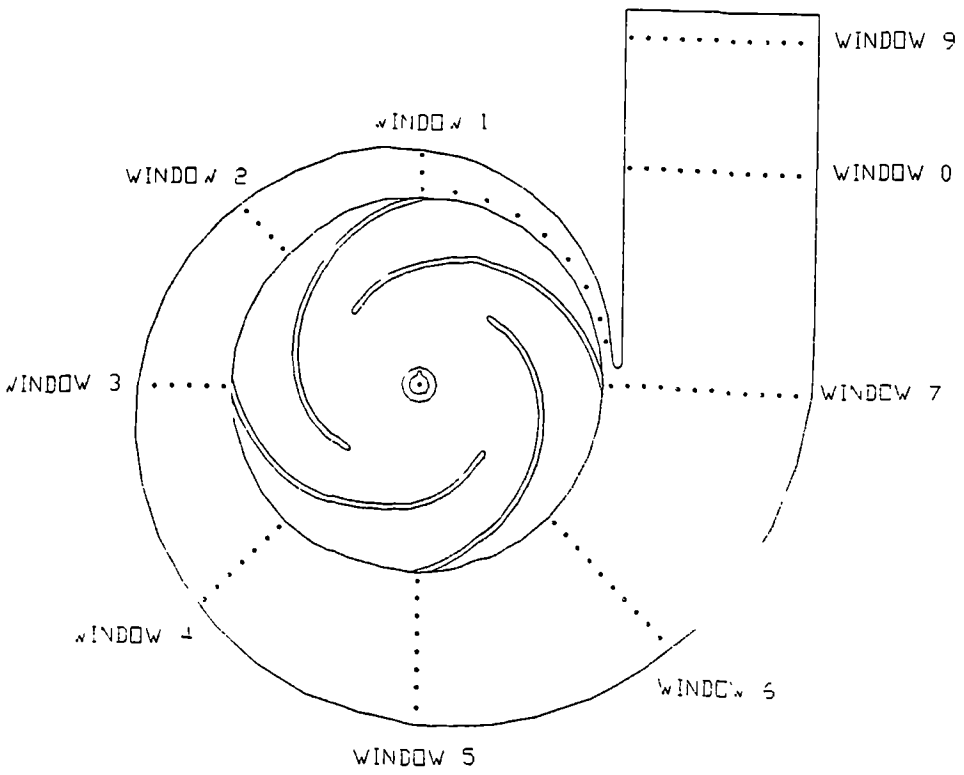

Figure 6.1 Position Used For Comparison of Pressure and Fluent Data.

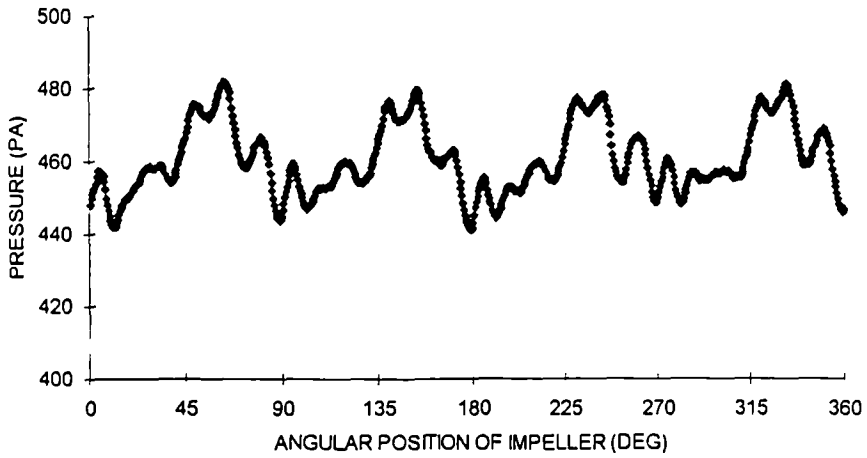

Figure 6.2 Raw Pressure Data for One Complete Impeller Revolution Window 3, R=0.156m.

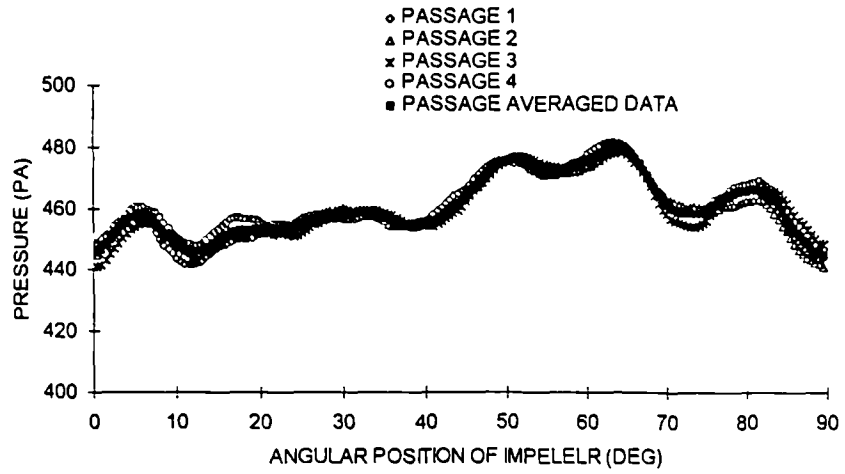

Figure 6.3 Comparison of Raw Passage Data and Data Averaged over Four Passages. Window 3, R=0.156m.

6.3 Comparisons of Pressure Distribution Around Volute At Shut-Off

To enable a realistic comparison to be made between the computational and experimental pressures, the pressure boundary at the inlet of the computational model was set at atmospheric pressure.

Figures 6.4 through 6.6 display the comparison of the experimental pressure measurements with the computational model for Window 1. The comparison at the exit of the impeller, R=0.156m displayed in Figure 6.4, shows that Fluent over predicts the experimental pressure by approximately 120Pa across most of the blade passage. This over prediction reduces at the next radial position, R=0.170m, to 100Pa and then again to 80Pa at R=0.184m.

The measured data displays a remarkably flat profile with very little time variation. This was found to be a general characteristic of the pressure measurements and is exhibited in all Windows. Fluent however, predicts a distinct increase in pressure over the central position of the passage, falling off towards the blade surfaces, see Figure 6.4.

A comparison of the time-averaged pressures across the volute passage at Window 1, Figure 6.7, shows good qualitative and quantitative agreement between the measured and predicted results. The computed mean pressure consistently over predicts the measured values by approximately 50Pa across the volute passage.

The pressure measurements made circumferentially between the tongue and Window 1 are time-averaged and displayed in Figure 6.8. This figure shows Fluent obtains both good qualitative and quantitative agreement with the experimental mean pressures at these positions. The poorest agreement was found closest to the tongue where Fluent under predicted the mean pressure by approximately 160Pa. At all other angular positions, Fluent predicted the mean pressure to within approximately ±40Pa.

An analysis of the all results shows there is very little variation in the pressure across the blade passage at each radial position. This can be clearly seen for Window 1. Therefore, only a selection of blade passage profiles together with the radial variation of the time-averaged pressure across the volute will be shown for all other Windows.

The results of the comparison between the experimental measurements and the computational model for Window 2 appear in Figure 6.9 through Figure 6.11. For this window Fluent over predicts the experimental pressure across the blade passage at all radial positions.

At R=0.156m, the impeller exit, the measurements display a virtually flat pressure profile across the blade passage. Fluent, however, shows the pressure rises near the pressure surface before falling towards the mid blade passage. This rise and fall in the pressure occurs at all the radial positions considered, however, its dominance reduces as the radial distance from the impeller exit increases.

Figure 6.11 displays the radial variation of time-averaged pressure across the volute passage for Window 2. The computed values show both qualitative and quantitative agreement with the experiment. The graph also shows a similar trend of over prediction by the computational model to that found at Window 1. Fluent over predicts the time-averaged pressure by approximately 80Pa across the volute passage for Window 2.

The measured time averaged pressures between impeller exit and volute wall display a similar pressure rise to that found in all other Windows, and is 20Pa, see Table 6.1. Fluent predicts a slightly higher pressure rise of 44Pa across the volute passage for Window 2.

Figures 6.12 through 6.15 display a selection of the comparisons made at Window 3.

The results show that the pressure distribution at Windows 3, 4, 5 and 6 are very similar with only minor differences between each Window. Therefore the following section describes the general features of both the computed and measured pressure distributions found at these positions. These features are:

◊ Negligible variation in the measured pressure from suction surface to pressure surface. This is in contrast to the computed pressure which shows a distinct rise and fall during blade passing, with the maximum value occurring at mid passage.

◊ Almost constant time averaged pressure at each window with only a slight rise between impeller exit and the volute outer wall. This small variation in the measured time-averaged pressure is correctly predicted by Fluent, see Table 6.1.

◊ The model over predicts the pressure at all radii across the volute passage. However, this over prediction is constant and within 100±20Pa of the measured value, see Table 6.2.

WINDOW	RADIAL PRESSURE RISE ACROSS VOLUTE PASSAGE (Pa)	
	FLUENT	EXPERIMENT
3	20	30
4	20	32
5	20	20
6	25	25

Table 6.1. Comparison of Experimental and Predicted Results for the Radial Pressure Rise across the Volute Passage from R=0.156m to Volute Wall.

WINDOW	FLUENT'S OVER PREDICTION OF THE PRESSURE(Pa) ACROSS VOLUTE PASSAGE
3	100
4	80
5	100
6	120

Table 6.2. Over Prediction of Mean Pressure across Volute for Increasing Circumferential Displacement.

The results of the comparison between the experimental pressure measurements and the computational model for Window 4 are displayed in Figures 6.16 through 6.20. These results exhibit the general features described previously. However, the rise in pressure across the blade passage for the model is skewed towards the pressure surface, similar to the results found in Window 2. As the radius increases, the circumferential pressure variation decays and towards the volute wall the computational model displays an almost flat pressure profile. This is clearly demonstrated in Figures 6.18 and 6.19.

The results for Window 5 are displayed in Figure 6.21 through 6.25. The results demonstrate the general flow features described above with the pressure increasing towards mid passage. However, unlike Window 4 the circumferential pressure variation does not decay noticeably with an increase in radius.

The results for Window 6, shown in Figures 6.26 through 6.29, again display some of the general features described previously. The blade to blade pressure profiles near the impeller exit are similar to those found in Window 5, with pressure rising towards the mid blade passage. However, this variation reduces significantly with an increase in radius, producing almost flat pressure profiles similar to those found in Window 4.

Figures 6.31 through 6.37 display the comparison between the experimental and predicted data for Window 7, just before the tongue. The experimental values show a flat profile across the blade passage at all radii with the computational model predicting a pressure increase towards the centre of the blade passage.

The over prediction of the experimental values by the model is clearly demonstrated in Figure 6.37, which displays the time-averaged results. However, both experimental and computed data for Window 7 differ from those found in previous Windows, having significantly lower pressure at the impeller exit than that found over the rest of the volute passage.
This low pressure results in a greater overall increase in pressure rise from impeller exit to volute wall, with the experimental data producing 77Pa rise and Fluent predicting a 100Pa rise.

Despite this, Fluent did produce very good qualitative agreement with the experimental time-averaged values for all radii, with an over prediction of the experimental values of 140Pa.

6.4 Comparisons of Pressure Distribution In Outlet Duct at Shut-Off

The results for Windows 0 and 9, positioned in the outlet duct, are displayed in Figures 6.38 and 6.39 respectively. The graphs for these windows, show that both the computational model and the experimental measurements give a flat pressure profile across the outlet duct.

The results show Fluent obtained good qualitative agreement with the experimental data. However, as with all other comparisons made, Fluent over predicted the pressure. This over prediction was approximately 140Pa for both Windows 0 and 9.

6.5 Circumferential Pressure Distribution Around Impeller at Shut-Off

The circumferential time-averaged pressure around the volute of the centrifugal pump at R=0.156m is shown in Figure 6.40. The predicted

values show good qualitative agreement around the volute, to within 120Pa of the experimental data at all positions.

The poorest agreement between the model and the experimental rig occurs near the tongue. At this position Fluent over predicted the pressure at the exit of the volute and then under predicted the drop in pressure after the tongue.

6.6 Summary

Fluent was able to produce good qualitative agreement with the measured unsteady pressures for both the blade to blade profiles and the time-averaged pressures across the volute passage.

Although variations existed between the computed and measured pressures around the volute, certain general features were constant. These were as follows:

- ◊ Small variation in pressure across the blade passage for the measured values. This was in contrast to the distinct pressure rise which occurred for the predicted values.
- ◊ Small radial variation in pressure was found for both the predicted and measured values. This radial variation was of the order of 20-30Pa for most Windows.
- ◊ Fluent consistently over predicted the measured pressure for both the blade to blade and time-averaged profiles. The largest over prediction for the time-averaged values occurred at Windows 7, 0 and 9. Here Fluent over predicted the overall pressure increase by approximately 26%.

Iversen(1960) found a similar pressure distribution to that shown in Figure 6.40 for the time averaged circumferential pressure. Iversen's experimental study found, at shut-off, the pressure increased steadily around the volute before dropping sharply at the tongue. The same circumferential pressure

variation was found here and demonstrates the diffuser like action of the volute.

The time-averaged pressure data show only a small radial pressure gradient exists across each window. Previous studies made of annular viscometer like geometries have shown the existence of a significant radial pressure gradient and it was originally believed a similar pressure gradient would occur in the volute at shut-off conditions, as suggested by Frost and Nilsen(1991). This, however, has been shown not to be the case, at any rate for the present, constant axial width volute geometry.

Further evidence to substantiate the non existence of radial pressure gradient is offered by Worster(1963). The measurements made by Worster showed the pressure across the volute throat to be constant at shut-off conditions. This is clearly demonstrated in Figure 6.37 which shows the mean pressure near the volute throat, at Window 7.

Worster(1963) also stated that 20% of the overall measured pressure rise at shut-off was generated by the volute. Table 6.3 presents a simple analysis of both the measured and predicted pressures in the pump at shut-off. Both sets of results produce a higher percentage pressure rise within the volute than that found by Worster. However, this could be attributed to the differing geometry of the pump.

	FLUENT		EXPERIMENT	
	ACTUAL PRESSURE (PA)	PERCENTAGE OF TOTAL PRESSURE (%)	ACTUAL PRESSURE (PA)	PERCENTAGE OF TOTAL PRESSURE (%)
IMPELLER	421	63.8	375	71.5
VOLUTE	239	36.2	150	28.5
TOTAL	660		525	

Table 6.3 Distribution of Pressures within the Pump at Shut-Off.

The results do show that Fluent over predicts the contribution of the volute to the overall pressure rise.

The two major discrepancies between Fluent and the experimental data are:

◊ Over prediction of pressures at all positions.

◊ Distinct rise and fall of pressure across blade passage.

It is safe to assume the reason for the over prediction of the pressure is linked to the rise and fall of the blade to blade pressure. A closer agreement therefore could be obtained if a flatter pressure profile across the blade passage was predicted.

There are many factors that could attribute to Fluent's inability to predict the blade to blade pressure distribution, such as the turbulence model and the application of first order schemes, discussed in Chapter 3. However, to determine the exact reasons would require an analysis of both the velocity and pressure data together. This analysis is performed in Chapter 7.

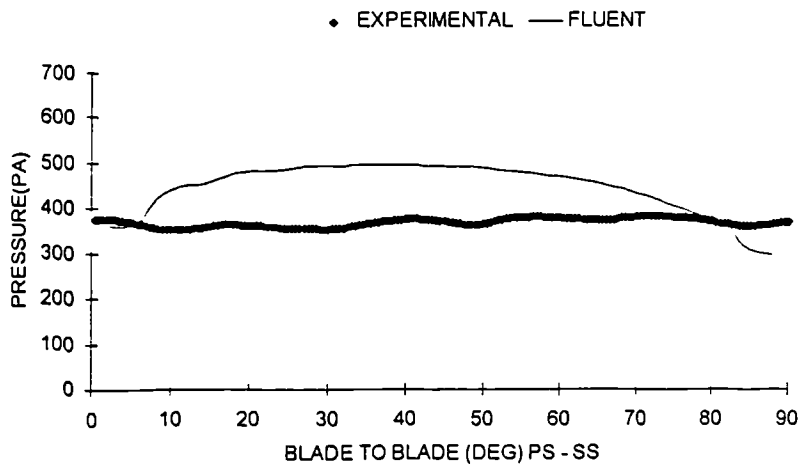

Figure 6.4. Comparison of experimental and computational pressure profiles R=0.156m, Window 1.

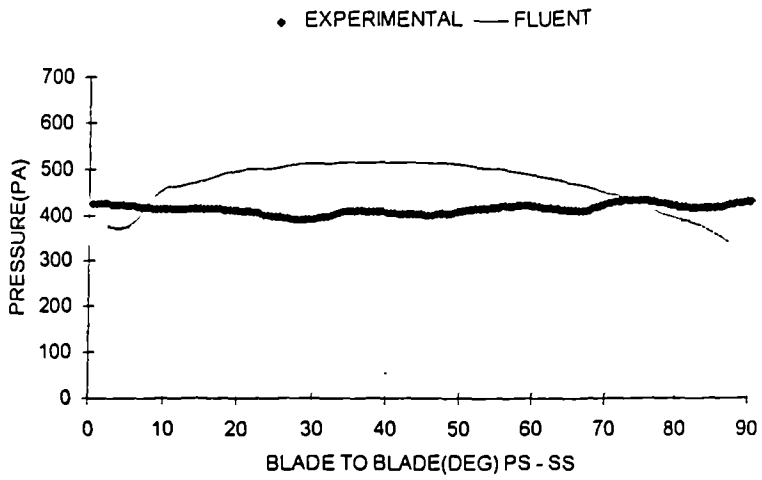

Figure 6.5. Comparison of experimental and computational pressure profiles R=0.170m, Window 1.

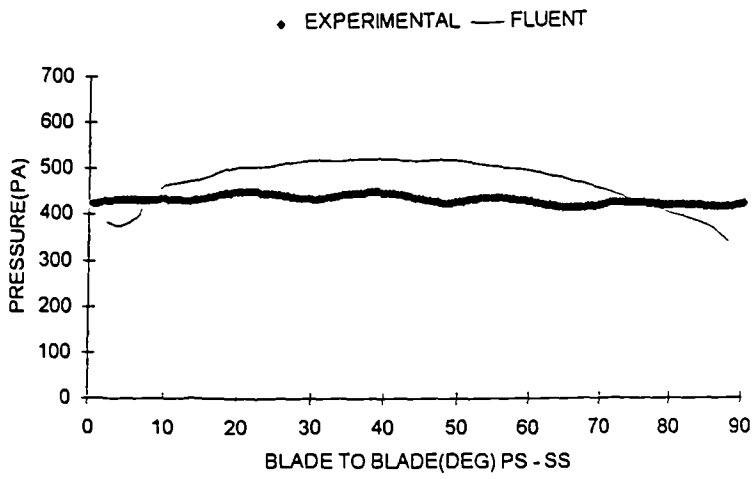

Figure 6.6. Comparison of experimental and computational pressure profiles R=0.184m, Window 1.

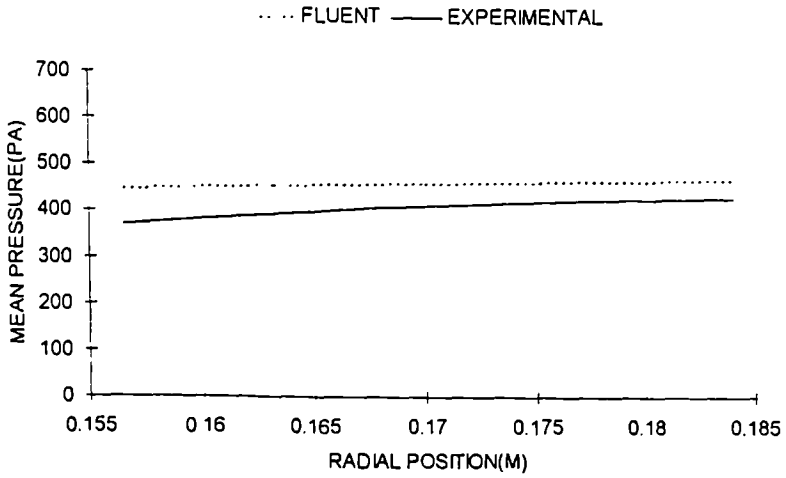

Figure 6.7 Comparison of Mean Pressure Profiles across the Volute, Window 1.

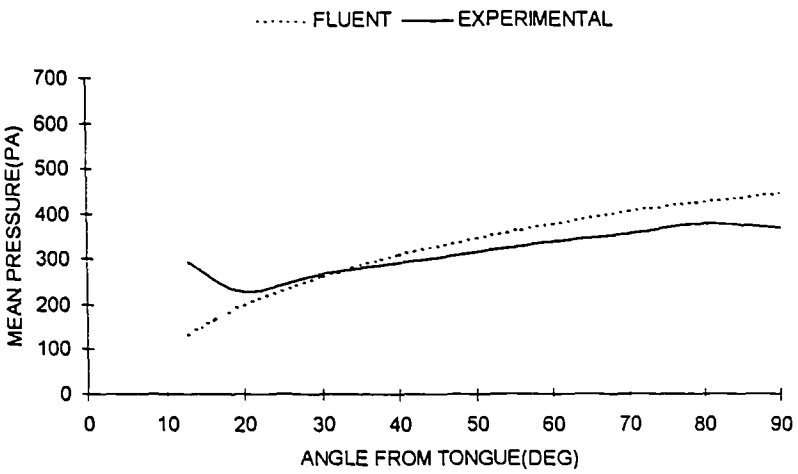

Figure 6.8 Comparison of Mean Pressure Profiles from the Tongue to Window 1, R=0.1565m.

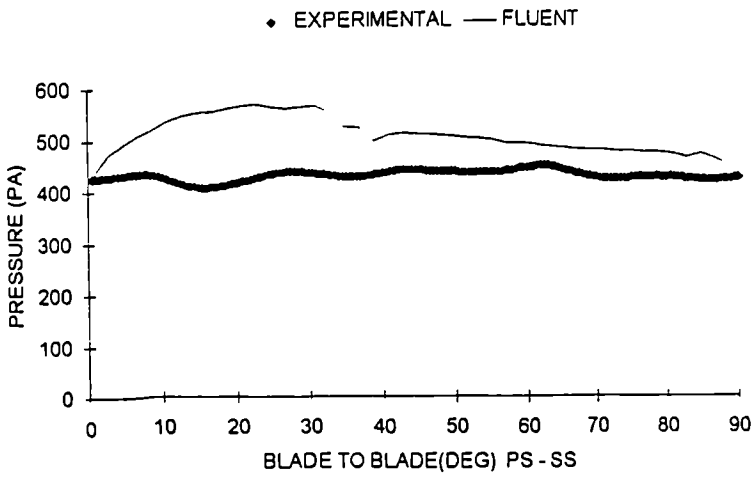

Figure 6.9 Comparison of experimental and computational pressure profiles R=0.156m, Window 2.

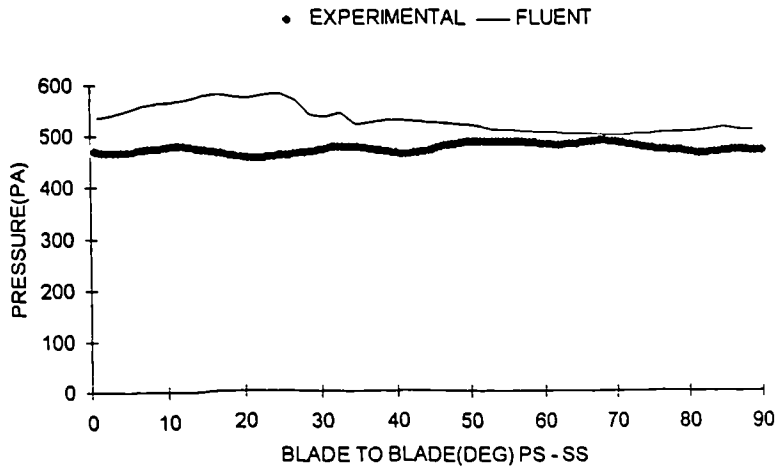

Figure 6.10 Comparison of experimental and computational pressure profiles R=0.197m, Window 2.

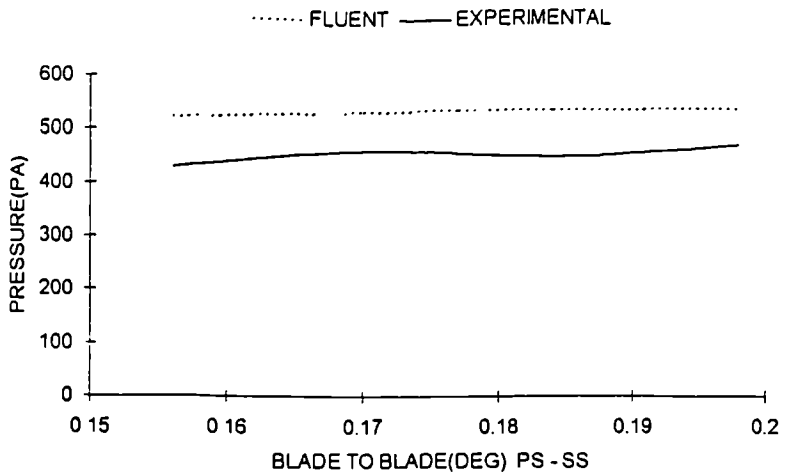

Figure 6.11 Comparison of Mean Pressure Profiles across the Volute, Window 2.

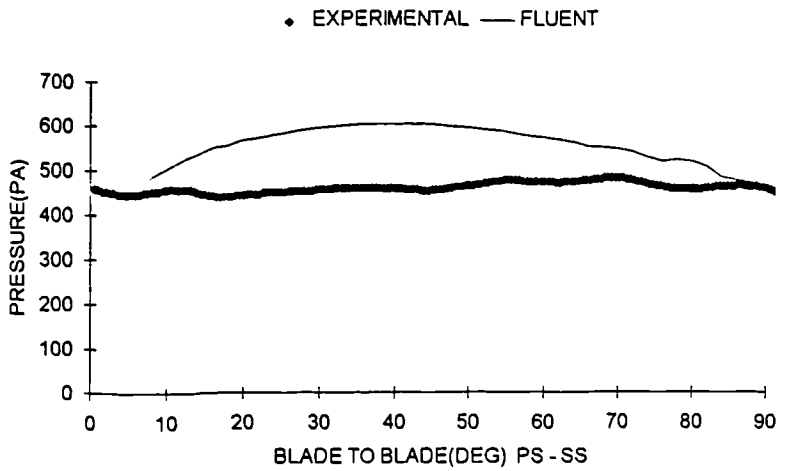

Figure 6.12 Comparison of experimental and computational pressure profiles R=0.156m, Window 3.

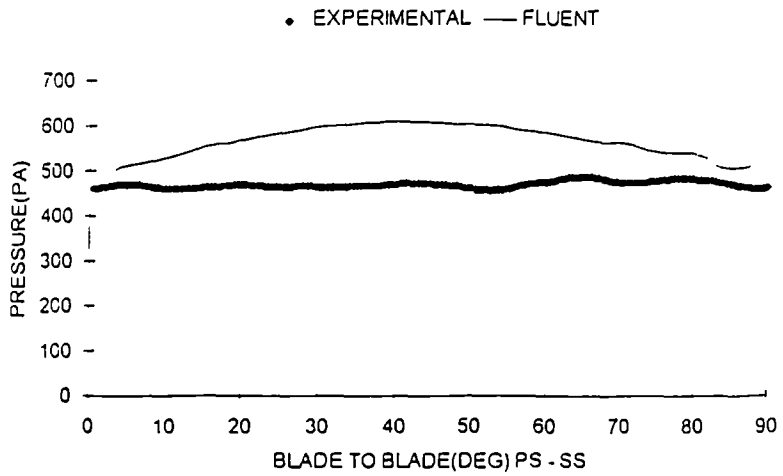

Figure 6.13 Comparison of experimental and computational pressure profiles R=0.184m, Window 3.

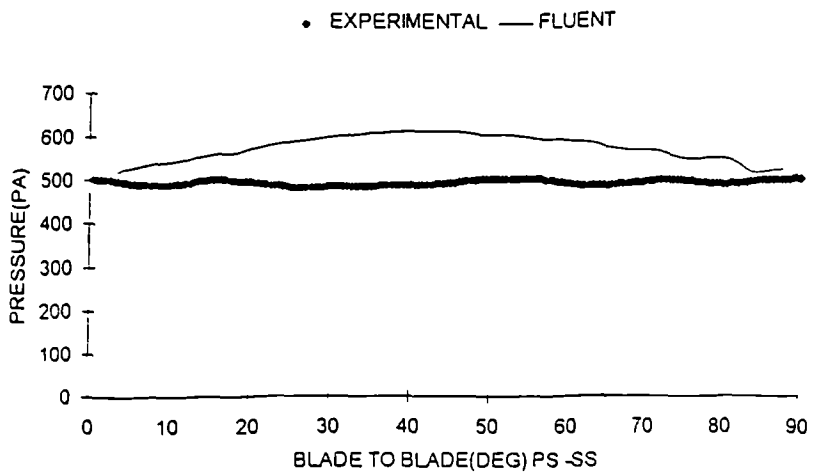

Figure 6.14 Comparison of experimental and computational pressure profiles R=0.212m, Window 3.

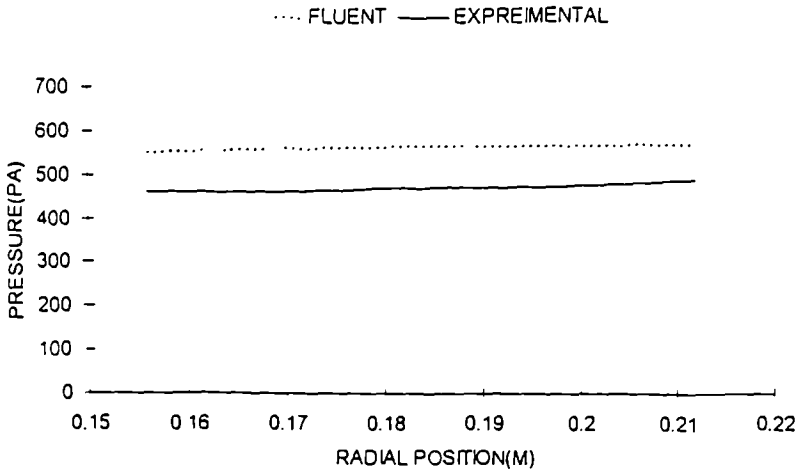

Figure 6.15 Comparison of Mean Pressure Profiles across the Volute, Window 3.

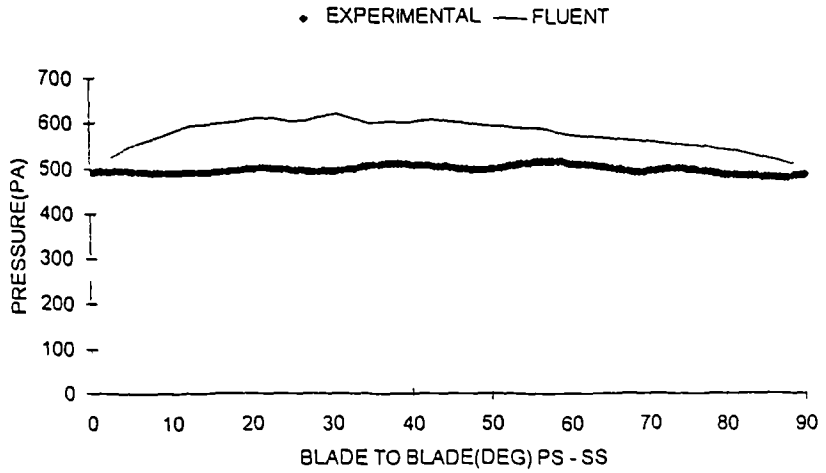

Figure 6.16 Comparison of experimental and computational pressure profiles R=0.156m, Window 4.

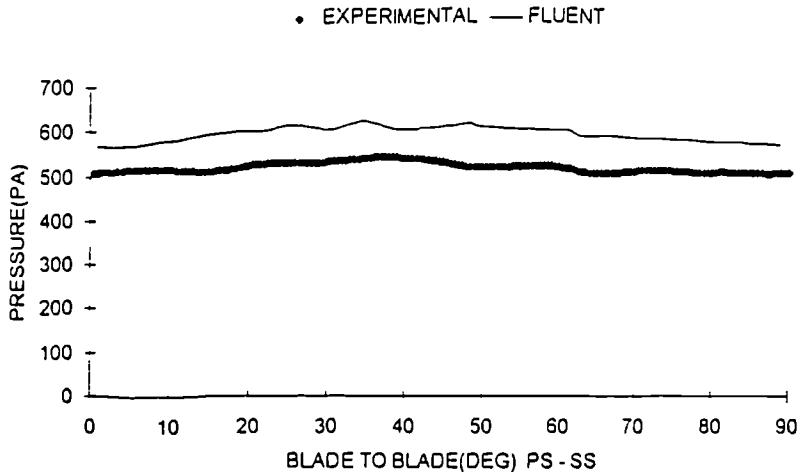

Figure 6.17 Comparison of experimental and computational pressure profiles R=0.184m, Window 4.

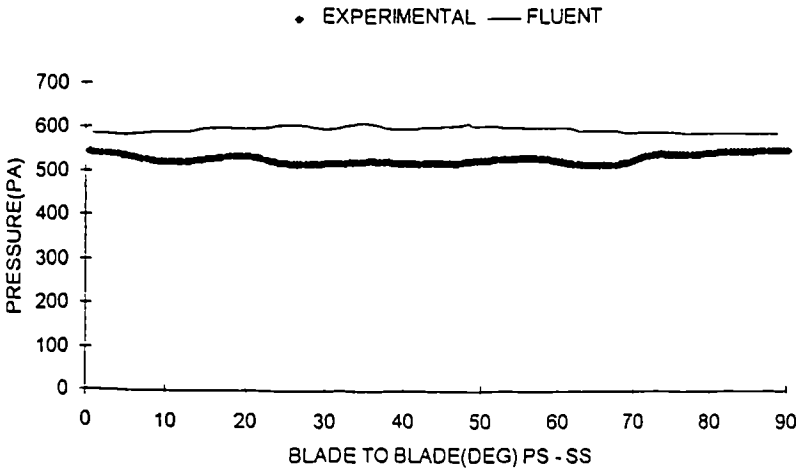

Figure 6.18 Comparison of experimental and computational pressure profiles R=0.212m, Window 4.

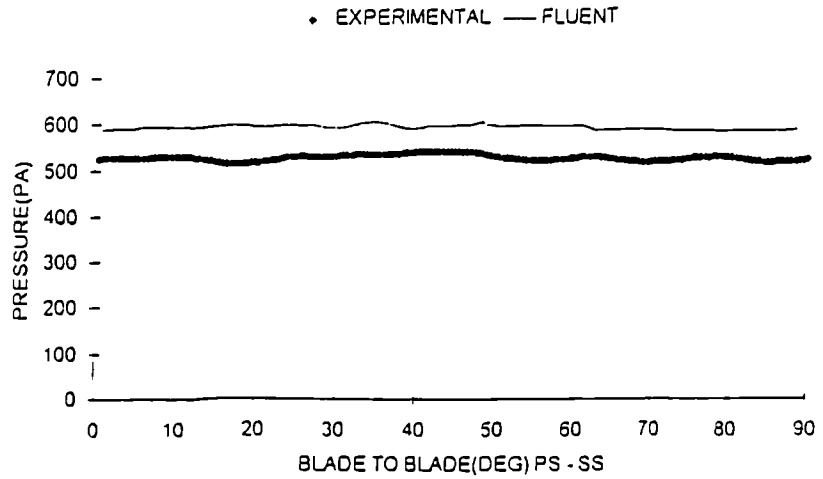

Figure 6.19 Comparison of experimental and computational pressure profiles R=0.240m, Window 4.

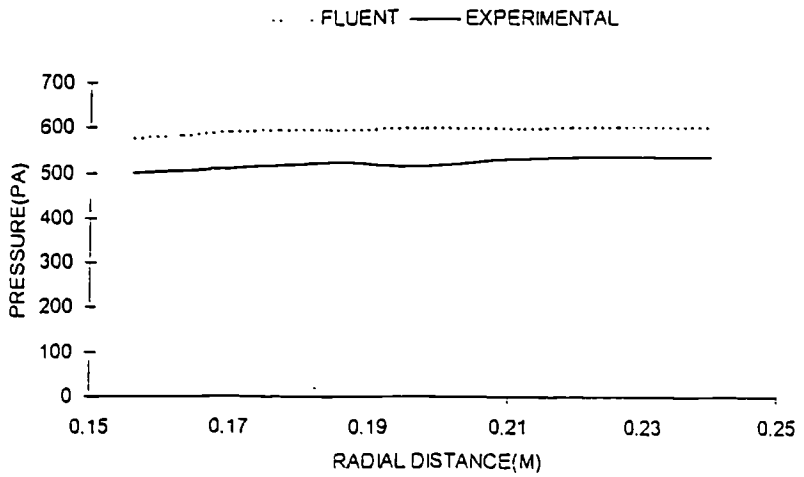

Figure 6.20 Comparison of Mean Pressure Profiles Across the Volute, Window 4.

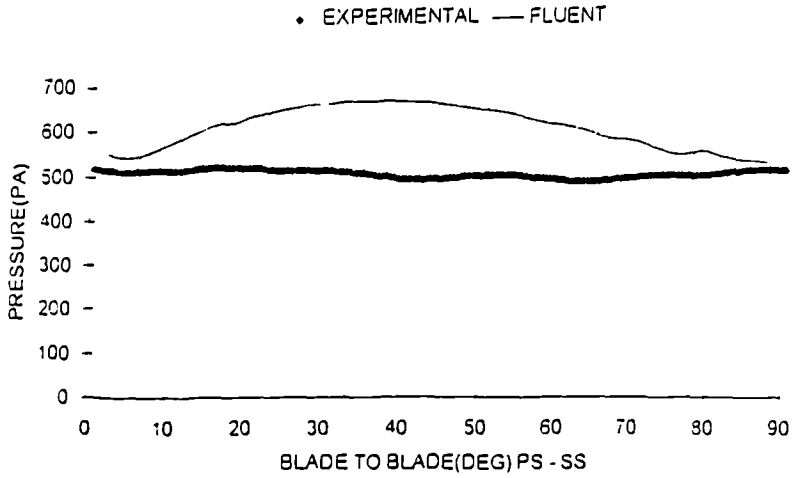

Figure 6 21 Comparison of experimental and computational pressure profiles R=0.170m, Window 5.

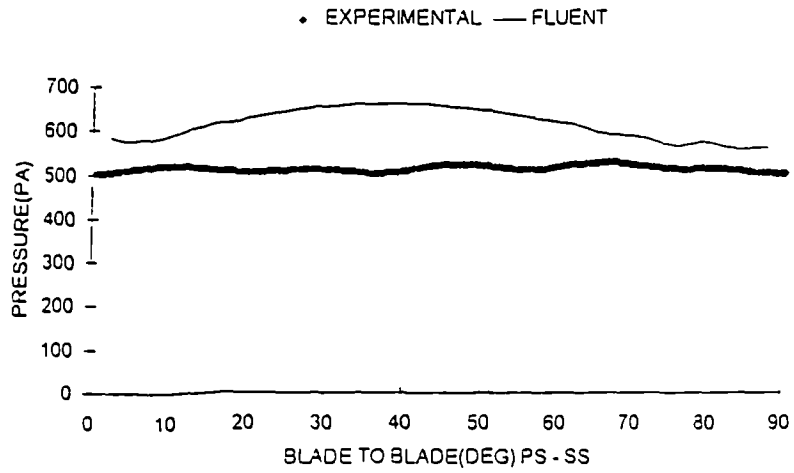

Figure 6.22 Comparison of experimental and computational pressure profiles R=0.198m, Window 5.

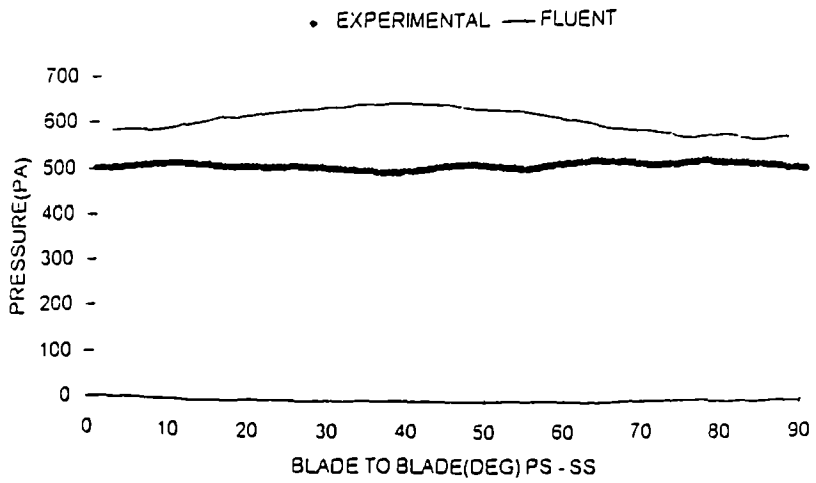

Figure 6.23 Comparison of experimental and computational pressure profiles R=0.226m, Window 5.

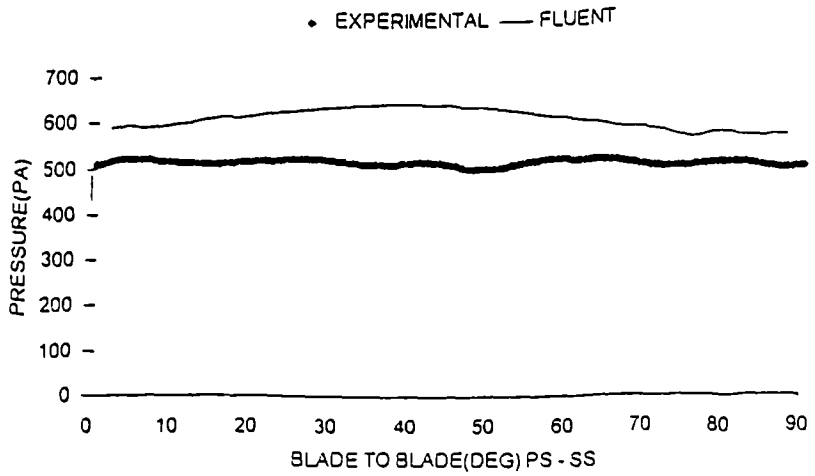

Figure 6.24 Comparison of experimental and computational pressure profiles R=0.254m, Window 5.

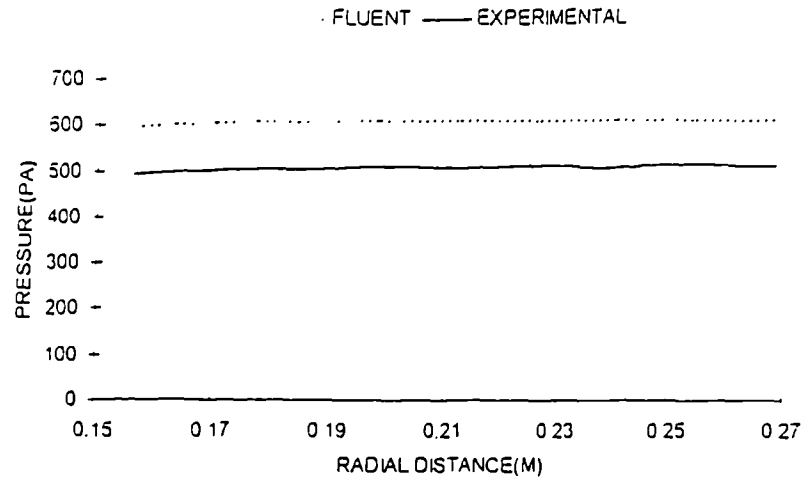

Figure 6 25 Comparison of Mean Pressure Profiles across the Volute, Window 5.

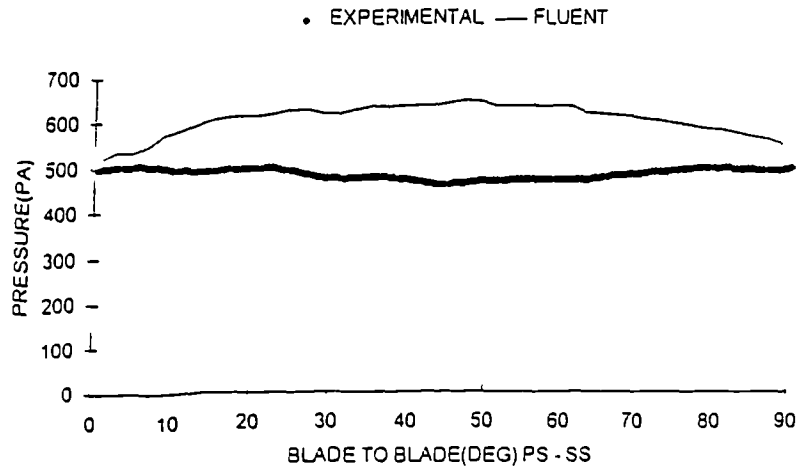

Figure 6.26 Comparison of experimental and computational pressure profiles R=0.156m, Window 6.

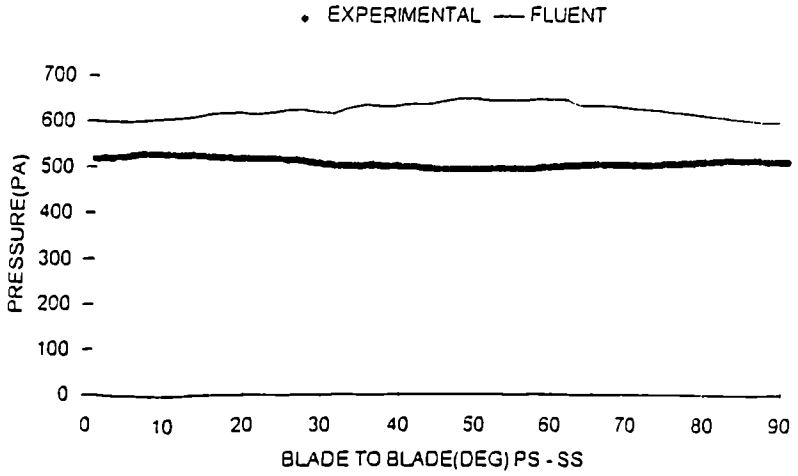

Figure 6.27 Comparison of experimental and computational pressure profiles R=0.184m, Window 6.

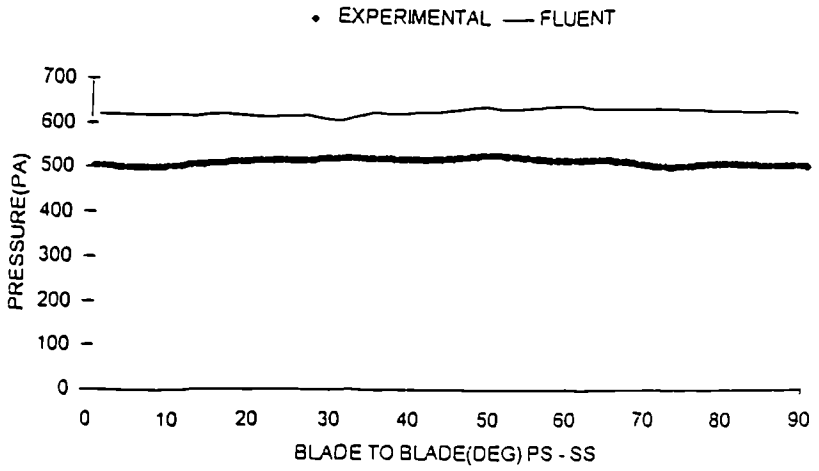

Figure 6.28 Comparison of experimental and computational pressure profiles R=0.212m, Window 6.

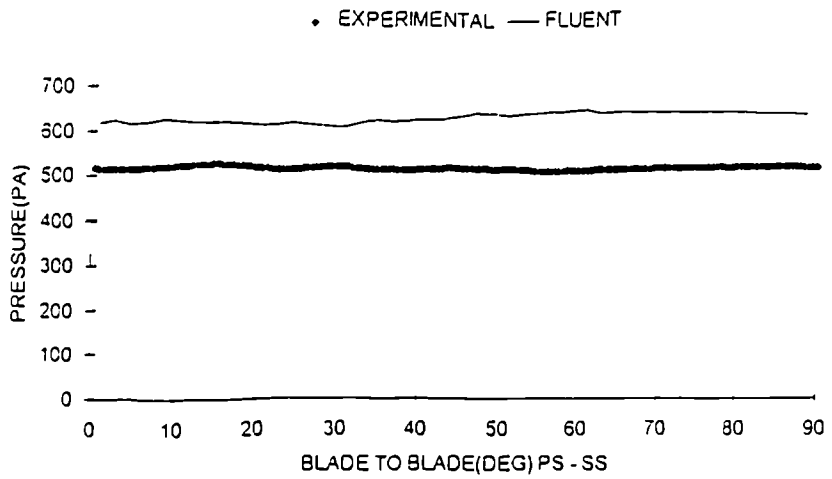

Figure 6.29 Comparison of experimental and computational pressure profiles R=0.240m, Window 6.

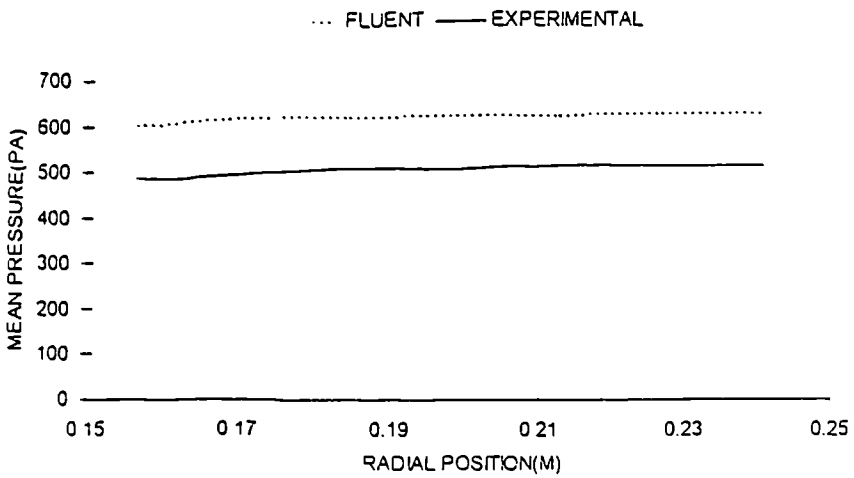

Figure 6.30 Comparison of Mean Pressure Profiles across the Volute, Window 6.

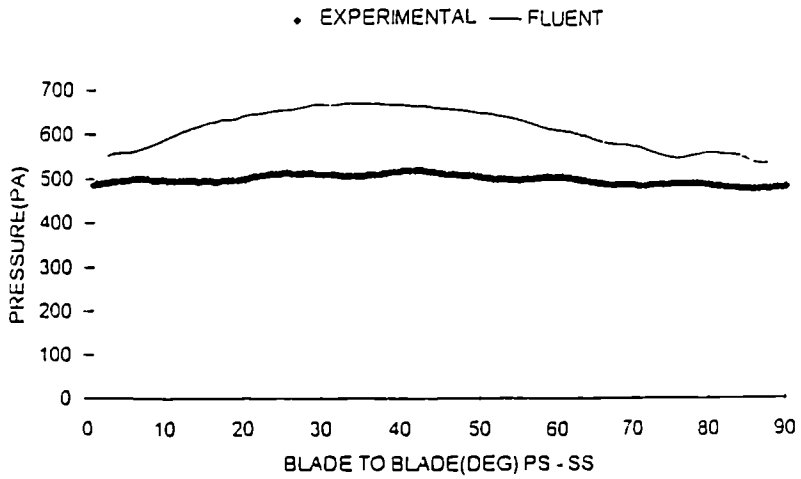

Figure 6.31 Comparison of experimental and computational pressure profiles R=0.170m, Window 7.

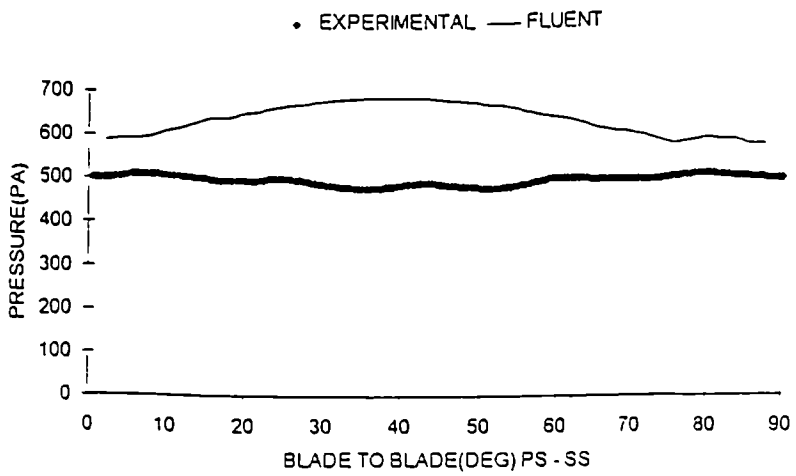

Figure 6.32 Comparison of experimental and computational pressure profiles R=0.198m, Window 7.

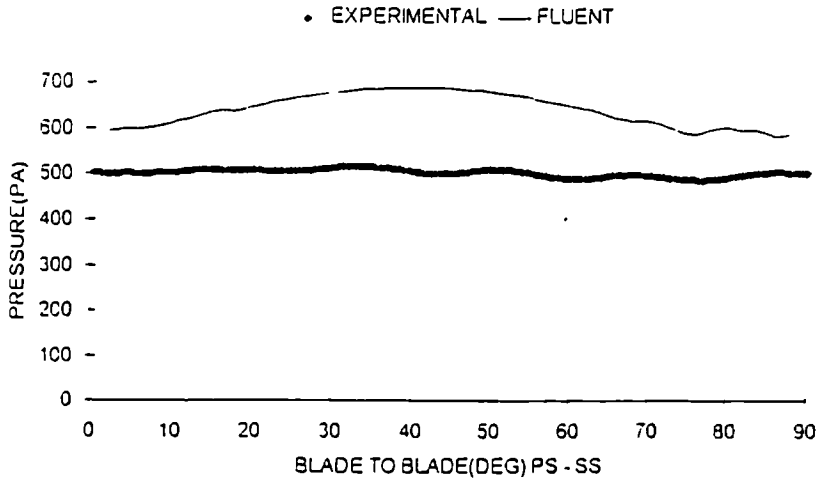

Figure 6.33 Comparison of experimental and computational pressure profiles R=0.226m, Window 7.

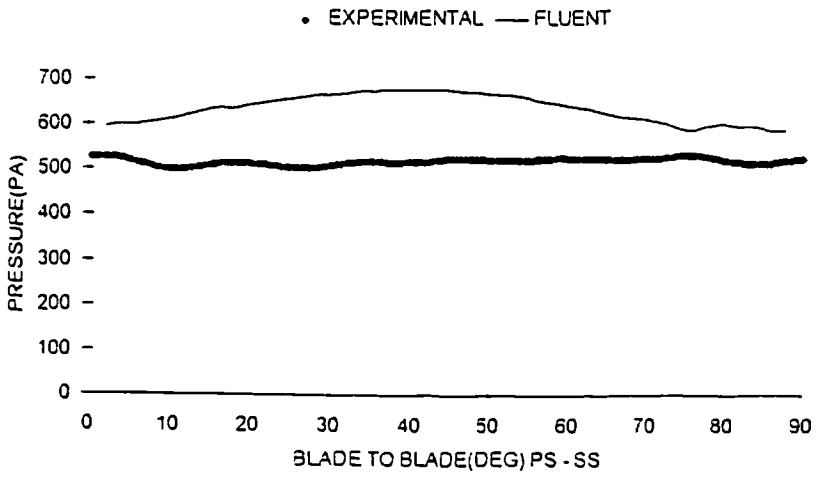

Figure 6.34 Comparison of experimental and computational pressure profiles R=0.254m, Window 7.

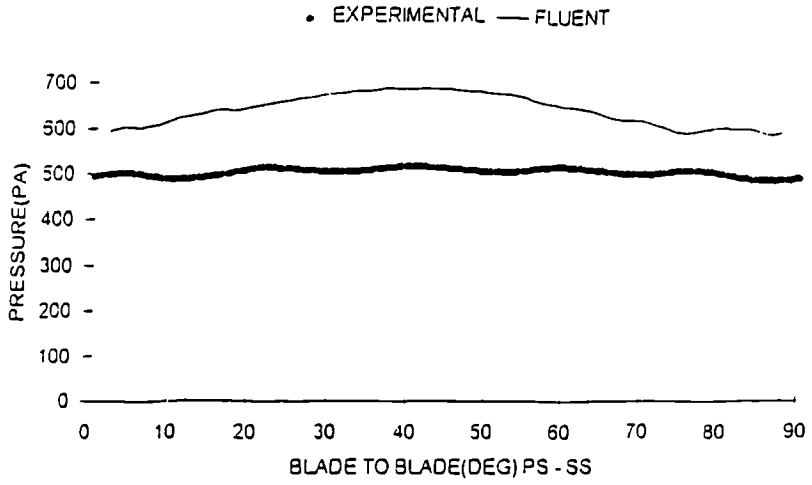

Figure 6.35 Comparison of experimental and computational pressure profiles R=0.282m, Window 7.

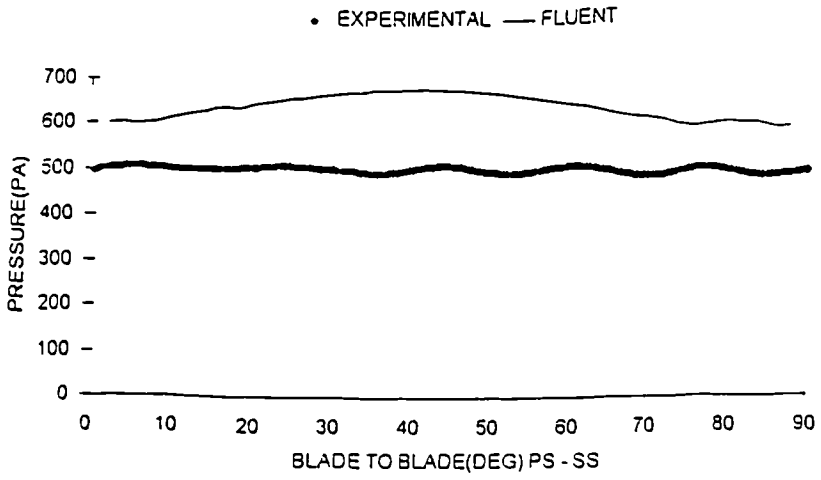

Figure 6.36 Comparison of experimental and computational pressure profiles R=0.310m, Window 7.

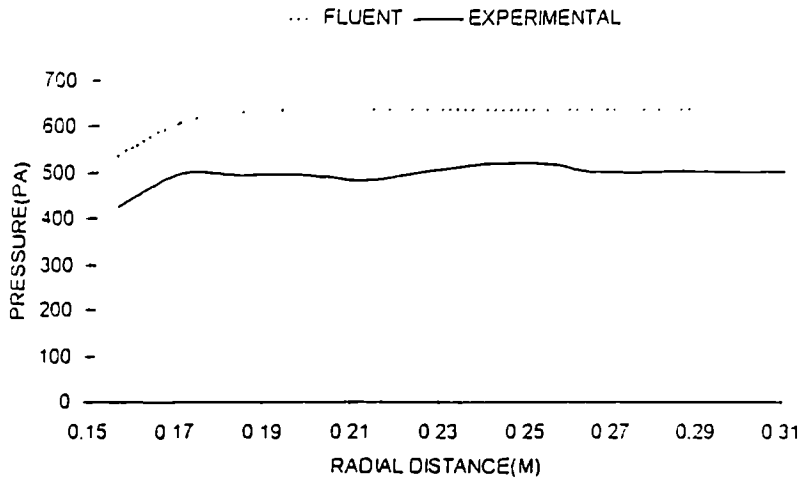

Figure 6.37 Comparison of Mean Pressure Profiles across the Volute, Window 7.

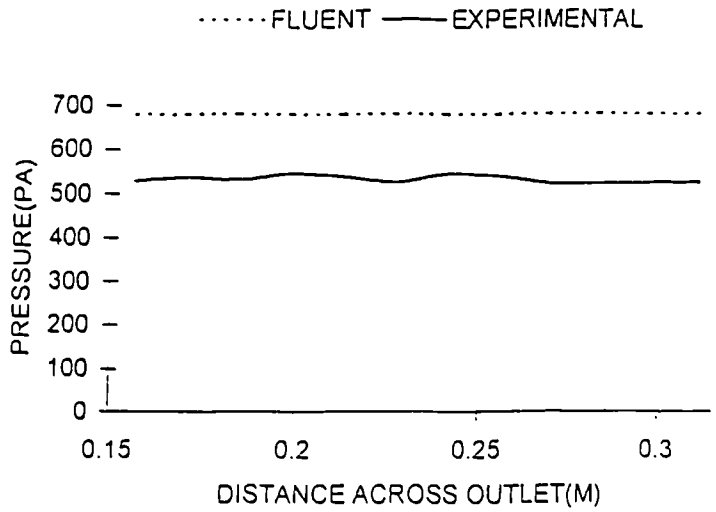

Figure 6.38 Comparison of Mean Pressure across the Outlet Duct, Window 0.

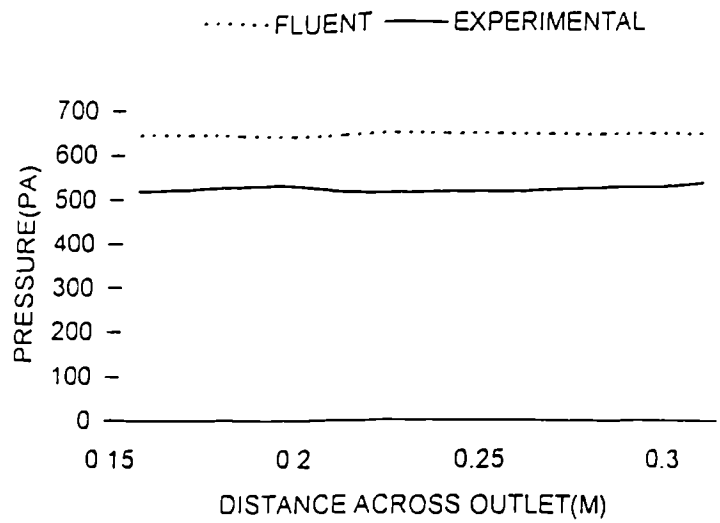

Figure 6.39 Comparison of Mean Pressure across the Outlet Duct, Window 9.

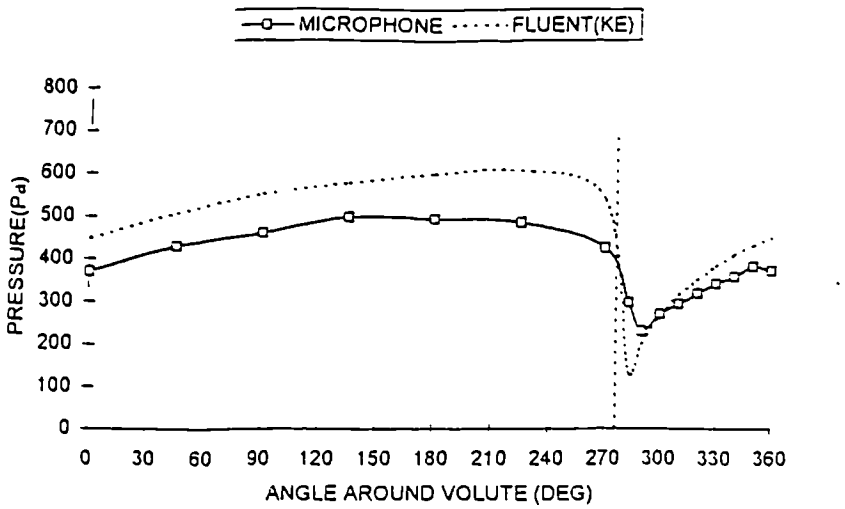

Figure 6.40 Circumferential Pressure around the Volute of The Centrifugal Pump at Shut-off.

CHAPTER 7:
CONCLUSIONS & FURTHER WORK

7.1 Introduction

This study had two main objectives. The first was to gain understanding of the flow physics within a radial pump or fan operating at shut-off, using both experimental and computational data. The second was to determine the capability of the commercial CFD package Fluent to predict the overall shut-off head within a pump.

The following chapter is split into five sections. The first section describes the flow in the volute using both the experimental and computational data. In the second section an insight is gained of the flow in the impeller using the results from the computational model. The third section takes a more detailed look at the shortcomings of the computational model with the fourth section summarising the main conclusions. The fifth and final section presents possible further work which would, in the opinion of the author, build on the success of this project.

7.2 Description of Volute Flow

This section describes the flow in the volute based on the results presented in chapters five and six.

To visualise the flow patterns within the volute streamline plots were obtained from the computational model. Figures 7.1 and 7.2 display streamlines in the volute at two angular positions of the impeller, one rotated at forty-five degrees from the other.

The figures below show generally the volute flow at shut-off does not change significantly with the impeller rotation, although the detailed shape of the outlet branch vortex may vary.

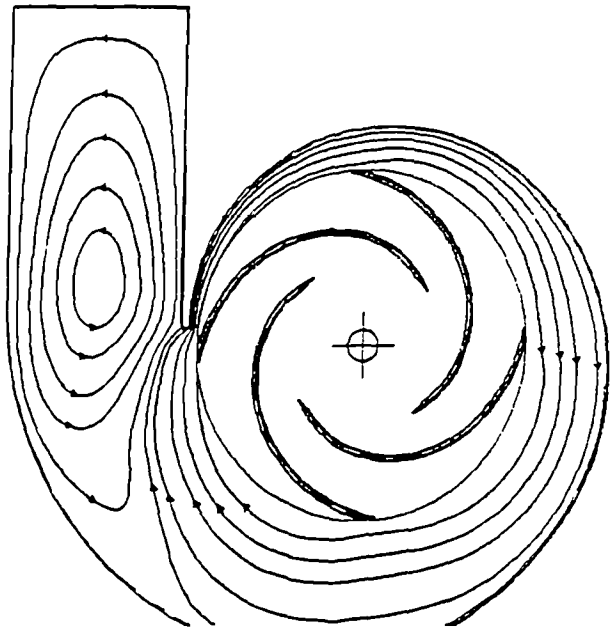

Figure 7.1 Volute Streamlines Generated using Fluent
(Impeller zero degrees).

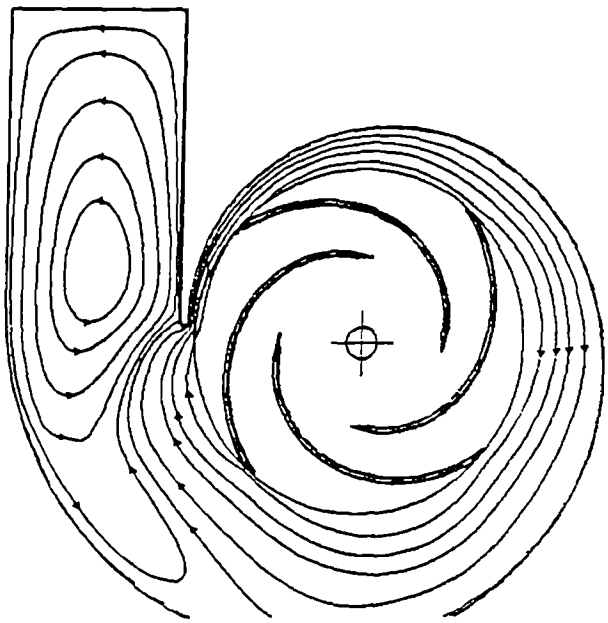

Figure 7.2 Volute Streamlines Generated using Fluent
(Impeller rotated forty-five degrees).

From the above figures the volute flow can be characterised as a recirculating eddy in the outlet duct together with a volute flow circulating around the rotor. These two flow patterns are supported by the experimental visualisation of Yedidiah(1985).

A comparison of the time-averaged circumferential pressure distribution for both experimental and computational results is shown in Figure 7.3 (taken from chapter 6). This shows that the volute acts primarily as a diffuser, with the majority of the pressure rise occurring in the one hundred and twenty degrees directly after the tongue.

The predicted pressure distribution for the full 2D-pump model at a fixed angular position is shown in Figure 7.4. This figure clearly shows the diffusive action of the volute.

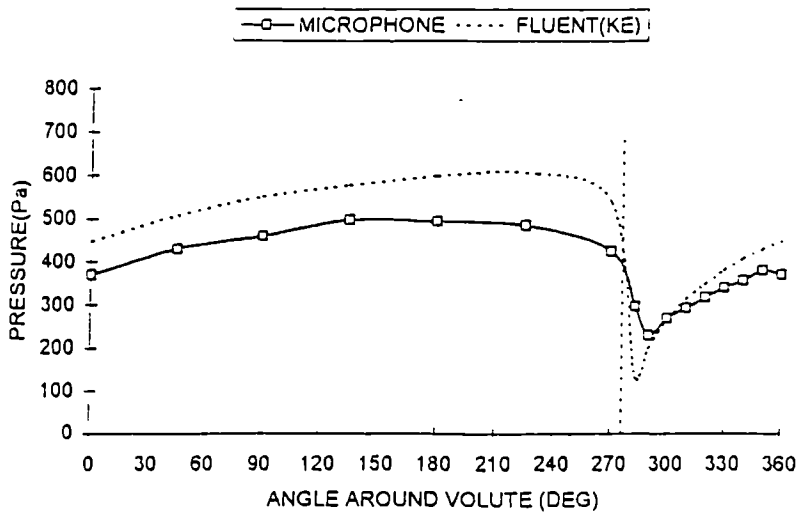

Figure 7.3 Circumferential Pressure around the Volute of The Centrifugal Pump at Shut-off.

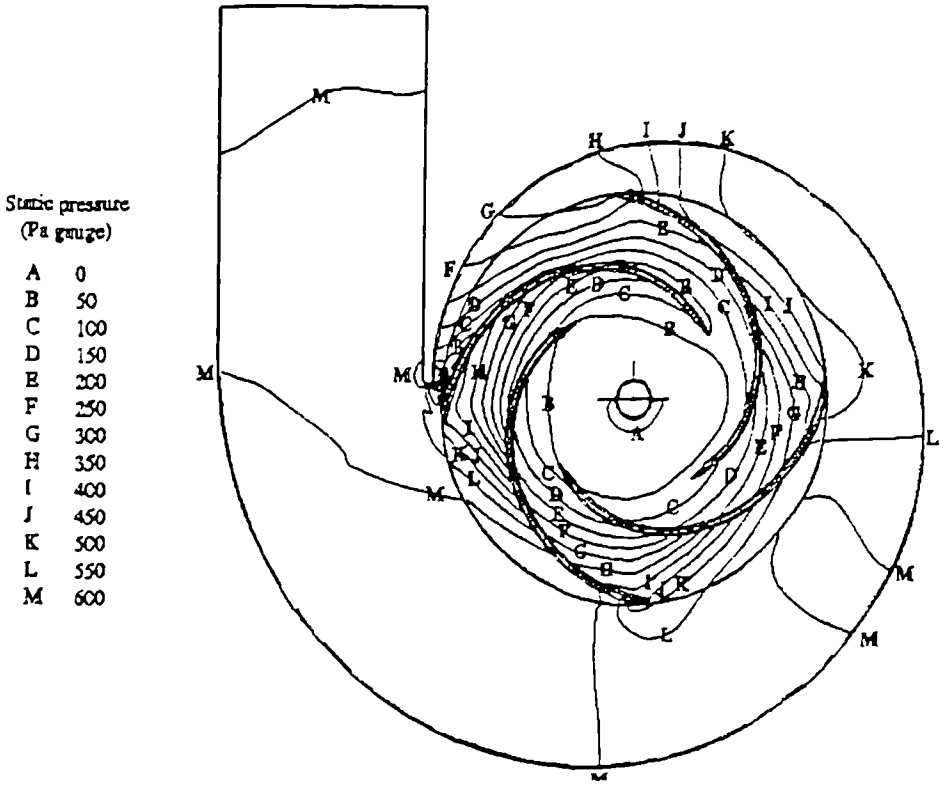

Figure 7.4 Predicted Pressure Distribution within Pump Model at Shut-off.

Chapter six shows that the experimental pressure measurements at fixed positions in the volute did not vary greatly with the rotation of the impeller. This is in contrast to the results obtained from the computational model which displayed an increase in pressure occurring approximately in the centre of each impeller passage. It is believed that this skewed pressure distribution, found in the computational model, is linked to the prediction of the effective viscosity and is discussed later in this chapter.

The computational model predicts very little circumferential variation in the radial flow, see Figure 7.5, with the majority of the variation occurring within one hundred and thirty-five degrees of the tongue. The experimental measurements show there is significant variation in the radial velocity around the whole circumference of the impeller.

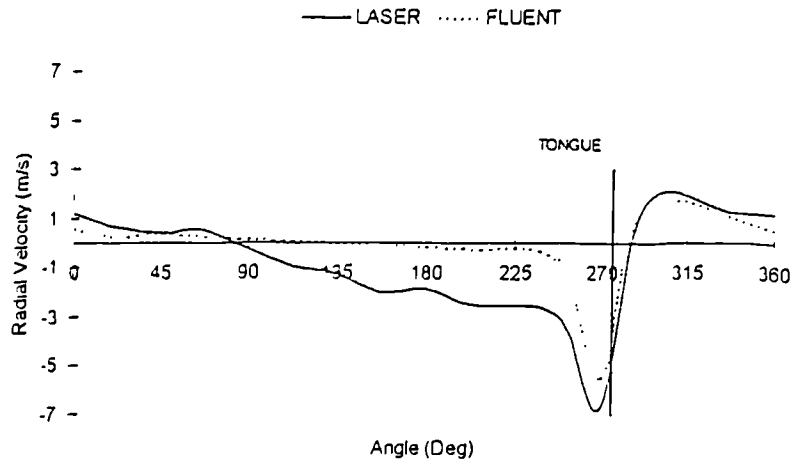

Figure 7.5 Circumferential Variation of the Mean Radial Velocity.

The under prediction of the radial velocity by the computational model can be linked to the skewed pressure rise shown across the blade passage. The experimental results show that a circumferential pressure distribution exists around the volute, rising from the tongue to the outlet duct. As the pressure increases around the volute, the experimental results show the radial velocity increases as flow is forced into the impeller.

The computational model balances the circumferential pressure distribution applied by the volute, which in turn prevents flow from entering the impeller.

The computational model predicted a decrease in the mean tangential velocity from the impeller exit to the volute wall. This is in contrast to the measured results which display a flat mean tangential velocity profile across the volute passage, at Windows 3 and 8, and a gradually decreasing profile at Windows 1,2 and 4.

The reason for the reduction in the predicted mean tangential velocity is most likely due to the use of a two-dimensional grid. It is believed that secondary flow patterns exist in the volute and they help to redistribute the tangential velocity across the volute passage, producing a flatter profile.

The use of a two-dimensional grid makes it impossible to model the effect of these secondary flows. Also the standard k-ε turbulence model would be oblivious to the normal stress anisotropy driving the secondary flow. To predict these secondary flows would require a three-dimensional grid and the use of a RSM turbulence model, or at least a non-linear k-ε model.

In conclusion the flow in the volute of this two-dimensional pump can be characterised as follows:

- ◊ A recirculating eddy in the outlet duct together with a volute flow circulating around the rotor.
- ◊ For this pump geometry only a small radial variation in pressure exists. It had previously been thought that the volute pressure distribution might be similar to that found in a viscometer. This study shows the volute acts primarily like a diffuser. Radial variations may occur in three-dimensional volutes with much lower spiral angles, however.
- ◊ High velocities are found at the entrance to the volute, between the tongue and rotor. However, no flow separation was predicted or measured.
- ◊ The pressure measurements in the volute show very little blade passing effect.
- ◊ The experimental measurements show significant variation of radial velocity around the circumference of impeller, with flow into the impeller over the last one-hundred and eighty degrees before the tongue.

7.3 Description of Impeller Flow

This study concentrated on the collection of experimental results in the volute and diffuser only. However, due to the agreement between the CFD prediction and the measured data at the exit of the impeller, it is assumed that the computational results will provide an insight into the impeller flow.

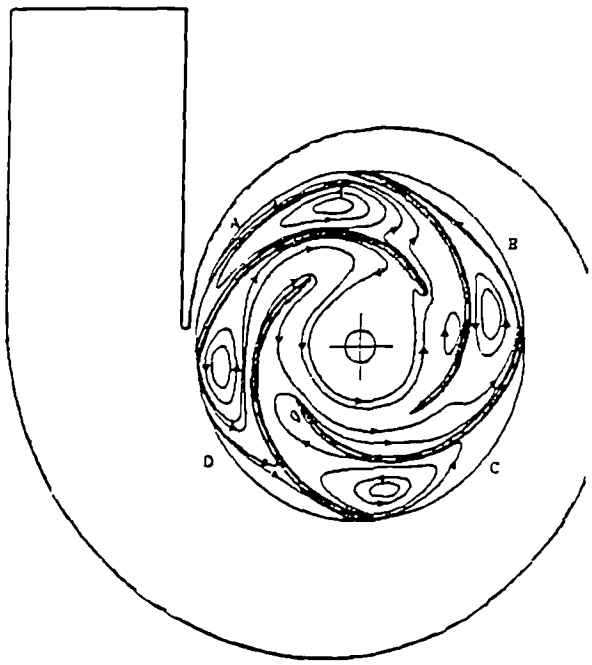

Figure 7.6 Impeller Streamlines Generated using Fluent (Impeller zero degrees).

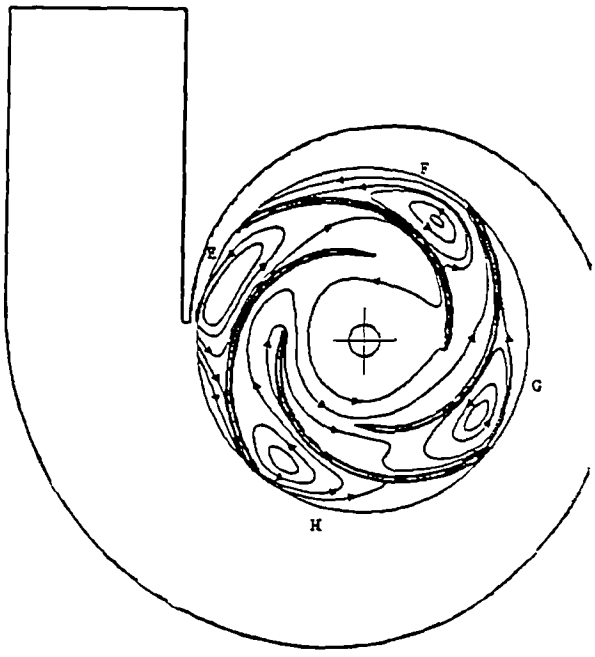

Figure 7.7 Impeller Streamlines Generated using Fluent (Impeller rotated forty-five degrees).

Rotating Eddy

The flow visualisation studies of Acosta and Bowerman(1957), Simpson and Cinnamond(1963), Senoo and Yamaguchi(1987) and Lennemann and Howard(1970) have all shown a rotating eddy at the exit of the impeller. This eddy rotates in the opposite sense to that of the impeller.

At design, with significant through flows, the eddy formed at the exit of an impeller is caused by the persistence of irrotationality in the absolute frame. The computational flow patterns, however, show that the rotation of the eddy at shut-off is driven by shear at the rotor periphery in a way similar to that of a driven cavity.

Lennemann and Howard(1970) stated that the impeller eddies extended out into the volute, leading to momentum exchange. However, this is not shown in either the computational or experimental solutions which suggest that the eddies are contained within the impeller and interaction with the volute flow exists via the shear stresses.

The following section of work examines the major flow patterns within the blade passages for the two impeller orientations.

Before considering the streamlines, it is important to recognise the major effect the circumferential pressure distribution found in the volute has on the impeller flow. Depending on the position of the impeller within the volute the impeller passage either contains inflow or outflow. The pressure applied by the volute determines whether this is inflow or outflow.

Over the one hundred and eighty degrees before the tongue, high pressure exists forcing the flow into the impeller, thus creating inflow. This inflow then travels down an impeller passage into the inlet of the pump where it locates an impeller passage at a lower pressure, which enables it to exit into the volute as outflow. Impeller passages C, D, E and H are all contained

within the region of high pressure and demonstrate inflow. Impeller passages A, B, F and G are all contained within the region of low pressure and demonstrate outflow.

Consider first the zero degree impeller position as shown in Figure 7.6.

Impeller Passage A

Impeller passage A is contained in the low pressure region of the volute. Flow, which originated from impeller passage D, enters this impeller passage at inlet. This inflow moves towards the exit of the impeller passage along the pressure surface until it reaches the rotating eddy. At this point the eddy drives the inflow over to the suction surface of the blade where the flow continues its path, sandwiched between the suction surface and the eddy

The flow then crosses from the suction surface to the pressure surface before exiting the impeller passage as outflow.

A small second rotating eddy exists in this impeller passage at inlet, similar to that seen by Simpson and Cinnamond(1963) and Senoo and Yamaguchi(1987).

Impeller Passage B

This passage is contained in the lower pressure region of the volute, as with impeller passage A. At the inlet to this impeller passage, inflow exists which originated from impeller passage C. This inflow enters the impeller passage and becomes sandwiched between the suction surface and the eddy. Once past the eddy the inflow moves across the blade passage from suction surface to pressure surface before exiting the impeller and entering the volute.

Impeller Passage C

Impeller passage C is contained in the region of higher pressure in the volute, therefore generating inflow into the impeller passage. The inflow enters at the suction surface of the impeller and is driven by the eddy towards the pressure surface and then on towards the inlet of the pump. This flow separates from the blade pressure surface as it moves towards the inlet. The flow then feeds the inflow found in impeller passage B.

Impeller Passage D

Similarly to impeller passage C, this passage exists in the high pressure region of the volute. Flow enters the exit of the impeller passage and is driven towards the pressure surface by the rotating eddy. Once past the eddy the flow continues towards the inlet of the impeller filling the whole passage. The flow then enters the inlet of the pump and feeds the inflow in passages A and B.

Consider now the impeller rotated to the forty-five degree position, as shown in Figure 7.7.

Impeller Passage F

This passage is in the lower pressure region of the volute and follows the same trends seen in impeller passages A and B. Flow originating from the previous impeller passage E, enters the impeller passage at inlet. The inflow follows a similar path to that described for impeller passage A, with two exceptions. Firstly no secondary eddy exists at the entrance to the impeller. The second exception is that the flow at outlet cuts across the blade exit from suction surface to pressure surface before entering the volute.

Impeller Passage G

Flow originating from impeller passage H, enters the inlet of this impeller passage. This inflow follows a similar route to that described for impeller passage B and exits to the volute.

Impeller Passage H

This impeller passage shows similar features to that found in passage C, with the flow from the volute entering the impeller passage. The passage eddy drives this inflow, at exit, to the pressure surface where it moves towards the inlet of the impeller passage. The flow then enters the inlet of the pump where it feeds both impeller passages F and G.

Impeller Passage E

At this angular position the impeller passage is affected both by a region of high pressure in the outlet duct and low pressure found at the tongue. This has the effect of distorting the eddy found at the impeller exit.

At the suction surface of the blade, a low-pressure region exists in the volute allowing flow to leave from the impeller passage. But, at the pressure surface of the blade, high pressure exists. This drives the flow back into the impeller passage. Some of the flow is driven past the eddy to the inlet of the pump where it circulates around the pump eventually feeding impeller passage F.

Complicated interaction between impeller flow passages.

The previous analysis clearly demonstrates the complicated interactions which exist between individual impeller passages. It also shows how the circumferential pressure within the volute dominates the impeller flow patterns. The high pressure in the volute at impeller passages C, D, E and H causes the substantial inflow, which travels via the inlet of the pump before it re-enters at impeller passages A, B, E and F. Although no measurements could be taken in the impeller to confirm these CFD predictions, the

measured radial velocities just outside the impeller indicate outflow from the impeller over the first one hundred and eighty degrees after the tongue. This together with the backflow into the impeller from the volute over the next one hundred and eighty degrees, strongly suggests that the predicted patterns are correct.

7.4 Analysis of Computational Results

The CFD model provided generally good qualitative agreement with experimental data for the volute flow. Unfortunately despite this agreement, the model over predicted the shut-off pressure rise by approximately 25% as shown in Table 7.1. It is noted however, that the correlation proposed by Frost also significantly over predicts the pressure rise (by 36%) for this pump geometry despite good accuracy for the commercial pump geometries shown in Frost and Nilsen(1991).

	Δp inlet vent to rotor tip (Pa)*	Δp rotor tip to volute outlet (Pa)*	Overall Δp (Pa)
Experiment	375	150	525
Fluent**	421	239	660
Correlation Frost (199)	471	241	712

*rotor tip conditions average values around rotor circumference.

** using standard k-ε turbulence model.

Table 7.1 Comparison between the prediction methods and experiment.

Improvements in the CFD prediction should have been possible with the use of the RNG k-ε turbulence model. However, as shown in Chapter three, this model produces an increased overall pressure rise of approximately 800Pa. The higher overall pressure rise can be attributed to the increase in effective viscosity found in this model.

The RNG k-ε generated areas of significant high pressure in front of the pressure surface and towards the blade tip. In turn this produced areas of localised high effective viscosity. This may have been due to the use of a two-dimensional grid, which did not allow the development of secondary flows within the volute. However, another explanation could lie with the implementation of the RNG k-ε model by Fluent. In the Fluent Users' Manual it is stated that the RNG model is not fully validated and to compare predictions with experimental data.

In order to gain a greater insight into the CFD solution, the limitations imposed by the sliding mesh model in terms of the available discretisation schemes and turbulence models have to be removed. To achieve this a new model was created, as shown in Figure 7.8.

In this new model the volute was replaced with a cylindrical concentric casing allowing the use of a rotating reference frame model. To further improve computational efficiency only a ninety degree section of the impeller and casing was modelled, with pitchwise-repeating cyclic boundaries. The advantages of this model were, as follows:

◊ The rotating reference frame model allowed the use of all the turbulence models and higher order schemes available in Fluent.

◊ The model contained fewer cells than the full two-dimensional pump model, so therefore obtained convergence more quickly.

◊ The rotating reference frame simulation produced a steady state solution. Therefore any errors introduced by the first order accurate time dependence scheme implemented with the sliding mesh were not present.

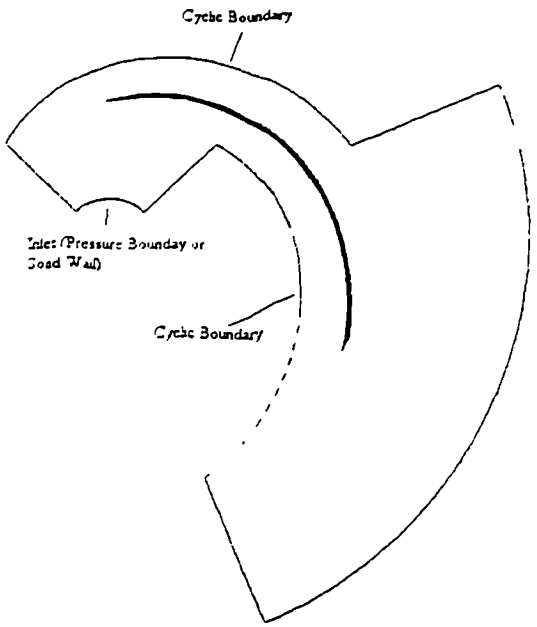

Figure 7.8 Outline of Grid Used for Rotating Reference Frame/Sliding Mesh Comparison.

The geometric dimensions of the impeller were based on the experimental rig described in chapter four, with the exception of a cylindrical casing which was positioned at the volute mean radius (midway between tongue and diffuser wall).

7.4.1 Comparison of Sliding Mesh and Rotating Reference Frame Solutions.

This first investigation compared the pressure distribution obtained using the sliding mesh model with the results from the rotating reference model.

The rotating reference frame model has been used successfully for many years so is widely validated. The sliding mesh model is only a recent addition to Fluent and has not yet received the same level of validation.

The mean pressure rise across the impeller was determined from the mean inlet and exit pressures.

Initial results indicated that the sliding mesh model was over predicting the pressure rise across the impeller by approximately 9% when compared with the rotating reference frame model.

Fluent attributed the discrepancy between sliding mesh and rotating reference frame models to the pressure boundary at the inlet to the computational domain.

To investigate this hypothesis a slip wall was placed at inlet for both the sliding mesh and rotating reference frame models. The investigation found this change in inlet conditions had a negligible effect on the overall pressure rise

However, an examination of the solutions from the sliding mesh and rotating reference frame showed the standard convergence criteria was not strict enough to obtain a torque balance between casing and rotor. A reduction by an order of magnitude in the convergence criteria produced a more satisfactory torque balance. The reduced convergence criteria also reduced the over prediction of the sliding mesh model to approximately 5%.

The errors between the sliding mesh and rotating reference frame can possibly be attributed to:

- The method of interpolation between the rotating and stationary grid in the sliding mesh model which may generate errors that propagate through the solution.
- The implementation of a time differencing scheme, only first order accurate, which may again be a source of error.

7.4.2 Effect of Higher Order Spatial Differencing Scheme

The use of the higher order differencing scheme, QUICK, surprisingly had very little effect on the rotor solution. This is probably due to the flow being dominated by body force terms, with advection effects being small.

7.4.3 Effect of Turbulence Model

During the investigation of the computational pump model, it was believed a weakness of the analysis was the use of the k-ε turbulence model. This model is unable to represent the effects of either flow rotation or boundary curvature, Wilcox(1994).

A possible improvement would be the implementation of the RNG k-ε or RSM turbulence models. Initially it was hoped that a comparison of all three turbulence models, k-ε, RNG k-ε and RSM could be made. Unfortunately the author was unable to obtain realistic converged solution for the Reynolds stress model. Fluent suggested this could be due to grid skewness, which is inevitable when using a structured mesh for the present geometry.

It was noted in chapter six that the computed blade to blade pressure distribution for the full two-dimensional model displays a distinct pressure rise, mid impeller passage, that is not seen in the experimental measurements. This rise in pressure, found in the computational model, can be explained by the torque transmission mechanism between the rotor and volute.

The torque is transmitted from the impeller to the volute by both the tangential shear stresses and a moving pressure field. The tangential stresses drive the eddy at the exit of the impeller, which impinges on the leading surface of each blade, producing a high pressure region on the leading surface of the blade.

Therefore the prediction of the effective viscosity by the turbulence model is particularly important. The higher the effective viscosity, the higher the velocity of the eddy and the greater the momentum change and therefore, the blade surface pressure rise.

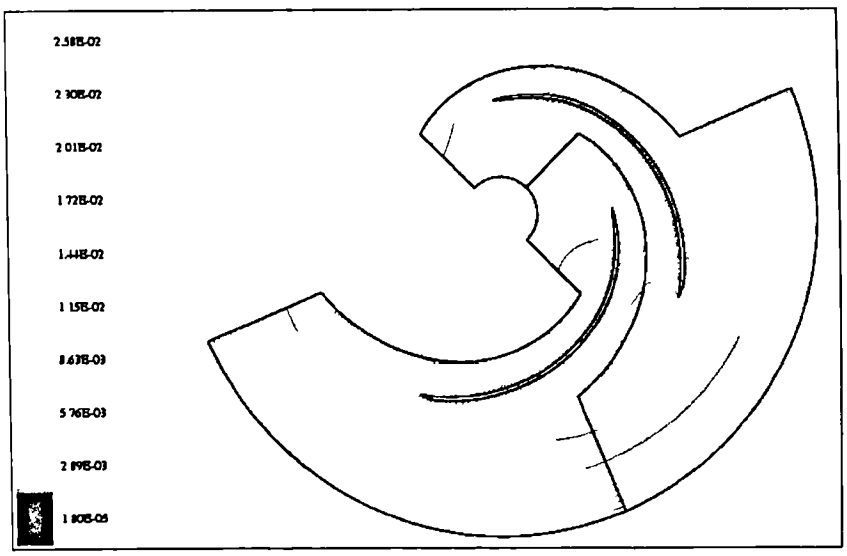

Figure 7.9 Effective Viscosity Contours Predicted using the k-ε Turbulence.

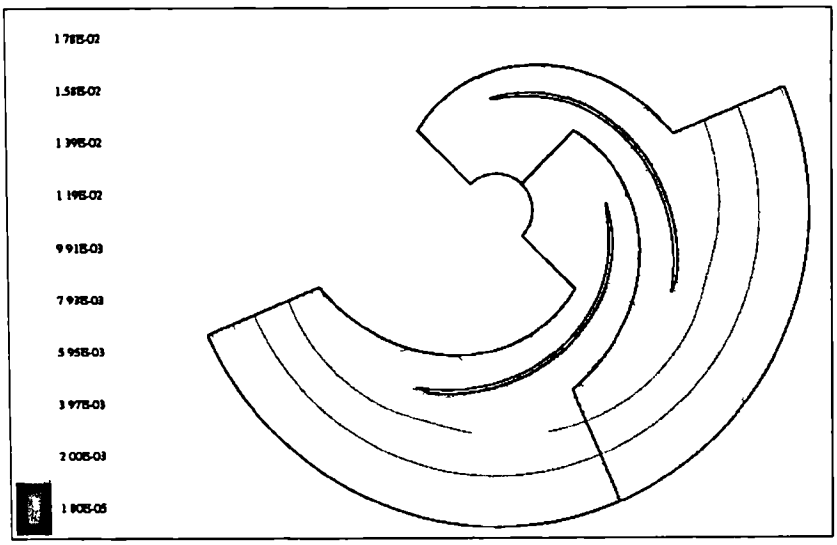

Figure 7.10 Effective Viscosity Contours Predicted using the RNG k-ε Turbulence Model.

Figures 7.9 and 7.10 display the effective viscosities within the impeller passages for both the k-ε and RNG k-ε turbulence. As expected the figures above show that the RNG k-ε model predicts an effective viscosity that is almost 40% lower than that predicted by the standard k-ε model.

A comparison of the pressure rise for the rotating reference frame model using the two turbulence models is given in Table 7.2. This table shows that although the RNG k-ε model predicts a much lower effective viscosity its effect on the overall pressure distribution for the model is minimal.

However, this is in sharp contrast to the full pump model where the RNG k-ε model predicts effective viscosities, which are 150% higher than the standard k-ε model as well as predicting a higher overall pressure rise. Such differences must be attributed to the circumferential variations associated with the full two-dimensional pump model.

	Turbulence Models Employed	
	k-ε	RNG k-ε
Mean Impeller Inlet Pressure(Pa)	149	190
Mean Impeller Exit Pressure(Pa)	482	527
Mean Pressure Rise Across Impeller(Pa)	333	337

Table 7.2 Comparison of Pressure Distribution across the Impeller Passage for Different Turbulence Models.

One explanation for the higher effective viscosity in the full pump model becomes apparent when considering energy contours for the turbulent kinetic energy, seen in Figure 7.11. In the region between the tongue and rotor, high velocity and strong shearing generate very high levels of turbulent kinetic energy. This turbulent energy is then convected into the

local blade passage. The effective viscosity generated by this turbulent kinetic energy decays more slowly than the energy itself, and persists within the blade passage of the rotor, Figure 7.12.

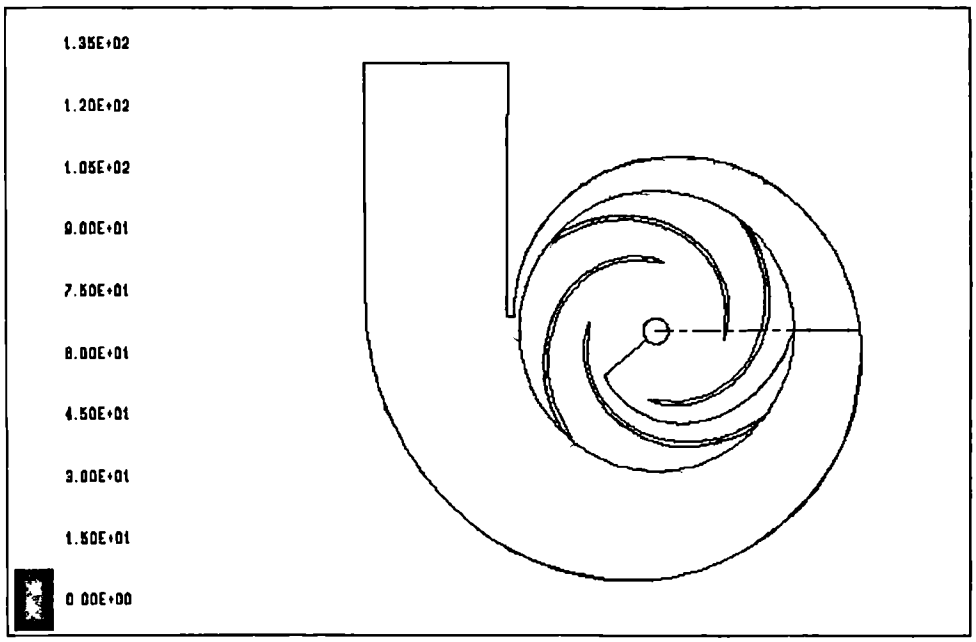

Figure 7.11 Predicted Turbulent Kinetic Energy in the two-dimensional pump model.

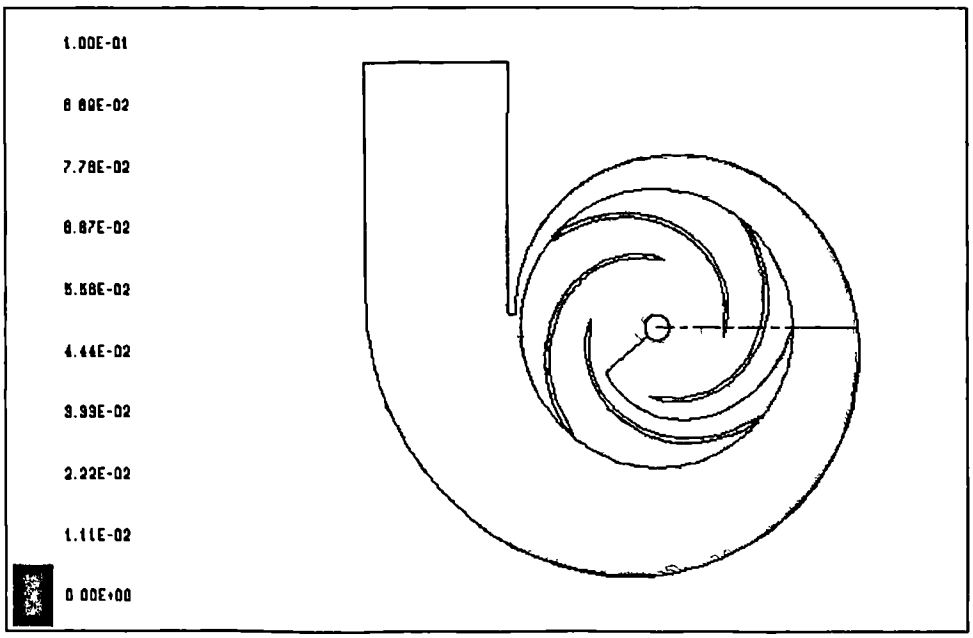

Figure 7.12 Predicted Effective Viscosity in the two-dimensional pump model.

It is impossible, using the available data, to determine the exact cause of the over prediction by the CFD model as this would require experimental data regarding both the turbulence quantities and impeller flow. Nevertheless, the following observations and suggestions can be made:

- ◊ The turbulence model has a significant effect on the effective viscosity especially for the full pump model and there is evidence that this has a major impact on the pressure rise prediction at shut-off.
- ◊ Grid skewness due to the use of the structured grid version of Fluent may be responsible for errors. The sudden change in skew between impeller and volute is a particular problem. Use of an unstructured code could possibly alleviate this problem.
- ◊ The convergence criteria has to be a lot stricter than normal to achieve a torque balance between rotor and stator. In the full two-dimensional pump solutions torque balance errors of approximately twenty percent could not be eliminated.
- ◊ The use of the sliding mesh can cause an over prediction of the rotor flow by 5%. This could be linked to grid skewness within the impeller, and therefore the use of an unstructured mesh could reduce or eliminate this problem.
- ◊ The two-dimensional grid will not recognise any three-dimensional secondary flow effects. Wilcox(1994) discusses the difficulty in predicting the secondary flow in rectangular channels. These flow patterns can only be predicted when the RSM is used. The current CFD model does not, at present, take into account the side walls of the volute, which could help reduce the predicted pressure rise.
- ◊ Finally, Fraser and Zhang(1993) demonstrated that the standard wall functions based on the standard law of the wall relationship, are inappropriate for impeller flows which are effected by rotation and curvature.

7.5 Final Conclusions

The numerical accuracy of the shut-off head obtained using CFD is at present no better than the semi-empirical correlations. This is however, based on a general purpose CFD package which is not "tuned" for modelling rotating problems. There are also some known weaknesses in the modelling assumptions with the present code.

Despite these weaknesses, CFD gives an insight into the flow mechanisms, where most of the available correlations, apart from Frost and Nilsen(1991), have little physical basis.

The following section of work presents the insights gained from this study:

◊ The flow in the impeller is rotational at shut-off, and not solid body rotation as suggested by Stirling(1982) and Frost and Nilsen(1991). The generating mechanism for this rotation is not the persistence of irrotationality in the absolute frame(which is assumed at design flow) but is driven by shear at the rotor periphery in a similar manner to that of a driven cavity flow.

◊ The flow pattern in the volute, suggested by Frost and Nilsen(1991), with separation part-way around and re-attachment on the discharge side of the tongue together with re-circulation in the outlet duct, has been validated.

However, for the geometry of the pump used in this investigation, Frost's assumption that the volute pressure rise is due to a radial pressure gradient associated with the centrifugal body forces, is shown to be incorrect. Very little radial pressure gradient was predicted or measured and the body forces provided the radial acceleration associated with the large spiral angle of the volute.

The major effect of the volute is to act as a diffuser with a strong circumferential pressure over approximately the first 120^0 after the tongue.

◊ Overall qualitative and quantitative agreement was obtained between the CFD model and experimental results.

7.6 Further Work

This section will consider possible further work, which would improve the overall understanding of the flow at shut-off and the use of CFD for modelling pump flows. The further work is split into experimental and CFD work.

7.6.1 Further Work CFD

The study has highlighted a number of problems encountered when using a general CFD package and this section considers possible areas that, with further research, could improve the accuracy of the model.

The further work regarding CFD can be divided into two parts. The first considers ways in which the CFD package itself could be improved. The second considers improvements and advancements to the actual model.

The previous analysis demonstrates that the sliding mesh model over predicts overall pressure rise in the pump. There are a number of limitations placed on Fluent when using the sliding mesh model. Possible improvements to the overall predictive capabilities could be made if these limitations could be removed. Such improvements could entail the following:

1) The implementation of a higher order time differencing scheme such as the second order accurate Crank-Nicolson.

2) The spatial accuracy could possibly be improved with the implementation of higher order schemes such as QUICK.

3) Although problems existed during this investigation with the RSM model, it is believed that ultimately the implementation of this turbulence model would improve the overall accuracy of the solution.

4) The implementation of an unstructured mesh may reduce problems of grid skew within the impeller and volute.

It may be worthwhile creating a specific CFD program, which would model radial flow machines. This could allow improvements in terms of computational efficiency. Currently, the computational models generated by Fluent contain two large dead cell regions that not only use the resources of the computer but also have no benefit to the user.

The next significant stage in terms of the modelling of pump flows would be the development of a three-dimensional model. This could be achieved in two stages. The first stage would involve extending the pump model to enable the inlet pipe recirculation. The second stage would involve the modelling of a three dimensional volute.

The development of a three dimensional model would require significant computer resources in terms of run times and memory. Therefore an optimised CFD package for pump flows maybe the only realistic way forward.

7.6.2 Further Work Experimental

The measurement of the pressure and velocity in the impeller of the pump would provide important detailed information which would allow a full description of the flow within the pump at shut-off.

The implementation of a two component LDA system could be used to take measurements in the impeller and volute, thus allowing the Reynolds stresses to be measured. With the present single-component LDA system it is not possible to measure these stresses.

The experimental Reynolds stresses could then be used to validate the turbulence models used in the CFD calculations, and could therefore lead to improvements in the predictive capabilities.

APPENDIX A:

COMPARISON OF SHUT-OFF PREDICTION METHODS

The following section examines the ability of the prediction methods described in Chapter 1 to calculate the shut-off head for the pump described by Miner et al.(1989).

The geometry of Miner's pump is unconventional compared to an industrial centrifugal pump design and should therefore pose a test to the prediction methods. The pump was designed specifically to allow laser Doppler measurements within the volute and impeller. To simplify the flow field being measured the pump was designed to eliminate three dimensional effects which are always found in centrifugal pumps.

The volute of the Miner's pump is a logarithmic spiral with an angle of 83 degrees (FigureA1). The impeller has four blades each describing a 16 degree logarithmic spiral. The width of the impeller, 24.6mm, is constant from inlet to exit, and the volute has the same width as the impeller.

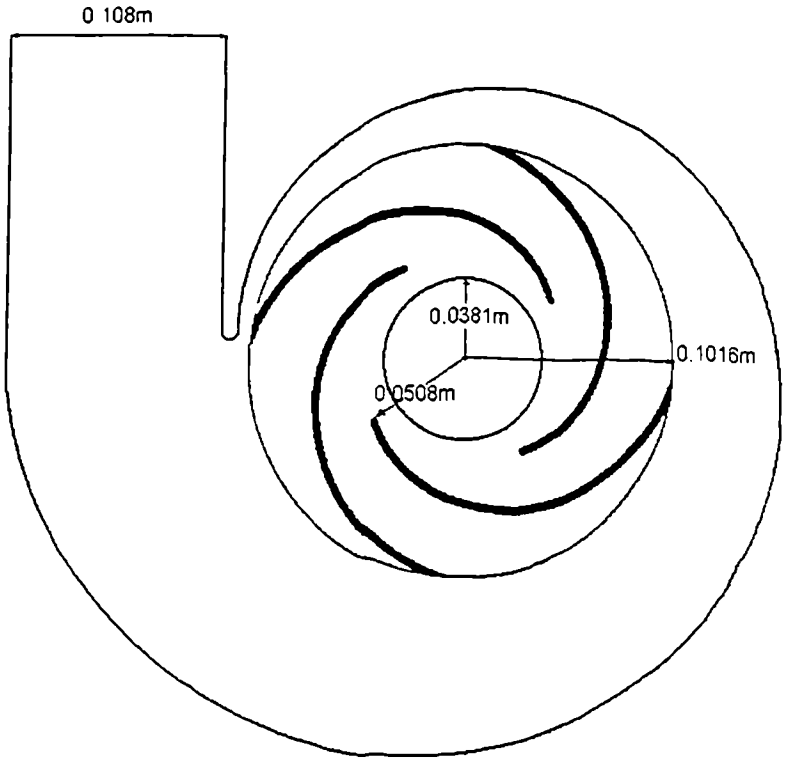

Figure A1. Geometry of Miner's Pump. Miner et al(1989).

The pump was designed to run at a rotational speed of 619rpm with the design point at 6.3l/s at 1.78m of H_2O. The design point was based on an estimate of the impeller-volute matching point. The measured shut-off head was 2.44m of H_2O with no estimation is given on the amount of leakage flow.

Table A1 displays the values of the common variables used in the investigation.

Table A2 displays the predicted shut-off head calculated using each of the methods.

Name of Variable	Value	Comment
u_1	3.29m/s	Inlet blade velocity
u_2	6.58m/s	Exit blade velocity
G	9.81m/s^2	Gravity
D_1	0.1016m	Impeller diameter at blade inlet
D_2	0.203m	Impeller diameter at blade exit
r_4	0.219m	Radius of outer wall of volute
r_3	0.108m	Radius of lip of volute
r_m	0.164m	Mean radius of volute
Ω	64.8rad/s	Angular Velocity of Impeller

Table A1. Common Variables used for Miner's pump.

The average of the all the shut-off head methods provides a value of 2.58m which presents a six-percent over prediction of the actual measured value.

Method Proposed by	Predicted Shut-off Head(m of H_20)	Comments
Stepanoff	2.58	$\psi so = 0.585$ (fixed value)
Peck	2.21 for $K_{H0} = 1.0$ 2.43 for $K_{H0} = 1.1$	$K_{H0} = 1.0$ or 1.1 depending on volute casing.
Thorne	2.94	a = 0.77 casing factor z = 4, number of blades β = 16 degrees, blade angle SLIP = 1.44, A = 0.5, B=0.463 C_{1r}=0.52m/s (calculated from Stirling)
Patel	2.48	For pumps with a metric specific speed between 12 to 50. Miner's pump nsq = 21.94.
Chiappe	2.46 for k = 0.8 2.22 for k = 0.72	Hydraulic Efficiency η_H = 0.90. k = 0.72 to 0.8 depending on flow conditions at impeller eye. ψso = 0.775 obtained from dimensionless velocity diagram.
Stirling	2.21m	H_{SO}^{IMP} = 1.93m, impeller head rise *AR* = 1.87, Area ratio ϕ_r = 0.079, Recirculatory flow coefficient h_O = 0.801, Wiesner slip factor. θ_2 = 16deg, blade exit angle δ_A = 1.23deg , deviation angle P_2 = 0.115, equivalent pitch $C_m = 1.21 \times 10^{-3}$

Method Proposed by	Predicted Shut-off Head(m of H_20)	Comments
Frost and Nilsen	2.67	Case(i) r_1 = impeller blade inlet radius, H_{SO}^{IMP} = 1.65m
	2.92	Case(ii) r_2 = radius of suction pipe, H_{SO}^{IMP} =1.90m
	3.23	Case(iii) r_3 = zero due to forced vortex rotation, H_{SO}^{IMP} = 2.21m

Table A2. Shut-off Prediction Methods applied to Miner's(1989) pump.

APPENDIX B:
DERIVATION OF EQUATIONS OF MOTION IN A ROTATING REFERENCE FRAME

Consider initially the general case, where the moving reference frame rotates about all three fixed coordinate axes with an angular velocity vector

$$\omega = \omega_x \mathbf{i} + \omega_y \mathbf{j} + \omega_z \mathbf{k} \qquad \text{(B.1)}$$

The position vector describing a point A in the moving reference frame with respect to the fixed origin O can be written as

$$\mathbf{r}_A = x\mathbf{i} + y\mathbf{j} + z\mathbf{k} \qquad \text{(B.2)}$$

where **i, j** and **k** are orthogonal unit vectors fixed to the moving frame.

To find the velocity and accelerations of point A it is necessary to differentiate equation(B.2) with respect to time, remembering that as the directions of the unity vectors **i, j** and **k** are changing they will have time derivatives. Thus the velocity of the point A in the absolute frame may be written as:

$$\left(\frac{d\mathbf{r}_A}{dt}\right)_{abs} = (\dot{x}\mathbf{i} + \dot{y}\mathbf{j} + \dot{z}\mathbf{k}) + (x\dot{\mathbf{i}} + y\dot{\mathbf{j}} + z\dot{\mathbf{k}}) \qquad \text{(B.3)}$$

From consideration of the incremental change $\delta\mathbf{j}$ in the unit vector **j** over a time δt, as shown in Figure B1:

$$\delta\mathbf{j} = -(\omega_z . 1.\delta t)\mathbf{i} + (\omega_x . 1.\delta t)\mathbf{k} \qquad \text{(B.4)}$$

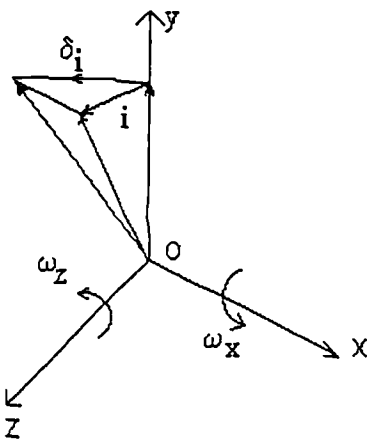

Figure B1. Incremental Change in unit Vectors.

Taking the limit, as δt tends to zero:

$$\dot{\mathbf{j}} = \frac{d\mathbf{j}}{dt} = -\omega_z \mathbf{i} + \omega_x \mathbf{k} \qquad (B.5)$$

Similar expressions may be obtained for $\dot{\mathbf{i}}$ and $\dot{\mathbf{k}}$.

Consequently the second term on the right hand side in equation(B.3) may be written as:

$$\begin{vmatrix} \mathbf{i} & \mathbf{j} & \mathbf{k} \\ \omega_x & \omega_y & \omega_z \\ x & y & z \end{vmatrix} = \omega \times \mathbf{r}_A \qquad (B.6)$$

where the x symbol indicates a vector product, whilst the first right hand side term can be recognised as the relative velocity of A in the moving coordinate system. That is the absolute velocity $\mathbf{v}_A$ is:

$$(\mathbf{v}_A)_{abs} = \left(\frac{d\mathbf{r}_A}{dt}\right)_{abs} = \left(\frac{d\mathbf{r}_A}{dt}\right)_{rel} + (\omega \times \mathbf{r}_A) \qquad (B.7)$$

The acceleration of point A in the absolute frame is found by differentiating equation(B.7) with respect to time, which produces:

$$(\mathbf{a}_A)_{abs} = \frac{d}{dt}(\mathbf{v}_A)_{abs} = \dot{\mathbf{v}}_{rel} + \dot{\omega} \times \mathbf{r}_A + \omega \times \dot{\mathbf{r}}_A \qquad (B.8)$$

where

$$\dot{\omega} \times \mathbf{r}_A = \omega \times \frac{d}{dt}(\mathbf{r}_A)_{abs} = \omega \times \mathbf{v}_{rel} + \omega \times (\omega \times \mathbf{r}_A) \qquad (B.9)$$

and

$$\dot{\mathbf{v}}_{rel} = \mathbf{a}_{rel} + \omega \times \mathbf{v}_{rel} \qquad (B.10)$$

The absolute and relative accelerations may therefore be linked by:

$$(\mathbf{a}_A)_{abs} = \dot{\omega} \times \mathbf{r} + \omega \times (\omega \times \mathbf{r}) + (2\omega \times \mathbf{v}_{rel}) + \mathbf{a}_{rel} \qquad (B.11)$$

APPENDIX C:
PHOTOGRAPHS OF EXPERIMENTAL RIG
LDA MEASUREMENTS

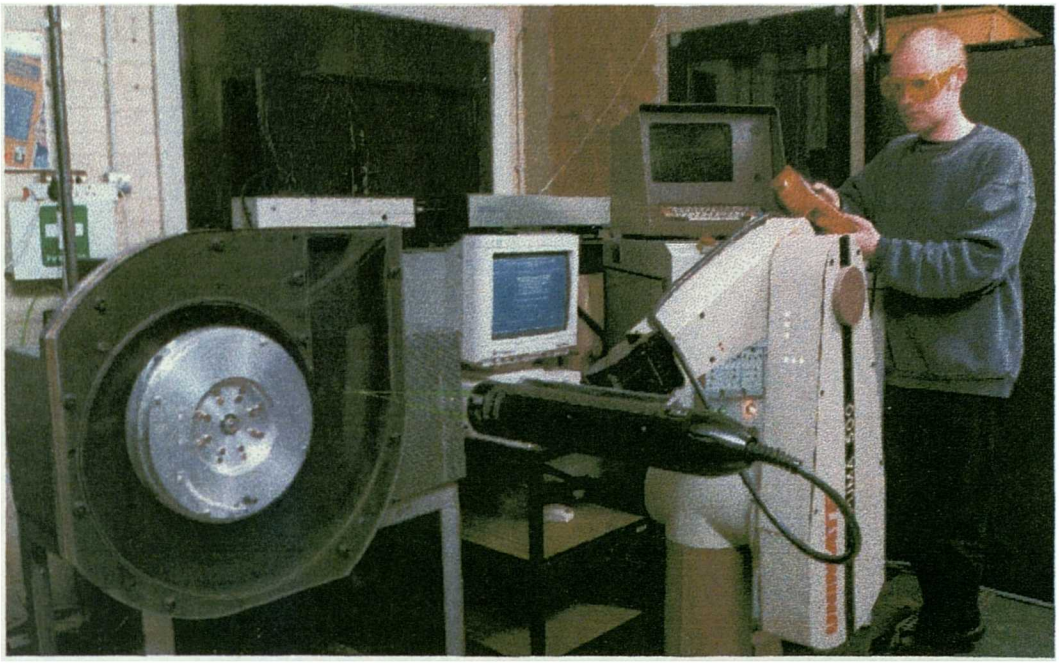

Figure C1. LDA Measurement in Outlet Duct.

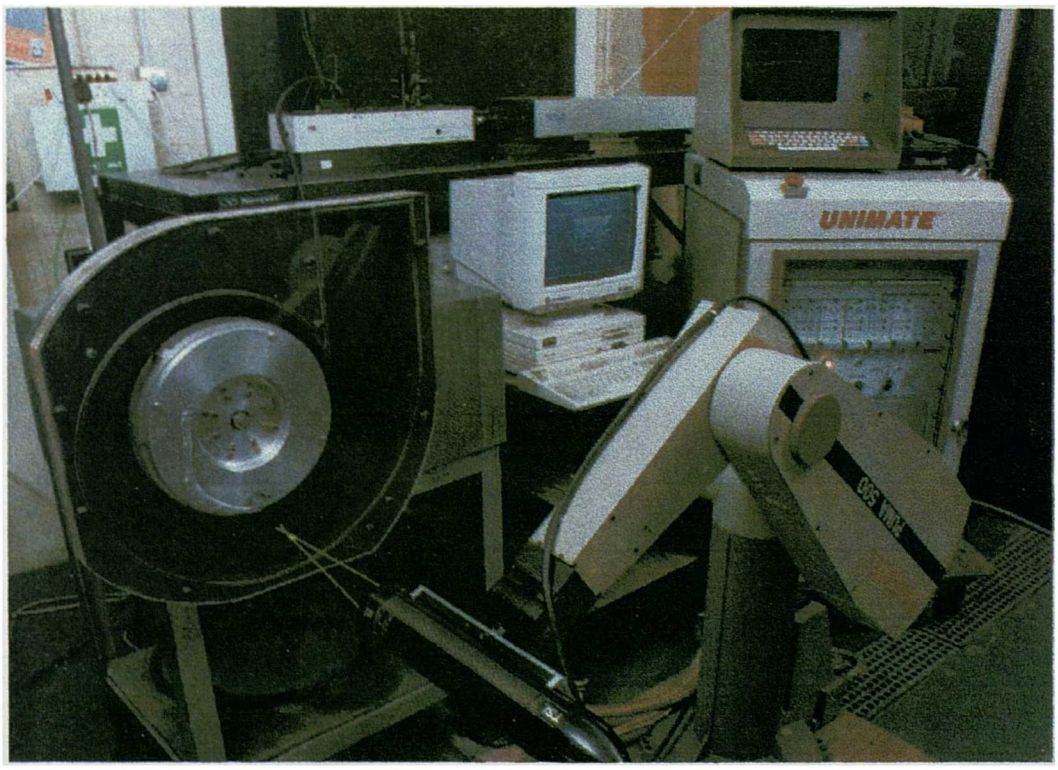

Figure C2. LDA Measurement in Volute Passage.

APPENDIX D:

MEASUREMENT POSITIONS

The following table presents the position used to collect the LDA measurements.

WINDOW No.	RADIUS (m)	WINDOW No.	RADIUS (m)
1	0.156	6	0.156
	0.166		0.170
	0.176		0.184
	0.186		0.198
			0.212
2	0.156		0.226
	0.170		0.240
	0.184		0.254
	0.198		0.268
			0.282
3	0.156		
	0.166	7	0.156
	0.176		0.166
	0.186		0.176
	0.196		0.186
	0.206		0.196
	0.216		0.206
			0.216
4	0.156		0.226
	0.170		0.236
	0.184		0.246
	0.198		0.256
	0.212		0.266
	0.226		0.276
	0.240		0.286
			0.296
5	0.156		0.306
	0.166		0.316
	0.176		
	0.186	8	0.156
	0.196		0.158
	0.206		0.160
	0.216		0.162
	0.226		0.164
	0.236		0.166
	0.246		0.168
	0.256		0.170

Continued

DIFFUSER 1	X-POSITION (m)	DIFFUSER 2	X-POSITION (m)
Y-POSITION = 0.100m	0.176	Y-POSITION = 0.200m	0.176
	0.186		0.186
	0.196		0.196
	0.206		0 206
	0.216		0.216
	0 226		0.226
	0.236		0 236
	0.246		0.246
	0.256		0 256
	0.266		0 266
	0.276		0.276
	0.286		0 286
	0.296		0 296
	0.306		0 306
	0 316		0 316

Table D1. LDA Measurement Positions.

The following table presents the position used to collect the pressure measurements.

WINDOW No.	RADIUS (m)	WINDOW No.	RADIUS (m)
1	0.156	5	0.156
	0.170		0.170
	0.184		0.184
			0.198
Circumferential	13		0.212
Positions(Deg)	20		0.226
Measured from	30		0.240
Window 7	40		0.254
All measurements	50		0.268
made at R=0.156m	60		
	70	6	0.156
	80		0.170
			0.184
2	0.156		0.198
	0.170		0.212
	0.184		0.226
	0.198		0.240
			0.254
			0.268
3	0.156		0.282
	0.170		
	0.184	7	0.156
	0.198		0.170
	0.212		0.184
			0.198
4	0.156		0.212
	0.170		0.226
	0.184		0.240
	0.198		0.254
	0.212		0.268
	0.226		0.282
	0.240		0.296
			0.310

WINDOW 0	X-POSITION (m)	WINDOW 9	X-POSITION (m)
Y-POSITION = 0.174m	0.170	Y-POSITION = 0.278m	0.170
	0.184		0.184
	0.197		0.197
	0.210		0.210
	0.223		0.223
	0.236		0.236
	0.249		0.249
	0.262		0.262
	0.275		0.275
	0.288		0.288
	0.301		0.301

Table D2. Pressure Measurement Positions

APPENDIX E:
REFERENCES

Abramian M. and Howard J.H.G.,1994a, "A rotating laser-Doppler anemometry system for unsteady relative flow measurements in model centrifugal impellers", ASME Journal of Turbomachinery, Vol. 116., pp.260-268.

Abramian M. and Howard J.H.G.,1994b, " Experimental investigation of the steady and unsteady relative flow in a model centrifugal impeller passage", ASME Journal of Turbomachinery, Vol. 116., pp.269-279.

Acosta A.J. and Bowerman R.D., 1957,"An experimental study of centrifugal pump impellers", Trans. ASME, pp.1821-1839.

Acosta A.J., 1954, " An experimental and theoretical investigation of two-dimensional centrifugal pump impellers", Trans. ASME, pp.749-763.

Adler D. and Levy Y., 1979, "A laser-Doppler investigation of the flow inside a backswept, closed, centrifugal impeller", IMechE Journal Mechanical Engineering Science, Vol.21, No. 1, pp.1-6.

Agarwal J.K and Johnson E.M., 1981, "Generating aerosol for laser velocimeter seeding", TSI Quarterly, Vol. III, No. 3.

Agostinelli A., Nobles D. and Mockridge C.R.,1960 , "An experimental investigation of radial thrust in centrifugal pumps", ASME Journal of Engineering for Power, pp.120-126.

Barrand J.P., Caignaert G., Canavelis R. and Guiton P.,1984,"Experimental determination of the reverse flow onset in a centrifugal impeller", Proceedings of the 1st International Pump Symposium, pp.63-71.

Barry B.A., 1978,"Errors in Practical Measurement in Science, Engineering, and Technology", John Wiley & Sons, USA.

Binder R.C. and Knapp R.T.,1958, " Experimental determinations of the flow characteristics in the volutes of centrifugal pumps", Trans. ASME, Paper No. HYD-58-4.

Bladwin B.S. and Lomax H., 1978, "Thin layer approximation and algebraic model for seperated turbulent flow", AIAA Paper 78-257.

Bowerman R.D. and Acosta A.J., 1957, "Effect of the volute on performance of a centrifugal pump impeller", Trans. ASME, pp.1057-1069.

Brownell R.B., Flack R.D. and Kosrezewsky G.J.,1985,"Flow visualisation in the tongue region of a centrifugal pump", The Journal of Thermal Engineering,Vol.4, No.2, pp. 35-45.

Busemann, A., 1928, "The delivery head of radial centrifugal pumps with logarithmic spiral blades", Z. angew. Math Mech., Vol. 8(5), 372.

Caignaert G. and Morel P.,1995,"Mean pressure measurements within a centrifugal pump impeller at partial flow rates", Conf. Proceedings Turbomachinery: Fluid Dynamic and Thermodynamic Aspects : 1st European Conf. Vol.2 Experimental fluid dynamics.

Caignaert G., Barrand J.P. and Desmet B.,1988,"Recirculation at impeller inlet and outlet of a centrifugal pump", C337/88, Proc. IMechE Conf. "Part-Load Pumping operation, control and behaviour".

Caignaert G., Desmet B., Maroufi S. and Barrand J.P., 1985, "Velocities and pressures measurements and analysis at the outlet of a centrifugal pump impeller", ASME Paper No. WA/FE-6, Miami Beach, Florida, November 17-21.

Chiappe E.A., 1982, "Pump performance prediction using graphical technique and empirical formulae", Paper No. C181/82. IMechE Conf. Proc., "Centrifugal Pumps - Hydraulic Design", London, 16th November 1982.

Combes J.F. and Rieutord E.,1992,"Numerical and experimental analysis of the flow in a centrifugal pump at nominal and partial flow rate", Presented at the International Gas Turbine and Aeroengine Congress and Exposition, Cologne, Germany, Paper No.92-GT-284.

DISA Information, 1970, "A new low-pressure transducer. For pressure measurements in fluid mechanics", No.9, February, pp. 45-46.

Dixon S.L., 1975, "Fluid Mechanics, Thermodynamics of Turbomachinery", third Edition, Pergamon Press.

Dong R., Chu S. and Katz J., 1992a, "Quantitative visualization of the flow within the volute of a centrifugal pump. Part A: technique", ASME Journal of Fluids Engineering, Vol.114, No.3, pp.390-395.

Dong R., Chu S. and Katz J., 1992b, "Quantitative visualization of the flow within the volute of a centrifugal pump. Part B: results and analysis", ASME Journal of Fluids Engineering, Vol.114, No.3, pp.396-403.

Drain L.E., 1980, "The laser doppler technique", John Wiley & Sons Ltd.

Engeda A. and Rautenberg M., 1989, "On the flow in a centrifugal pump near shut-off head with positive and negative flows", Paper No.1, Eleventh International Conference of the British Pump Manufacturers' Association, April 18-20, pp. 1-7.

FLUENT Users' Manual Version 4.4, 1996, Fluent Europe Ltd, Sheffield, UK.

Fraser S.M. and Zhang Y., 1993, "Improved k-ε modelling of impeller flow performance of a mixed-flow pump under off-design operating states", Proc. Instn. Mech. Engrs., Vol. 207, pp.219-229.

Frost T.H. and Nilsen E., 1991, "Shut-off head of centrifugal pumps and fans", Proc. Instn. Mech. Engrs, Vol. 205, pp. 217-223.

Gostelow J.P., 1977, "A new approach to the experimental study of turbomachinery flow phenomena", ASME Journal of Engineering for Power, January, pp. 97-105.

Goulas A. and Truscott G., 1988, "The flow at the tip of an impeller at off-design conditions", C336/88, Proc. IMechE Conf. "Part-Load Pumping operation, control and behaviour".

Graf E., 1993, "Analysis of centrifugal impeller BEP and recirculation flows: comparison of Quasi-3D and Navier-Stokes solutions", ASME FED - Vol.154 Pumping Machinery.

Hamill I.S., Hope C.B., Ng R,1995,"Pump-related applications of CFDS-FLOW3D",14th BPMA Technical Conference, *Using Pumps Better*, pp.653-667.

Hereau F., Kermarec J. Stoffel B. and Weiss K.,1993,"Study of internal recirculation in centrifugal impellers", ASME FED-Vol.154, Pumping Machinery, pp.151-157.

Iversen H.W., Rolling R.E. and Carlson. J.J.,1960,"Volute pressure distribution, radial force on the impeller, and volute mixing losses of a radial flow centrifugal pump", ASME Journal of Engineering for Power, pp.136-144.

Jenson L., Menon R.K., and Fingerson L.M., 1988, "An automatic signal processor for LDV systems", Presented at the Fourth International Symposium on Applications of Laser Anemometry, Lisbon, July.

Kacker S.C.,-Pennington B. and Hill R.S., 1973,"Fluctuating lift coefficient for a circular cylinder in cross flow", Report No. Tb. 27, April 1973, Design Unit, University of Newcastle-upon-Tyne.

Kannemans H., 1980, " Radial pump impeller measurements using a laser Doppler velocimeter", ASME Gas Turbine Conf., Paper No. 80-GT-94.

Kearton W.J., 1973, "Steam Turbine Theory and Practice", Seventh Edition, Pitman Publishing, Great Britain.

Kikuyama K., Minemura K., Hasegawa Y., Asakura E. and Murakami M.,1987, "Unsteady pressure distributions on the impeller blades of a centrifugal pump-impeller operating off-design", ASME Gas Turbine Conf. And Exhibition, Paper No. 87-GT-144.

Launder B.E. and Spalding D.B., 1974, "The numerical computation of turbulent flows", Comput. Methods Appl. Mech. Eng., Vol. 3, pp. 269-289.

Lawless P.B. and Fleeter S.,1993,"Rotating stall acoustic signature in a low speed centrifugal compressor part 2 - vaned diffuser", ASME International Gas Turbine and Aeroengine Congress and Exposition, Paper No. 93-GT-254.

Lennemann E. and Howard J.H.G.,1970,"Unsteady flow phenomena in rotating centrifugal impeller passages", ASME Journal of Engineering for Power, pp.65-72.

Leonard B.P. and Mokhtari S., 1990, "Beyond first-order upwinding. The ultra-sharp alternative for non-oscillatory steady-state simulation of convection", International Journal for Numerical Methods in Engineering, Vol.30, No.4, pp.729-766.

Levin A.A. and Poliokovsky,1965,"To calculate the pressure characteristic of centrifugal pumps and fans at zero discharge", Isvestya AN SSSR Energetika I Transport,2, pp.129-133.

Lipski W.,1979,"Influence of shape and location of the tongue of spiral casing on the performance of single stage radial pumps", Proceedings of the sixth conference on Fluid Machinery, pp. 673-683.

Majumdar S., 1988, "Role of underrelaxtaion in momentum interpolation for calculation of flow with non-staggered grids", Numerical Heat Transfer, Vol.13, pp.125-132.

Miner S.M., 1988, "Potential flow analysis of a centrifugal pump: Comparison of finite element calculation and laser velocimeter measurement", PhD. Thesis, University of Virginia, USA.

Miner S.M., Beaudoin R.J. and Flack R.D.,1989,"Laser velocimeter measurements in a centrifugal pump", ASME Journal of Turbomachinery, Vol. 111, pp.205-212.

Miner S.M., Flack R.D. and Allaire P.E.,1992,"Two-dimensional flow analysis of a laboratory centrifugal pump", ASME Journal of Turbomachinery, Vol. 114, pp.333-339.

Myles D.J.,1965,"A design method for mixed-flow fans and pumps." NEL Report No 177. East Kilbride, Glasgow: National Engineering Laboratory.

Nilsen E., 1989, "Centrifugal pump shut-off head and power", Final year project. Dept. of Mech. Eng., University of Newcastle-upon-Tyne, UK.

Patankar S.V. and Spalding D.B., 1972, "A calculation procedure for heat, mass and momentum transfer in three-dimensional parabolic flows", Int. Journal Heat and Mass Transfer, Vol. 15, p.1787.

Patankar S.V., 1980, "Numerical heat transfer and fluid flow", Hemisphere Publishing Corporation, Taylor & Francis Group, New York.

Patel D.P., Srivastava R.K., and Shah C.S., 1981, "Performance prediction in complete range of centrifugal pumps", Seventeenth Technical Conference, British Pump Manufacturers' Association.

Peacock G. and Goulas A., 1985, "LDA measurements of the flow at the inlet of a centrifugal pump", Paper No. 7, Ninth Technical Conference of the British Pump Manufacturers' Association, April 16-18, pp. 71-80.

Peck J.F., 1968,"Design of centrifugal pumps with computer aid", Proc. Instn. Mech. Engrs, Vol. 183, Part 1, pp. 321-352.

Peric M., Kessler R. and Scheuerer G., 1988," Comparison of finite-volume numerical methods with staggered and colocated grids", J. Computers & Fluids, Vol. 16, No.4, pp. 389-403.

Perng C.Y. and Murthy J.Y., 1993, "Sliding-mesh technique for simulation of flow in mixing tanks", Paper No. 93-WA/HT-33, Proceedings of the ASME Winter Annual Meeting, New Orleans, LA, USA, pp.1-9.

Pfleiderer C., 1961, "Die Kreiselpumpen fur Flussigkeiten und Gase", fifth edition, Springer-Verlag, Berlin.

Rai M.M., 1985, "Navier-Stokes simulation of rotor-stator interaction using patched and overlaid grids", AIAA Paper 85-1519, Reno, Nevada, Jan 14-17.

Rhie C.M. and Chow W.L., 1983, "Numerical study of the turbulent flow past an aerofoil with trailing edge separation", AIAA J., Vol. 21, No. 11, pp. 1525-1532.

Richardson E.G., 1953, "Technical aspects of sound", New York: Elsevier Pub. Co.

Roco M.C., Hamelin P., Cader T. and Davidson G., 1990, "Animation of LDV measurements in a centrifugal pump", Fluid Machinery Forum 1990, Vol. 96.

Rose M.G.,1987, "Flow in the impeller of a centrifugal water pump with three-dimensional blading", C274/87, Proc. IMechE Conf.

Sayers A.T., 1990, "Hydraulic and compressible flow turbomachines", Pub. McGraw-Hill.

Schachenmann A., Muggli F. and Guelich J.F., 1993,"Comparison of three Navier-Stokes codes with LDA measurements on an industrial radial pump impeller", ASME FED-Vol. 154, Pumping Machinery, pp.247-252.

Senoo Y. and Yamaguchi M., 1987, "A study on unstable S-shape characteristic curves of pump turbines at no-flow", Journal of Turbomachinery, Vol. 109, pp.77-82.

Simpson H.C. and Cinnamond, 1964, "Studies of flow through centrifugal pump impellers", IMechE Proc. 1963-64, Vol. 178, Pt. 3 1(ii), Paper 8.

Stepanoff A.J., 1957, "Centrifugal and axial flow pumps", John Wiley, New York; Chapman and Hall, London.

Stirling T.E.,1982,"Analysis of the design of two pumps using NEL methods", C183/82, Proc. IMechE Conf. "Centrifugal Pumps-Hydraulic Design".

Stodola A., 1927,"Steam and Gas Turbines", Vols. I and II McGraw-Hill, New York. (Reprinted, Peter Smith, New York,1945).

Stoffel B. and Weiss K., 1994, "Experimental investigation on part load flow phenomena in centrifugal pumps", Word Pumps, October,Elsevier Science Ltd, No.337, pp.46-50.

Tennekes H. and Lumley J.L., 1972, "A first course in turbulence", MIT Press, Cambridge MA.

Throne E.W.,1988, "Head and power at closed valve", C331/88, Proc. IMechE Conf. "Part-Load Pumping operation, control and behaviour".

Tourlidakis A., Elder R.L., and Tan S.C., 1995, "Applying computational fluid dynamics to real fluid machinery and pump flow problems",14th BMPA Conference, *Using Pumps Better*, April 25-27, pp.623 - 651.

Tourret J., Badie-Cassagnet G., Foucault J.P. and Kermarec J., 1985, "Experimental studies of the noise emission and noise generation from a centrifugal pump", Presented at the ASME Winter Annual Meeting, Miami Beach, Florida, November 17-21, Paper No.85-WA/FE-8.

Tourret J., Kamga M., Godefroi B., Kermarec J., Pluviose M., Bertinier M., 1991, "Hydraulic noise generation studies in centrifugal turbomachine through visualization of the non stationary pressure field in the volute and in the impeller", ASME Fluids Engineering Division (Publication) FED,Vol.128., pp.239-246.

TSI Model 9230 COLORLINK Multicolor Receiver Manual, 1994, Revision B, Part No. 1990559.

Ubaldi M., Zunino P. and Cattanei A.,1993,"Relative flow and turbulence measurements downstream of a backward centrifugal impeller", ASME Journal of Turbomachinery, Vol. 115, pp.543-551.

Ubaldi M., Zunino P., Barigozzi G. and Cattanei A., 1996, "An experimental investigation of stator induced unsteadiness on centrifugal impeller outflow", ASME Journal of Turbomachinery, Vol. 118.

Uchida N., Imaichi K. and Shirai T.,1971,"Radial force on the impeller of a centrifugal pump", Bull. Of Jap. Soc. Of Mechanical Engineers, Vol. 14, No. 76, pp. 1106-1117.

Versteeg H.K. and Malalasekera W., 1995, "An introduction to computational fluid dynamics. The finite volume method", Addison Wesley Longman Ltd.

Warfield M.J. and Lakshminarayana B.,1987,"Calculation of a three-dimensional turbomachinery rotor flow with a Navier-Stokes code", ASME Gas Turbine Conference and Exhibition, Paper No. 87-GT-232.

Whiffen M.C., 1976, "Polar response of an LDV measurement volume", Minnesota Symposium on Laser Velocimetry, ASME Paper No. 76-6T-49.

Wiesner F.J., 1967, "A review of slip factors for centrifugal impellers", Journal Engineering Power, Vol. 89(4), pp.558-572.

Wilcox D.C., 1993, "Turbulence modelling for CFD", La Canada, CA: DCW Industries Inc.

Wilcox D.C. and Chambers T.L., 1977, "Streamline curvature effects on turbulent boundary layers", AIAA Journal, Vol. 15, No. 4, pp. 574-580.

Wislicenus G.F., 1947, "Fluid Mechanics of Turbomachinery", McGraw-Hill, New York.

Worster R.C., 1963, "The flow in volutes and its effect on centrifugal pump performance", Proc. Instn Mech. Engrs, Vol. 177(31), pp 843-865.

Yakhot V., Orszag S.A., Thangam S., Gatski T.B. and Speziale C.G., 1992, "Development of turbulence models for shear flows by a double expansion technique", Phys. Fluids A, Vol.4, No. 7, pp. 1510-1520.

Yates M.K., Rhodes I.N. and Elder R.L.,1995,"The application of computational fluid dynamics (CFD) to centrifugal fuel pumps - A user's perspective",14th BPMA Technical Conference, *Using Pumps Better*, pp.669-687.

Yeddiah S., 1985, "Certain unexplained phenomena, observed in centrifugal pumps part A and B", Joint ASME/ASCE Applied Mechanics & Fluids Engineering and Bioengineering Conference, Paper No. 85-FE-3.

Yedidiah, 1993, "The drooping curve of a centrifugal pump", Proc. ROCON '93, Rotating Machinery Conf. And Exposition, Nov. 12-13, New England, USA.

Yuasa T. and Hinata T., 1979,"Fluctuating flow behind the impeller of centrifugal pump", Bulletin of the JSME, Vol.22, No. 174. Paper No. 174-7.